

Chemical Reactions in The Supramolecular Hosts

Zur Erlangung des akademischen Grades eines

DOKTORS DER NATURWISSENSCHAFTEN

(Dr. rer. nat.)

von der KIT-Fakultät für Chemie und Biowissenschaften

des Karlsruher Instituts für Technologie (KIT)

genehmigte

DISSERTATION

von

M.Sc. Xujun Qiu

aus Jiangshan, China

Dekan: Prof. Dr. Martin Bastmeyer

Referent: Prof. Dr. Stefan Bräse

Koreferent: Prof. Dr. Michael Meier

Tag der mündlichen Prüfung: 16.07.2024

"When I walk along with two others, they may serve me as my teachers. I will select their good qualities and follow them, their bad qualities and avoid them."

三人行，必有我师焉。择其善者而从之，其不善者而改之

Kong Qiu, Confucius, 孔子

Honesty Declaration

This work was carried out from January 04, 2021, through June 02, 2024, at the Institute of Organic Chemistry, Faculty of Chemistry and Biosciences at the Karlsruhe Institute of Technology (KIT), under the supervision of Prof. Dr. STEFAN BRÄSE.

Die vorliegende Arbeit wurde im Zeitraum vom 04. Januar 2021 bis 02. Juni 2024 am Institut für Organische Chemie (IOC) der Fakultät für Chemie und Biowissenschaften am Karlsruher Institut für Technologie (KIT) unter der Leitung von Prof. Dr. STEFAN BRÄSE angefertigt.

Hiermit versichere ich, XUJUN QIU, die vorliegende Arbeit selbstständig verfasst und keine anderen als die angegebenen Hilfsmittel verwendet, sowie Zitate kenntlich gemacht zu haben. Die Dissertation wurde bisher an keiner anderen Hochschule oder Universität eingereicht.

Hereby, I, XUJUN QIU, declare that I completed the work independently, without any improper help, and that all material published by others is cited properly. This thesis has not been submitted to any other university before.

German Title of this Thesis

**Chemische Reaktionen in den
supramolekularen Wirten**

Preface

Some of the presented results were published or submitted during the preparation of this thesis (*vide infra*). The relevant content is reprinted with permission from WILEY-VCH Publishing and the Royal Society of Chemistry.

If applicable, each chapter includes a list of authors with the individual contributions described briefly. Additionally, if some of the presented results have already been partly discussed in other theses, it is stated at the beginning of the respective chapters.

X. Qiu, J. Seibert, O. Fuhr, F. Biedermann, S. Bräse, *Chem. Commun.*, **2024**, 60, 3267-3270.

DOI: 10.1039/d3cc05783f

Reversing the stereoselectivity of intramolecular [2+2] photocycloaddition utilizing cucurbit[8]uril as a molecular flask

X. Qiu, Y. Wang, S. Leopold, S. Lebedkin, U. Schepers, M. M. Kappes, F. Biedermann, S. Bräse, *Small*. **2024**, 20, 2307318.

DOI: 10.1002/sml.202307318

Modulating aryl azide photolysis: synthesis of a room-temperature phosphorescent carboline in cucurbit[7]uril host

X. Qiu, E. Pohl, Q. Cai, J. Seibert, Y. Li, S. Leopold, O. Fuhr, M. A. R. Meier, U. Schepers, S. Bräse, *Adv. Funct. Mater.* **2024**, 2401938.

DOI: 10.1002/adfm.202401938

Modulating and accelerating photolysis of photoactivatable [2.2]paracyclophane aryl azide in supramolecular host for bioimaging

X. Qiu, E. Pohl, A. Jung, Q. Cai, H. Su, O. Fuhr, U. Schepers, S. Bräse, *submitted*.

Modulating the photolysis of aryl azides in supramolecular host to develop photoactivatable fluorophores

Table of Contents

Kurzzusammenfassung	1
Abstract.....	2
1. Introduction	3
1.1. Supramolecular Hosts	3
1.1.1. Macrocyclic molecules.....	4
1.1.2. Self-assembled capsules.....	5
1.1.3. Coordination cages.....	7
1.2. Cucurbit[n]urils.....	8
1.2.1. Cucurbit[n]urils based host-guest systems.....	9
1.2.2. Reactions within cucurbit[n]urils.....	11
2. Objective.....	14
3. Main Section.....	16
3.1. Reversing the Intramolecular [2+2] Photocycloaddition Stereoselectivity	16
3.2. Modulating Aryl Azide Photolysis in Aqueous	29
3.3. Modulating and Accelerating Photolysis of [2.2]Paracyclophane Aryl Azide.....	43
3.4. Modulating the Photolysis of Aryl Azides for Bioimaging	60
4. Summary and Outlook.....	76
4.1. Reversing the Intramolecular [2+2] Photocycloaddition Stereoselectivity	76
4.2. Modulating Aryl Azide Photolysis in Aqueous	76
4.3. Modulating and Accelerating Photolysis of [2.2]Paracyclophane Aryl Azide.....	77
4.4. Modulating the Photolysis of Aryl Azides for Bioimaging	77
5. Experimental Section.....	78
5.1. General Remarks.....	78
5.2. Reversing the Intramolecular [2+2] Photocycloaddition Stereoselectivity	83
5.3. Modulating Aryl Azide Photolysis in Aqueous	91

5.4.	Modulating and Accelerating Photolysis of [2.2]Paracyclophane Aryl Azide.....	100
5.5.	Modulating the Photolysis of Aryl Azides for Bioimaging	111
5.6.	Crystallographic Data	128
6.	List of Abbreviations	134
7.	Bibliography	138
7.1.	List of Publications	144
7.2.	Acknowledgments.....	146

Kurzzusammenfassung

Die supramolekulare Chemie, ein aufstrebendes Fachgebiet, erforscht intra-/intermolekulare Wechselwirkungen durch verschiedene nichtkovalente Bindungen wie ionische Wechselwirkungen, Wasserstoffbrücken, Dipol-Dipol-Wechselwirkungen, π - π -Wechselwirkungen und hydrophobe Effekte. Die Wirt-Gast-Chemie, ein zentraler Aspekt der supramolekularen Chemie, umfasst die Erkennung und strukturell komplementäre Zusammensetzung von Molekülen zur Bildung von Komplexen durch nichtkovalente Wechselwirkungen. Synthetische supramolekulare Wirte wie Käfige, Kapseln und makrozyklische Moleküle haben aufgrund ihrer potenziellen Anwendungen in Katalysatoren, Materialwissenschaften und Pharmazeutika großes Forschungsinteresse geweckt.

Unter diesen Wirten wurden Cucurbit[n]urile (CBn), die aus methylenverbrückten Glycolurilmonomeren bestehen, umfassend untersucht. Ihre hohe Affinität zur Erkennung und Bindung kationischer Gäste in hydrophoben Hohlräumen in wässrigen Umgebungen hat zu zahlreichen Anwendungen geführt, darunter als Reaktionsgefäße, Arzneimittelträger und biokompatible Hydrogele.

Chemische Reaktionen, die in den begrenzten Räumen supramolekularer Wirte stattfinden, können sich von denen in Lösung stark unterscheiden. Moleküle können in Wirtshohlräumen durch nichtkovalente Wechselwirkungen vororganisiert und komplementär arrangiert werden, was zu einer signifikanten Erhöhung der lokalen Substratkonzentration im Vergleich zur Reaktion in herkömmlichen Lösungsmitteln führt. In dieser Arbeit wurden verschiedene Photoreaktionen in wässrigen Medien und innerhalb von CBn untersucht und ihre potenziellen Anwendungen in den Materialwissenschaften und der Biologie erforscht.

Das erste untersuchte klassische Beispiel einer Photoreaktion ist die [2+2]-Cycloaddition, die mit UV-Licht einer Wellenlänge von 365 nm zwischen zwei Alkenen ausgelöst werden kann. Das Szenario wird kompliziert, wenn sich die beiden Alkene voneinander unterscheiden oder asymmetrisch sind, was aufgrund verschiedener Kombinationen möglicherweise zu einer Vielzahl an Produkten führt. Die Durchführung solcher Reaktionen innerhalb der Grenzen des Cucurbit[8]uril-Hohlraums (CB8) ermöglicht jedoch die komplementäre Organisation und Bindung von Alkenen, was zur Bildung eines einzigartigen Produkts führt.

Die zweite untersuchte Photoreaktion ist die Arylazid-Photolyse. Organische Azide sind vielseitig einsetzbar und für die Erreichung anspruchsvoller Funktionen unerlässlich. Durch Photoreaktion können Azide aktive Nitrene erzeugen, die verschiedene Reaktionswege durchlaufen können, um diverse funktionelle Produkte zu bilden. Das gleichzeitige Auftreten mehrerer Photoreaktionspfade stellt jedoch eine Herausforderung dar. Durch die Implementierung entworfenen Arylazide in CBn-Hohlräumen in wässrigen Umgebungen kann die Photolyse moduliert werden. Die hydrophobe Wand von CBn verhindert Wasserangriffe und schränkt die Molekülbewegung ein, was zur hochselektiven Bildung von C-H-aminieren Carbolinen führt. Diese in CBn-Hohlräumen erhaltenen Carboline können zur Herstellung von phosphoreszierenden Materialien bei Raumtemperatur für potenzielle Anwendungen in der Sauerstoffsensorenik verwendet werden. Die Bildung von Carbolin in CBn-Hohlräumen weist eine deutlich verstärkte Fluoreszenz auf, die für die In-situ-Überwachung von Zellen in zellulären Umgebungen genutzt werden kann.

Abstract

Supramolecular chemistry, an emerging field, explores intra/inter-molecular interactions through various non-covalent bonds like ionic interactions, hydrogen bonding, dipole-dipole interactions, π - π interactions, and hydrophobic effects. Host-guest chemistry, a key aspect of supramolecular chemistry, involves molecules recognizing and assembling with structural complementarity to form complexes *via* non-covalent interactions. Synthetic supramolecular hosts such as cages, capsules, and macrocyclic molecules have garnered significant research interest due to their potential applications in catalysts, materials science, and pharmaceuticals.

Among these hosts, cucurbit[n]urils (CB n), constructed from glycoluril monomers bridged with methylene, have been extensively studied. Their high affinity for recognizing and binding cationic guests within hydrophobic voids in aqueous environments has led to numerous applications, including reaction vessels, drug delivery carriers, and biocompatible hydrogels.

Chemical reactions occurring within the confined spaces of supramolecular hosts can differ from those in bulk solutions. Non-covalent interactions can preorganize and complementarily arrange molecules within host cavities, leading to a significant increase in local substrate concentration compared to bulk solvents. This thesis investigated various photoreactions in aqueous media and within CB n , exploring their potential applications in materials science and biology.

The first classic photoreaction example studied is [2+2] cycloaddition, which can be triggered with 365 nm UV light between two alkenes. The scenario becomes intricate when the two alkenes differ from each other or are asymmetric, potentially resulting in various products due to different combinations. However, conducting such reactions within the confines of the cucurbit[8]uril (CB8) cavity allows for the complementary organization and binding of alkenes, forming a unique product.

The second studied photoreaction is aryl azide photolysis. Organic azides are versatile and essential for achieving sophisticated functions. Photoreaction allows azides to generate active nitrenes, which can undergo various reaction pathways to form diverse functional products. However, the simultaneous occurrence of multiple photoreaction pathways poses a challenge. Photolysis can be modulated by implementing designed aryl azides within CB n cavities in aqueous environments. The hydrophobic wall of CB n prevents water attacks and restricts molecular motion, leading to the high-selectivity formation of C-H aminated carbolines. These carbolines, obtained within CB n cavities, can fabricate room-temperature phosphorescent materials for potential applications in oxygen sensing. The formation of carboline within CB n cavities exhibits significantly enhanced fluorescence, which can be utilized for in situ monitoring of cells in cellular environments.

1. Introduction

The term “supramolecular chemistry”, coined as “chemistry beyond the molecule,” gained widespread recognition following the awarding of the Nobel Prize to Donald J. Cram, Jean-Marie Lehn, and Charles J. Pedersen in 1987^[1]. Supramolecular chemistry explores functional systems driven by non-covalent interactions^[2]. These interactions encompass a range of phenomena including hydrophobic interaction^[3], hydrogen bonding^[4], halogen interaction^[5], π - π stacking^[6], dipolar interaction^[7], and ionic interaction^[8]. The diverse array of non-covalent interactions enables small molecules to recognize and assemble into well-organized structures with distinct functions^[9].

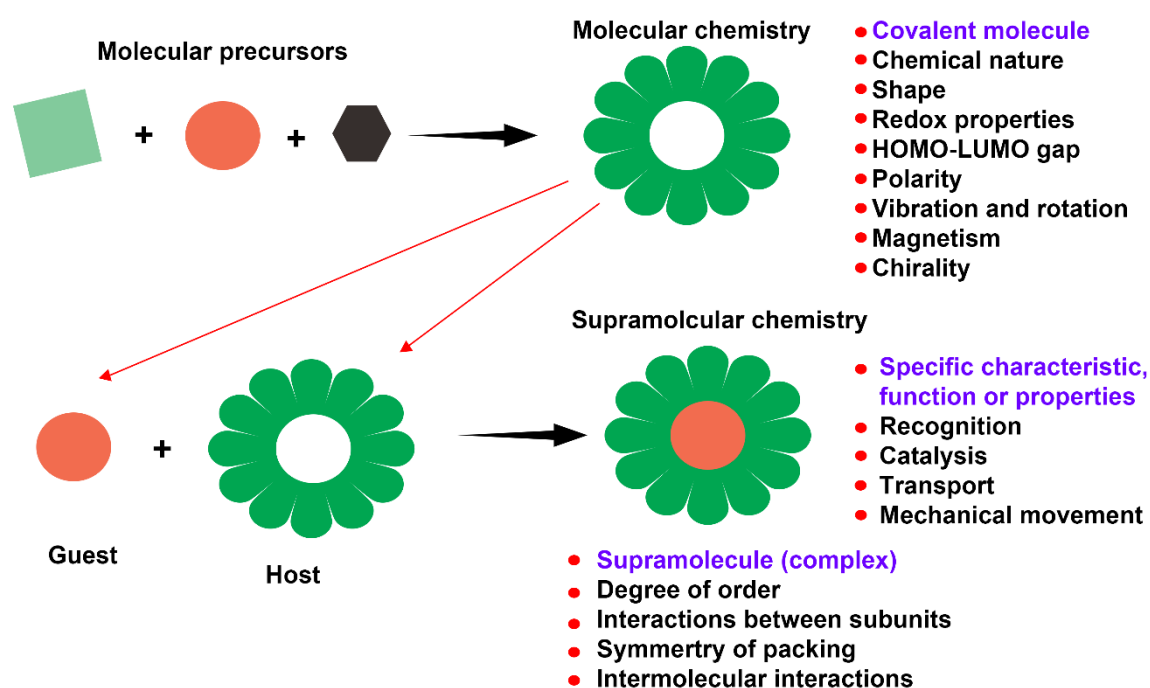


Figure 1 The scope of molecular and supramolecular chemistry comparison according to Lehn^[10].

After decades of development, supramolecular chemistry has transformed from a mere concept into a burgeoning field with practical applications from material science to biology^[11]. More recently, the Noble Prize in 2016 was allocated to Jean-Pierre Sauvage^[12], Sir J. Fraser Stoddart^[13], and Bernard L. Feringa^[14] for their discovery of molecular machines further underscored the immense potential of supramolecular chemistry.

1.1. Supramolecular Hosts

One of the fundamental concepts in supramolecular chemistry is “molecular recognition”, which entails the precise binding of two or more molecules to each other through single or multiple noncovalent interactions^[15]. Molecular recognition serves as a crucial mechanism in maintaining fundamental biological functional systems^[16], including molecule-protein interaction^[17], RNA-ribosome^[18], and antigen-antibody^[19].

Host-guest interaction involves encapsulating guest molecules within the interior space of larger molecular containers^[20]. This process demonstrates molecular complementarity and structural selectivity. Synthetic molecules, known as supramolecular hosts, have been extensively studied to mimic the natural voids found in proteins, providing confined spaces, such as nanotubes^[20] cages^[21]. Host-guest systems have witnessed significant advancements in various applications, including serving as reaction vessels^[22], separation science^[23], drug delivery^[24], and material science^[25], owing to their unique advantages.

1.1.1. Macrocyclic molecules

Molecules possessing a ring-shaped structure with a hollow internal portal, capable of accommodating smaller molecules, are favored as guest molecules can dynamically associate with the hosts^[26]. Cyclodextrins are the most abundant and classic macrocyclic hosts, constructed with repeated glucose subunits^[27]. Depending on the repeating units, typical cyclodextrins include α -cyclodextrin (α -CD, **1**) with 6 glucose units, β -cyclodextrin (β -CD, **2**) with 7 glucose units, and γ -cyclodextrin (γ -CD, **3**) with 8 glucose units, respectively. The size of the cyclodextrins has been documented with 7.9 Å height and internal diameter of 4.7-5.3 Å for α -CD, 6.0-6.5 Å for β -CD, and 7.5-8.3 Å for γ -CD, respectively^[28] (Figure 2).

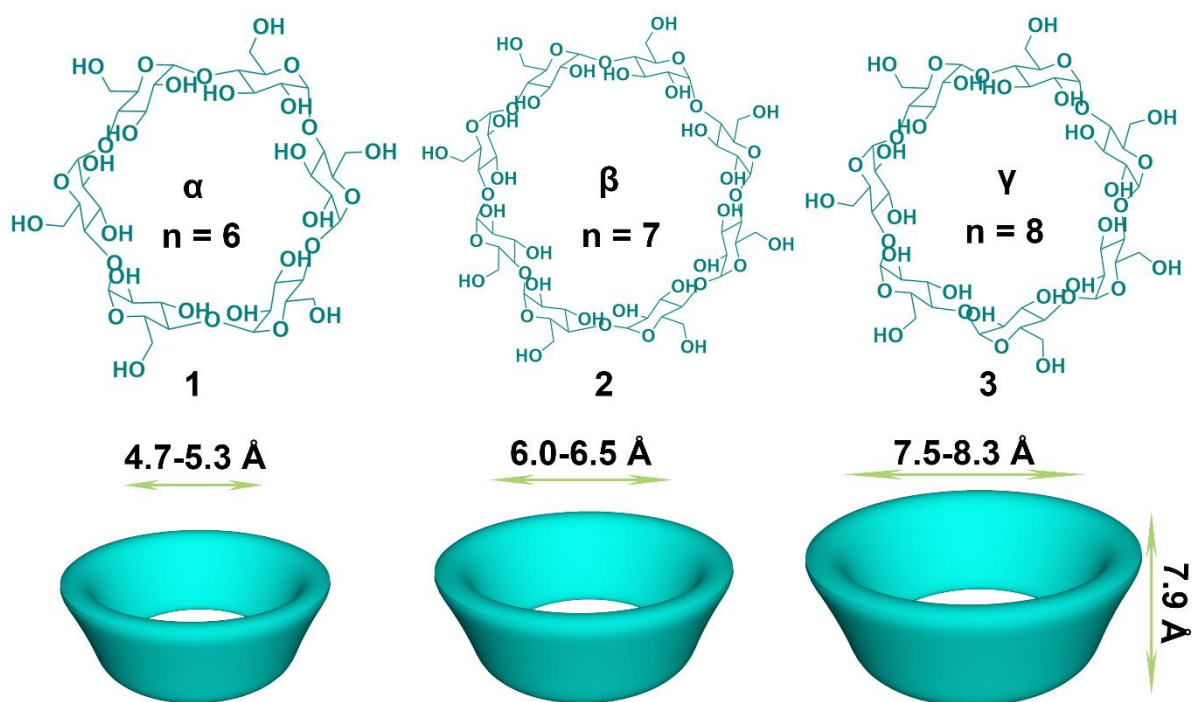


Figure 2. schematic illustration of the α -CD (**1**), β -CD (**2**), and γ -CD (**3**), and their dimensions.

Due to their water-soluble and non-toxic properties, cyclodextrins have been extensively utilized across various applications^[29], particularly in pharmaceutical science^[30]. For instance, the host-guest complexation of cyclodextrin with bioactive molecules serves as a drug delivery mechanism, enhancing the solubility of drugs and their ability to penetrate cell membranes^[31]. Additionally, the chiral secondary hydroxyl moieties in the wider ring portion of cyclodextrins enable the pure enantiomeric recognition and encapsulation of chiral molecules.

Consequently, using cyclodextrins as chiral selectors in the chiral separation of bioactive molecules has demonstrated superiority and practicality^[32].

Calix[n]arenes, another type of macrocycle constructed with methylene-conjugated phenol units^[33]. A prototypical representation of calixarene is calix[4]arene (**4**), which comprises 4 phenol units exhibiting C_4 and C_2 symmetry^[34]. The shape of calixarenes resembles a cup or basket, featuring a wider upper ring and a smaller lower ring. Possessing a hydrophobic interior cavity and modifiable hydroxyl groups, calixarenes can encapsulate small hydrophobic molecules, leading to their applications in various fields, such as drug delivery^[35], catalyst^[36], and sensors^[37].

Another class of macrocycles, pillar[n]arenes, has been discovered more recently. These macrocycles are constructed from repeated hydroquinone units connected by methylene bridges at the para-positions, resulting in two equal cavity portals with planar chirality^[38]. Among pillar[n]arenes, pillar[5]arene (**5** and **6**) is the most conformationally stable and exhibits two reversible stereoisomers, *Rp* (**5**) and *Sp* (**6**), due to their spatial arrangements^[39]. Pillar[n]arenes have been demonstrated as potential applications in drug delivery^[40], porous materials^[41], rotaxane^[42], and organic light-emitting materials^[43].

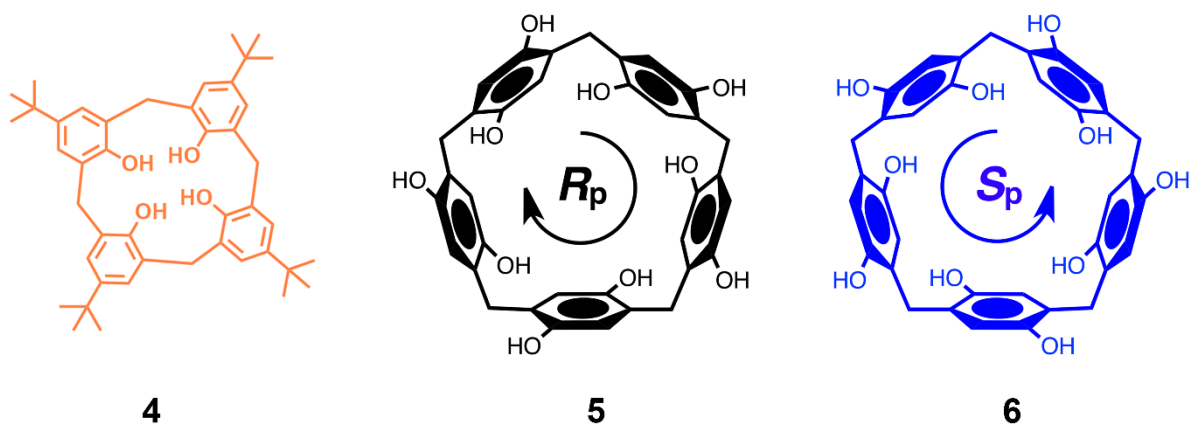


Figure 3 shows the chemical structure of a) calix[4]arene; b) pillar[5]arene two enantiomers, as shown in the graphic reproduced from Wikipedia.

1.1.2. Self-assembled capsules

Self-assembled capsules are capsule-like aggregates with voids that form spontaneously in the solution when complimentary small molecular units interact through revisable non-covalent interactions^[44]. The formation of these capsules typically involves multiple binding sites rather than single binding sites. Among the various self-assembled capsules documented, many are driven by hydrogen bonding. This is because hydrogen bonding strength ranges from weak to strong, and multiple hydrogen bonds can effectively stabilize the structures and lead to the formation of intricate capsules^[45].

Within the realm of hydrogen-bonded capsules, the most basic form is the dimeric capsule, which consists of two integral monomers. The concept of dimeric nanocapsules traces back to 1993 when Rebek^[46] identified a spherical structure held together by eight hydrogen bonds (**7**). Subsequently, larger-sized dimeric hydrogen-bonded capsules have been discovered, and their capacity for host-guest encapsulation has been extensively explored^[47].

Nevertheless, efforts to construct various hydrogen-bonded capsules have yielded positive results. For instance, the encapsulation of adamantane derivatives and tetraethylammonium cations within the cavity of tetrameric capsules (**8**) was reported^[48], highlighting how strategic design can create more complex hydrogen-bonded capsules.

Hexameric hydrogen-bonded capsules typically involve multiple and more intricate hydrogen binding interactions. These capsules have been observed to self-assemble six resorcin[4]arene (**9**) monomers in solution^[49]. With the giant cavity, hexameric capsules can capture multiple guests spontaneously. With their spacious cavities, hexameric capsules can capture multiple guest molecules spontaneously. Their reversible assembly properties allow for the accommodation of new guest molecules and the release of previously encapsulated guests from the microenvironment. As a result, hexameric capsules have been identified as excellent supramolecular catalysts.^[50] For instance, Tiefenbacher demonstrated the utility of self-assembled hexameric resorcinarene capsules as reaction chambers and metal-free catalysts for various chemical reactions, including acetal hydrolysis^[51], terpene cyclization^[52], and carbonyl-olefin metathesis^[53].

On the contrary, documentation on hydrogen-bonded octameric (**10**) and decameric (**11**) capsules is relatively sparse. This scarcity could be attributed to the exceptionally vast internal cavity, which may compromise the stability of the capsule and result in a more unpredictable structure. Mastalerz^[54] reported an octameric hydrogen-bonded capsule using a chirality-assisted synthesis strategy, highlighting the importance of employing enantiopure monomers to construct stable capsules. This strategy was further evidenced in another octameric capsule^[55]. Orentas^[56] employed solvent as a pivotal tool to break the symmetry of the monomer building blocks, successfully designing an unconventional decameric capsule. This breakthrough may pave the way for a novel class of larger capsules.

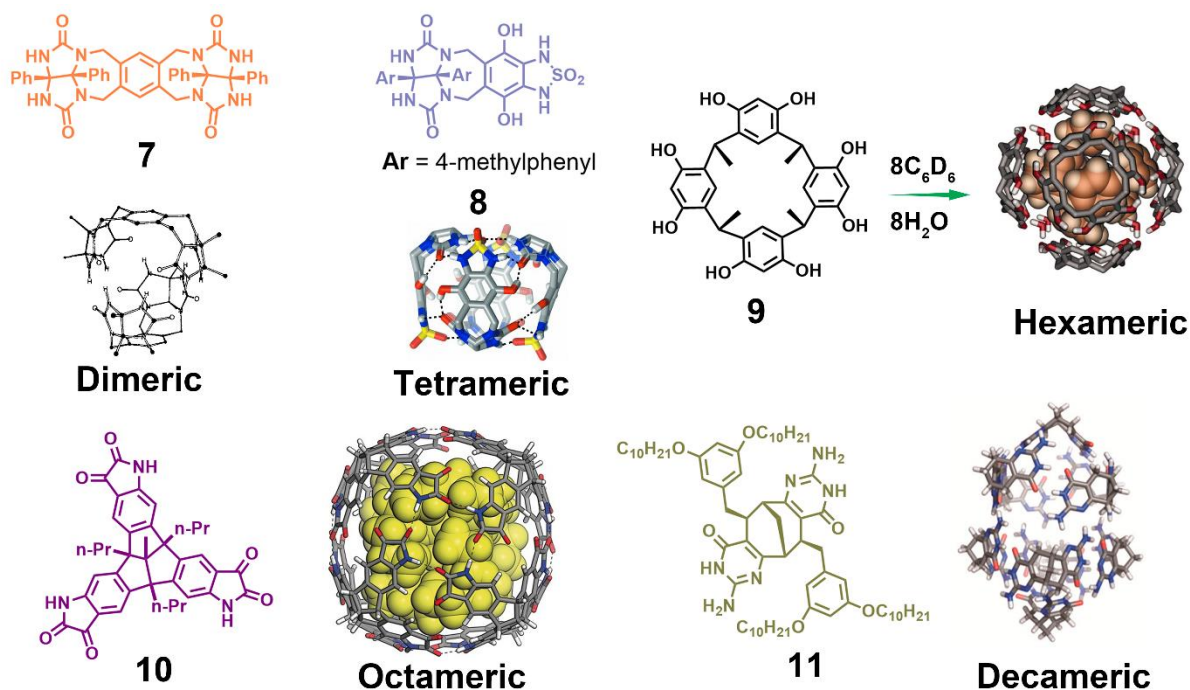


Figure 4. Self-assembled hydrogen-bonded capsules. Graphic reproduced from references^[47a, 48-49, 54, 56].

1.1.3. Coordination cages

In contrast to hydrogen-bonded capsules, coordination cages, constructed by stronger metal ion complex interactions with ligands, exhibit higher rigidity and stability. The rational design of coordination cages involves carefully selecting suitable combinations of metal ions and organic ligands. Metal ions determine the binding directions, symmetry, and kinetic lability, while organic ligands dictate the dimensions and size of the coordinated architectures^[57]. The formation of coordination cages under thermodynamic conditions is crucial because the association and dissociation of metal ions and ligands are reversible. This ensures the most thermodynamically stable cages are formed, thanks to the anti-error checking process during metal-ligand breakage and re-conjugation.

Depending on the composition of ligands, coordination cages can be classified into homometallic and heterometallic cages. Pioneering work by researchers such as Fujita^[58], Raymond^[59], Nitschke^[60], and Yoshizawa^[61] has showcased the potential of creating and utilizing diverse and intricate coordination cages.

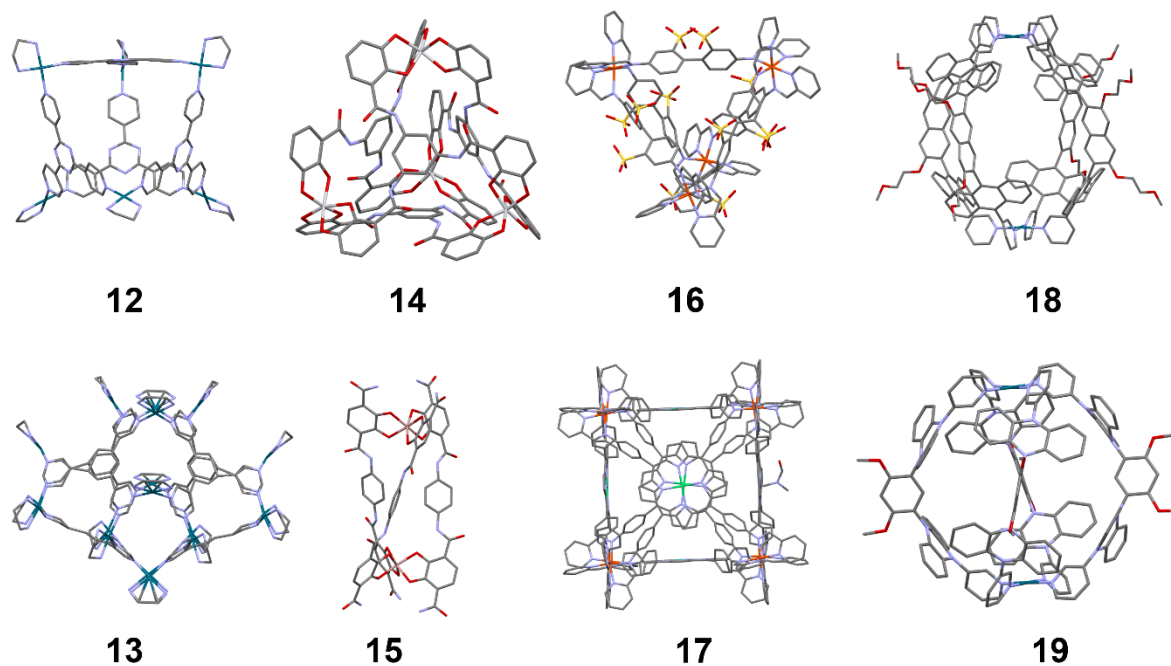


Figure 5. Selected coordination cages. Graphic reproduced from references^[58-61]

1.2. Cucurbit[n]urils

Cucurbit[n]urils (CB n) are macrocyclic molecules resembling a pumpkin shape, composed of glycoluril subunits linked by methylene bridges. The carbonyl groups are positioned along the ring's edges, slightly inclined toward the center, creating interpenetrating cavities^[62]. The size of the portals and the volume of the cavities in cucurbit[n]urils are determined by the arrangement of the repeated glycoluril monomers.

The first successful synthesis of cucurbituril dates back to 1905,^[63] achieved through the condensation of glycoluril and formaldehyde in hydrochloric acid. The crystallographic structure was later confirmed in 1981^[64]. Commonly studied cucurbit[n]urils include cucurbit[5]uril (CB5), cucurbit[6]uril (CB6), cucurbit[7]uril (CB7), cucurbit[8]uril (CB8), and cucurbit[10]uril (CB10), which are constructed by 5, 6, 7, 8, and 10 glycoluril units, respectively. These CB n vary in cavity diameters, ranging from 4.4 Å for CB5 to 12.4 Å for CB10, with a height of 9.1 Å. Their cavity volumes also differ, which feature values 82 Å³ for CB5, 164 Å³ for CB6, 279 Å³ for CB7, 479 Å³ for CB8, and 870 Å³ for CB10, respectively^[65].

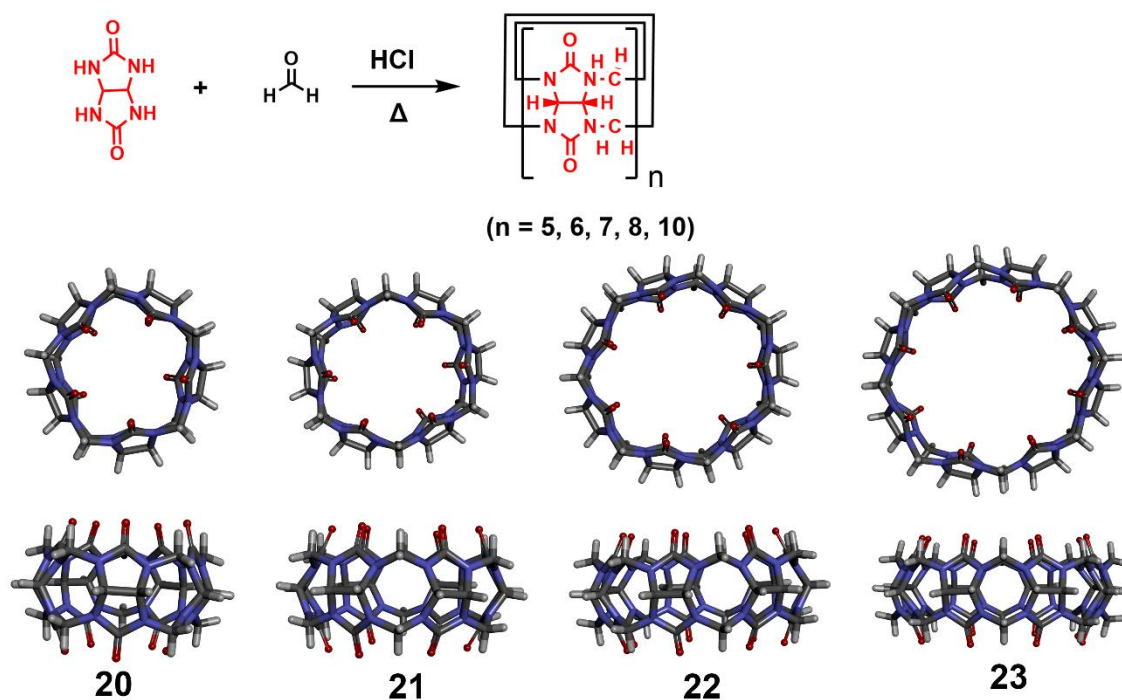


Figure 6. Cucurbi [n]turils are synthesized by condensation of glycoluril and formaldehyde in the hydrochloride and the structures of CB5, CB6, CB7, and CB8.

Table 1. The summary of the parameters of CBn^[66].

	CB5 (20)	CB6 (21)	CB7 (22)	CB8 (23)
portal diameter (Å)	2.4	3.9	5.4	6.9
cavity diameter (Å)	4.4	5.8	7.3	8.8
cavity volume (Å³)	82	16.4	279	479
outer diameter (Å)	13.1	14.4	16.0	17.5
height (Å)	9.1	9.1	9.1	9.1

1.2.1. Cucurbit[n]urils based host-guest systems

With the highly symmetric cavity, where no existing electronic pair or any other functional groups, the interior voids of CBn are featured as highly hydrophobic, which shows a priority to accommodate hydrophobic molecules. With the negatively charged carbonyl moieties located at the portals of the ring, ion-dipole interaction can occur, which leads to the attraction of the positively charged cation species^[62]. The electrostatic potentials

(EP) of CB_n (Figure 7) indicate high electron density at the two portals, underscoring their diverse cation capture capabilities^[67].

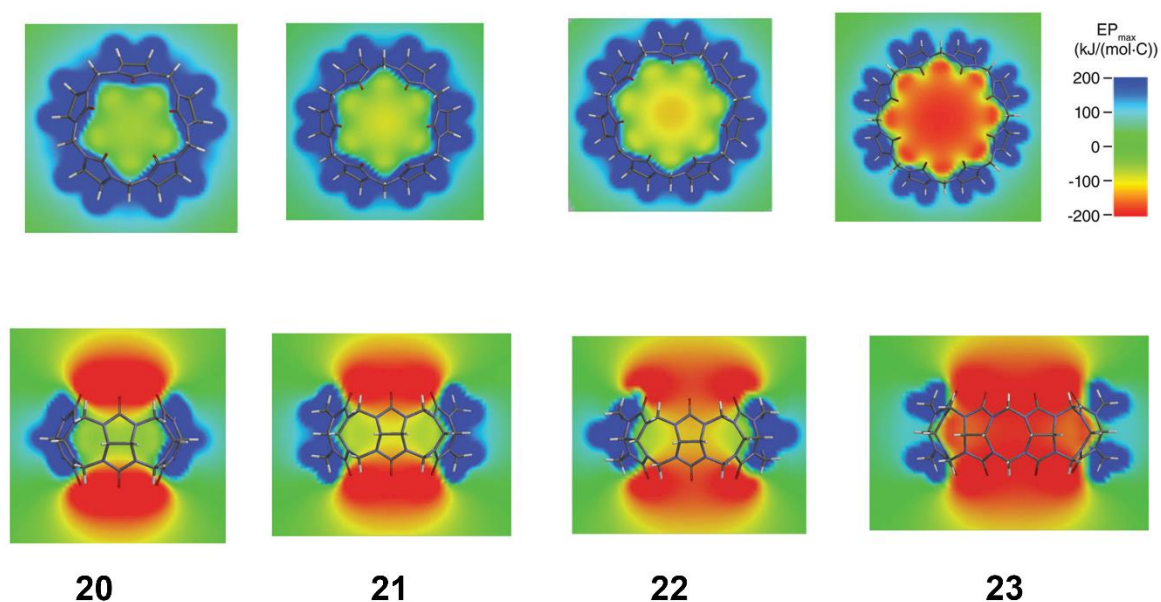


Figure 7. The electrostatic potentials of CB_5 (**20**), CB_6 (**21**), CB_7 (**22**), and CB_8 (**23**). Graphic reproduced from reference^[67].

The structured nature of the CB_n determines their solubility in polar solvents like water and dimethyl sulfoxide. Nevertheless, investigating host-guest relations with CB_n typically occurs in aqueous environments, where water can solvate the cationic guests and bind strongly with CB_n . Encapsulation of other cationic guests involves competitively breaking in and releasing the high-energy water, which accumulates within the hydrophobic cavity volume through hydrogen bonding. This process can be clarified as isolated water within the cavity of CB_n features with less hydrogen bonding than those in the bulk water media, resulting in high energy^[68]. In the meantime, when a guest molecule enters and expels the energetically suppressed water molecules, it can lead to a lower energy system, which provides a large enthalpy and entropy gain to form a stable host-guest complex.

Another parameter to evaluate the stability of CB_n host-guest complexes is the packing coefficient (PC), which can be defined as the ratio of the guest molecule size to the host cavity capacity. A PC value of approximately 55% is considered the best binding affinity of the guest-host system^[69]. By studying the known guests, the packing coefficient of the common CB_n can be estimated as 47% for CB_5 , 58% for CB_6 , 52% for CB_7 , and 53% for CB_8 , respectively^[70].

Lastly, CB_n tends to encapsulate structurally complimentary guests, minimizing the inclusion energy in a key-and-lock manner. Hydrophobic effects, ion-dipole interactions, and packing coefficients are key driving forces for forming stable host-guest complexes with CB_n . The binding affinity of these complexes can be evaluated by a binding constant ($\log K$), which can be determined by different techniques, such as nuclear

magnetic resonance (NMR) spectroscopy, ultraviolet-visible spectrophotometry (UV-Vis), fluorometer (FL), and isothermal titration calorimetry (ITC)^[71].

To date, the host-guest chemistry of CB n has been extensively investigated, ranging from primarily fundamental studies to cutting-edge applications in various areas, highlighting its versatility. In pharmaceutical science, the low toxicity and biocompatibility of the CB n macrocycles enable them to be applied in capturing bioactive molecules and transferring them through the cell membrane as drug delivery cargo^[72]. In biomaterial science, applying high binding affinity guests with CB n assembling with bio-degradable polymers can be used as biogels for cell cultures^[73]. In the field of organic luminescent material science, the stiff and hydrophobic walls provided by CB n effectively protect encapsulated chromophores from oxygen, moisture, and impurities, thereby significantly enhancing photophysical properties such as room temperature phosphorescence (RTP)^[74]. In sensing applications, the binding or exchanging of an encapsulated guest within the CB n inner cavities can cause noticeable electronic changes in the surroundings, which can be observed by NMR spectra, absorption spectra, fluorescence spectra, and other techniques^[75].

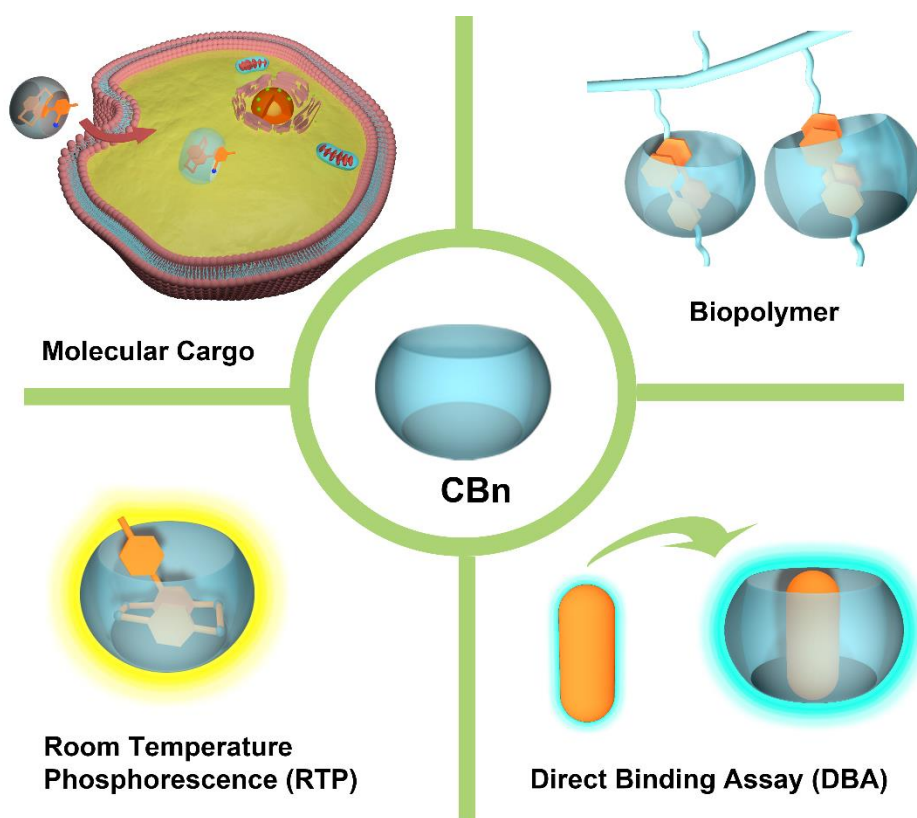


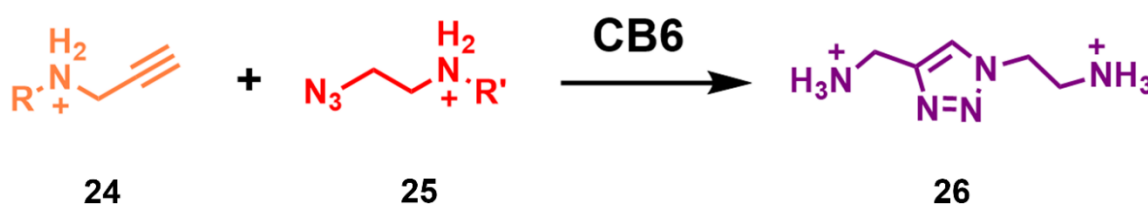
Figure 8. The applications of CB n in different fields.

1.2.2. Reactions within cucurbit[n]urils

Reactions within confined spaces often differ from those in bulk solvents. The microenvironment provided by the host can selectively accommodate the reaction substrates, allowing the reagents to pre-organize in a manner that results in the substrates better interacting with each other and the reaction rates being tuned. Additionally, the complimentary encapsulation of reagents can lead to high selectivity in product formation.

Consequently, implementing reactions in the supramolecular hosts has become a burgeoning topic, offering new synthetic approaches to more complicated reactions that are not feasible in bulk reaction conditions^[76].

Chemical reactions implemented within the CB n cavities have been extensively investigated^[77], and numerous types of chemical reactions, such as 1,3-dipolar [3+2] cycloadditions, hydrolysis reactions, oxidation reactions, Diels-Alder reactions, and photoreactions. The first example of using CB6 as a reaction catalyst and template was reported by Mock and coworkers^[78] in 1989 (Scheme 1), where azide (**24**) and alkyne (**25**) were found forming triazole product **26** within the CB6 cavity, with the reaction being catalyzed as well. With this fundamental discovery being established, more following application works have been explored, including click reactions on protein surfaces for the modification^[79] and construction of rotaxanes^[80] and polyrotaxanes^[81] using this strategy.



Scheme 1. The [3+2] cycloaddition of azide (**24**) and alkyne (**25**) forming triazole product (**26**) tuned by CB6.

Nau^[82] and Garica-Rio^[83] reported that hydrolysis processes can be catalyzed with CB n . The mechanism behind this catalytic reaction can be attributed to the host-guest complexation causing a pK_a change upon the photolysis, facilitating the necessary protonation of the guest molecule. Regarding oxidation reactions mediated by CB n cavities, Zhu and coworkers^[84] found that the oxidation of alcohols can be catalyzed by adding CB8, which shows a crucial relation with the reaction temperature and pH. Readdy and coworkers^[85] demonstrated that using a halogen-CB6 complex can efficiently accelerate the Prins cyclization. Tao and coworkers also revealed that the furan and thiophene oxidation reaction in the aqueous media can be tuned by HemiCB6, where the protonation of HemiCB6 reduces the pH, resulting in the speeded-up oxidation process of the substrates.

Another typical reaction, the Diels-Alder reaction, a type of pericyclic reaction when diene and dienophile moieties cyclic form a cyclohexane product, has also been reported to be catalyzed within the CB7 cavity^[86] and designed guest molecules with diene and alkene moieties, once encapsulation and preorganization within the CB7, are brought into proximity to facilitate the Diels-Alder reaction. This process is further accelerated by the confined rigid space of the CB7 cavity, which can adjust the conformation of the reagents and the hydrophobic microenvironment, which promotes the reaction.

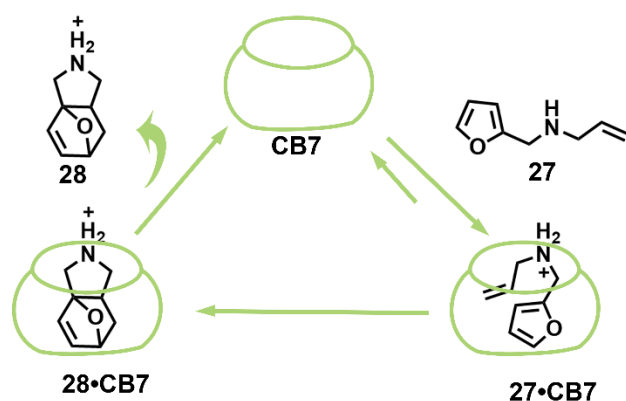


Figure 9. CB7 catalyzed Diels-Alder reaction—graphic reproduced from reference^[86a].

The most prevalent reactions observed within the CB_n cavity are photoreactions. The photophysical properties of the reagents undergo significant changes upon complexation with CB_n , and the rigidly confined space can also shield them from solvent effects. For instance, Kim and coworkers^[87] reported the first case of CB8-catalyzed photodimerization, where alkenes are accommodated within the restricted cavity, forming a 2:1 host-guest complex that can extensively enhance the reaction selectivity. As larger-sized products are formed, they can be expelled from the cavity, allowing new reagents to be introduced simultaneously, thus facilitating the dimerization process. This dimerization process can be exploited to fabricate supramolecular polymers^[88] and hydrogels^[89].

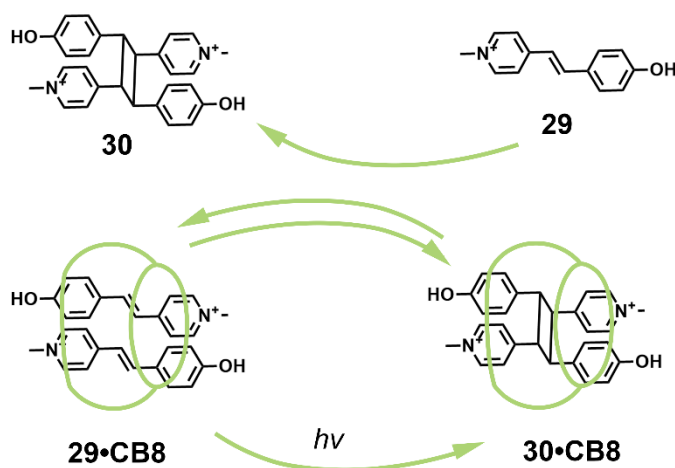


Figure 10. CB8-catalyzed photodimerization—graphic reproduced from reference.

2. Objective

Cucurbit[n]urils feature hydrophobic and rigid walls with two electrons negatively charged portals. Within these confined spaces, chemical reactions can take place. Moreover, due to their non-toxic and water-soluble properties, chemical reactions within CBn can be conducted under biocompatible conditions, such as within cellular environments. This thesis explored various chemical reactions, predominantly photoreactions, within the CBn cavities and their potential applications. (Figure 11).

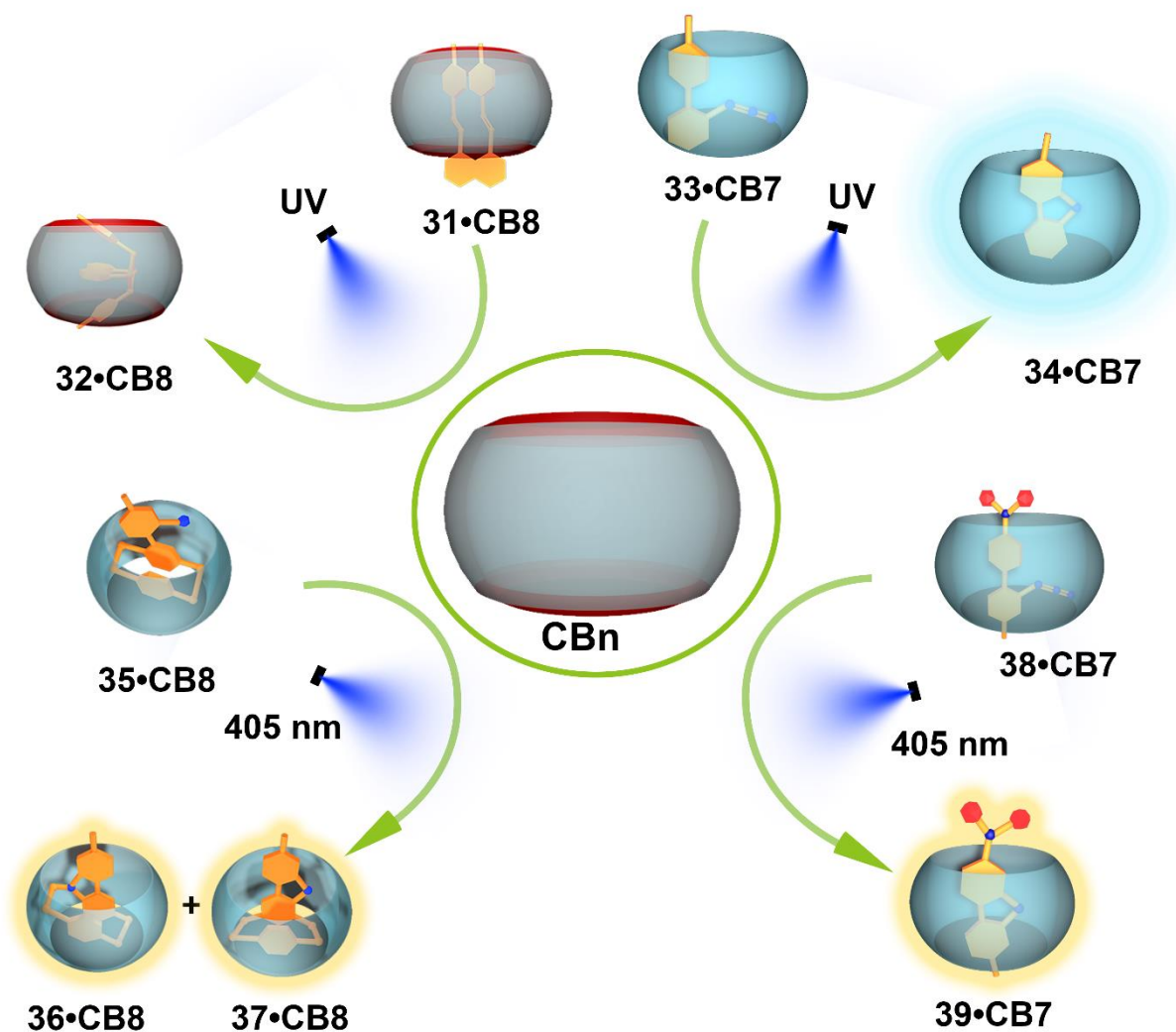


Figure 11. photoreactions modulated by CBn studied in this thesis

In the first part of the thesis, a water-soluble naphthyl molecule incorporating two olefin moieties was designed, and its photoreaction in the bulk water was investigated, which predominantly formed an anti-head-to-tail (1,3) [2+2] photoreaction product. On the contrary, when the molecule was restricted within the $CB8$ cavity, the photoreaction pathway was altered, yielding a syn-head-to-tail (1,3) [2+2] product with a significantly increased binding constant with $CB8$. No reaction occurred upon the irradiation when the two olefins were immobilized by a 1,4-bis(bromomethyl)benzene bridge. Intriguingly, when the photoreaction took place within $CB8$, a syn-head-to-head (1,2) product was obtained. These findings underscore the potential for

modulating stereoselectivity within the CB8 cavity and the prospect of inducing reactivity in otherwise unreactive reagents.

In the second part of the thesis, an aryl azide was meticulously crafted and synthesized, followed by an investigation into its photolysis in bulk water. This process predominantly yielded azepine derivatives through intramolecular rearrangement. However, when this reaction was confined within the protective embrace of the CB7 cavity, it formed a carboline derivative *via* a C-H amination reaction. The resulting carboline and CB7 complex exhibited long-lived room temperature phosphorescence (RTP) in the solid state, extending lifetimes to 2.1 s. These results underscore the capacity of supramolecular hosts to influence the photolysis of aryl azides and facilitate the development of innovative pure organic phosphorescent materials.

In the third part of the thesis, a [2.2]paracyclophane (PCP) based aryl azide was designed and studied. The photolysis of this aryl azide unveiled three distinct pathways, resulting in the formation of three distinct carboline derivatives exhibiting remarkably enhanced fluorescence. Intriguingly, when this photoreaction occurred within the confines of the CB8 host, water was effectively excluded, accelerating the reaction and modulating the product ratio. Furthermore, this photoreaction was applied within live cells, offering promise in optical imaging.

Aryl azides featuring push-pull structures were meticulously designed and synthesized in the fourth part of the thesis. Their photoreaction was meticulously controlled within the CB7 cavity, resulting in the formation of emissive carbolines. The mechanism underlying this "turn-on" phenomenon was elucidated through time-dependent density functional theory (TD-DFT) calculations. Ultimately, this photoactive process was effectively employed in mitochondria-targeted optical imaging.

3. Main Section

3.1. Reversing the Intramolecular [2+2] Photocycloaddition Stereoselectivity

Preface

Parts of the following chapter were published in *Chemical Communications* (Royal Society of Chemistry, RSC)

X. Qiu, J. Seibert, O. Fuhr, F. Biedermann, S. Bräse, Reversing the Stereoselectivity of Intramolecular [2+2] Photocycloaddition Utilizing Cucurbit[8]uril as a Molecular Flask. *ChemComm.*, **2024**, 60, 3267-3270.

Author contributions. The first author contributed to the study conception, design, material synthesis, data collection, analysis, and manuscript preparation. J. Seibert contributed to the data analysis, and O. Fuhr contributed to the X-ray analysis.

Acknowledgments. This work is supported by the China Scholarship Council (CSC grant: 202010190002) and the Deutsche Forschungsgemeinschaft (DFG) under Germany's Excellence Strategy – 3DMM2O – EXC-2082/1–390761711.

Introduction

Cyclobutanes, with their inherently strained scaffold, play a crucial role in many natural products and biological systems.^[90] Synthetic approaches to cyclobutanes typically involve inter/intramolecular [2+2] photocycloadditions using olefin precursors.^[91] Intramolecular [2+2] cycloadditions are widely used to synthesize bioactive natural products.^[92] However, precisely controlling the stereoselectivity of these photo [2+2] cycloadditions remains an unneglectable challenge.

Recent advances in performing organic reactions within “molecular flasks,” particularly using supramolecular hosts like macrocycles,^[77, 93] cages^[94], and capsules^[50, 95], have opened up novel reaction pathways. The microenvironment controls the reactivity and selectivity of reagents, *e.g.*, the confined space within the voids of molecular flasks helps to preorganize the substrates,^[96] thereby modulating reaction rates and guiding reactions differently than in bulk solutions.

Cucurbit[*n*]urils (CB*n*) are notable for their symmetrical, rigid, and hydrophobic cavities capable of hosting other molecules.^[62, 65] These nanocavities are excellent at binding with hydrophobic molecules in aqueous environments, while the carbonyl-fringed portal regions provide enhanced binding affinity for cationic guests. Consequently, CB*n* has been used both as reaction vessels and as supramolecular catalysts^[97] to control or accelerate organic reactions, including Diels-Alder reaction, 1,3-dipolar Huisgen cycloaddition^[80a, 98], and photodimerization^[88, 99].

This subchapter synthesized and characterized a naphthyl derivative with two olefin moieties (**31**). The photolysis of compound **31** in the bulk water was investigated, revealing an intramolecular [2+2] cycloaddition process that preferentially yielded an *anti*-head-to-tail (1,3) product (**40**). This process was altered when the

reaction occurred within the CB8 cavity, resulting in a *syn*-head-to-tail (1,3) product (**32**) with a significantly enhanced binding constant. Additionally, no photoreaction occurred upon irradiation when the molecule was constrained using a 1,4-bis(bromomethyl)benzene bridge (**41**). However, encapsulating molecule **41** within the CB8 cavity activated the unreactive diene, leading to a *syn*-head-to-head (1,2) product **42** (Figure 12).

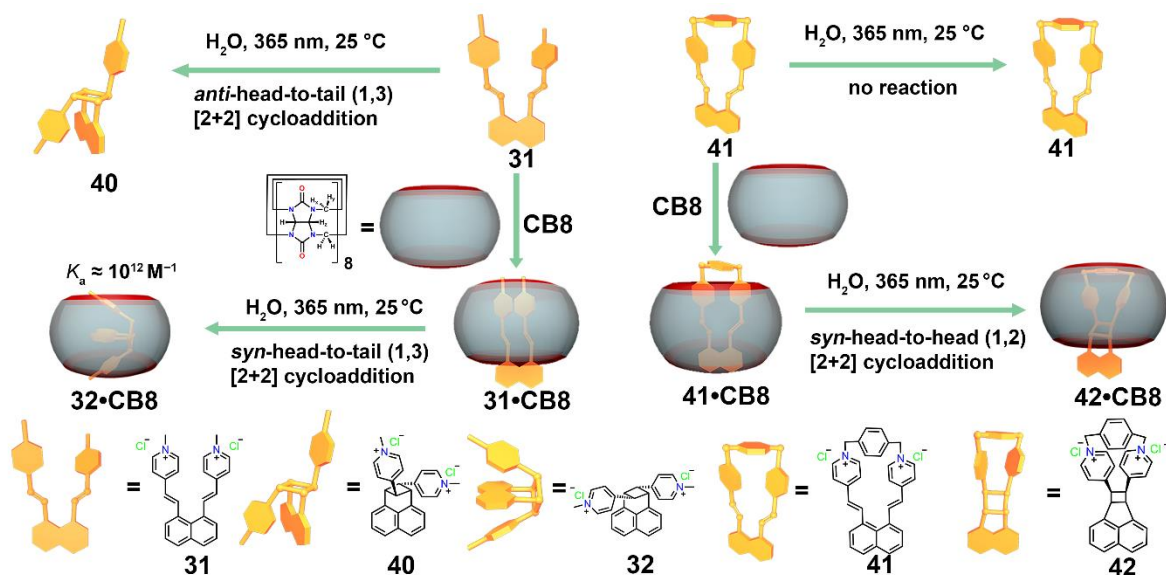
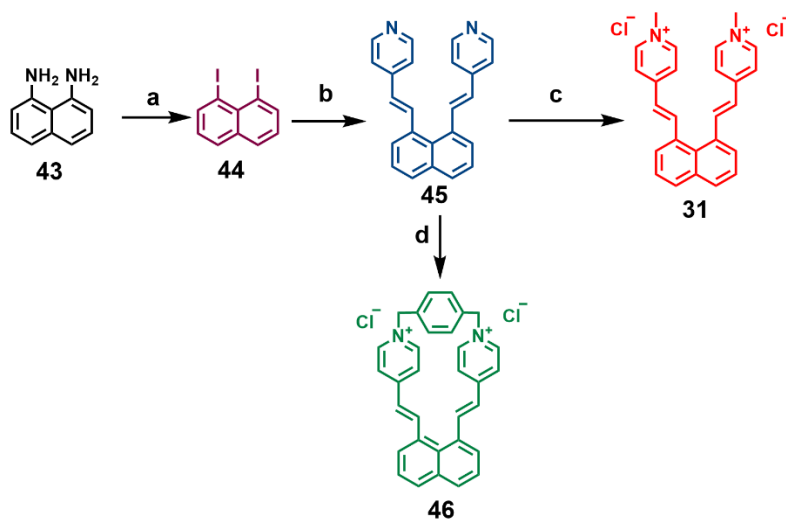


Figure 12. Schematic illustration of modulating the photoreaction process to different products using CB8 as a molecular flask.

Synthesis. The synthesis of the designed dienes is straightforward: the precursor diiodonaphthalene (**43**) was synthesized by the conversion of amines to iodine from 1,8-diaminonaphthalene (**44**)^[100]. After the palladium-catalyzed Heck reaction^[101], the pyridine diene was formed (**45**), and after the methylation and ion exchange, the desired diene (**31**) was obtained. The bridged diene (**46**) was obtained by reacting **45** with 1,4-bis(bromomethyl)benzene.



Scheme 2. a) NaNO_2 (3.0 equiv), H_2SO_4 , KI (6.1 equiv), H_2O , $-20\text{ }^\circ\text{C}$ to $80\text{ }^\circ\text{C}$, 30 min (46 %); b) vinylpyridine (4.0 equiv), $\text{Pd}(\text{OAc})_2$ (0.02 equiv), $\text{P}(\text{o-tol})_3$ (0.04 equiv), TEA, $90\text{ }^\circ\text{C}$, 48 h (67 %); c) MeI (4.0 equiv), AgCl (4.0 equiv), DMF, H_2O , $50\text{ }^\circ\text{C}$, 92%; d) 1,4-Bis(bromomethyl)benzene (1.0 equiv), TBAI (0.1 equiv), DMF, $50\text{ }^\circ\text{C}$, 63%.

Results and discussion.

The photolysis of compound **31** was conducted in a standard LZC-4X photoreactor, equipped with 14 UVA (365 nm) lamps, including six on the top and eight on the side. The reaction mixture was placed in a four-face quartz cuvette with stirring and positioned in the center of the photoreactor. During the irradiation, the ^1H NMR peaks corresponding to compound **31** gradually disappeared, while new signals of a single intramolecular cycloaddition product emerged. After about 18 minutes of UV exposure, no further significant changes were observed in the NMR spectra, signaling the completion of the photolysis (Figure 13). The photoreaction process was also monitored using UV absorbance and fluorescence emission, which confirmed that the reaction was completed within approximately 18 minutes.

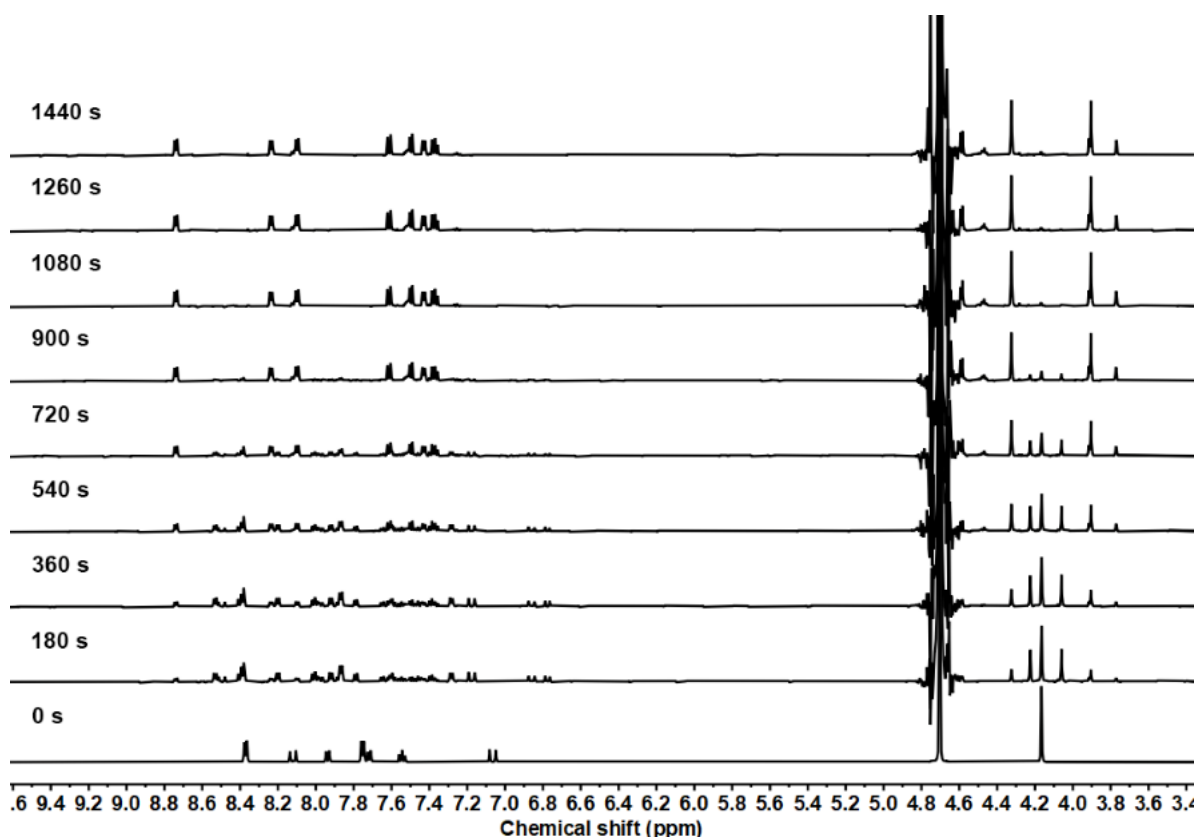


Figure 13. ^1H NMR spectra of **31** (0.5 mM) photolysis after different reaction times, 500 MHz, D_2O (4.79 ppm).

The structural analysis of the product peaks indicated that UV irradiation of compound **31** in water leads to photoisomerization and [2+2] cycloaddition, resulting in an *anti*-head-to-tail (1,3) product (**40**). This dissymmetric configuration minimizes the charge repulsion between the pyridinium moieties, the ^1H NMR spectrum can be seen in Figure 14.

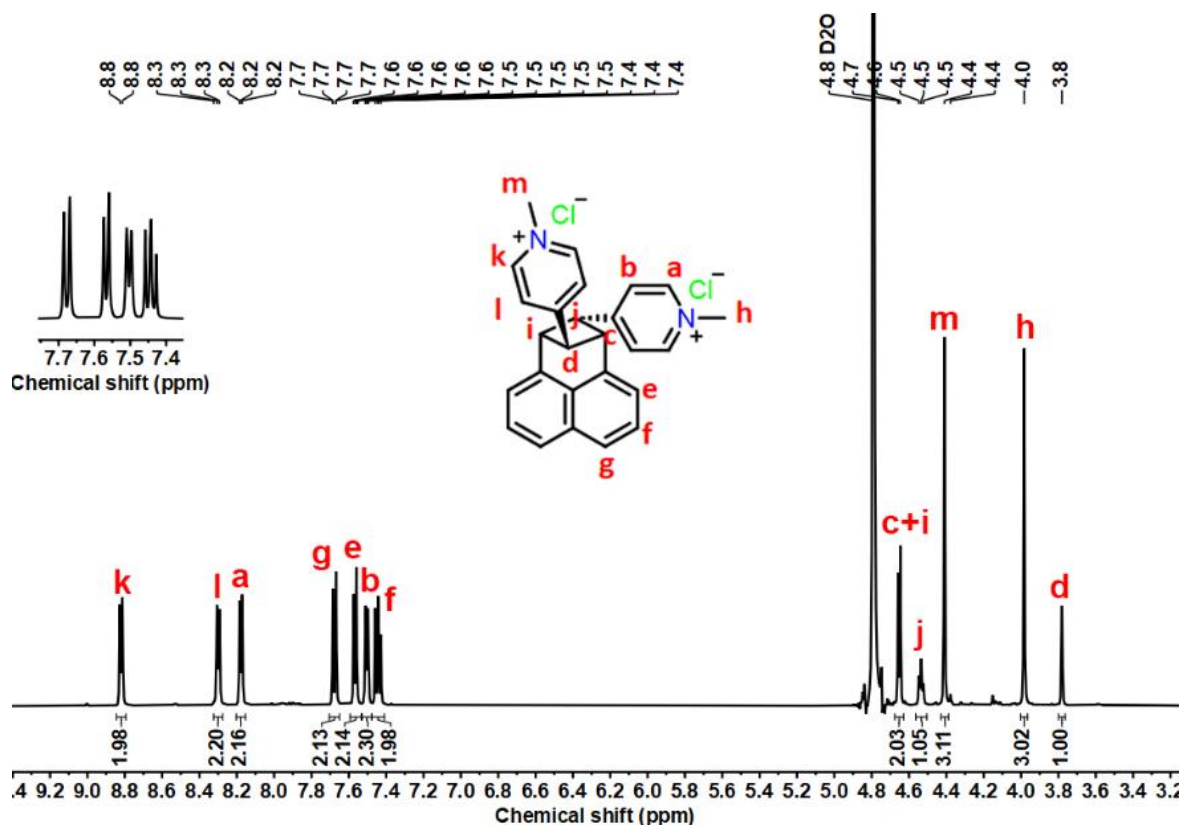


Figure 14. ^1H NMR spectra of **40**, 500 MHz, D_2O (4.79 ppm).

To investigate how a confined environment affects the photoreaction process, assumption was proposed that the photoisomerization of compound **31** could be inhibited within the cavity of a molecular host, altering the outcome of the [2+2] cycloaddition. The water-soluble molecular host CB8 was chosen for this study due to its spacious and hydrophobic cavity, which is capable of simultaneously accommodating both vinylpyridinium residues of compound **31**. The host-guest properties between compound **31** and CB8 were examined using ^1H NMR to test this binding hypothesis.

As shown in Figure 15a, when an aqueous solution of compound **31** and CB8 was mixed in a 1:1 ratio in D_2O , the NMR signals a-d, corresponding to the vinylpyridinium residues, exhibited significant upfield shifts, indicating these residues were bound inside the shielding CB8 cavity. In contrast, the peaks associated with the naphthyl moieties exhibited slight downfield shifts, indicating that these moieties are likely positioned outside or near the edge of the CB8 portal^[102]. Notably, the signals H_x and H_y from CB8 split into four sets, reflecting the deformation of CB8 upon accommodating compound **31** within its cavity. The formation of the 1:1 complex of **31**•CB8 was further confirmed by ESI-MS experiments (Figure 15d), which revealed a peak with a mass-to-charge ratio (m/z) of 846.2923 corresponding to $[\mathbf{31}\cdot\text{CB8}\cdot 2\text{Cl}]^{2+}$.

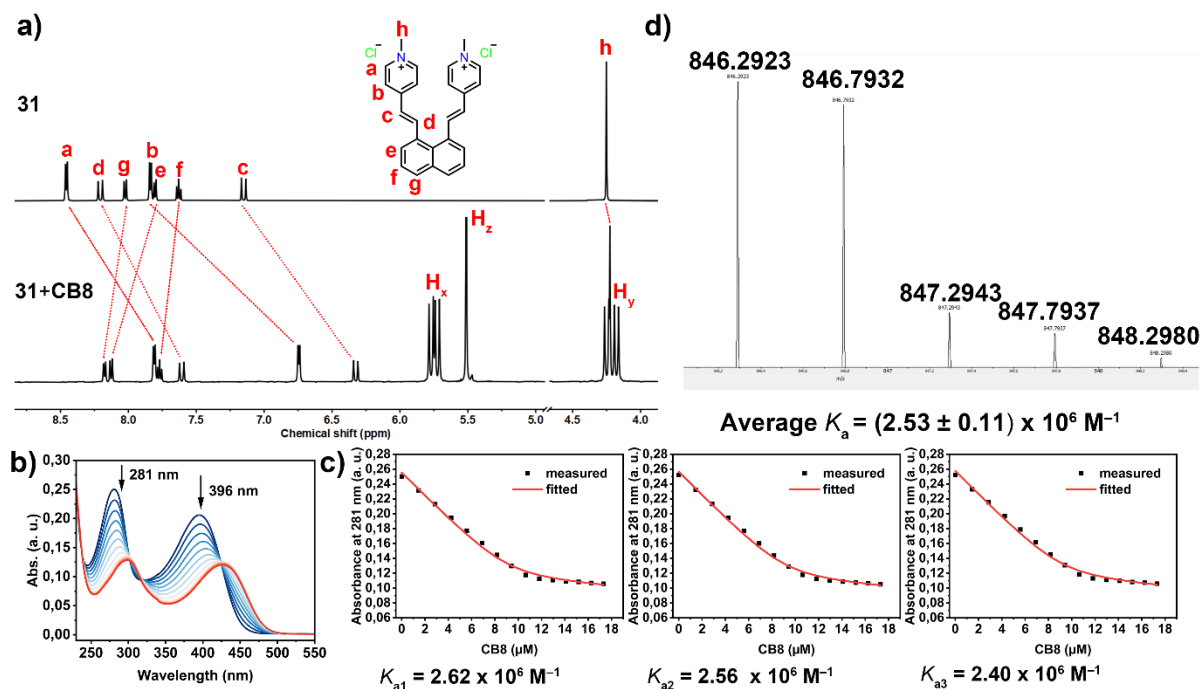


Figure 15. a) Partial ¹H NMR spectra of **31** (0.5 mM) and **31**+CB8 (1:1, 0.5 mM) in D₂O; b) UV–vis titration spectra of **31** (**31** = 10 μM) upon addition of CB8 (CB8 = 0–17.3 μM) in an aqueous solution at 298 K; c) Least-square curve fitting of the UV absorbance changes at 281 nm against the concentration of CB8 for binding constant between **31** and CB8 determining; d) HRESI-MS spectra of **31**•CB8 (1:1), HRESI-MS(m/z): [M-2Cl]²⁺, calc. For C₇₄H₇₂N₃₄O₁₆²⁺, 846.2928, 846.7944, 847.2961, 847.7946, 848.2982; found 846.2923, 846.7932, 847.2943, 847.7937, 848.2980.

The binding affinity between compound **31** and CB8 was further investigated through UV titration, wherein CB8 was gradually introduced into a solution of compound **31**. As illustrated in Figure 15b, the addition of CB8 resulted in a decreased absorbance, with the two maximum absorbance peaks at 281 nm and 396 nm shifting to isobestic points 293 nm and 421 nm, respectively. The changes in absorbance at 281 nm were plotted against the concentration of CB8, as depicted in Figure 15c. Least-square fitting of this data with a direct binding assay (DBA) model determined a binding constant of $(2.53 \pm 0.11) \times 10^6 \text{ M}^{-1}$, indicating a strong interaction between compound **31** and CB8.

Furthermore, the photoreaction of compound **31** encapsulated within the CB8 cavity was conducted under the same photoreaction conditions as for compound **31** in water, allowing for comparison. Upon irradiation, the ¹H NMR signals exhibited a complete transformation from the initial state, indicating the formation of the new species (Figure 16). After approximately 21 minutes, no significant further variation in the NMR spectra was observed, suggesting the completion of the reaction.

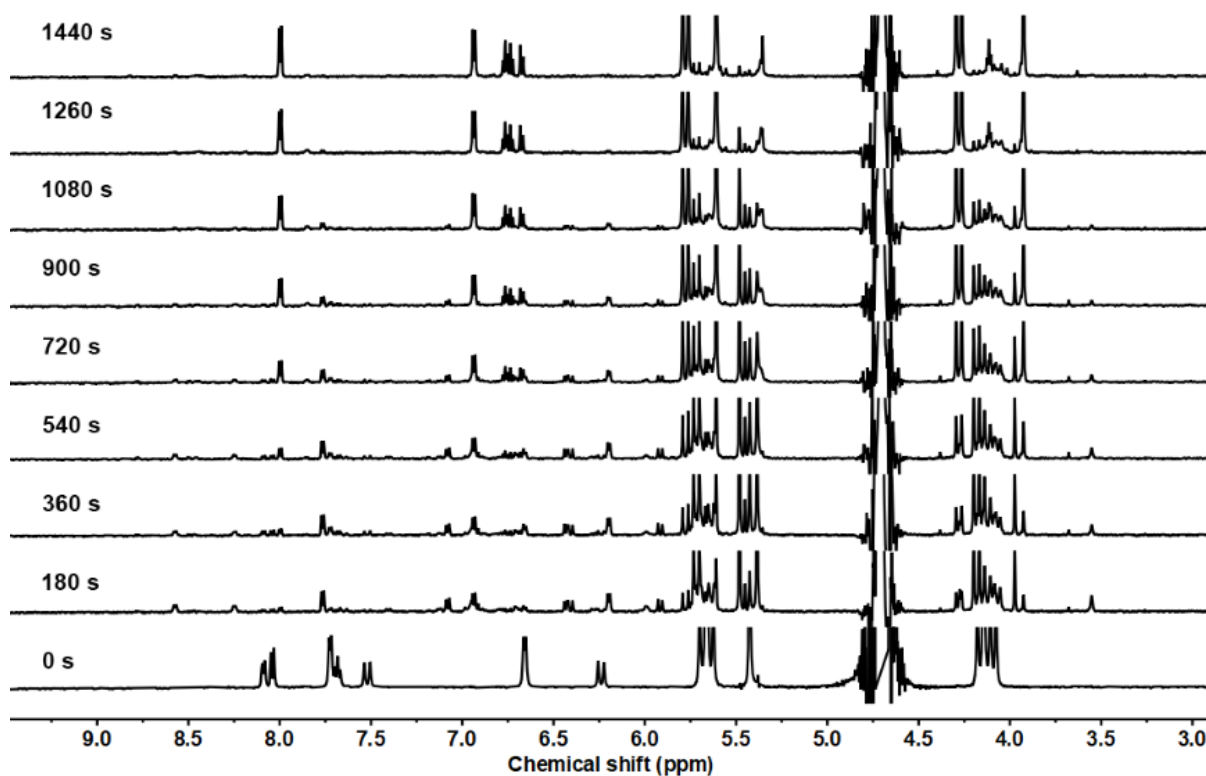


Figure 16. ^1H NMR spectra of photolysis of **31**•CB8 (1:1, 0.5mM) after different reaction, 500 MHz, D_2O (4.79 ppm).

A similar trend was observed in UV absorbance and fluorescence emission. As depicted in Figure 16b, a notable decrease in the absorbance within the initial 3 minutes of irradiation was observed, with the maximum absorption peak at 421 nm eventually becoming barely discernible after 21 minutes of exposure. The fluorescence intensity exhibited an analogous pattern during UV irradiation, decreasing rapidly until no emission was detected by the end of the process, as illustrated in Figure 16c. Additionally, evidence of the formation of the [2+2] cycloaddition product **32** within the CB8 cavity was observed through ESI-MS. A strong signal peak with a mass-to-charge ratio (m/z) of 846.2927, corresponding to $[\mathbf{32}\cdot\text{CB8-2Cl}]^{2+}$, was detected. This suggests no change in the mass of compound **32** encapsulated in the CB8 cavity compared to the starting reagent **31**.

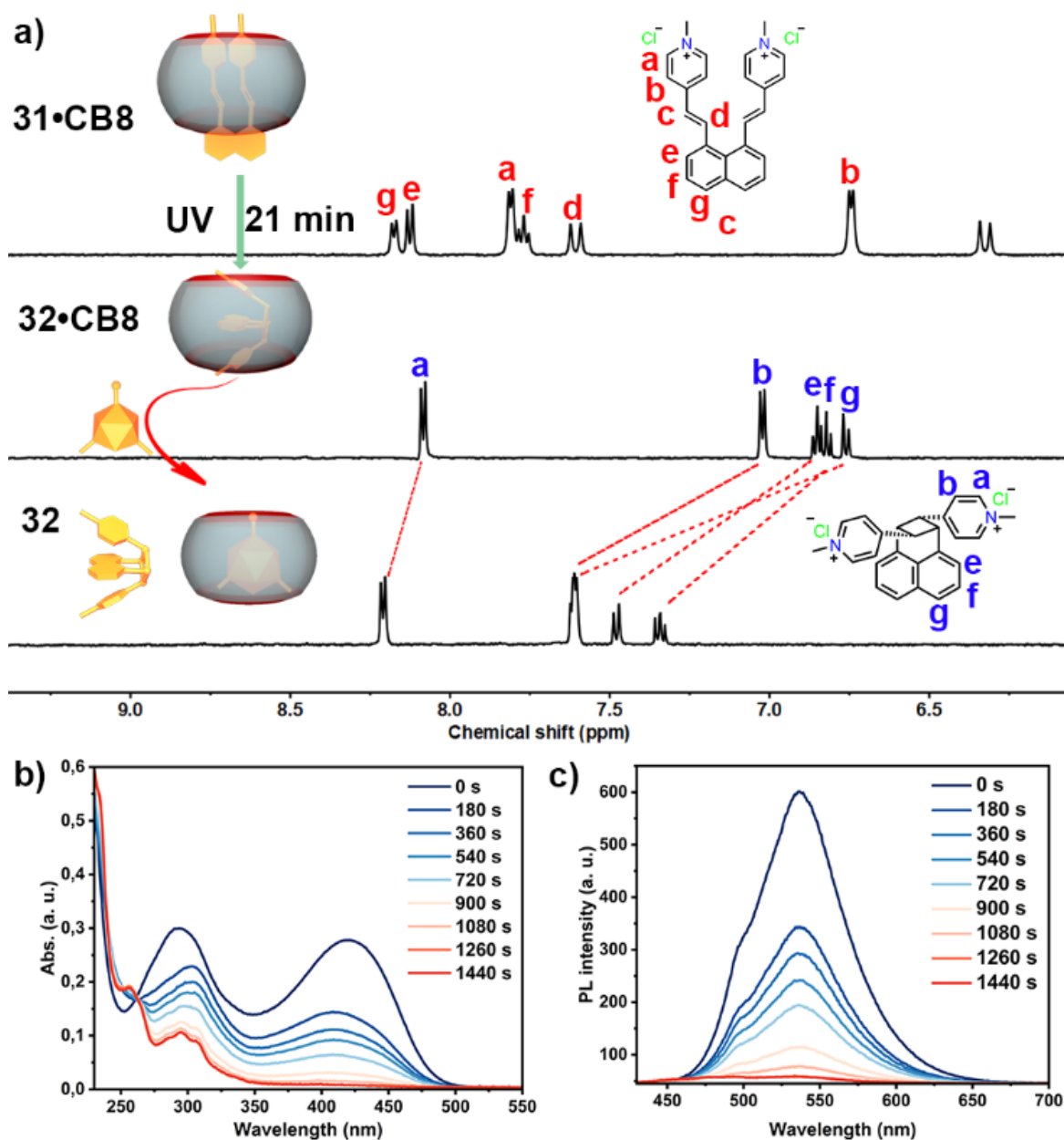


Figure 17. a) ¹H NMR spectra of **31**•CB8 (1:1, 0.5 mM), **32**•CB8 (1:1, 0.5 mM), and **32** (0.5 mM) in aromatic region in D₂O; b) UV-vis spectra of **31**•CB8 (1:1, 0.5 mM, diluted to 20 μM for UV-vis measurements) upon irradiation at 298 K; c) emission spectra of **31**•CB8 (1:1, 0.5 mM, diluted to 20 μM for UV-vis measurements) upon irradiation at 298 K (excited at 410 nm).

After the strongly CB8-binding competitive guest memantine hydrochloride was added to the **32**•CB8 complex, unbound compound **32** was obtained, as shown in Figure 17a. The symmetric signals in Figure 17a indicate a *syn*-head-to-tail (1,3) photo cycloaddition product **32**, which differs from a similar structure reported in the literature^[103]. Remarkably, the binding constant of compound **32** between CB8 was determined to be $(2.04 \pm 0.29) \times 10^{12} \text{ M}^{-1}$ using competitive binding assay (CBA), where memantine served as the competitive guest (Figure 18)^[104]. The significantly increased binding constant of compound **32** compared with the starting molecule **31** could be attributed to the rigidified structure **32**, which exhibits a better complementary effect with the CB8 void.

The method was based on the competitive binding assay (CBA), in which memantine hydrochloride was utilized as a competitive guest whose binding constant with cucurbit[8]uril $K_{CB8 \cdot Mem} = (4.3 \pm 1.1) \times 10^{11} M^{-1}$ was reported.⁶

$$K_{rel} = \frac{[CB8 \cdot 32][Mem]_{free}}{[CB8 \cdot Mem][32]_{free}} \quad \text{Eq.1}$$

$$[CB8]_{Total} = 0.5023 \text{ mM} = [CB8 \cdot 32] + [CB8 \cdot Mem] \quad \text{Eq.2}$$

$$[Mem]_{Total} = 4.6348 \text{ mM} = [Mem]_{free} + [CB8 \cdot Mem] \quad \text{Eq.3}$$

$$[3]_{Total} = 0.5011 \text{ mM} = [32]_{free} + [CB8 \cdot 32] \quad \text{Eq.4}$$

The interaction of **32** and memantine with cucurbit[8]uril K_{rel} was determined by equation 1. The equilibrium of CB[8] (0.5023 mM), Mem (4.6348 mM), and **32** were attained in the D₂O, where two similar proportions peaks with 5.54ppm [CB8•Mem] and 5.70ppm [CB8•32] chemical shift in NMR spectra were observed. The relative concentration of [CB8•32] was calculated as 0.1430 mM by integrating the relative resonances in the NMR spectra. Then, equation 2 allows us to calculate the [CB8•Mem] as 0.3593 mM, which was substituted in equation 3 to calculate [Mem]_{free} as 4.2755 mM. With the same method, [32]_{free} was calculated as 0.3581 mM using equation 4.

The K_{rel} value was calculated by substitution of [CB8•32], [32]_{free}, [CB8•Mem], and [Mem]_{free} into equation 1, which was obtained as 4.7518. Substitution of $K_{CB8 \cdot Mem} = (4.3 \pm 1.1) \times 10^{11} M^{-1}$ and K_{rel} in equation 5 to obtain $K_{CB8 \cdot 32} = 2.04 \times 10^{12} M^{-1}$ (equation 6). The uncertainty of $\sigma K_{CB8 \cdot 32}$ can be calculated by equation 7, where $\sigma(K_{CB8 \cdot Mem}) / \sigma K_{CB8 \cdot Mem} = 0.1006$ and $\sigma(K_{rel}) / \sigma K_{rel} = 0.10$ [Note that we are using the even more conservative 10% error in this analysis] to give the percent error in $K_{CB8 \cdot 32}$ equation 8. Substituting equation 6 into equation 9 gives $\sigma K_{CB8 \cdot 32}$ as $0.29 \times 10^{12} M^{-1}$, which was finally combined into equation 10 to give the final binding constant $K_{CB8 \cdot 32} = (2.04 \pm 0.29) \times 10^{12} M^{-1}$.

$$K_{CB8 \cdot 32} = (K_{CB8 \cdot Mem})(K_{rel}) \quad \text{Eq.5}$$

$$K_{CB8 \cdot 32} = 2.04 \times 10^{12} M^{-1} \quad \text{Eq.6}$$

$$\left(\frac{\sigma K_{CB8 \cdot 32}}{K_{CB8 \cdot 32}}\right)^2 = \left(\frac{\sigma K_{CB8 \cdot Mem}}{K_{CB8 \cdot Mem}}\right)^2 + \left(\frac{\sigma K_{rel}}{K_{rel}}\right)^2 \quad \text{Eq.7}$$

$$\frac{\sigma K_{CB8 \cdot 32}}{K_{CB8 \cdot 32}} = 0.1418 \text{ (14.18\%)} \quad \text{Eq.8}$$

$$\sigma K_{CB8 \cdot 32} = 0.1418 \times (2.04 \times 10^{12} M^{-1}) = 0.29 \times 10^{12} M^{-1} \quad \text{Eq.9}$$

$$K_{CB8 \cdot 32} = (2.04 \pm 0.29) \times 10^{12} M^{-1}. \quad \text{Eq.10}$$

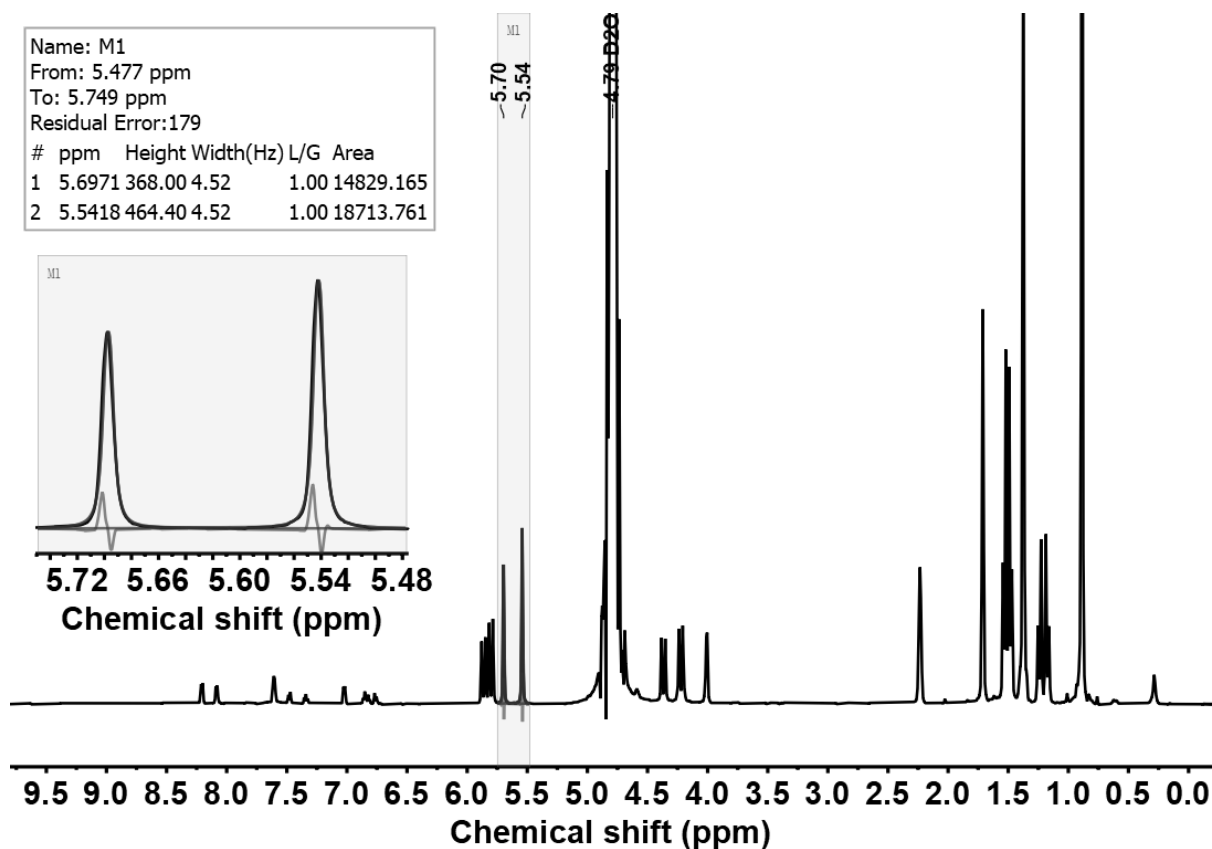


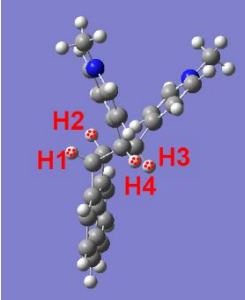
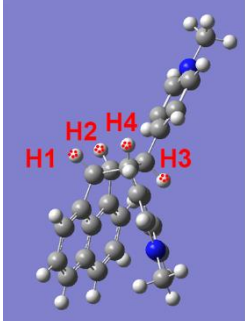
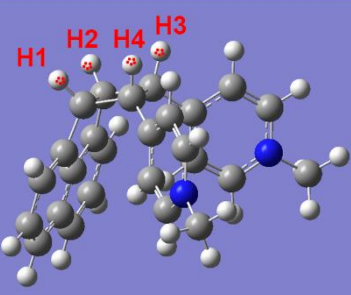
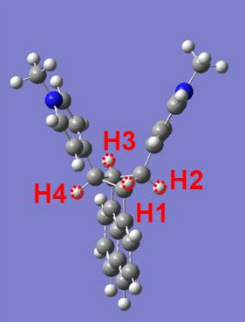
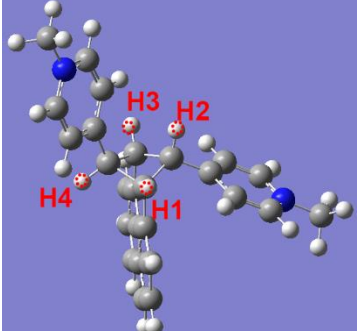
Figure 18. ^1H NMR spectra were used in the competitive binding assay determination of K_{rel} value for $[\text{CB8}\cdot\mathbf{32}]$ and $[\text{CB8}\cdot\text{Mem}]$. $[\text{CB8}]_{\text{Total}} = 0.5023$ mM, $[\text{Mem}]_{\text{Total}} = 4.6348$ mM, $[\mathbf{32}]_{\text{Total}} = 0.5011$ mM, 500 MHz, D_2O .


Further investigations were carried out to elucidate the mechanistic pathway of the reaction. It was found that the rate of product formation was significantly influenced by the concentration of CB8, indicating the pivotal role of the macrocycle in the reaction kinetics. Control experiments conducted in the absence of CB8 or in the presence of the smaller macrocycle CB7, which cannot fully encapsulate compound **31** due to steric reasons, further supported its role in directing the reaction towards the *syn*-head-to-tail (1,3) cycloaddition product.

Simultaneously, controlled experiments conducted in the dark under thermal conditions were performed for both **31** and **31**•CB8, revealing no traces of reaction in either case. To gain further insights into the stereostructures of the various possible products, theoretical calculations were performed, and the NMR composition was predicted (Table 2), supporting the conclusions drawn.

Table 2 Summary of the computed NMR prediction

3D structure	Predicted NMR	Observed NMR	Comment

		<p>H1 s 4.56 ppm H3 s 4.49 ppm H2 s 4.56 ppm H4 s 4.49 ppm</p>		<p>Not fit to the NMR observed</p>
		<p>H1 dd 5.04 ppm H3 dd 4.53 ppm H2 dd 4.74 ppm H4 dd 3.93 ppm</p>		<p>Not fit to the NMR observed</p>
		<p>H1 d 5.28 ppm H3 d 5.00 ppm H2 d 5.28 ppm H4 d 5.00 ppm</p>		<p>Not fit to the NMR observed</p>
		<p>H1 t 4.42 ppm H3 t 4.42 ppm H2 t 4.22 ppm H4 t 4.22 ppm</p>		<p>Pyridinium and naphthyl protons are similar to 31, so they are not likely to be completely included within the CB8 cavity. The binding constant should be similar to 31.</p>
 <p data-bbox="416 1823 560 1848">Molecule 40</p>		<p>H1 s 4.17 ppm H3 dd 4.65 ppm H2 d 4.16 ppm H4 d 4.22 ppm</p>	<p>4.66 ppm, 4.65 ppm doublet peak with two protons, 4.53 ppm triplet peak with one proton, 3.78 ppm with one proton.</p>	<p>One singlet peak refers to H4, one triplet peak refers to H2, and one doublet peak refers to H1 and H3. It is expected to show a largely different binding constant than 31.</p>

 <p style="text-align: center;">Molecule 32</p>	<p>H1 t 4.85 ppm H3 t 4.85 ppm H2 t 4.38 ppm H4 t 4.38 ppm</p>	<p>4.20 ppm triplet peak with two protons, 4.02 ppm hidden triplet peak with two protons.</p>	<p>Different NMR spectra than molecule 40 with two triplet peaks were observed. Pyridinium and naphthyl protons will likely be completely included within the CB8 cavity with a smaller molecular size. It is expected to show a largely different binding constant than 31.</p>
--	---	--	--

a: The computation was performed using ω B97X-D 6-31G* method.

Another hypothesis was formulated to investigate whether the photo cycloaddition process could still occur if the two olefin branches were covalently locked. To explore this, compound **41**, featuring pyridine moieties bridged by 1,4-bis(bromomethyl)benzene, was designed, synthesized, and fully characterized. As illustrated in Figures 19a and 19b, the crystal structure of compound **41** reveals a rigid configuration with distinct separation of the olefin groups. Consequently, photolysis of compound **41** in aqueous media resulted in no observable change.

Similarly, the host-guest interaction between compound **41** and CB8 was also investigated. It was observed that compound **41** could be encapsulated within the CB8 cavity, as indicated by the ESI-MS (Figure 19c) and NMR spectra (Figure 19d). Analysis of the NMR spectra of molecules **41** and **41**•CB8 suggests that CB8 selectively encapsulates the naphthyl moiety. At the same time, the bridged pyridinium is positioned at the carbonyl portal of the CB8, consistent with previous literature findings^[105]. The binding constant of compound **41** and CB8 was determined using UV-vis titration, yielding a value of $(2.52 \pm 0.15) \times 10^6 \text{ M}^{-1}$ (Figure 19e).

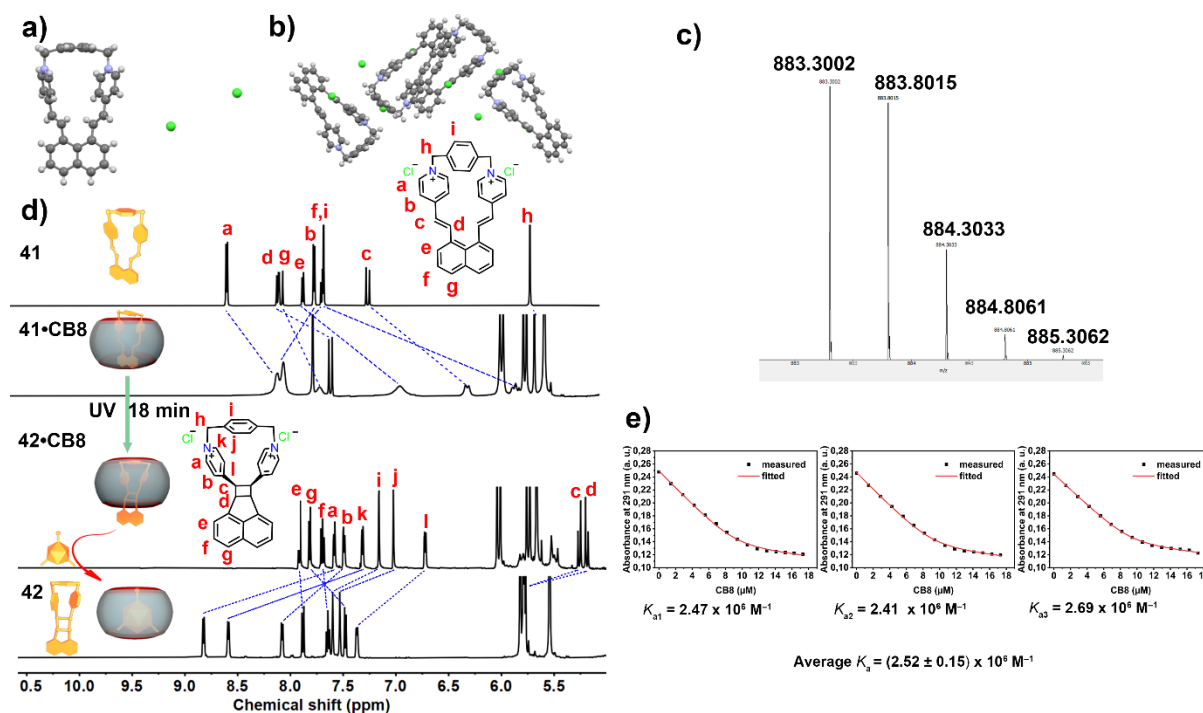


Figure 19. a) Crystal structure of compound **41**, front view, water molecules are omitted for clarity; b) crystal packing of **4**, water molecules are omitted for clarity; c) HRESI-MS spectra of **41**•CB8 (1:1), HRESI-MS(m/z): $[\text{M}-2\text{Cl}]^{2+}$, calc. For $\text{C}_{80}\text{H}_{74}\text{N}_{34}\text{O}_{16}^{2+}$, 883.3006, 883.8022, 884.3039, 884.8064, 885.3060; found 883.3002, 883.8015, 884.3033, 884.8061,

885.3062; d) ^1H NMR spectra of **41**, **41**•CB8 (1:1, 0.5 mM), **42**•CB8 (1:1, 0.5 mM), and **42** (0.5 mM) in D_2O ; e) UV absorbance changes of compound **41** at 291 nm upon increasing the concentration of CB8 in Milli Q water. The binding constant value was determined by a non-linear curve fitting. The black squares represent acquired data. The fitting according to a 1:1 model is shown as a red line. The error was calculated from 3 replica experiments as the standard deviation.

Surprisingly, upon the irradiation of **41**•CB8 with the same reaction conditions as the photolysis of molecule **31** and **31**•CB8, new species were observed in the NMR spectra (Figure 20). Absorption (Figure 21a) and emission spectra (Figure 21b) also indicated the occurrence of the photoreaction. Mass spectra (Figure 21c) of the **42**•CB8 complex suggested no change in the mass of the photoreaction product. The NMR spectra (Figure 19d) indicated the formation of a dissymmetric product, with the identical signal at 5.18-5.27 ppm suggesting the generation of the *syn*-head-to-head (1,2) cycloaddition product, which is comparable to the similar structure reported in the literature^[103]. Memantine hydrochloride was introduced to the reaction mixture to obtain the unbound product **42** from the CB8 cavity (Figure 19d).

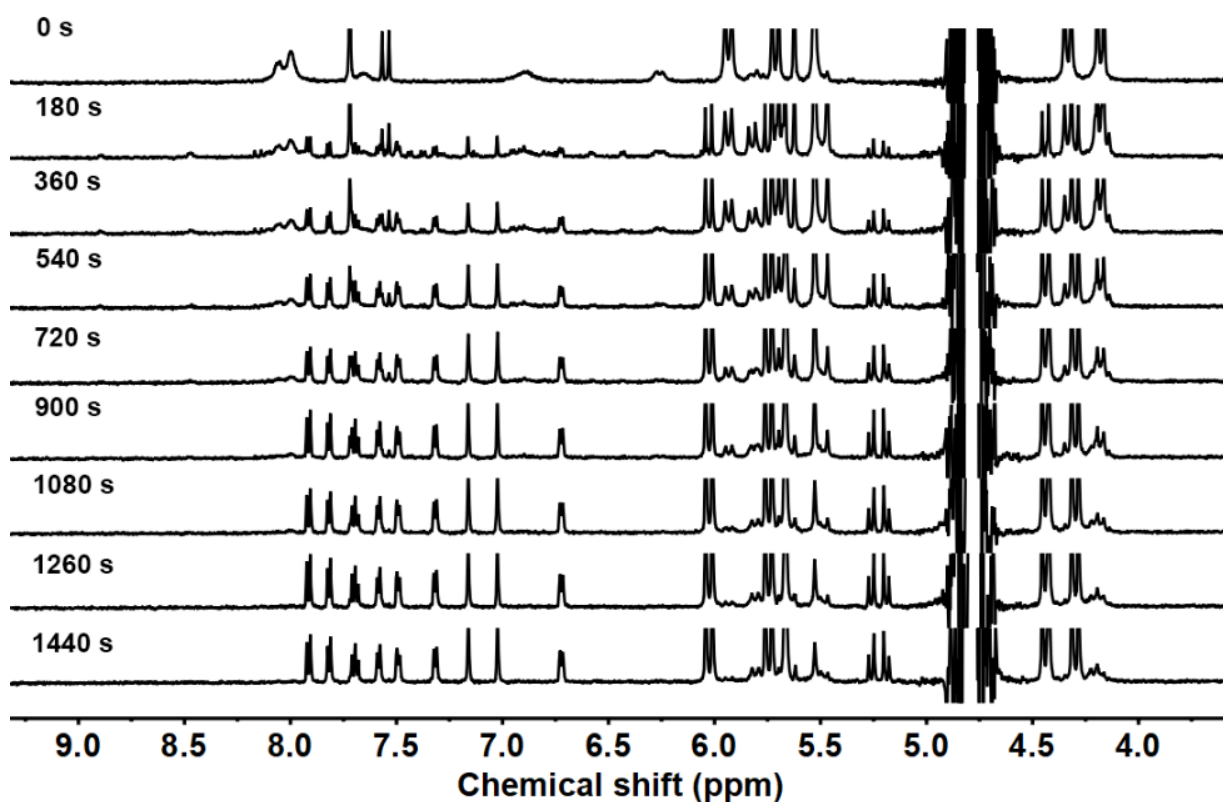


Figure 20. ^1H NMR spectra of photolysis of **41**•CB8 (1:1, 0.5mM) after different reaction, 500 MHz, D_2O (4.79 ppm).

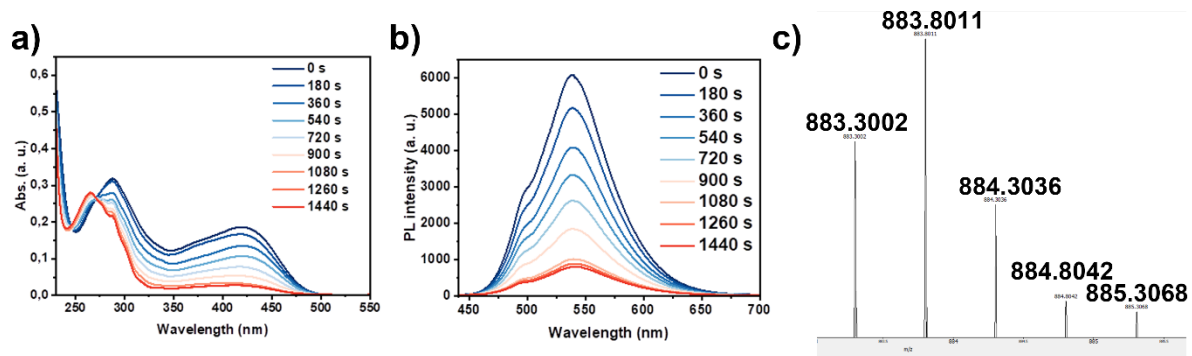


Figure 21. a) UV spectra and b) emission spectra ($\lambda_{exc}=421$ nm) of photolysis of **41**•CB8 (1:1, 0.5 mM) after different reaction times in Milli Q water at 25 °C. The reaction mixture was diluted with Milli Q water to 2×10^{-4} M for UV measurement; c) HRESI-MS spectra of **42**•CB8 (1:1), HRESI-MS(m/z): $[M-2Cl]^{2+}$, calc. For $C_{80}H_{74}N_{34}O_{16}^{2+}$, 883.3006, 883.8022, 884.3039, 884.8064, 885.3060; found 883.3002, 883.8011, 884.3036, 884.8042, 885.3068.

3.2. Modulating Aryl Azide Photolysis in Aqueous

Preface

Parts of the following chapter were published in *Small* (WILEY-VCH)

X. Qiu, Y. Wang, S. Leopold, S. Lebedkin, U. Schepers, M. M. Kappes, F. Biedermann, S. Bräse, Modulating Aryl Azide Photolysis: Synthesis of a Room-temperature Phosphorescent Carboline in Cucurbit[7]uril Host. *Small*, **2023**, 2307318.

Author contributions. The first author contributed to the study conception, design, material synthesis, data collection, analysis, and manuscript preparation. Y. Wang contributed to the data analysis. S. Leopold and S. Lebedkin contributed to the data collection and analysis.

Acknowledgments. This work is supported by the China Scholarship Council (CSC grant: 202010190002) and the Deutsche Forschungsgemeinschaft (DFG) under Germany's Excellence Strategy – 3DMM2O – EXC-2082/1–390761711.

Introduction

Since their discovery in 1864, organic azides have been integral to the annals of chemistry due to their rich nitrogen composition and versatility for transformation under different reaction conditions.^[106] Their utility spans diverse reactions such as 1,3-dipolar cycloaddition,^[107] Staudinger/aza-Wittig reaction,^[108] and C-H insertion.^[109] The photolysis of aryl azides serves as a foundation for vital functionalization methods in chemical biology.^[110]

Mechanistically, aryl azide photolysis involves expelling a nitrogen molecule, generating a highly reactive singlet nitrene intermediate. This intermediate can follow one of three distinct reaction pathways.^[111] Firstly, it may aminate an X-H bond (X = C, N, O, or S). Secondly, it might undergo an intramolecular rearrangement to form ketenimines, which are subsequently susceptible to nucleophilic insertion, yielding azepine derivatives. Thirdly, it may undergo an intersystem crossing to triplet nitrenes, which can dimerize to form azobenzenes products. Controlling such diverse reactivity of nitrenes poses an intriguing yet challenging task for chemists.

One promising approach to modulating the photoreaction pathways of aryl azides is using supramolecular hosts as “reaction vessels.” Supramolecular catalysis, demonstrated successfully with entities like macrocycles,^[112] capsules,^[50, 52a, 95a] and cages,^[113] involves creating a microenvironment that influences the direction of the reaction through various non-covalent interactions.^[96a] These hosts also afford selective encapsulation of reagents.^[96b]

Cucurbit[*n*]urils (CB*n*), a class of glycoluril-based supramolecular hosts, are noteworthy for their high affinity, particularly for cationic guests, in aqueous solutions.^[62, 65] Their pumpkin-shaped structure provides a well-defined hydrophobic cavity capable of encapsulating molecules of various sizes to form 1:1,^[114] 1:2,^[115] or 1:3^[116] host-guest complexes. This adaptability of CB*n* makes them promising contenders for controlling chemical reactions. Indeed, numerous reactions have been carried out within the CB*n* host cavities, spanning from the azide-

alkyne cycloaddition^[80a, 98, 117] and Diels–Alder reaction^[86a, 97, 118] to photodimerization.^[87-88, 99, 119] Notably, even when only partial confinement of (large) reagent molecules by CB n can experience a significant acceleration in the reaction rate.^[120]

In this subchapter, the distinctive characteristics of the cucurbit[7]uril host were utilized to selectively alter the photolysis reaction of an aryl azide in an aqueous media. The resulting controlled photoreaction product, carboline, created long-lived room-temperature phosphorescence (RTP) materials for potential oxygen-sensing applications (Figure 22).

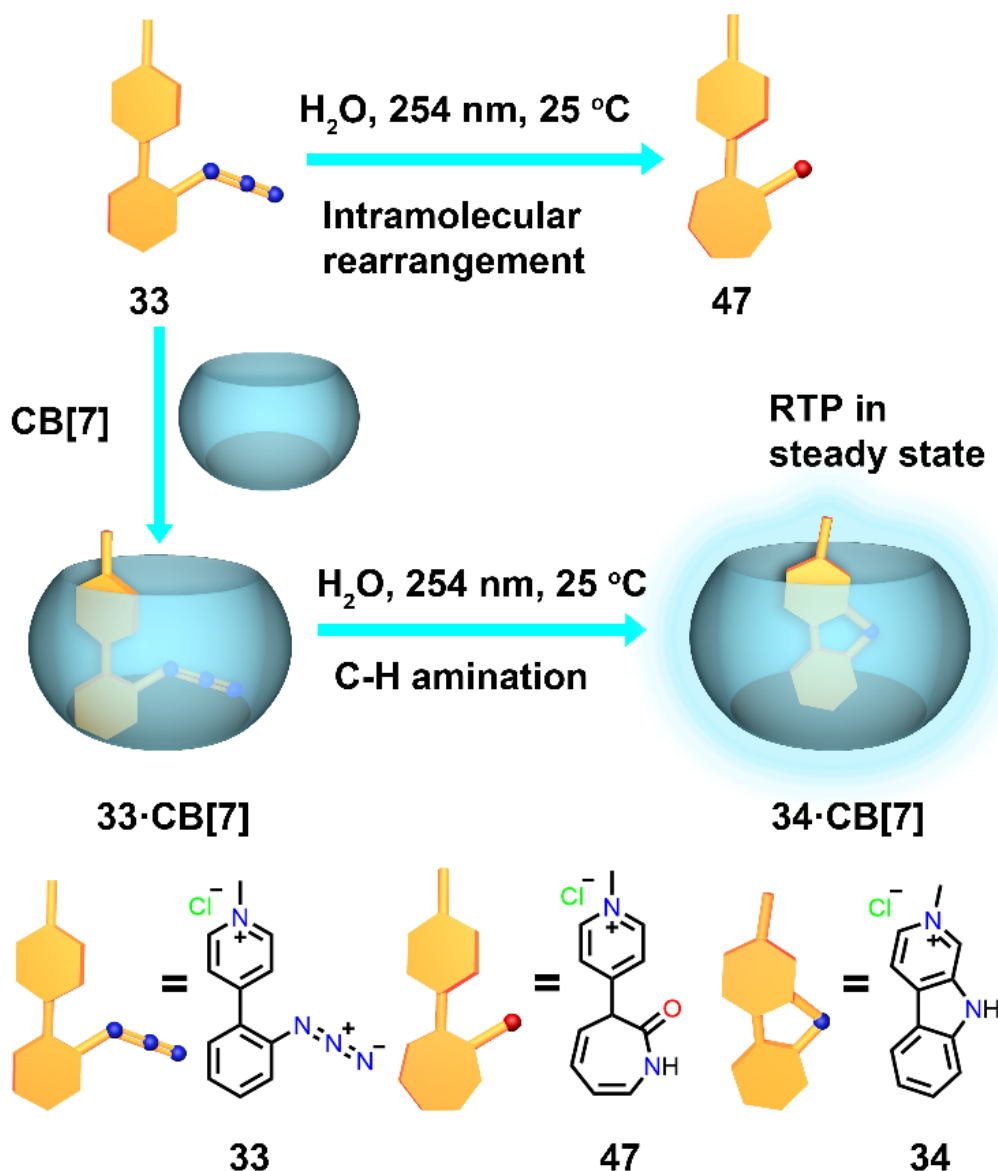
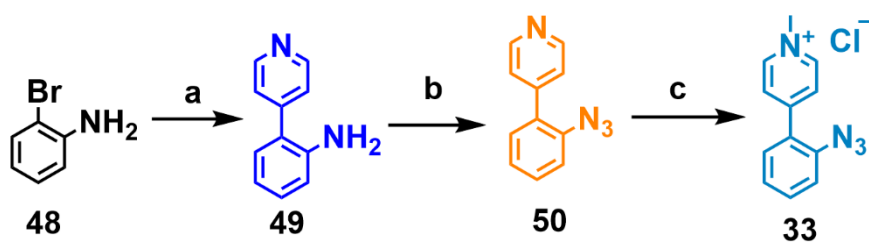


Figure 22. Modulation of the outcome of the photolysis of aryl azide **33** by using cucurbit[7]uril (CB7). **47**: photolysis product in bulk water, **34**: in a CB7 cage. Complex **34·CB7** shows long-lived room temperature phosphorescence (RTP) in the solid state.

Synthesis. The synthesis of the desired aryl azide is straightforward. The aryl amine (**49**) was synthesized by Suzuki coupling of 2-bromo-aniline (**48**) with 4-pyridylboronic acid^[121], which was converted to azide intermediate^[122](**50**). After methylation and ion exchange, the final aryl azide (**33**) was obtained.



Scheme 3. a) 4-pyridylboronic acid (1.3 equiv), Na_2CO_3 (4.0 equiv), $\text{Pd}(\text{dppf})\text{Cl}_2$ (0.05 equiv), dioxane, H_2O , 80°C , 2.5 h (82 %); b) $p\text{-TsOH}\cdot\text{H}_2\text{O}$ (1.5 equiv), TBN (1.5 equiv), NaN_3 (3.0 equiv), ACN, H_2O , 21°C , 6 h (97 %); c) MeI (1.2 equiv), AgCl (2.0 equiv), DMF, H_2O , 25°C , 5 days, 84%.

Results and discussion.

Several factors, such as substrate properties, solvents, additives, light wavelength, and temperature, influence the photolysis pathways of aryl azides. Azepine derivatives typically dominate as the primary reaction product, especially when the ortho position is substituted with an electron-withdrawing group, particularly in the presence of a nucleophile.^[123] The designed aryl azide (**33**) features a pyridinium salt in the ortho position, functioning as an electron-withdrawing unit.

Initially, the photoreaction of aryl azide **33** was explored under UV light irradiation (254 nm) in various organic solvents, including dichloromethane, chloroform, and acetonitrile. In these solvents, the photolysis resulted in the formation of colored species and polymeric precipitates. However, in DMSO, no distinct NMR signals were observed, indicating the formation of mixtures of various products along different reaction pathways (and possibly cross-reactions). Figure 23 illustrates potential initial reaction steps and intermediates in the photolysis of aryl azide **33**.

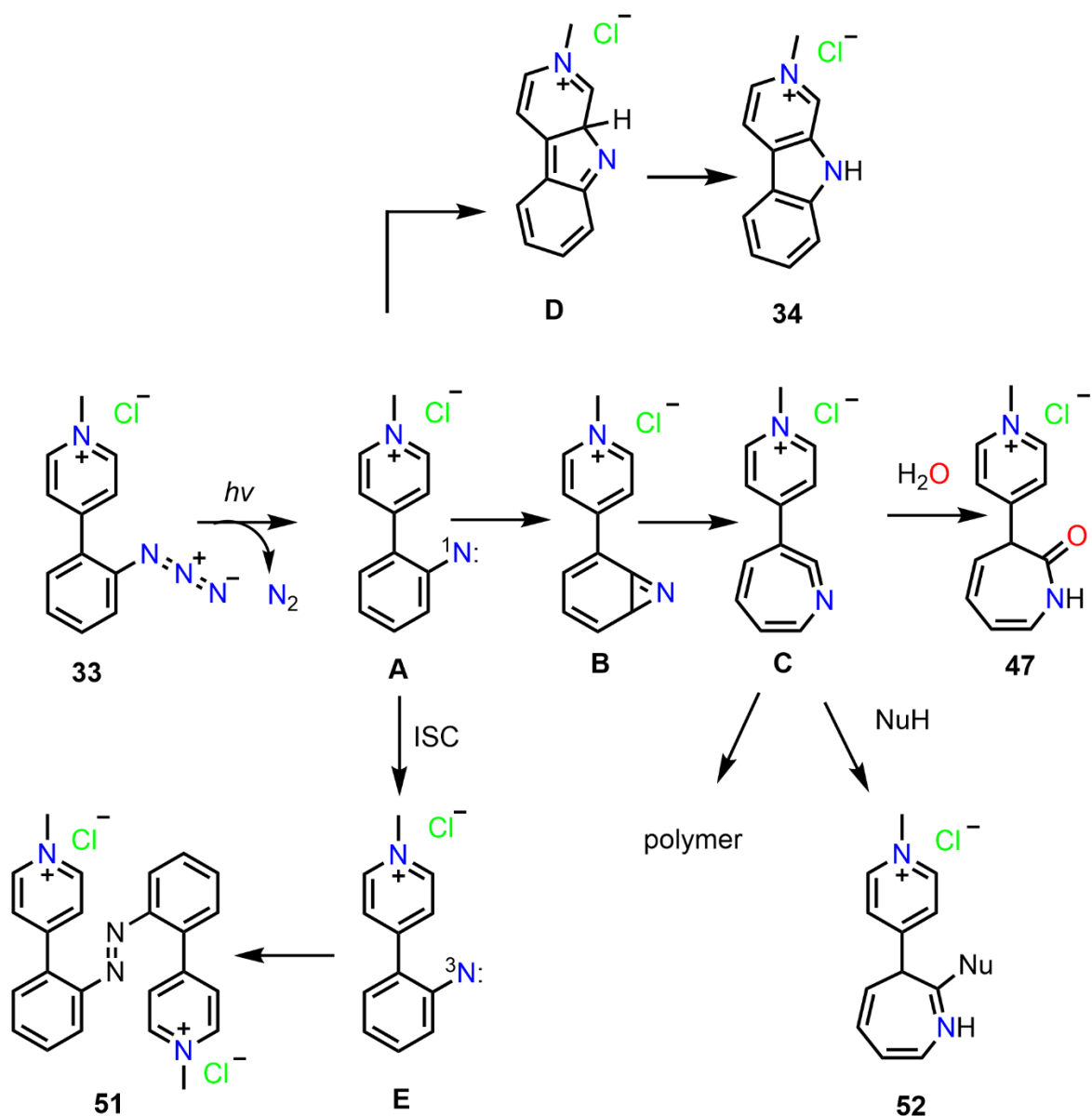


Figure 23. Possible initial reaction steps and intermediates in the photolysis of aryl azides^[111] adapted to aryl azide **33**. Upon the irradiation of aryl azide **33**, the generation of singlet nitrene **A** is expected. This extremely reactive intermediate can go through three different reaction pathways: 1) intramolecular rearrangement forming 1,2- didehydroazepine **C**, which nucleophiles can further attack. Nucleophilic addition reactions can form products such as **47** and **52**, leading to polymeric (oligomeric) species. 2) intramolecular C-H amination to form isocarboline intermediate **D**, which, after 1,5-hydrogen, shifts to carboline **34**. 3) through intersystem crossing to generate triplet nitrene **E**, which can dimerize forming azobenzene species **51**.

The subsequent step involved conducting the photoreaction of aryl azide **33** in either H_2O or D_2O , especially if time-dependent ^1H NMR spectroscopy was employed to monitor the reaction progress. Upon irradiation, new NMR peaks emerged, indicating the formation of novel species (Figure 24). Approximately 8 minutes of irradiation led to the completion of the reaction, as evidenced by the absence of significant changes in the NMR spectra. UV-vis spectroscopy further supported this observation, which showed a decrease in absorbance at 254, 286, and 331 nm (Figure 25).

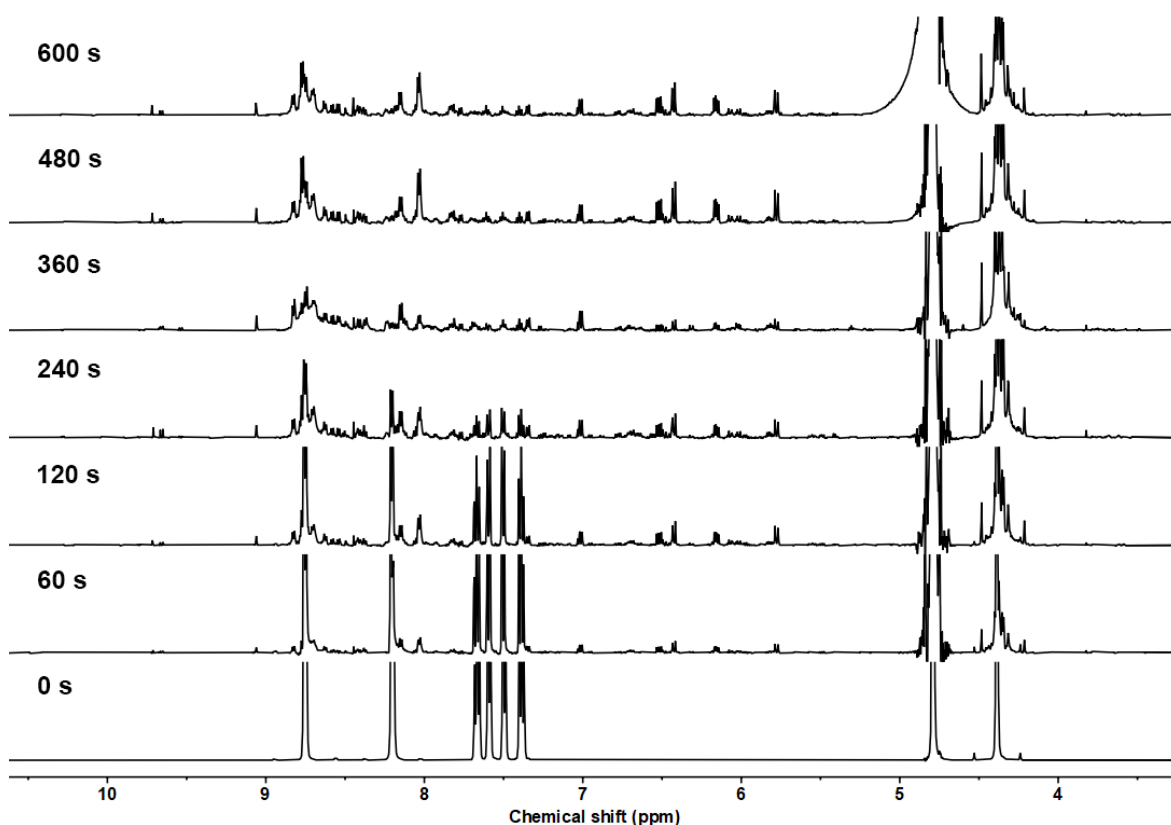


Figure 24. ^1H NMR spectra of photolysis of aryl azide **33** (2 mM) after different reaction times in D_2O (4.79 ppm) at 298 K, 500 MHz.

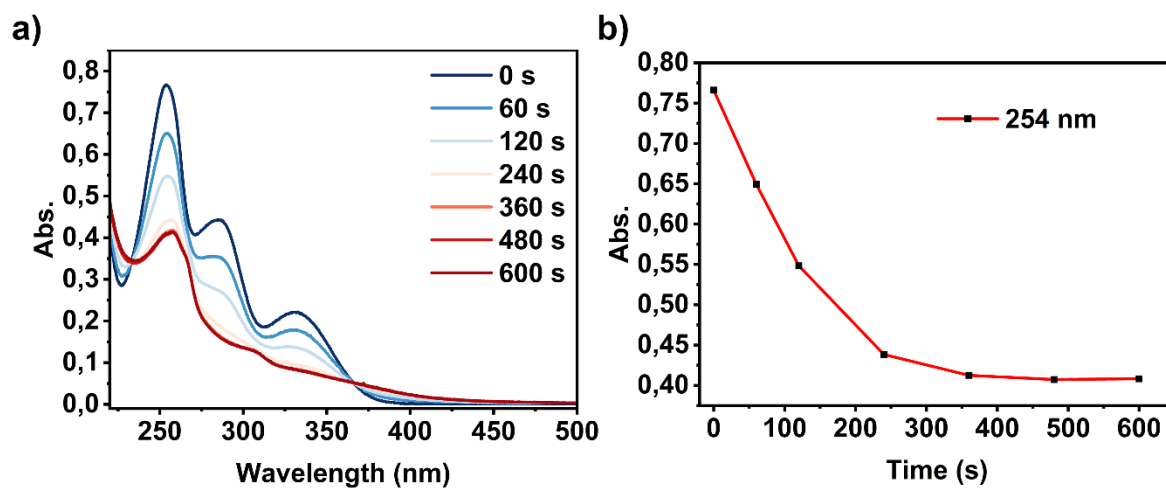


Figure 25. a) UV spectra and b) UV absorbance change at 254 nm of photolysis of aryl azide **33** (2 mM) after different reaction times in Milli Q water at 298 K. The reaction mixture was diluted with Milli Q water to 5×10^{-4} M for UV measurement.

The NMR and UV/Vis spectra following photolysis displayed relatively sharp signals, indicating the formation of a predominant product. This product was isolated via preparative chromatography, yielding 42%.

NMR characterization (see Figure 26) confirmed the identity of this product as an azepine derivative **47** based on the expectations above for the reaction course.

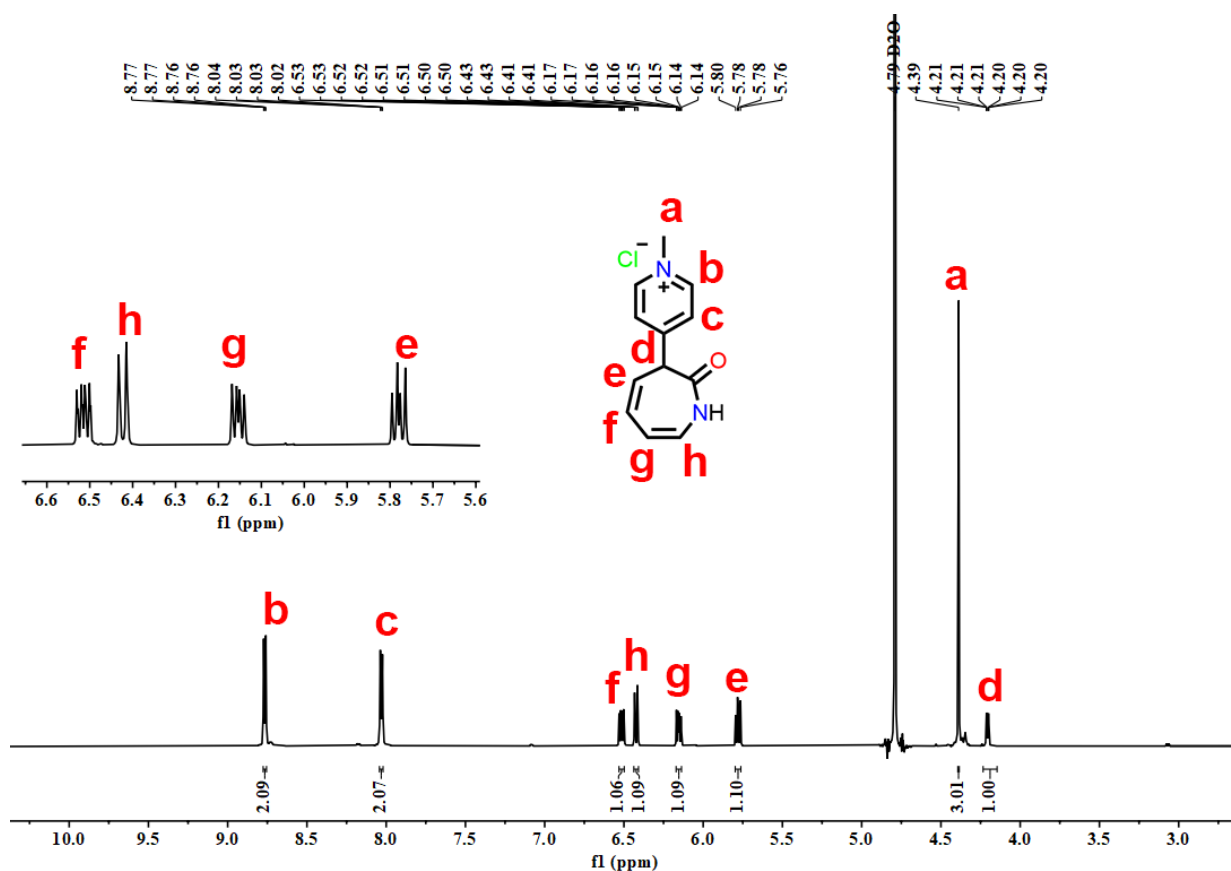


Figure 26. ^1H NMR of 1-methyl-4-(2-oxo-2,3-dihydro-1H-azepin-3-yl)pyridin-1-ium chloride (**47**), 500 MHz, D_2O (4.79 ppm).

According to literature data^[111], aryl azide **33** releases N_2 in the proposed mechanism to generate the highly reactive singlet nitrene **A** (Figure 27). Subsequently, this intermediate undergoes an intramolecular rearrangement, forming 1,2-didehydroazepine **C**. A water molecule in a nucleophilic addition then attacks it, forming the azepine derivative **47**.

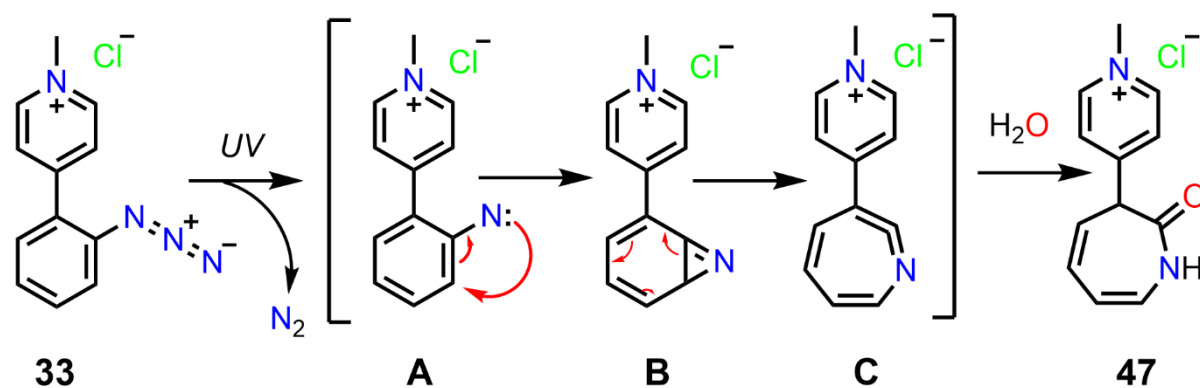


Figure 27. Proposed mechanism of photolysis of aryl azide **33** in water (H_2O). When photolysis is performed in D_2O , e.g., for ^1H NMR analysis, product **47** attains ND instead of NH as the structural fragment in the azepine ring.

A hypothesis emerged suggesting that the reaction pathway might be altered if aryl azide **33** was shielded from water by a macrocyclic host. Cucurbit[7]uril (CB7) was selected as a promising candidate. The host-guest interactions between compound **33** and CB7 were investigated using ^1H - ^1H COSY NMR spectroscopy. As depicted in Figure 28a, significant changes were observed in the ^1H NMR spectra of **33** upon the addition of CB7 in a 1:1 molar ratio in D_2O . Specifically, six sets of aromatic proton signals (b-e, g) originating from the aryl and pyridine groups exhibited substantial upfield shifts, indicating encapsulation by CB7. The formation of a 1:1 host-guest complex, **33**•CB7, was further corroborated by the detection of a MALDI-MS peak at m/z 1346.28, corresponding to $[\mathbf{33}+\text{CB7}-\text{N}_2-\text{Cl}]^+$ ions (Figure 28d). The binding strength of **33** and CB7 in water was evaluated through UV-vis titration (Figure 28b), revealing a decrease in absorbance at 254, 286, and 331 nm. The binding constant, K_a , was determined to be $(1.43 \pm 0.11) \times 10^5 \text{ M}^{-1}$ by fitting the binding isotherms (three replicated measurements) to the 1:1 host-guest binding model (Figures 28c).

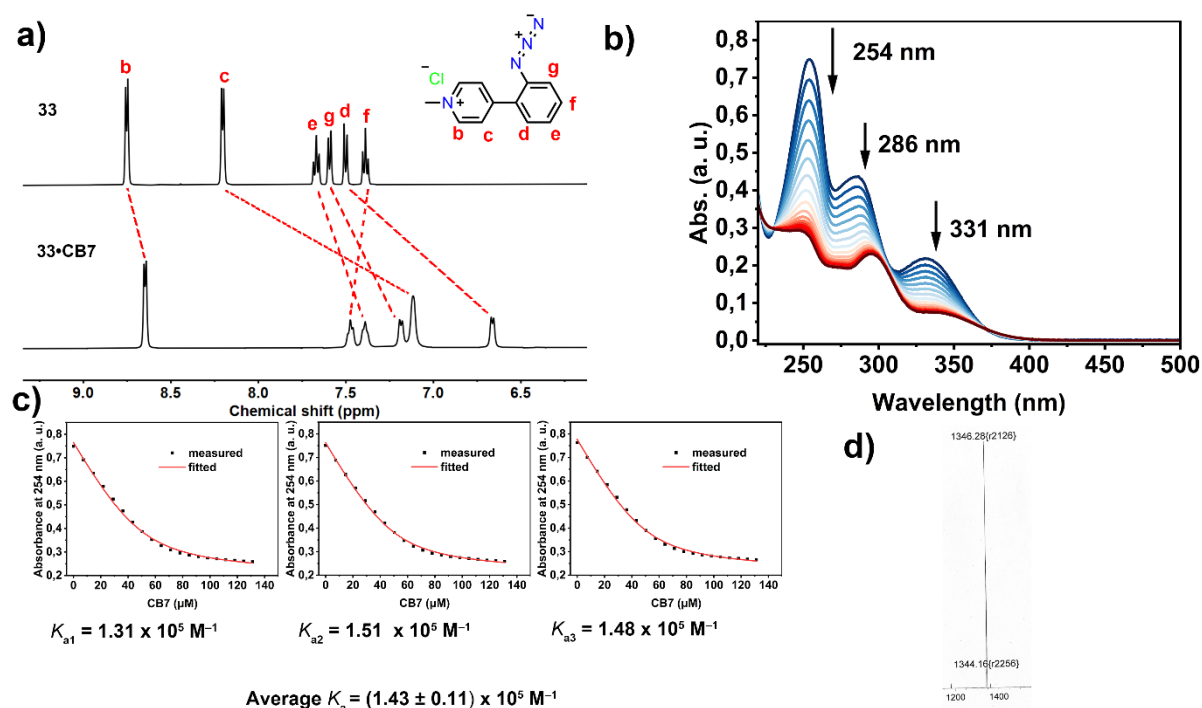


Figure 28. a) ^1H NMR spectra (500 MHz, D_2O , 298 K) of **33** (2 mM) and an equimolar mixture of **33** and CB7 (2 mM each); b) UV-vis titration spectra of **33** (50 μM) upon addition of CB7 (0–131 μM) in water at 298 K; c) the corresponding binding isotherm fitted with a 1:1 host-guest binding model, and d) MALDI-MS spectra of aryl azide **33**•CB7 in 1:1 molar ratio.

Additionally, compound **33** encapsulated by CB7 (2 mM each) were photolyzed under the same conditions as compound **33** in bulk water. The reaction process was initially monitored using ^1H NMR spectroscopy. New sets of ^1H NMR peaks (b-h in blue color) emerged during irradiation, which was distinct from the signals of the azepine derivative **47** (Figures 29 and 30a(i-iii)).

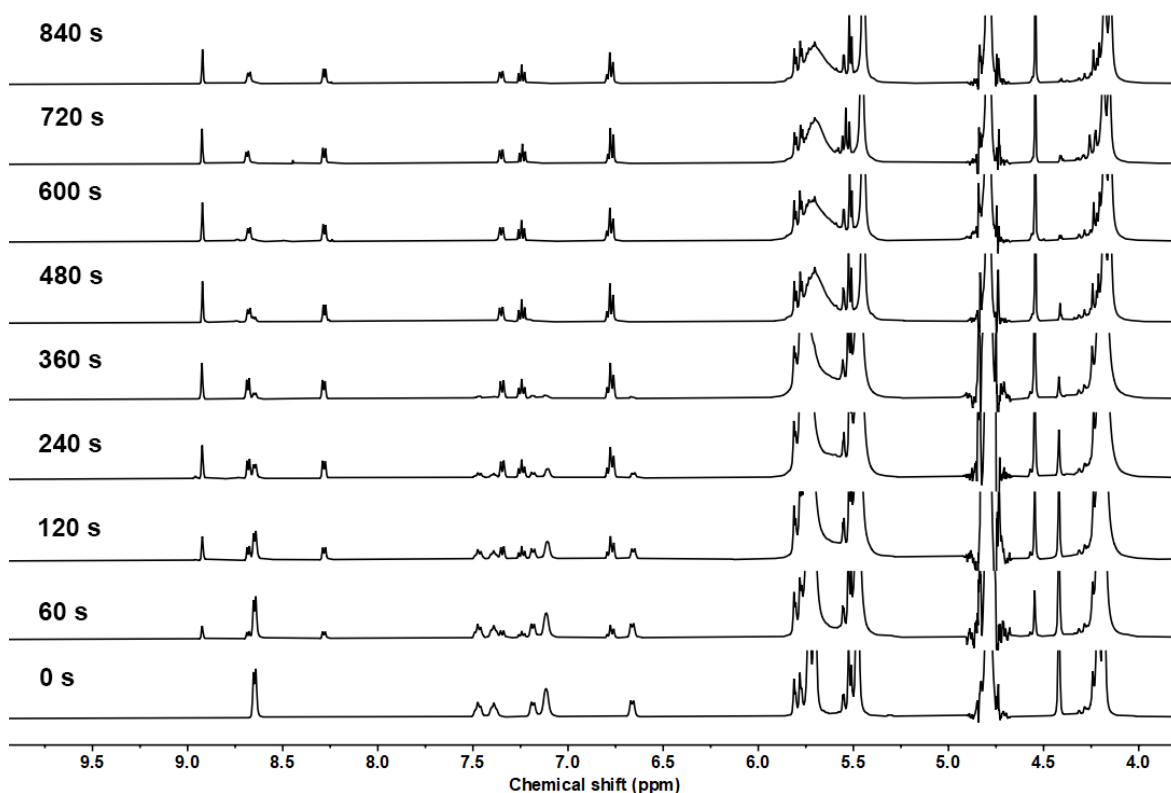


Figure 29. ^1H NMR spectra of photolysis of aryl azide **33**•CB7 in 1:1 molar ratio (2 mM) after different reaction times in D_2O at 298 K, 500 MHz.

A single peak b appeared at approximately 8.92 ppm in the ^1H - ^1H COSY NMR spectra, showing no coupling with any other peak, indicating a desymmetrization of the pyridinium moiety. Coupled peaks were observed at 8.68 ppm (c) and 8.28 ppm (d). The reaction concluded in about 10 minutes, with no further changes observed in the ^1H NMR peaks afterward. Subsequently, amantadine, a competitive guest with a high binding affinity to CB7, was introduced into the solution to displace reaction product **34** from its complex with CB7 (Figure 30a). Compound **34** was subsequently isolated through preparative chromatography with a yield of 95%. Its analytical data matched the carboline derivative depicted in Figure 3b and previously reported.^[124]

Upon comparison with the typical ^1H NMR shifts caused by CB7 (de)complexation (Figure 30a), we concluded that in the **34**•CB7 complex, the aryl ring of **34** (e-h, Figure 3a (iv)) is entirely encapsulated within the CB7 cavity, while the pyridine ring (b-d, Figure 3a (iv)) positioned near one of the portal areas of CB7.

The findings above indicate that in bulk water, the photolysis of compound **33** follows a ring expansion pathway primarily influenced by solvolysis (Figure 27), consistent with existing literature.^[123] However, water attack is obstructed when compound **33** is encapsulated within the hydrophobic CB7 cavity. Consequently, upon irradiation, the singlet nitrene intermediate **A**, formed from compound **33** after loss of N_2 , likely transforms isocarboline intermediate **D** through an intramolecular insertion. The intermediate **D** then undergoes rearomatization through an exothermic 1,5-hydrogen shift to yield carboline compound **34** (Figure 3b).^[125]

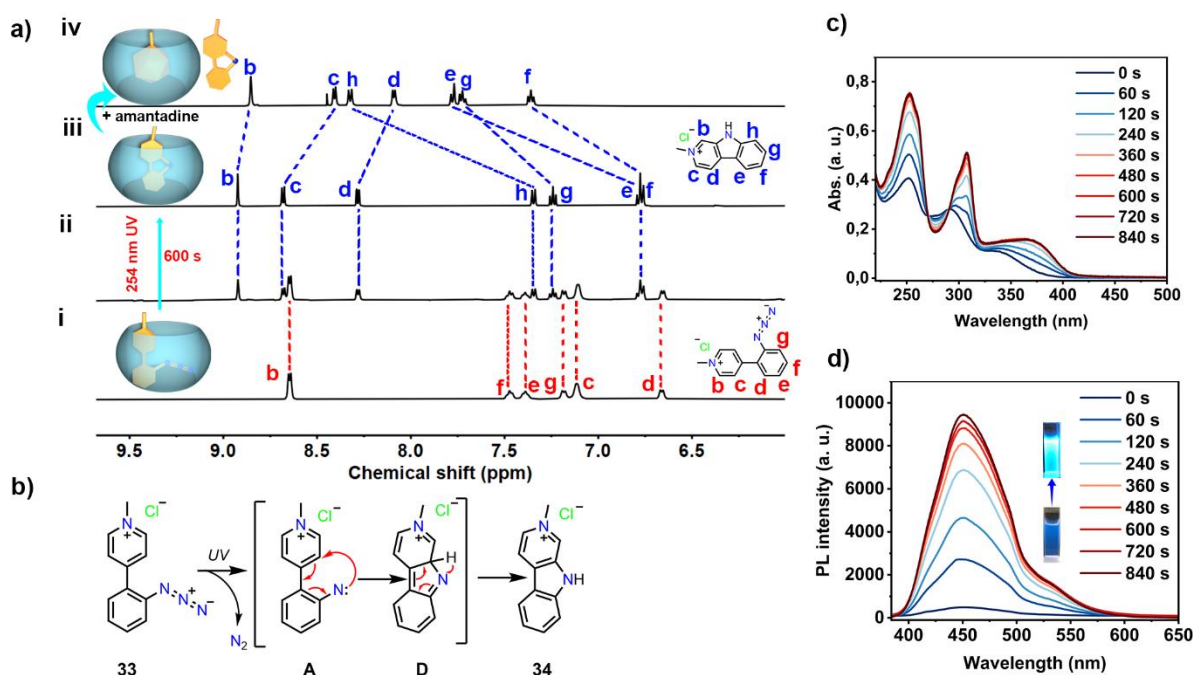


Figure 30. a) ¹H NMR spectra of (i) an equimolar ratio of compound **33** and CB7 (each 2 mM) in D₂O, after UV-light irradiation for (ii) 120 s and (iii) 600 s and (iv) after addition of amantadine as a CB7-sequestering guest; b) Proposed mechanism for the photolytic formation of carboline **34** in the CB7 cavity; c) UV-vis spectra of an equimolar reaction mixture of compound **33** and CB7 (each 2 mM) in water during the photolysis reaction with the 254 nm UV light source. Aliquots were taken at the specified time intervals and diluted to 50 μM before the UV-vis measurements; d) corresponding fluorescence spectra of the reaction mixture, obtained after dilution to 50 μM at 308 nm light excitation. The inset shows photographic images of the reaction mixture in a cuvette before and after 600 s UV light exposure.

The photolysis of compound **33** encapsulated within CB7 was additionally investigated using UV-Vis spectrometry and fluorometry, utilizing identical samples for ¹H NMR analysis. Figure 3c shows an initial rise in absorption peaks during irradiation, leveling off to a stable plateau after approximately 10 minutes. The appearance of fresh peaks at 254, 308, and 375 nm signals the formation of carboline **34**. The conversion to compound **34** is also accompanied by a substantial enhancement in fluorescence, which also stabilized after 10 minutes of irradiation (Figure 3d).

The binding constant of complex **34**•CB7 was determined as $(3.14 \pm 0.16) \times 10^5 \text{ M}^{-1}$ via UV-vis titration (Figure 31), which is comparable to that for **33**•CB7 $((1.43 \pm 0.11) \times 10^5 \text{ M}^{-1})$.

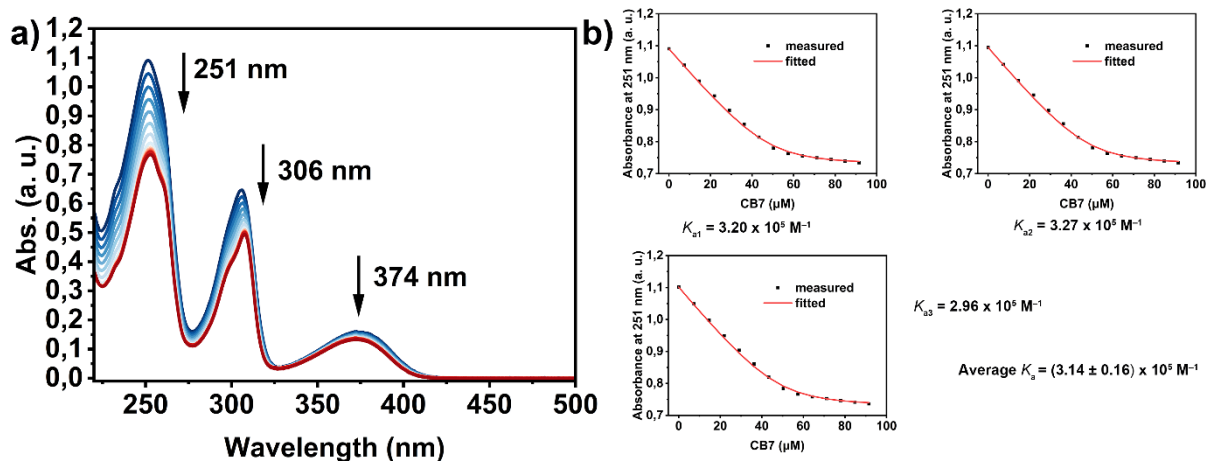


Figure 31. a) UV-vis titration spectra of **34** ($[34] = 50 \mu\text{M}$) upon addition of CB7 ($[CB7] = 0\text{--}91 \mu\text{M}$) in Milli Q water at 298 K; UV absorbance changes of **34** at 251 nm upon increasing concentration of CB7 in Milli Q water. The binding constant value was determined by a non-linear curve fitting. The black squares depict the acquired data. The fit according to a 1:1 binding model is shown as a red line. The error was calculated from 3 replica experiments as the standard deviation.

The photolysis of aryl azide **33** in CB6 and CB8 were also explored. However, due to the smaller cavity size, CB6 cannot encapsulate aryl azide **33** effectively. Regarding CB8, photolysis experiments involving aryl azide **33** within CB8 were conducted using the 1:1 and 2:1 binding model. LC-MS analysis indicated the formation of carboline product **34** alongside other byproducts.

The aqueous solutions of compound **34** and **34**•CB7 complex show bright blue fluorescence around 460 nm, with quantum yields (Φ_{FL}) of 77% and 90% and lifetimes of 21.9 and 25.4 ns, respectively. These properties suggest potential applications as blue fluorescent labels. In a test experiment, carboline **34** successfully stained HeLa cells, visualized using confocal microscopy (Figure 32).

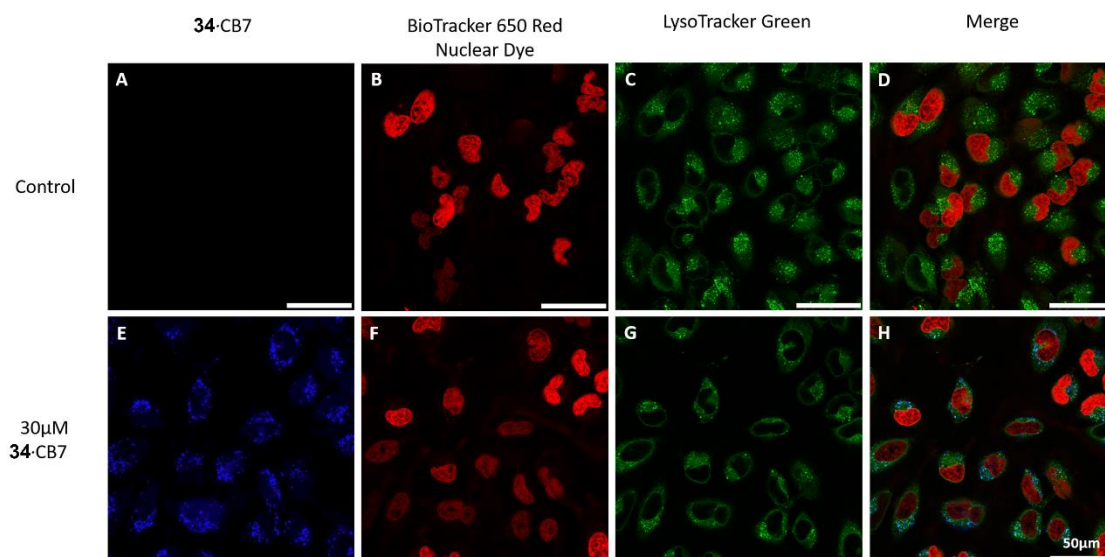


Figure 32. Cellular uptake and staining of HeLa cells with carboline **34** after incubation of the cells with $30 \mu\text{M}$ **34**•CB7 (see experimental details above). The control, as well as the probe, have been further stained with BioTracker Red™ and LysoTracker Green™. BioTracker Red™ was used to visualize the cell nuclei, and LysoTracker Green™ stained the lysosomes. A Leica Stellaris 5 confocal microscope was used for the fluorescence imaging of the cells. The scale bar in all images corresponds to $50 \mu\text{m}$. Excitation wavelengths: **34**: 405 nm; LysoTracker Green™: 504 nm; BioTracker Red™: 650

nm. Image E shows a blue fluorescence of compound **34**, while the untreated control (A) displays no fluorescence as expected. Images B, F and, C, G correspond to BioTracker Red™ and LysoTracker Green™ staining, respectively. The co-localization of the green and blue fluorescence in the merged image H validates the endosomal uptake of compound **34** into the HeLa cells.

Photoluminescence of carboline compound **34** in solid state is of interest due to the long-lived (“ultralong”) phosphorescence reported for structurally related carbazoles.^[126] This phosphorescence can be enhanced by CBn hosts, which impede nonradiative relaxation processes.^[127] To obtain solid (amorphous) samples, lyophilization was used as a gentle solidification method for **34**•CB7 (1:1) and **34**•CB7+ β -CD (1:1:1), where β -cyclodextrin (β -CD) served as a photophysically neutral matrix compound^[128], partially separating **34**•CB7 molecules. These were compared with a polycrystalline sample of compound **34**. Similar blue fluorescence was observed in the solid state as in the solutions (with a shift to $\lambda_{\text{max}} = 490$ nm in crystalline sample **34**), yielding Φ_{FL} values of 20%, 49%, and 79% for compound **34**, **34**•CB7 and **34**•CB7+ β -CD, respectively, under typical conditions.

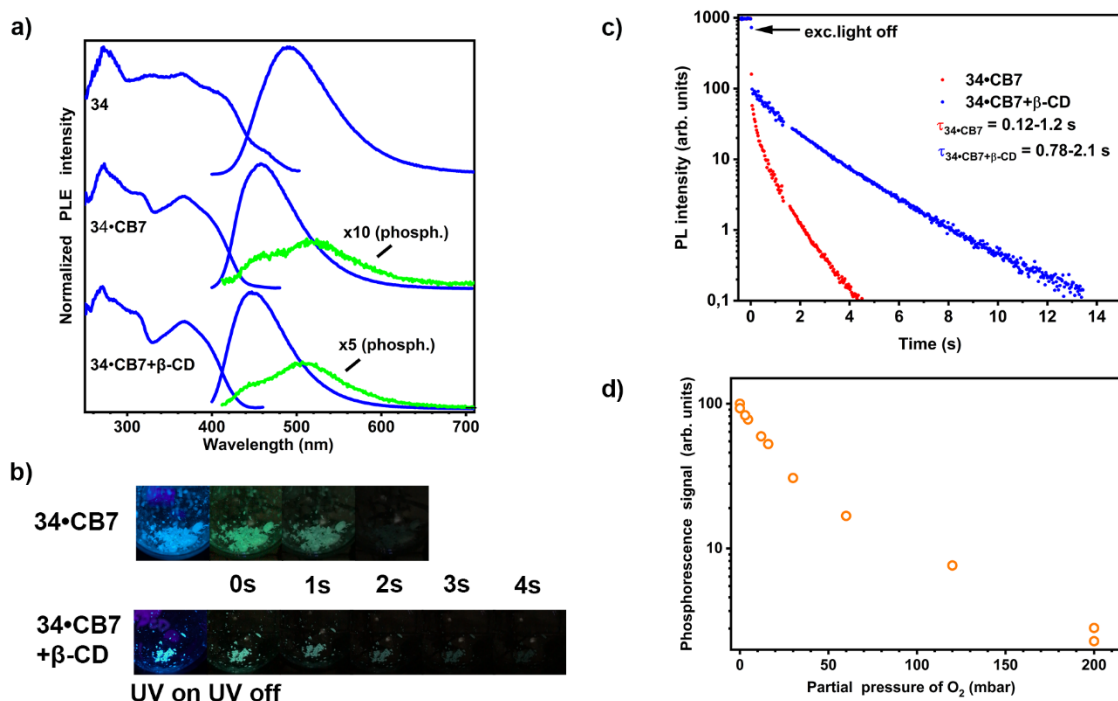


Figure 33. a) Fluorescence excitation and emission spectra (solid blue lines, left and right, respectively) of compound **34** and **34**•CB7 (1:1) and **34**•CB7+ β -CD (1:1:1) under normal conditions (at 295 K). Phosphorescence spectra (solid green line) for **34**•CB7 and **34**•CB7+ β -CD in vacuum or inert gas. b) Photographic images of **34**•CB7 and **34**•CB7+ β -CD in a vacuum, captured during and after exposure to 365 nm UV light. c) Phosphorescence decay curves of **34**•CB7 and **34**•CB7+ β -CD in vacuum. d) The total phosphorescence signal of **34**•CB7+ β -CD as a function of the partial pressure of oxygen. The values at 0 mbar and 200 mbar were measured twice, at the beginning and end of the variation of O₂ (air) pressure, and thus indicate the reproducibility of the measurements.

In addition to blue fluorescence, **34**•CB7 and **34**•CB7+ β -CD exhibited minor green long-lived phosphorescence ($\lambda_{\text{max}} \sim 520$ nm), only observable in a vacuum or an oxygen-free gas atmosphere (Figure 33b, c). The quantum efficiency of this glowing, compared to the fluorescence, was 3% for **3**•CB7 and 7% for **3**•CB7+ β -CD at 295 K, respectively. The phosphorescence was quenched by O₂ within 2-3 minutes (gas/vacuum

handling time), reduced by a factor of ~ 30 in air. This quenching effect was reversible and detectable at an O_2 pressure as low as 5 mbar (Figure 34)

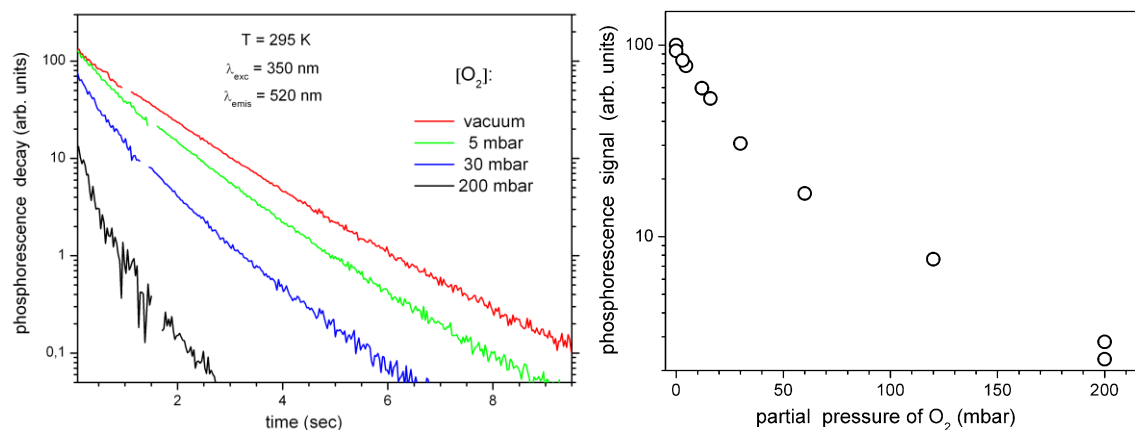
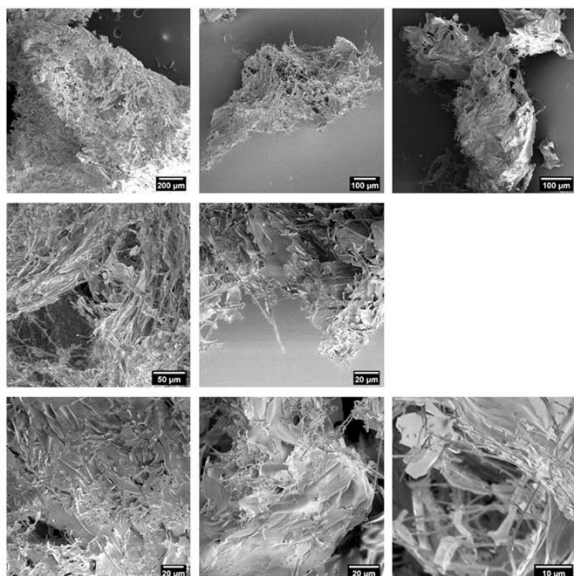


Figure 34. Left: phosphorescence decay of a lyophilized sample of $34\cdot CB7+\beta\text{-CD}$ (1:1:1) at 295 K, depending on the partial pressure of O_2 . Vacuum conditions correspond to the residual gas pressure of $\leq 10^{-2}$ mbar maintained for ≥ 2 -3 min. Evacuation and gas (air) filling of a quartz tube with the sample was done slowly to avoid disturbing the low-density sample flakes. The fluorescence and phosphorescence of $34\cdot CB7+\beta\text{-CD}$ were steadily excited at 350 nm; the excitation beam was then shuttered, and the phosphorescence decay measured at 520 nm, discriminated from the nsec-fast fluorescence. Right: the total phosphorescence signal as a function of the partial pressure of oxygen. The values at 0 mbar and 200 mbar were measured twice, at the beginning and end of the variation of O_2 (air) pressure, and thus indicate the reproducibility of the measurements.

The high sensitivity to O_2 is related to the solid structure of $3\cdot CB7$ and $3\cdot CB7+\beta\text{-CD}$: as typical lyophilized materials, they contain a significant volume fraction of open pores, as evidenced by SEM images (Figure 35); these pores are likely hierarchically structured from micro- to nanosized scale, allowing for efficient gas exchange throughout the entire structure.^[129]

a) $34\cdot CB7$



b) $34\cdot CB7+\beta\text{-CD}$

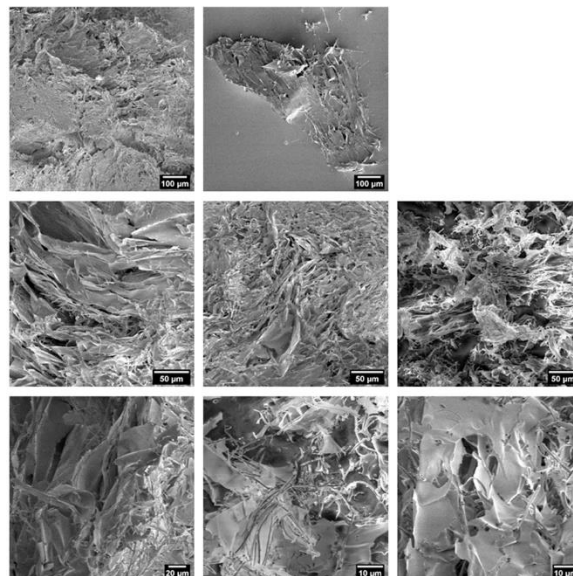


Figure 35. SEM images of lyophilized samples of a) $34\cdot CB7$ (1:1) and b) $34\cdot CB7+\beta\text{-CD}$ (1:1:1). SEM microscope: FEI Nova, beam voltage: 1 or 2 KV. For SEM measurements, flakes of the samples were glued on an SEM stub. The electron beam for both materials was stable during the operation. The images evidence a high volume of open pores and various morphologies, including sheet-like structures (particularly present in $34\cdot CB7+\beta\text{-CD}$) and fibrous and spherical agglomerates.

The quenching phenomenon is facilitated by the very long phosphorescence lifetimes. Decay curves for **34**•CB7 and **34**•CB7+ β -CD in vacuum at 295 K were measured up to approximately 5 and 13 seconds, respectively (Figure 33c). These curves deviate from monoexponential behavior, particularly for **34**•CB7. A multiexponential fit reveals lifetimes ranging from 0.12 to 1.2 seconds for **34**•CB7 and 0.78 to 2.1 seconds for **34**•CB7+ β -CD, respectively. The longer and more consistent lifetimes in **34**•CB7+ β -CD may result from a more homogeneous local environment of **34**•CB7 molecules, facilitated by the addition of β -CD as a matrix compound. Quenching of electronically excited states by molecular oxygen can generate singlet oxygen, which partially relaxes radiatively, producing a weak but characteristic emission band around 1275 nm.^[130] This emission was detected from lyophilized **34**•CB7+ β -CD irradiated at 375 nm in air (Figure 36).

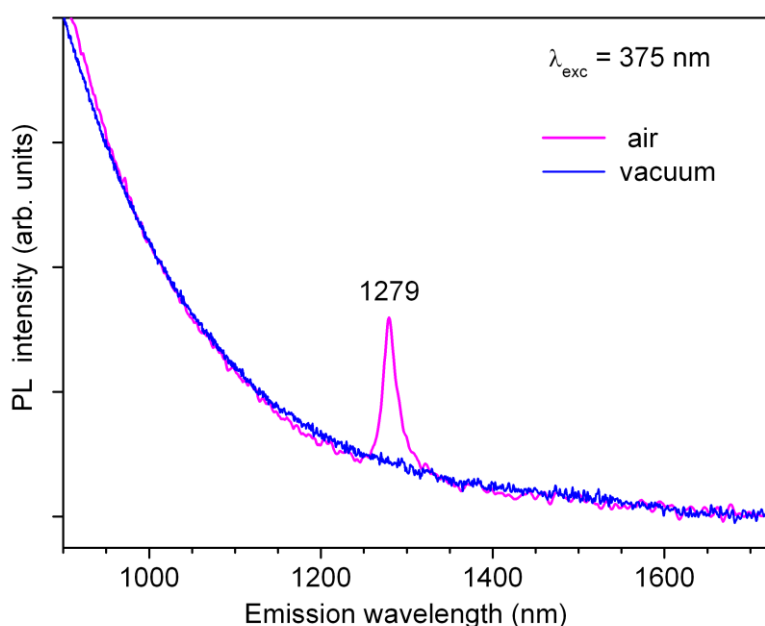


Figure 36. The emission peak of singlet oxygen ($^1\text{O}_2$) was detected at 1279 nm and generated in the lyophilized sample of **34**•CB7+ β -CD (1:1:1) exposed at 295 K to air and excited with a 375 nm laser diode (at a power of 5 mW). The $^1\text{O}_2$ emission disappears after the evacuation of a quartz tube with the sample and recovers after filling it again with air.

Crystalline sample **34** exhibits long-lived phosphorescence but only at temperatures below approximately 150 K (Figure 37). Consistent with previous observations,^[127] the CB7 host appears to limit nonradiative electronic relaxation pathways in the photoexcited carboline guest molecule, thereby enhancing photoluminescence (PL), particularly the long-lived room-temperature phosphorescence (RTP) emission.

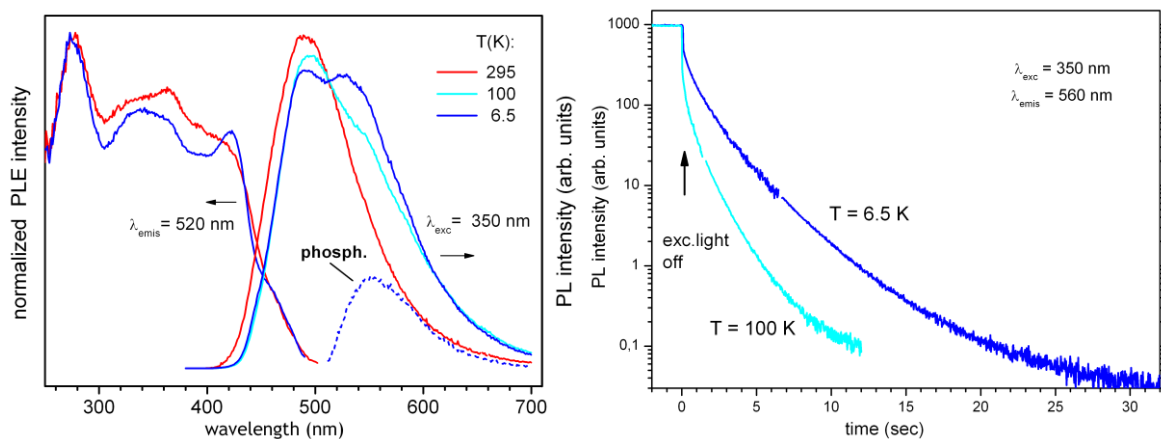


Figure 37. Left: PL emission and excitation spectra of polycrystalline carboline **34** at different temperatures between 295 and 6.5 K. The spectra were excited/ recorded at 350/ 520 nm, respectively. The emission at 295 K is an ns-fast fluorescence that also dominates the spectra at low temperatures. Right: ~150 K, a new band appears as a shoulder at ~540 nm and increases in intensity by decreasing the temperature to 6.5 K. This band is due to the long-lived phosphorescence of compound **34**; its estimated spectrum at 6.5 K is shown with the blue dashed line. Bottom: phosphorescence decay at 6.5 K vs. 100 K, recorded at a 560 nm emission wavelength after shutting off the excitation at 350 nm. The initial stepwise decrease in intensity corresponds to the contribution of fast fluorescence. The gaps in the decay curves are due to the removal of a neutral density filter that was applied to extend the accessible emission intensity range (see experimental details above). The 3-exponential fits (not shown) of the phosphorescence decay traces give lifetimes within 0.23-2.4 s (6.5 K) and 0.1-1.2 s (100 K).

The lyophilized samples were mechanically compressed into solid pellets under vacuum conditions to mitigate the pore structure and minimize oxygen gas intake. Specifically, a pellet was prepared from lyophilized **34**•CB7+ β -CD evacuated in a pellet die and pressed at 20 kN/cm². The resulting pellet exhibited room-temperature phosphorescence (RTP) under normal atmospheric conditions, showing similar characteristics to the initial **34**•CB7+ β -CD material under vacuum or inert gas environments.

As mentioned earlier, the oxygen sensitivity observed in the lyophilized phosphorescent compounds resembles the oxygen-reduced photoluminescence (PL) observed in certain metal-organic framework compounds studied as oxygen sensors.^[131] Hence, these findings suggest the potential utility of carbolines as phosphorescent emitters and cucurbiturils as their hosts for oxygen-sensing applications.

3.3. Modulating and Accelerating Photolysis of [2.2]Paracyclophane Aryl Azide

Preface

Parts of the following chapter were published in *Advanced Functional Materials* (WILEY-VCH)

X. Qiu, E. Pohl, Q. Cai, J. Seibert, Y. Li, S. Leopold, O. Fuhr, M. A. R. Meier, U. Schepers, S. Bräse, Modulating and Accelerating Photolysis of Photoactivatable [2.2]Paracyclophane Aryl Azide in Supramolecular Host for Bioimaging. *Adv. Funct. Mater.* **2024**, 2401938.

Author contributions. The first author contributed to the study conception, design, material synthesis, data collection, analysis, and manuscript preparation. E. Pohl and Q. Cai contributed to the data collection and analysis. J. Seibert, Y. Li, and S. Leopold contributed to the data analysis. O. Fuhr contributed to the X-Ray.

Acknowledgments. This work is supported by the China Scholarship Council (CSC grant: 202010190002) and the Deutsche Forschungsgemeinschaft (DFG) under Germany's Excellence Strategy – 3DMM2O – EXC-2082/1–390761711.

Introduction

The strategic development of photoactivatable fluorophores (PAFs), capable of transitioning from non-fluorescent or weakly fluorescent compounds to highly emissive dyes through specific photoreaction pathways, holds significant appeal, especially for applications in biology^[132]. The activation of fluorescence within living cells has garnered considerable interest in tracking dynamic biological processes, monitoring bioactive molecules, and enabling real-time localization bioimaging^[133]. Until now, a multitude of PAFs have been disclosed, primarily relying on various photoreaction mechanisms, notably including photoisomerization^[134], photoconversion^[135], and photouncaging^[136].

Organic azides hold significant promise in biological applications, capable of being integrated into various functional molecules via pathways like copper(I)-catalyzed azide-alkyne cycloaddition (CuAAC) click reaction^[107a, 137], Staudinger ligation^[108a, 138], or reduction to amines^[139]. Photolysis of aryl azides has emerged as a burgeoning area in chemical biology^[110]. Despite this, the development of photoactivatable fluorophores (PAFs) based on the photolysis of aryl azides within living cells has been rarely reported^[140]. This scarcity could be attributed to the highly reactive singlet nitrene generated upon the photolysis of azides, leading to unpredictable photoreaction pathways^[125]. Thus, there's an urgent need to develop mild and efficient methods to control aryl azide photolysis in chemical biology.

Benefitting from reactions occurring within a "molecular flask"^[141], namely reactions within a supramolecular host molecule, we've previously pioneered a novel method to regulate the photoreaction pathway of aryl azides within the cucurbit[7]uril (CB7) cavity, yielding carbolines with remarkable selectivity^[142]. Prior findings indicate that photolysis of the designed aryl azides in aqueous media yields various photoproducts. In contrast, when photoreactions were conducted within the CB7 cavity, the reaction pathway shifted towards intramolecular C-H amination, resulting in the selective formation of carbolines exhibiting significantly enhanced

fluorescence intensity^[142]. Considering these pivotal findings, there is a promising potential to apply this controlled photolysis process in biological contexts.

[2.2]Paracyclophane (PCP), an unusual molecule featuring two benzene rings arranged in a coplanar manner with a deck distance of 3.09 Å, smaller than Van der Waals distance observed between graphite layers (3.35 Å), enabling strong transannular electronic communication, has garnered attention for its intriguing photophysical properties. These properties position PCP as a promising candidate for developing optical materials^[143].

In this research, a newly developed photoactivatable aryl azide (**35**) featuring a PCP core structure was designed and synthesized. This compound can undergo three distinct reaction pathways in an aqueous environment, forming three unique emissive products (**53**, **54**, **55**, **Figure 38**). The study observed the modulation and acceleration of the photolysis of compound **35** when confined within the cavity of cucurbit[8]uril (CB8), transforming from a low-emissive aryl azide to highly fluorescent carbolines. Finally, the study successfully demonstrated the photoreaction of the aryl azide within living cells for optical imaging, showcasing the potential of this innovative photoactivatable system.

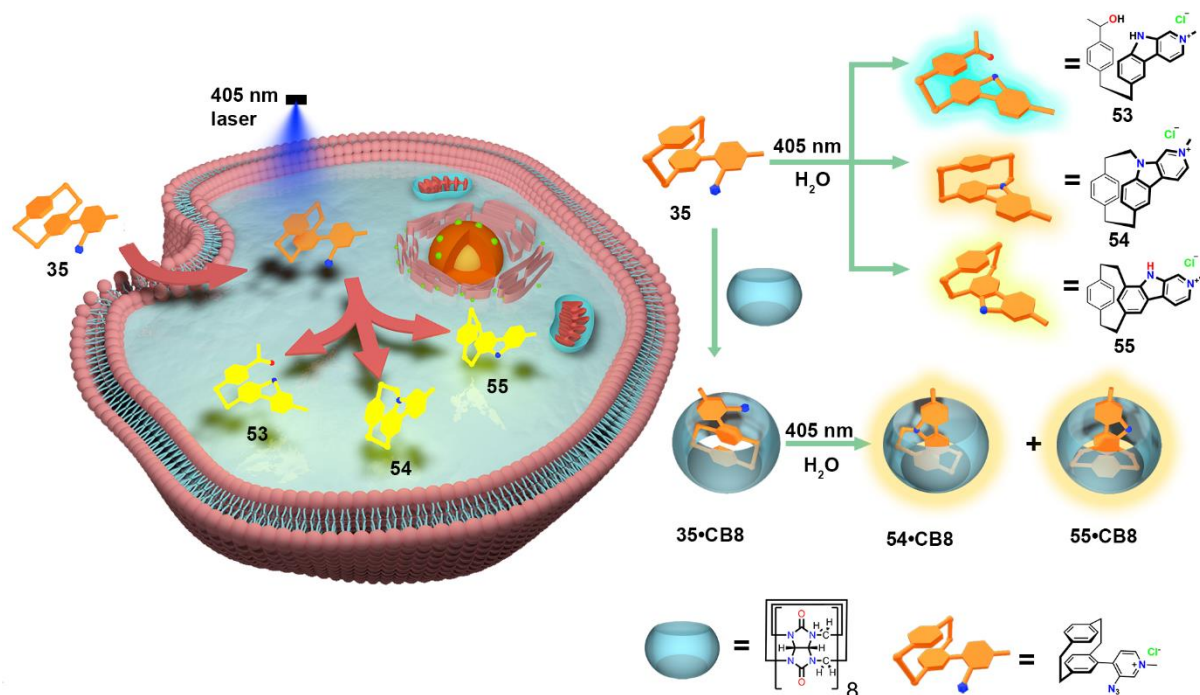
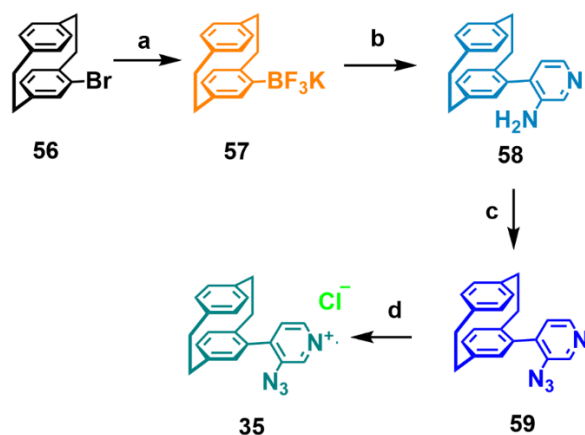


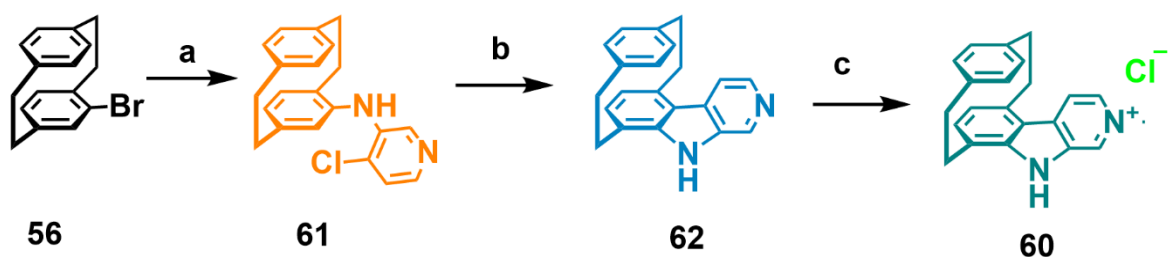
Figure 38. Schematic illustration of photoactivatable aryl azide (**35**) ‘turn on’ emission in a living cell (left) and modulating the photoreaction of the **35** with CB8 as reaction chamber (right).

Synthesis. The synthesis of the titled [2.2]paracyclophane azide is unambiguous, comprising the following steps (Scheme 4): 1) the synthesis of stable [2.2]paracyclophane trifluoroborate salt (**57**) from 4-bromo[2.2]paracyclophane (**56**) via a pinacol boronic ester route^[144]; 2) palladium-catalyzed Suzuki cross-coupling reaction to obtain amino pyridyl[2.2]paracyclophane (**58**); 3) preparation of azide from amino pyridyl[2.2]paracyclophane to yield azido pyridyl[2.2]paracyclophane^[122] (**59**); 4) methylation of azido pyridyl[2.2]paracyclophane and ion exchange resulting the desired **35**.



Scheme 4. a) *n*BuLi (1.1 equiv), triisopropyl borate (1.5 equiv), HF₂K (6.0 equiv), THF, H₂O, -78 °C, 17 h (75 %); b) 4-bromopyridin-3-amine (1.2 equiv), Pd(OAc) (0.05 equiv), K₃PO₄ (4.0 equiv), RuPhos (0.15 equiv), Toluene, H₂O, 80 °C, 24 h (66 %); c) *p*-TsOH·H₂O (1.5 equiv), TBN (1.5 equiv), NaN₃ (3.0 equiv), ACN, H₂O, 25 °C, 6 h (87 %); d) MeI (1.5 equiv), NH₄PF₆ (5.0 equiv), [Bu₄N]Cl (5.0 equiv), ACN, H₂O, 40 °C, 16 h, 81 %.

The compared paracyclophane carboline **60** was synthesized in the following methods: 1) Buchwald-Hartwig cross-coupling reaction to synthesize intermediate **61** from 4-bromo[2.2]paracyclophane (**56**); 2) ring close reaction forming carboline precursor **62**; 3) methylation and ion exchange to obtain the desired carboline **60**.



Scheme 5. a) XPhos (0.1 equiv), Pd₂(dba)₃ (0.1 equiv), NaOtBu (3.0 equiv), 4-chloropyridin-3-amine (1.2 equiv), Toluene, 105 °C, 16 h (45 %); b) Pd(OAc) (0.1 equiv), K₂CO₃ (2.0 equiv), (*t*-Bu)₃P (0.2 equiv), DMF, 120 °C, 24 h (63 %); c) MeI (1.5 equiv), NH₄PF₆ (5.0 equiv), [Bu₄N]Cl (5.0 equiv), ACN, H₂O, 40 °C, 16 h, 78 %.

Results and discussion.

The fascinating photophysical characteristics of carboline derivatives have been revealed across diverse applications^[145]. Notably, previously reported carboline derivatives exhibit exceptional emission properties in both aqueous environments and the solid state^[142]. A curiosity arises regarding the photophysical traits of a derivative where one of the benzene rings is substituted with a [2.2]paracyclophane system. To synthesize the desired PCP-carboline, the proposed approach involves photolyzing PCP aryl azide (**35**) within the supramolecular host CB8 using the reported method^[142].

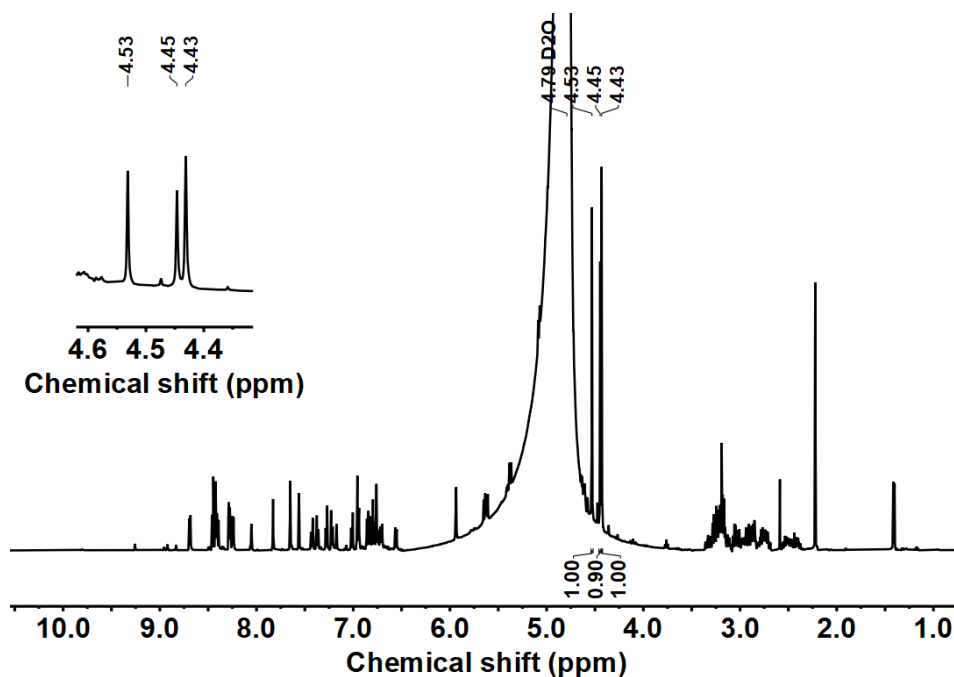


Figure 39. ^1H NMR spectra of **35** after irradiation with 405 nm LED, 500 MHz, D_2O (4.79 ppm).

The photolysis of compound **35** was first studied in water employing 405 nm LEDs for irradiation. Following irradiation, new peaks appeared in the ^1H NMR spectra (Figure 39). Notably, three identical main peaks corresponding to methyl protons in the aliphatic region appeared at approximately 4.53 ppm, 4.45 ppm, and 4.43 ppm, with an approximate 1:1:1 ratio.

Liquid Chromatography–Mass Spectrometry (LC–MS) was employed to analyze the reaction mixtures and their respective masses to obtain more insights into the photoreaction products. Indeed, three predominant fractions were observed at retention times of 3.7 minutes, 3.9 minutes, and 4.1 minutes. With molecular weights of 331.30 g/mol, 313.30 g/mol, and 313.31 g/mol, respectively (Figure 40).

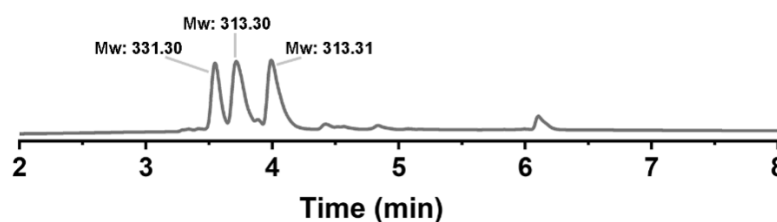


Figure 40. LC-MS of **35** after irradiation with 405 nm LED.

The previous study suggested that in aqueous conditions, the photoreaction of aryl azide can lead to a nucleophilic attack by water, resulting in the formation of an azepine product^[142]. Considering this, it can be inferred that one of the products from the photolysis of compound **35**, following the loss of nitrogen and addition of water, has a molecular weight of approximately 331 g/mol, consistent with the first fraction observed in LC-MS. Another potential reaction pathway may involve C-H amination, producing a carboline derivative with a molecular weight of around 313 g/mol, aligning with the LC-MS results' observations. Interestingly, the

subsequent fractions from LC-MS, showing the same molecular weight, suggest the possibility of two isomers emerging during the photoreaction.

To comprehensively investigate the formation of the three products resulting from the photolysis of compound **35**, the reaction mixture was fractionated using Preparative Reversed-Phase High-Performance Liquid Chromatography (RP-HPLC). Subsequently, NMR studies were conducted on these three species. As the first fraction, eluting at a retention time of 3.7 minutes, unexpected signals were detected in the aliphatic range. These signals differed from the typical signals from the PCP ethylene bridge, suggesting a disintegration of the ethylene bridge during the photolysis of compound **35**.

Upon characterizing the 2D NMR spectra, the structure (**53**) was determined, as illustrated in Figure 41. As for the second fraction with a retention time of 3.9 minutes, the NMR spectra still exhibited signals corresponding to the ethylene bridge, suggesting an intact PCP structure post-photoreaction. Intriguingly, aromatic protons appeared upfield shifted around 5.50 ppm and 4.95 ppm, indicating a shielded aromatic ring system formation. The third product also retained an intact ethylene bridge, displaying shielded aromatic ring signals from 5.23-5.84 ppm, possibly due to the rearrangement of PCP decks. For comparison, compound **60** was synthesized using a traditional approach involving Buchwald-Hartwig cross-coupling, C-H activated cyclization, methylation, and ion exchange. Notably, the NMR spectra of compound **60** indicated that neither of these C-H aminated products matched the desired structure.

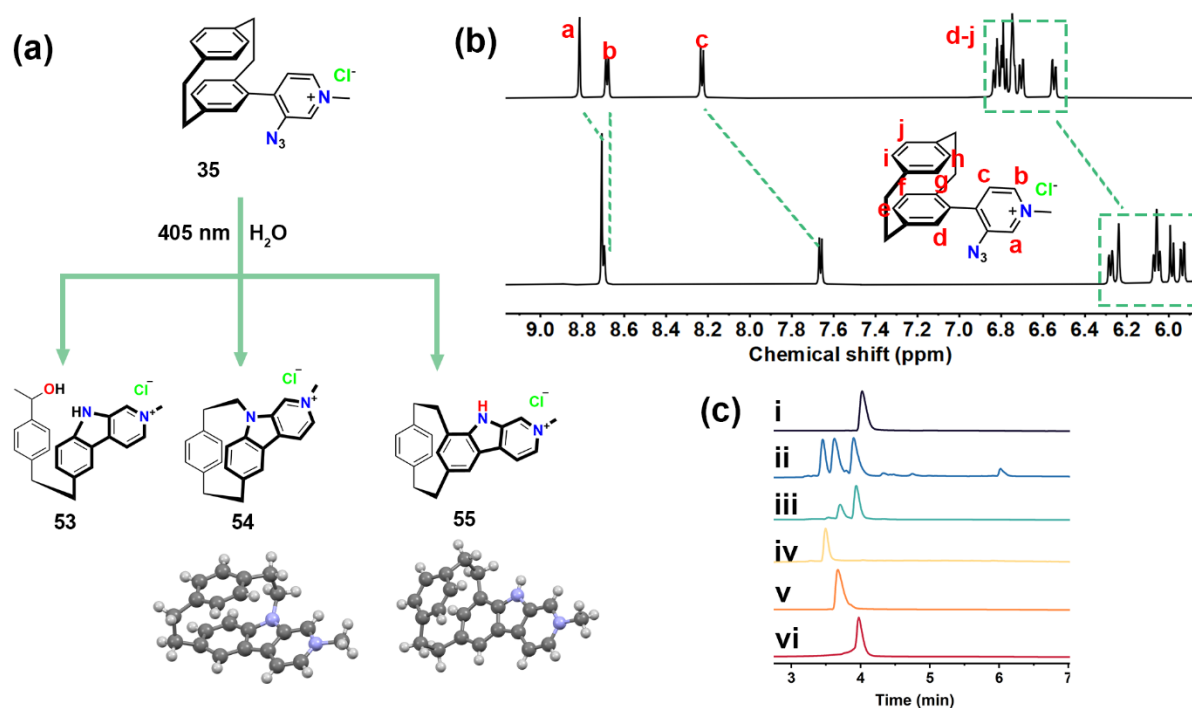


Figure 41. (a) Structures of photoreaction products from compound **35**, and molecular structures of compound **54** and compound **55**, counter ions were omitted for clarity; (b) ¹H NMR spectra (500 MHz, D₂O, 298 K) of compound **35** and **35**•CB8 (1:1, 0.5 mM); (c) LC-MS spectra of i) compound **35**; ii) compound **35** after photoreaction in bulk water; iii) **35**•CB8 after photoreaction; iv) compound **53**; v) compound **54**; vi) compound **55**.

Unfortunately, despite numerous attempts, we could not grow single crystals from the first and second products we obtained. Consequently, we exchanged the counter ion to PF₆⁻ and achieved successful crystallization

and structural evaluation for the second product, compound **54**, as illustrated in Figure 41a, Figure 42a, and Figure 42b. In contrast to the original PCP structure, we observed an expanded deck system with a maximum distance of 7.80 Å from one ethylene proton to the diagonal ethylene proton. A single crystal was also successfully obtained for the third product, compound **55** (Figure 41a, Figure 42c, and Figure 42d). Notably, we observed a migration of the ethylene bridge, resulting in a maximum distance of 7.01 Å from one ethylene proton to the diagonal ethylene proton.

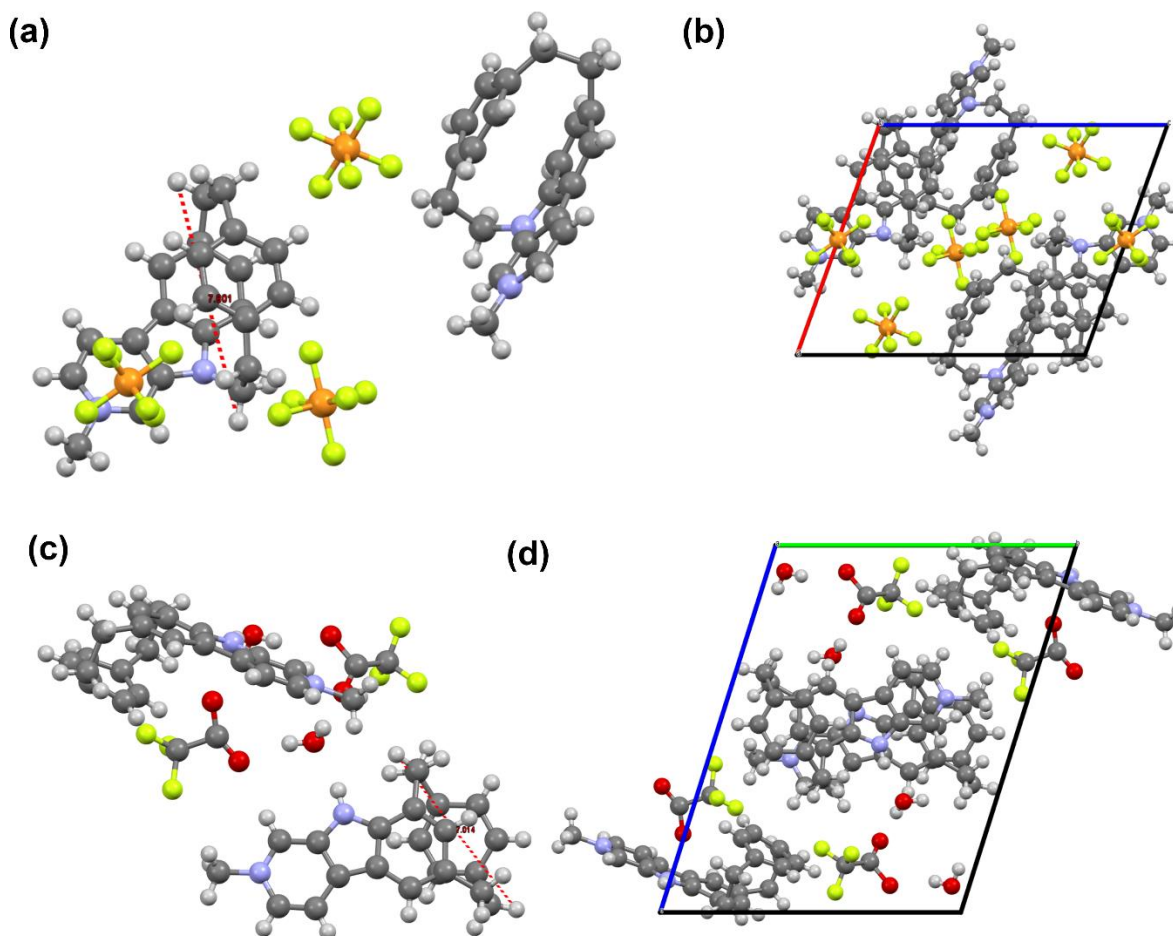


Figure 42. Molecular structure of (a) **54**•PF₆⁻, (b) **54**•PF₆⁻ in packing model; (c) **55**•C₂HF₃O₂, (d) **55**•C₂HF₃O₂ in packing model. (Please note, after the purification by HPLC, the counter ion was exchanged with the mobile phase additive trifluoroacetic acid (TFA)).

Previous studies^[143c] have demonstrated that the CB host can effectively modify the reaction pathway during the photolysis of aryl azide and PCP molecules. These molecules can be accommodated within the CB8 cavity, forming a 1:1 complex with a notable binding constant. Therefore, the potential of CB8 in influencing the photolysis of compound **35** needs to be assessed. We initially investigated the binding interaction between compound **35** and CB8 using ¹H NMR. As depicted in Figure 41b, upon adding equimolar CB8 to compound **35** in the D₂O, the aromatic and ethylene range protons exhibited significant upfield shifts, indicating the encapsulation of compound **35** within the CB8 cavity. The formation of a 1:1 host-guest complex was confirmed

by electrospray ionization (ESI) mass spectrometry, revealing a mass-to-charge ratio (m/z) of 1669.5964 for $[35+CB8]^+$.

The binding affinity of compound **35** with CB8 was investigated using a well-established competitive binding assay^[104], employing memantine hydrochloride (Mem) as a competitive guest with a binding constant of $8.28 (\pm 0.38) \times 10^{12} M^{-1}$. As illustrated in Figure 43, upon the addition of an excess of Mem to the mixture of compound **35** and CB8, two distinct proton signals appeared in the 1H NMR spectrum at 5.54 ppm and 5.47 ppm, corresponding to $35 \cdot CB8$ and Mem \cdot CB8, respectively. By applying binding equations, the binding constant was determined to be $(4.05 \pm 0.57) \times 10^{12} M^{-1}$, indicating the formation of a stable host-guest complex system.

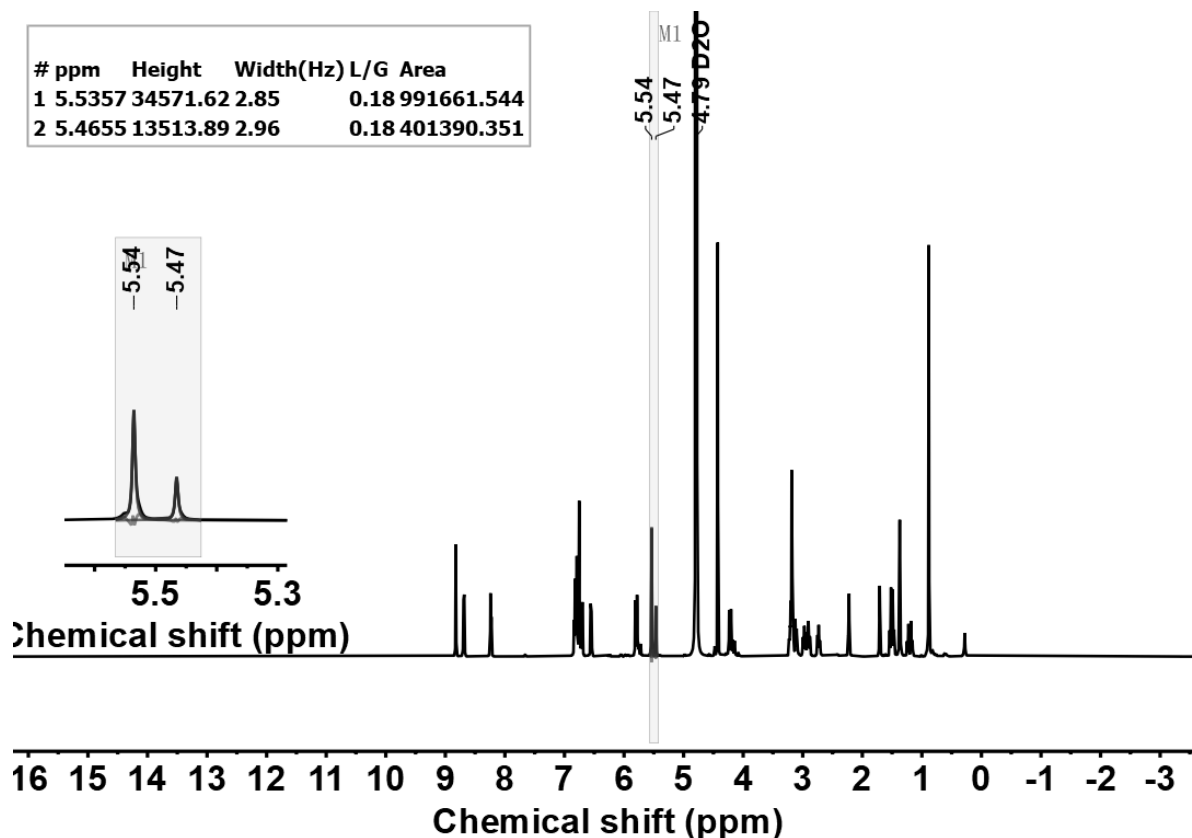


Figure 43. 1H NMR spectra were used in the competitive binding assay determination of K_{rel} value for $[CB8 \cdot 35]$ and $[CB8 \cdot Mem]$. $[CB8]_{Total} = 0.500$ mM, $[Mem]_{Total} = 2.2351$ mM, $[35]_{Total} = 2.4157$ mM, 500 MHz, D_2O .

Photolysis of $35 \cdot CB8$ was conducted under the same conditions as the photoreaction of compound **35** in water. Following the photoreaction, 1H NMR revealed two peaks at 4.65 ppm and 4.52 ppm, attributed to methyl protons (Figure 44). This suggests the formation of two main products when the photolysis of compound **35** was performed in the presence of CB8, as opposed to three without CB8. LC-MS chromatograms from the reaction mixtures also indicated the presence of two main products, corresponding to compound **54** and compound **55** (Figures 41c and 45), while preventing the nucleophilic addition of water. Interestingly, a lower ratio between compound **54** and compound **55** was observed in both NMR and LC-MS, potentially due to the smaller and more compatible size products being favored within the limited CB8 cavity.

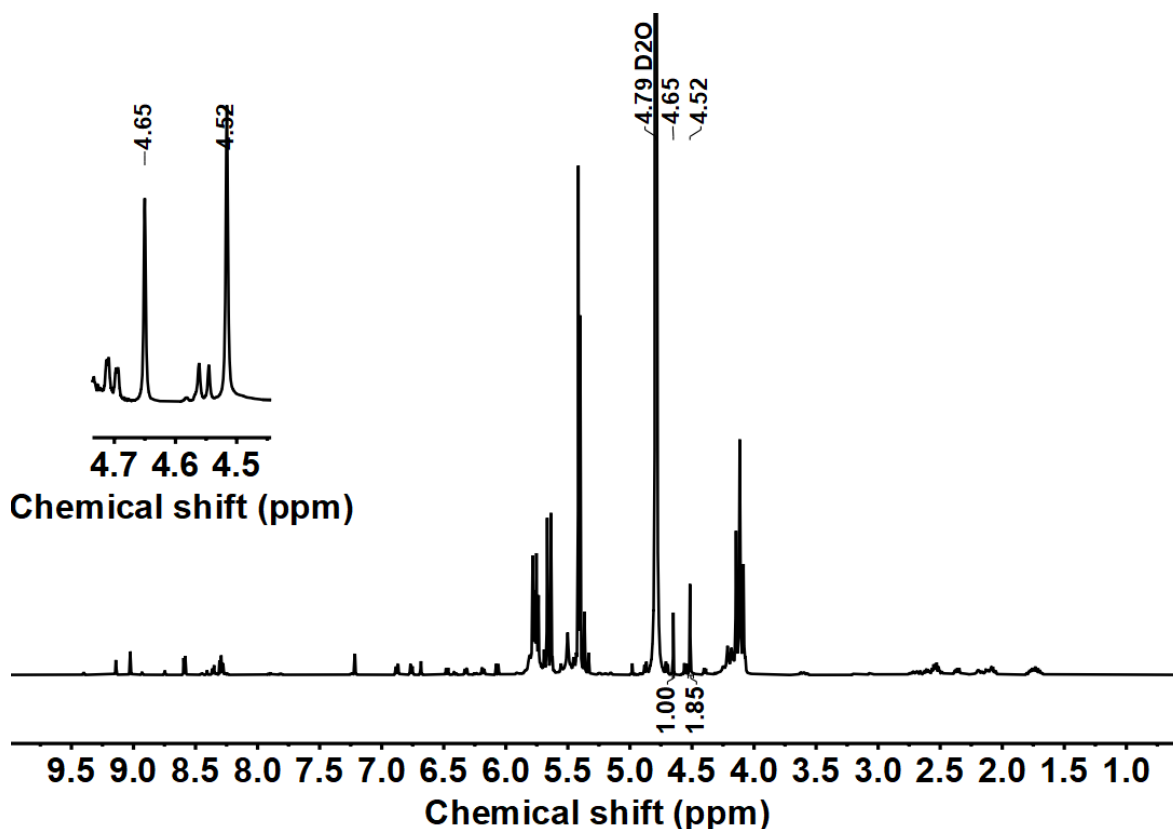


Figure 44. ^1H NMR spectra of **35**+CB8 in 1:1 molar ratio (0.5 mM) after the photoreaction in D_2O at 298 K, 500 MHz, D_2O .

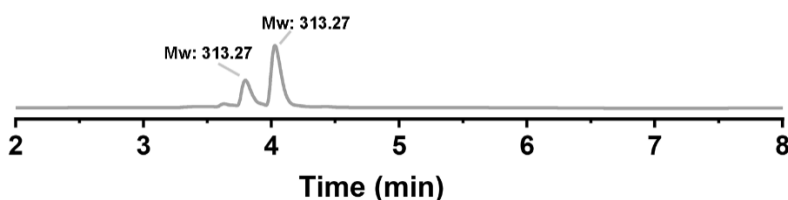


Figure 45. LC-MS of **35**+CB8 in 1:1 molar ratio after photoreaction.

The photolysis of aryl azides typically involves expelling a nitrogen molecule, forming an active nitrene species, which can undergo various reaction pathways depending on the reaction conditions. In this study, three distinct products were formed via different reaction pathways in water. Based on the previous findings^[142], a proposed reaction mechanism (Figure 46) sheds light on these processes. Upon irradiation, the loss of N_2 gives rise to a nitrene species (**Im1**), which can attack the PCP moiety, forming an intermediate with a five-membered ring (**Im2**). Subsequent re-aromatization leads to a bond break between the aryl and ethylene bridge, offering three reaction pathways: 1) Delocalization of the positive charge, generating carbocation-like intermediates Im3^+ and Im4^+ , followed by a nucleophilic attack of water molecule, leading to the formation of compound **53**; in-situ generation of a diradical, followed by migration of ethylene bridge in two directions, either 2) directly forming

compound **54**, or 3) forming the carboline product compound **55**, followed by a 1,3-sigmatropic rearrangement. There was no observed indication of the formation of compound **60** in the experiments.

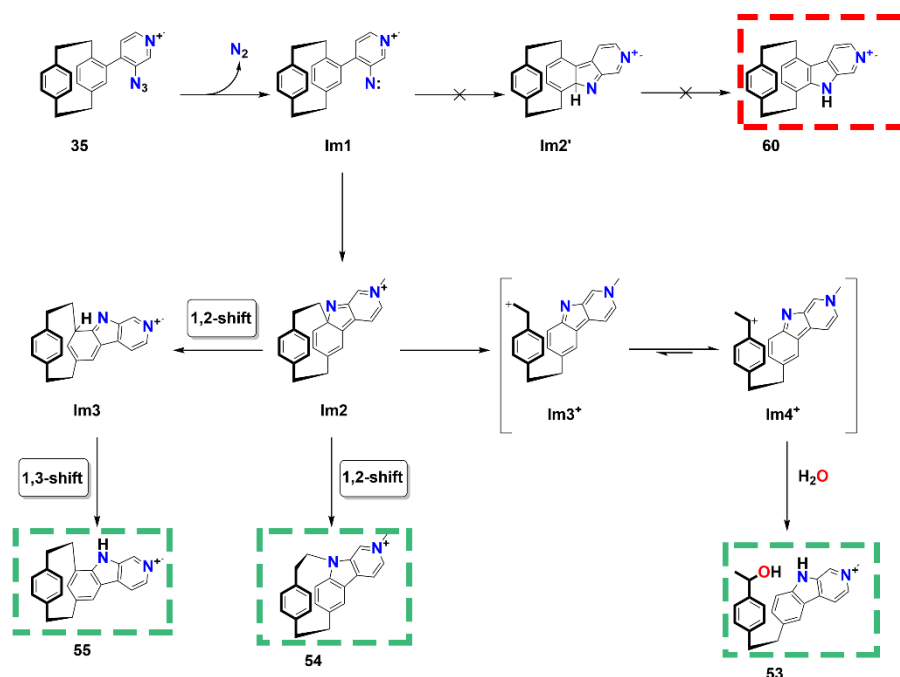


Figure 46. Proposed photoreaction mechanism of compound **35** in water.

DFT calculations were conducted at the B3LYP/6-31 G(d,p) level to investigate deeper into these potential transformations using the Gaussian 16 program package^[146]. The Gibbs free energy profile of the feasible reaction intermediates is depicted in Figure 47. The photolysis of the azide exhibits an activation energy of 30.4 kcal/mol, resulting in a nitrene intermediate. In the case of singlet nitrene **Im1**, this step is exothermic with a reaction-free energy of 37.6 kcal/mol. Following the breakage of the ethylene bridge induced by the positive charge delocalization, the carbocation **Im3+** is generated, which can transform into **Im4+** with an energy gain of 6.5 kcal/mol through a 1,2-H shift. The stabilized styrene-like cation **Im4+** can then be attacked by water, yielding the energetically stable product **53** with a total energy gain of 100.6 Kcal/mol. This step can also follow a radical mechanism. One possible reaction pathway is illustrated for forming the open-chained product **53**. In reaction pathways where water molecules are not involved, as is the case for reactions conducted in the CB8 cavity, **Im2** undergoes homolytic breakage. The in-situ formation of biradical accounts for the brief reaction time and the even distribution of products **54** and **55**. In this scenario, **Im2** either binds the neighboring nitrogen atom, forming product **54**, which results in an energy gain of 88.8 Kcal/mol, or undergoes two rearrangement steps to produce the lower-energy product **55**, located at -90.6 Kcal/mol of the reaction energy profile. The similar energies of compound **53**, compound **54**, and compound **55** indicate why the three species are obtained in approximately a 1:1:1 ratio after the photoreaction of compound **35**.

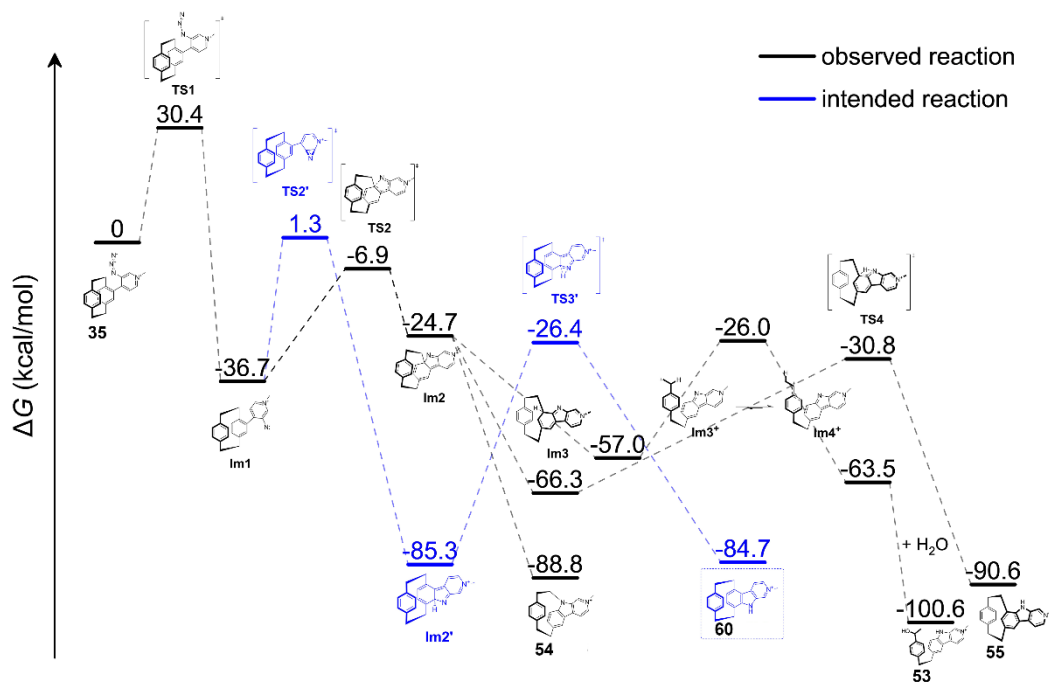


Figure 47. Calculated Gibbs free energy of the possible intermediates. All structures were optimized at the DFT B3LYP /6-31G(d,p) level with Grimme's D3 diffusion corrections using the software package Gaussian 16^[146].

The energies of possible reaction intermediates during the reaction were computed to understand why compound **60** was observed neither in the bulk water nor within the CB8 void (Figure 47 and Figure 48). The transition state **TS2'** was calculated with an energy barrier of 38 Kcal/mol, 8.2 Kcal/mol higher than **TS2**, leading to an intermediate of the more substituted carbon atom, **Im2**. The reaction energy within the CB8 cavity is depicted in Figure 48, where the energy barrier of the final products **54**•CB8 and **55**•CB8 were comparable to those of compound **54** and compound **55** formed in the bulk water.

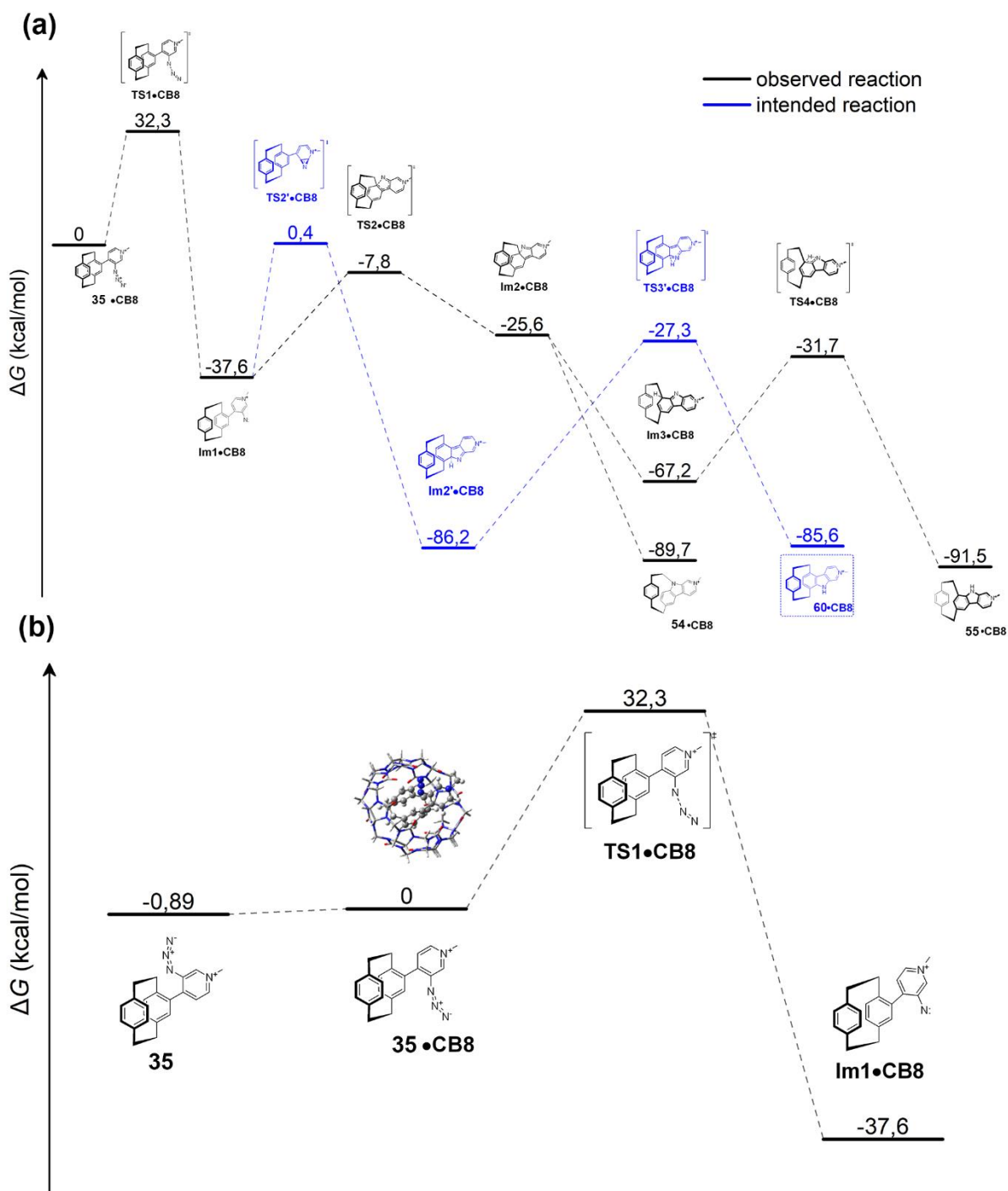


Figure 48. (a). Calculated Gibbs free energy of the possible intermediates for photoreaction compound **35** within CB8 cavity; (b) Compared Gibbs free energy of the compound **35** and **35 • CB8**. All structures were optimized at the B3LYP /6-31G(d,p) /ED=GD3 level of DFT using the software package Gaussian 16.

Subsequently, the photolysis of compound **35** and **35 • CB8** in phosphate-buffered saline (PBS) solution was investigated using UV-Vis and emission spectroscopy. As depicted in Figure 49, the reaction mixtures' absorption spectra showed gradual changes upon irradiation. Specifically, the maximum absorbance at 344 nm from compound **35** decreased, accompanied by the emergence of two new signals at 257 nm and 311 nm simultaneously (Figures 49a). A similar trend was observed upon the photoreaction of **35 • CB8**, with a decrease in absorbance at 357 nm and three new absorbance peaks at 264 nm, 326 nm, and 402 nm, respectively (Figures

49b). This behavior is comparable to the previously observed process of carboline formation within the CB host^[142].

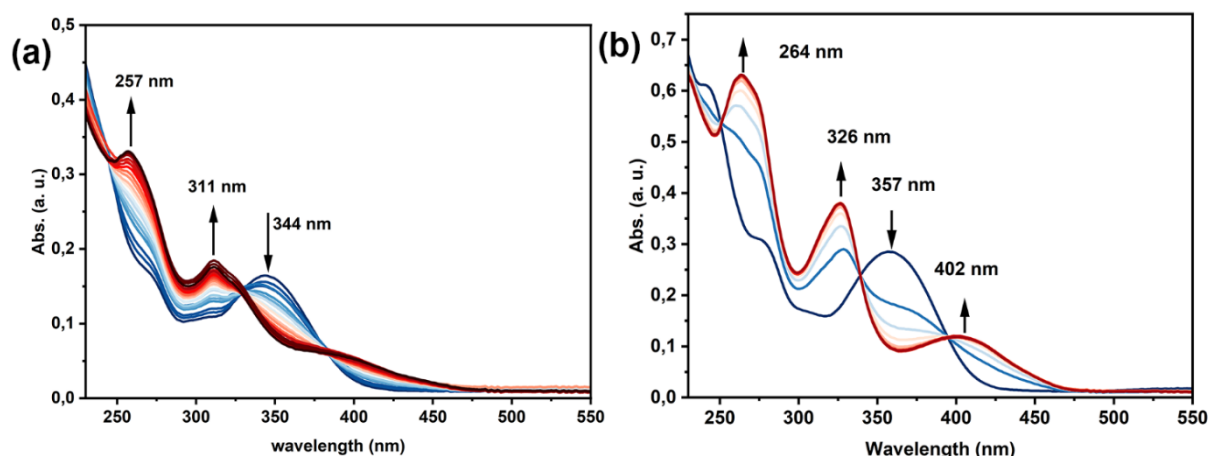


Figure 49. UV-vis spectra of (a) compound **35** and (b) **35**•CB8 (20 μ M) in PBS buffer solutions upon irradiation at 298 K.

The photoluminescence (PL) intensity significantly increased upon the photolysis of compound **35** and **35**•CB8, as illustrated in Figure 50. In Figure 3a, the emission intensity at λ_{493} nm experienced a remarkable 52-fold increase after the photoreaction, contrasting with the weak emission of compound **35** (Figure 50a). As for the **35**•CB8 complex, an 8-fold enhancement at λ_{496} nm was observed after the completion of the reaction, accompanied by a hypsochromic shift of the maximum emission wavelength from 520 nm to 496 nm (Figure 50b). Notably, CB8 acted as a reaction accelerator during the photolysis conducted within its cavity, with a reaction time of approximately 50s compared to 190s in water. This suggests that the reaction efficiency is nearly four times higher when CB8 is present. Such an enhancement effect was not observed in our previous study, possibly due to the confined space of CB8 sterically restricting the ring expansion process during the photoreaction, thereby accelerating the reaction.

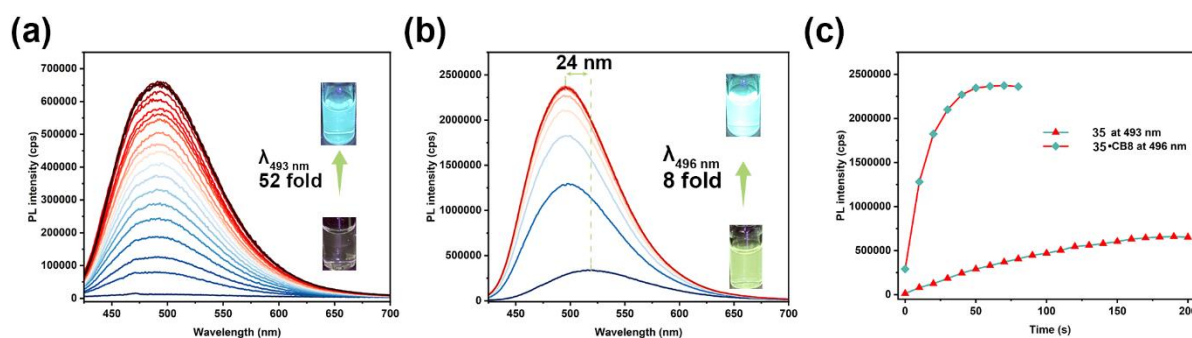


Figure 50. (a) The emission spectra of compound **35** upon the irradiation (20 μ M, excitation at 405nm, entrance and exit slit: 2nm); (b) emission spectra of **35**•CB8 upon the irradiation (20 μ M, excitation at 405nm, entrance and exit slit: 2nm); (c) PL intensity of compound **35** at 493 nm and **35**•CB8 at 496 nm against time upon the irradiation. The emission spectra were measured in PBS buffer solutions (pH = 7.4, 298 K).

The photophysical characteristics of the photoreaction products and their host-guest complexes with CB8 in PBS were further explored. Illustrated in Figure 51 and detailed in Table 3, upon complexation of compound **35** with CB8, bathochromic shifts in both absorbance and emission were observed, possibly due to alterations in conformation and the local environment polarity as compound **35** migrated from water to the hydrophobic cavity of CB8^[147]. Moreover, there were notable enhancements in luminescence quantum yields (QY), likely resulting

from the hydrophobic environment provided by CB8, which minimizes energy decay from molecular rotation and shields against water attack. Among the three photoproducts, compound **53** exhibited the highest QY (44.1 %). Similarly, elevated QY was observed when compound **54** and compound **55** were internalized within the CB8 cavity, with QY 41.7% and 35.5%, compared to the bulk solution with QY 18.3% and 16.3%, respectively.

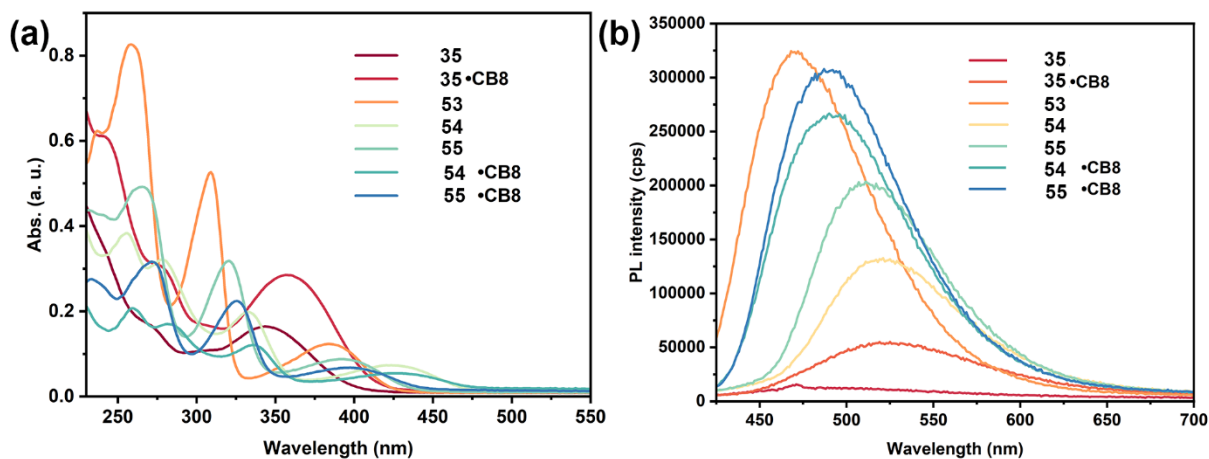


Figure 51. (a) UV-vis spectra of PCP samples; (b) emission spectra of PCP samples (excitation at 405nm, entrance, and exit slit: 2nm). All samples were measured in PBS buffer solutions (pH = 7.4, 20×10^{-6} M, 298 K).

Table 3. The summary of the photophysical properties of **35** and photoproducts.

Compounds ^a	λ_{Abs} (nm)	λ_{em} (nm)	Φ_{PL} (%)
35	344	489	1.1
35•CB8	357	520	8.6
53	258, 309, 384	472	44.1
54	256, 279, 333, 424	521	18.3
55	265, 320, 391	511	16.3
54•CB8	259, 281, 336, 426	490	41.7
55•CB8	271, 326, 398	492	35.5

(a) Abbreviations: λ_{abs} = absorption maximum, λ_{em} = emission maximum, Φ_{PL} = photoluminescence quantum yield. The absorption and emission spectra were measured in PBS buffer solutions (pH = 7.4, 20×10^{-6} M, 298 K).

DFT calculations were conducted to explore deeper into the ground state orbital contribution and electronic energy of the highest occupied molecular orbital (HOMO) and lowest unoccupied molecular orbital

(LUMO) of the PCP fluorophores. As illustrated in Figure 52a, the HOMO and LUMO energy levels of compound **35** were determined to be -5.12 eV and -9.83 eV, resulting in a HOMO-LUMO gap of 4.72 eV. However, the HOMO-LUMO gaps of the photoproducts increased to 6.10 eV for compound **53**, 5.71 eV for compound **54**, and 5.98 eV for compound **55**, respectively. Considering these findings, the absorption and fluorescence spectra of the mentioned molecules were computed (Figure 52b and Figure 52c), showing blue-shifts that align closely with the experimental results (Figure 51).

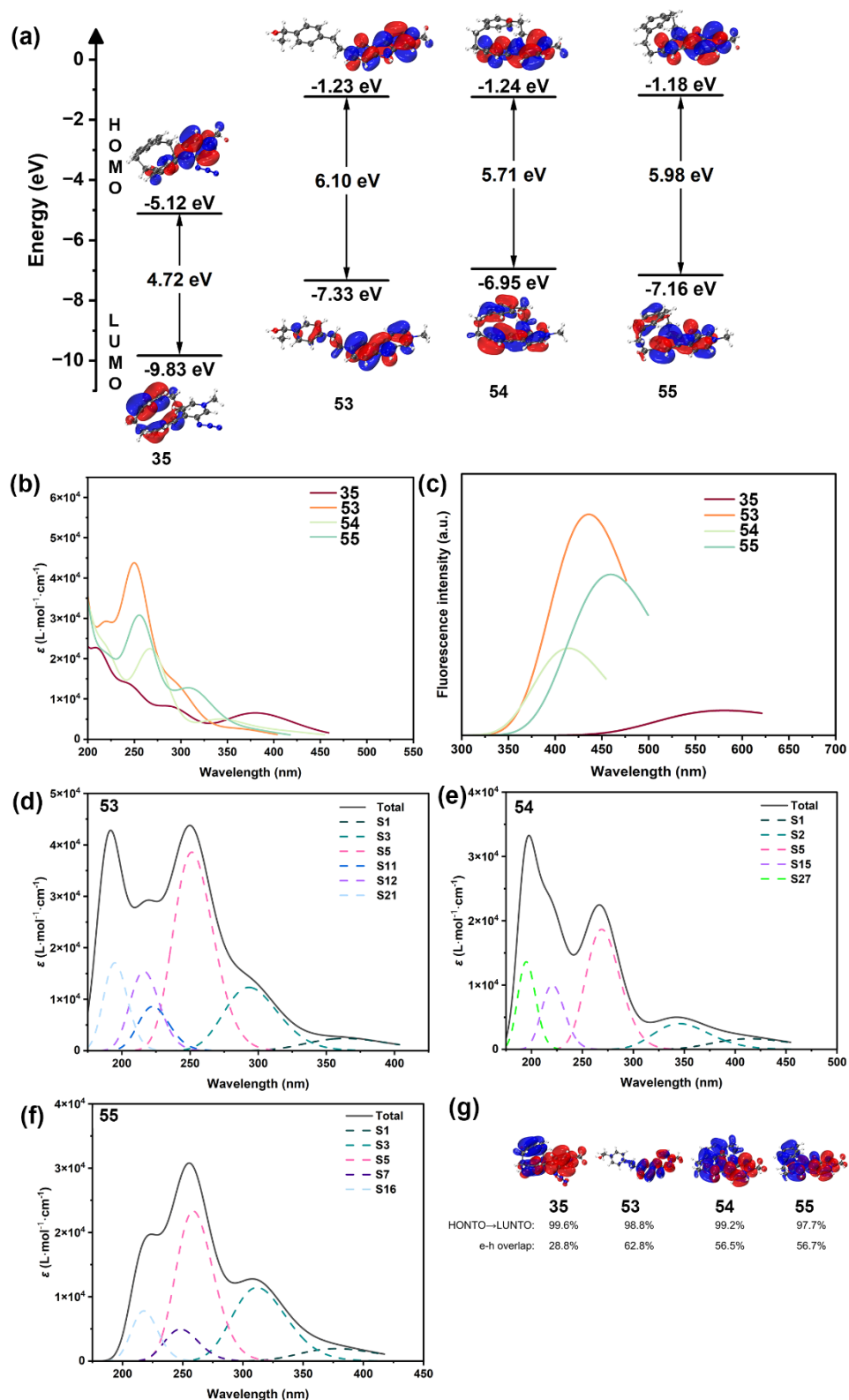


Figure 52. (a) Theoretical calculated ground state orbital contribution of PCP molecules.; (b) calculated absorption spectra of PCP samples; (c) calculated emission spectra of PCP samples; (d) calculated absorption spectra of compound **53**; (e) calculated absorption spectra of compound **54**; (f) calculated absorption spectra of **55**. (g) natural transition orbital (NTO) analysis of the excited state S₁ of compounds **35**, **53**, **54**, and **55**. Blue: The highest occupied natural transition is orbital (HONTO). Red: Lowest unoccupied natural transition orbital (LUNTO). All structures were optimized at the PBE0/6-31G(d,p) /ED=BJGD3 level of DFT using the software package Gaussian 16. The contributions of different vertical transitions and the NTO and electron-hole (e-h) overlap analyses were carried out on Multiwfn^[148].

Despite the remarkable photophysical properties of PCP derivatives in material science, their limited solubility in water has hindered their exploration in biological applications^[149]. However, considering the findings discussed above, there is potential for novel PCP molecules in live cell imaging. The higher quantum yield (QY) observed in the PCP-CB8 complex is particularly intriguing. To assess their suitability, cytotoxicity tests were conducted using HeLa cells at different concentrations (5 μ M, 10 μ M) of the seven PCP fluorophores. The results of the MTT assay in Figure 53 demonstrate that the obtained PCP fluorophores exhibit low toxicity (LD₅₀ > 10 μ M) in HeLa cells.

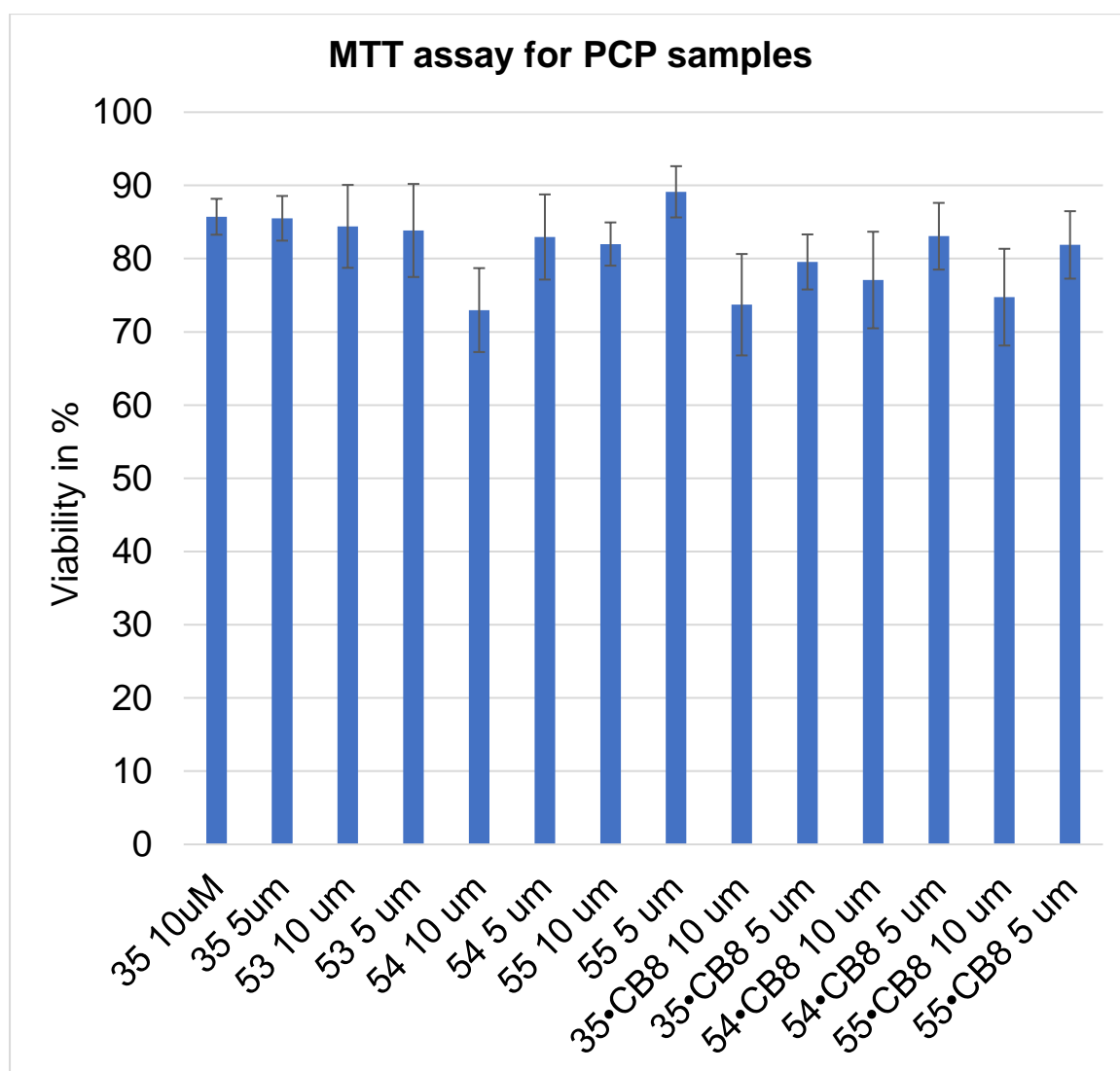


Figure 53. Cytotoxicity of different concentrations (5 μ M and 10 μ M) of PCP samples to HeLa cells determined *via* MTT-assay after 48 h treatment.

Additionally, cell imaging was conducted using the examined PCP fluorophores at a concentration of 5 μ M (**53**, **54**, **55**, **54•CB8**, **55•CB8**). As illustrated in Figure 54a, investigated fluorophores were internalized via endocytosis, primarily accumulating in endosomal vesicles. Notably, compound **54** and **54•CB8** exhibited endosomal escape, leading to cytosolic distribution. Interestingly, the presence of the CB8 cavity did not affect the biocompatibility or intracellular accumulation of compound **54** and compound **55** (Figure 54a).

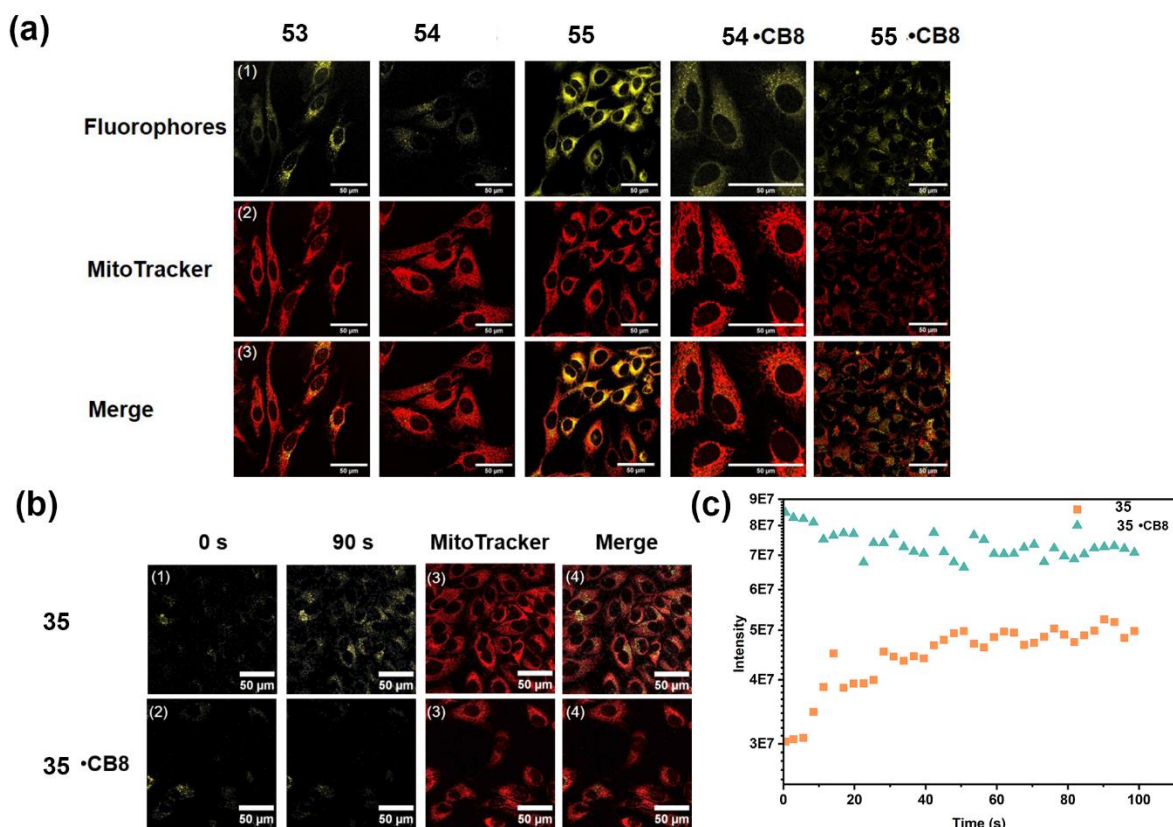


Figure 54. (a) Confocal imaging of HeLa cell stained with (1) **53**, **54**, **55**, **54•CB8**, **55•CB8** (5 μM), and (2) Mitotracker™ Red, and (3) merged images of (1) and (2); (b) confocal imaging of HeLa cell stained with (1) **35** and **35•CB8** (5 μM) at 0s and 60s, and (2) Mito-Tracker Red, and (3) merged images of (1) and (2); (c) the relative intensity upon the irradiation time increased of **35** and **35•CB8** (5 μM) in HeLa cell.

The photoreaction dynamic of compound **35** and **35•CB8** in cellular raised interest in their photoactivation behavior. Thus, the photoactivation of compound **35** and **35•CB8** was initially explored by incubating HeLa cells with a 5 μM concentration of each fluorophore. Imaging was conducted using time-dependent confocal fluorescence microscopy. In Figures 54b and 54c, the initial state (0 s) for the 5 μM compound **35** reveals a weak fluorescence. Upon irradiation at 405 nm, fluorescence (410-550 nm) gradually increased, reaching saturation after 60 seconds.

Additionally, compound **35** exhibited colocalization with perinuclear vesicles and the cytosol, suggesting endocytic uptake and endosomal escape. This observation correlated well with the intracellular colocalization of the corresponding activated fluorophores compound **53**, compound **54**, and compound **55**. no time-dependent increase in fluorescence for **35•CB8** was observed within the cells when coupled with the CB8 cavity (Figure 54b, 54c). This lack of enhancement might be attributed to the rapid photoreaction within CB8, as the response time from triggering the reaction to image capture was too rapid.

3.4. Modulating the Photolysis of Aryl Azides for Bioimaging

Preface

Parts of the following chapter were submitted.

X. Qiu, E. Pohl, A. Jung, Q. Cai, H. Su, O. Fuhr, U. Schepers, S. Bräse, Modulating the photolysis of aryl azides in supramolecular host to develop photoactivatable fluorophores. *submitted*.

Author contributions. The first author contributed to the study conception, design, material synthesis, data collection, analysis, and manuscript preparation. E. Pohl, A. Jung, Q. Cai and H. Su contributed to the data collection and analysis. O. Fuhr contributed to the X-Ray.

Acknowledgments. This work is supported by the China Scholarship Council (CSC grant: 202010190002) and the Deutsche Forschungsgemeinschaft (DFG) under Germany's Excellence Strategy – 3DMM2O – EXC-2082/1–390761711.

Introduction

Photoconvertible molecules capable of undergoing directed photoreactions, leading to a significant enhancement in emission from a weak or non-fluorescent state, are in high demand^[135a, 135e]. This ‘turn on’ process holds great potential for tracking biological activity and real-time localization imaging^[133e, 135f, 150]. Organic azides have demonstrated versatility in chemical biology due to their amenability to further functionalization using various methods, including C-H amination^[151], Staudinger reduction^[108a, 138], and copper(I)-catalyzed azide-alkyne cycloaddition (CuAAC) click reaction^[107a, 152]. The photolysis of aryl azides is particularly notable in chemical biology, with applications ranging from light-induced protein labeling^[110, 153] to RNA photo-crosslinking^[154]. However, using aryl azides as photoactivatable probes in living cells is relatively rare^[140a, 140c, 140d, 155]. This scarcity could come from generating highly toxic singlet nitrenes upon aryl azide photolysis, potentially reducing cell viability. Additionally, the reactivity of singlet nitrenes may lead to uncontrollable photoreaction pathways, yielding undesired products^[125].

To address the challenges above, we previously introduced a novel approach aimed at selectively controlling the photoreaction pathway of aryl azides toward the formation of carboline derivatives. This was achieved by leveraging a macrocyclic molecule, specifically the supramolecular host cucurbit[7]uril (CB7). In earlier investigations, we observed the generation of various undesired products through different reaction pathways during the photoreaction of designed aryl azides. However, when the aryl azide was encapsulated within the CB7 cavity to form a 1:1 host-guest complex, the photolysis process underwent selective alteration towards intramolecular C-H amination, resulting in the formation of carboline derivatives with significantly enhanced fluorescence intensity^[142].

In our previous work, we introduced the methylated aryl azide that could complementarily fit within the cavity of CB7 through various non-covalent interactions. Based on our fundamental molecule, we designed and synthesized a series of aryl azides with a push-pull composition featuring an azido pyridine moiety capable of recognizing the CB7 cavity and forming a 1:1 complex (Figure 55). By incorporating different electronic donating

groups ranging from dimethylamine to diphenylamine and carbazole into the designed azides, we aimed to modulate intramolecular charge transfer (ICT) and adjust the absorbing band of the azides to achieve enhanced biocompatible photolysis^[156]. We have demonstrated the ability to control photoreaction within the CB7 cavity, transforming low-emissive aryl azides into highly fluorescent carbolines. To further understand the mechanism of this 'turn-on' process, we conducted time-dependent density functional theory (TD-DFT) calculations. Additionally, we have successfully applied the photoactivation process in living cells for mitochondria-targeted optical imaging (Figure 55).

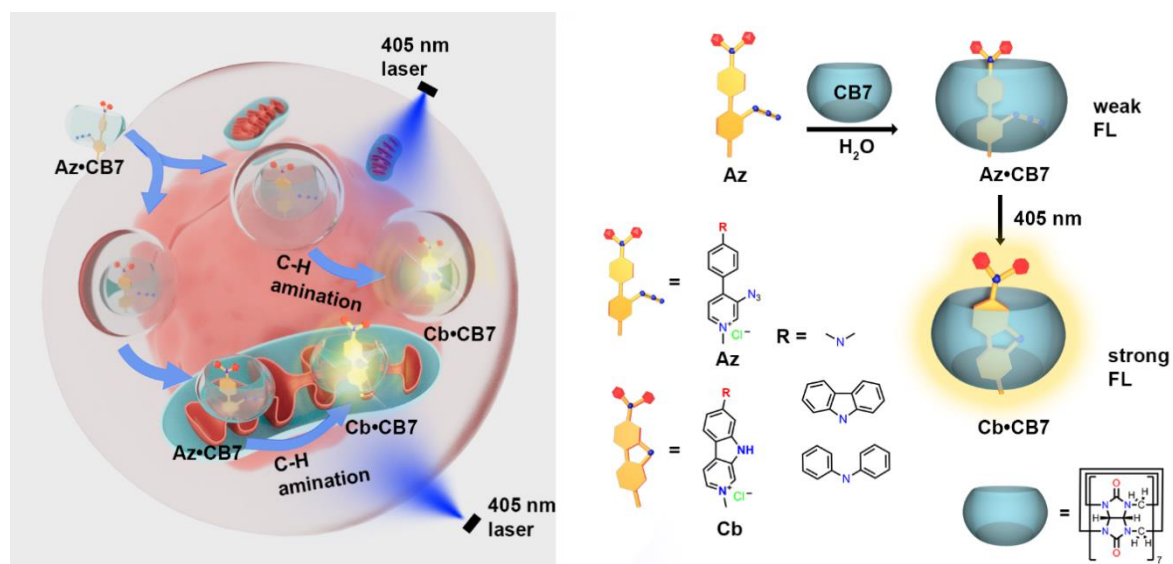
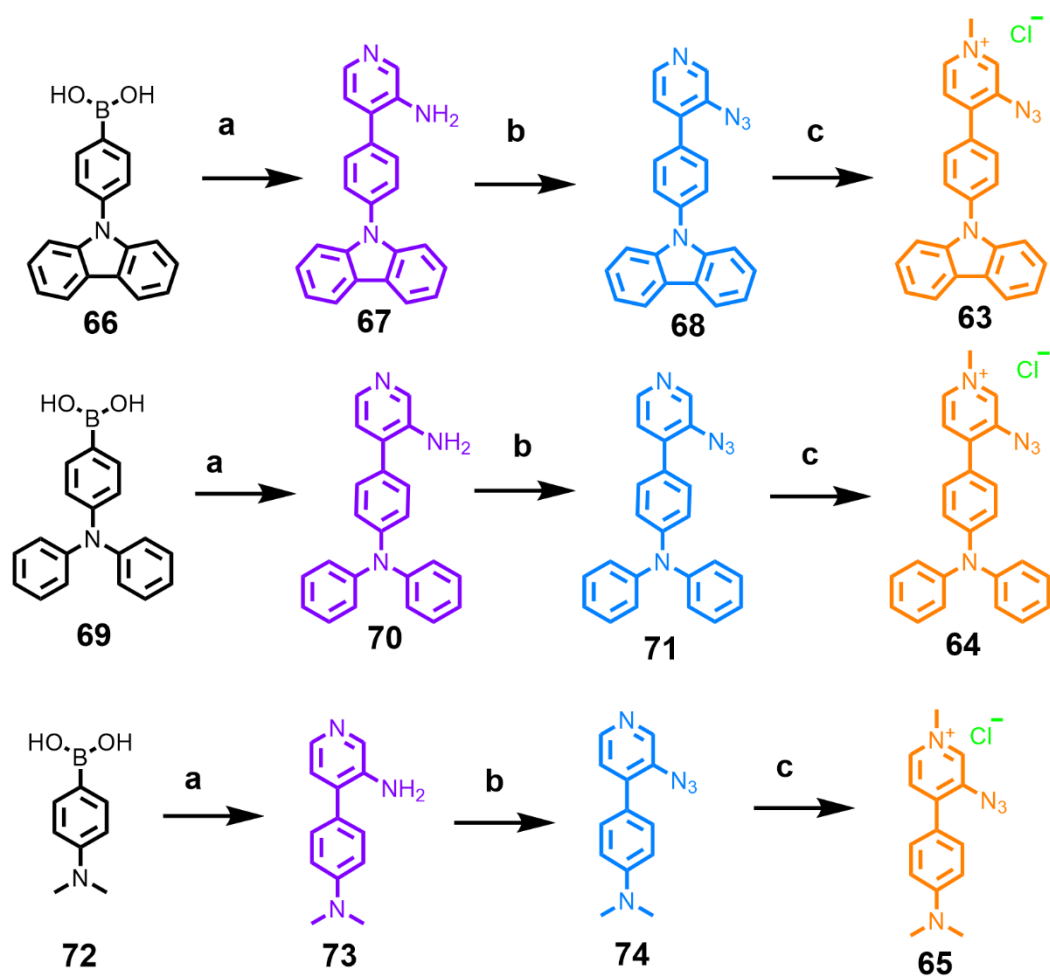


Figure 55. Schematic illustration of photoactivatable aryl azides 'turn on' emission within CB7 cavity (left) and chemical structures of the designed aryl azides (right).

Synthesis: The syntheses of the targeted aryl azides compound **63**, compound **64**, and compound **65** follow straightforward procedures (Scheme 6): Firstly, Initially, pyridine amines were synthesized by reacting boronic acid derivatives with 4-bromopyridin-3-amine via a Suzuki coupling. Subsequently, the formation of azides was adapted from our previously reported methods^[122]. In the last step, methyl iodide was utilized to methylate the azides. Following ion exchange, the desired aryl azides were obtained.



Scheme 6. a) 4-bromopyridin-3-amine (1.2 equiv), Pd(PPh₃)₄ (0.05 equiv), K₃PO₄ (1.5 equiv), 1,4-dioxane, H₂O, 105 °C, 16 h (**67**: 95 %, **70**: 91%, **73**: 98%); c) p-TsOH·H₂O (1.5 equiv), TBN (1.5 equiv), NaN₃ (3.0 equiv), ACN, H₂O, 25 °C, 6 h (**68**: 91 %, **71**: 92%, **74**: 94%); d) MeI (1.5 equiv), NH₄PF₆ (5.0 equiv), [Bu₄N]Cl (5.0 equiv), ACN, H₂O, 40°C, 16 h (**63**: 84 %, **64**: 89%, **65**: 92%).

Results and discussion.

The photolysis of the synthesized aryl azides was initially investigated in water using 405 nm LEDs at room temperature. As illustrated in the NMR spectra (Figure 56), new peaks emerged after the photolysis of compound **63**, compound **64**, and compound **65** in water, indicating photoconversions originating from the aryl azides. In the photolysis of compound **63** and compound **64**, two main peaks at 4.38 ppm corresponding to the methyl moiety were observed for both compounds after the photoreaction, suggesting that the photolysis of compound **63** and compound **64** in water predominantly forms one product.

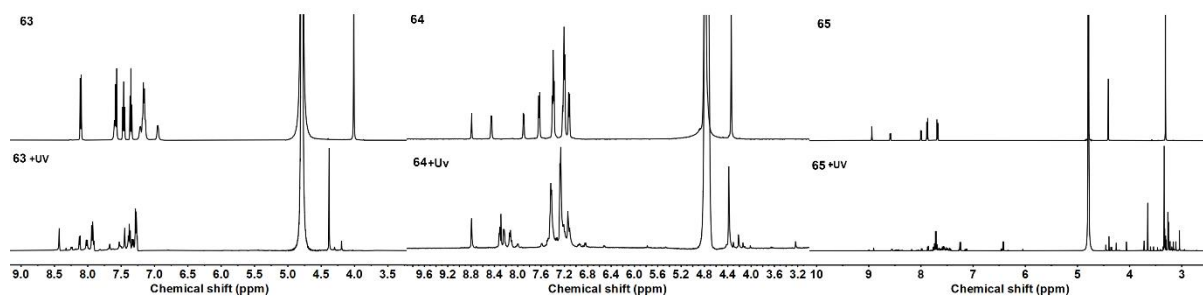


Figure 56. ^1H NMR spectra of photolysis of aryl azide **63**, **64**, and **65** (0.5 mM) in D_2O (4.79 ppm) at 25 °C, 500 MHz.

Liquid chromatography-mass spectrometry (LC-MS) analysis of the reaction mixtures of compound **63** and compound **64** (Figure 57) revealed product masses of 348.23 g/mol for the compound **63** reaction mixture and 350.27 g/mol for the compound **64** reaction mixture, respectively. Comparing the starting mass, 376.26 g/mol for compound **63** and 378.28 g/mol for compound **64**, it indicated that the photoreaction of compound **63** and compound **64** involves a loss of nitrogen followed by a C-H amination process, leading to the formation of carbolines products. However, this reaction pathway was unfavorable in our previously reported aryl azide studies.^[142]

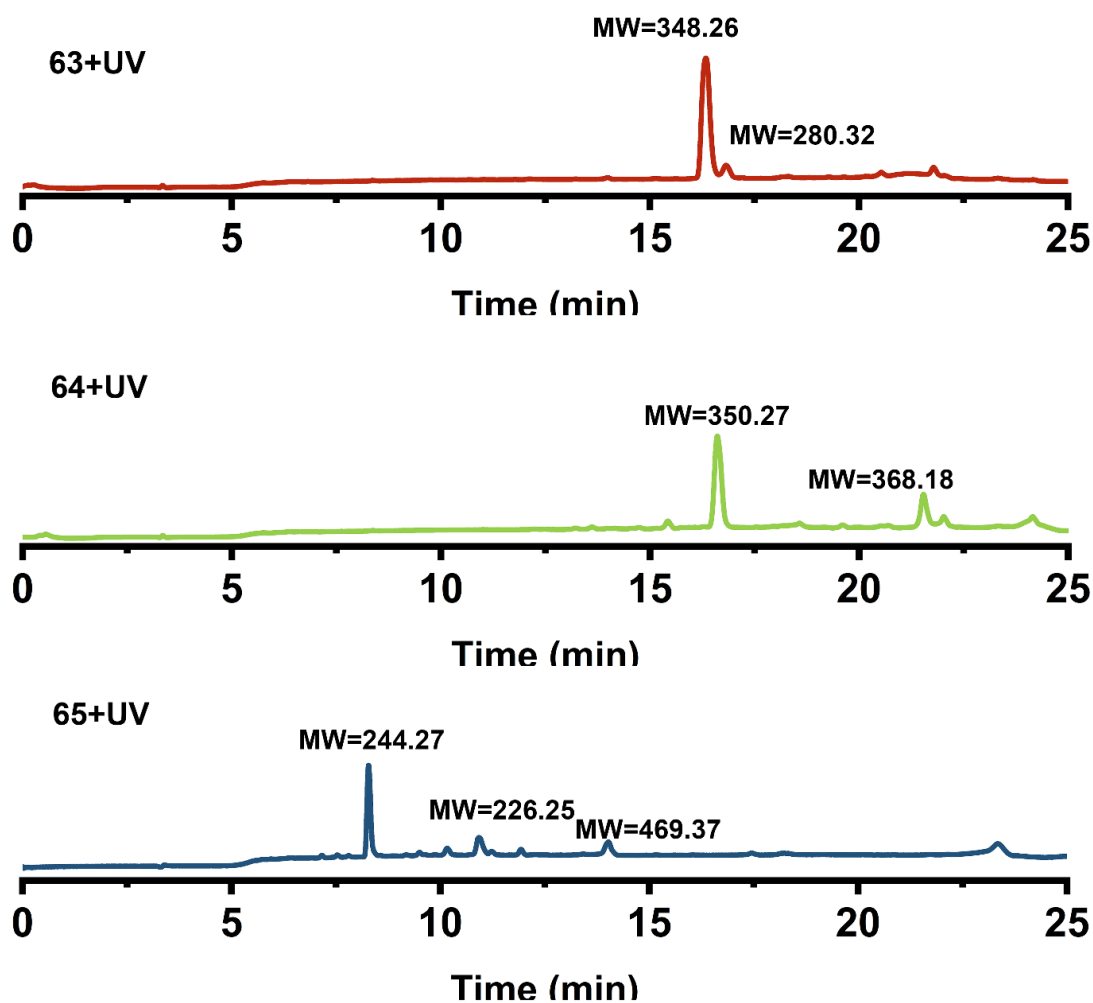


Figure 57. LC-MS of photolysis of aryl azides **63**, **64**, and **65** after photoreaction.

This could be attributed to the highly hydrophobic nature of aromatic ring conjugation in the aryl azides **63** and **64**, which facilitates their aggregation in water, forming non-covalent stacked systems^[157]. This aggregation suppresses molecular motion and impedes water from attacking, favoring intramolecular C-H amination. The hypothesis was further supported by the crystal structures of compound **63** and compound **64** (Figure 58).

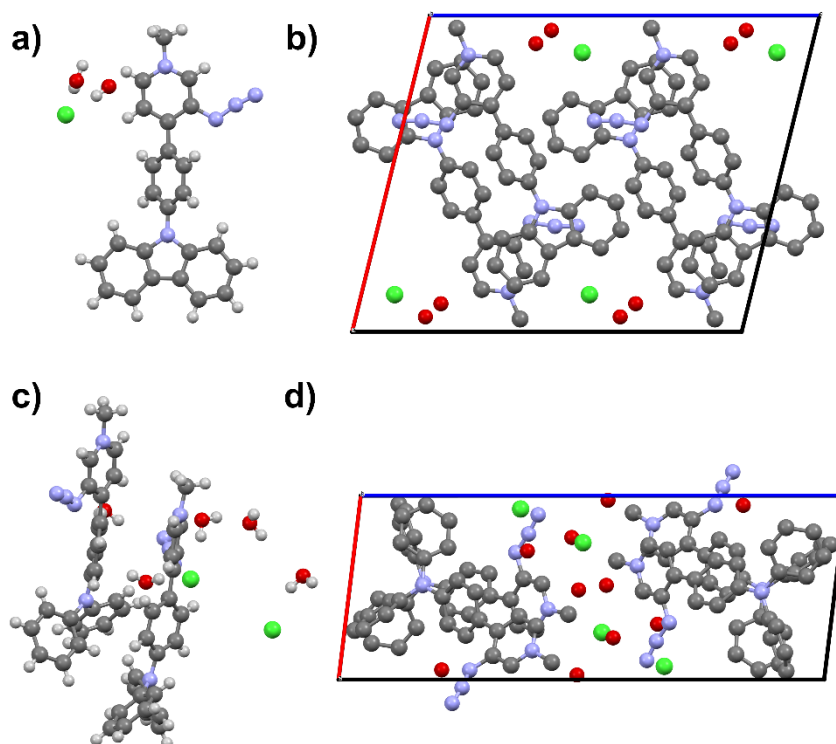


Figure 58. Crystal structure of a) **63**·2H₂O; b) **63**·2H₂O in packing model; c) **64**·2.5H₂O; and d) 2·**64**·2.5H₂O in packing model.

In contrast, aryl azide **65**, with a smaller aromatic conjugate, was observed to form various products upon irradiation, as indicated by multiple peaks corresponding to different molecular masses in the LC-MS analysis (Figure 56). This suggests that the photolysis of aryl azide **65** in water is uncontrollable, resulting in a mixture of photoproducts. (Figure 57).

The photoreaction processes were further tracked using UV-Vis and emission spectra (Figure 59). In the case of photolysis compound **63**, a decrease in absorbance was observed, reaching isosbestic points around 420s, indicating the completion of the reaction (Figure 59a). The emission spectra of compound **63** during photolysis exhibited an initial increase in emission followed by a decrease, eventually stabilizing at a weak emission state (Figure 59b). Similar decreases in absorbance were observed during the photolysis of compounds **64** and **65** (Figures 59c and 59e), reaching a state of completed reaction equilibrium at 240s for compound **64** and 180s for compound **65**, respectively. While no significant change in emission was detected for compound **64**, an increase in emission was observed for compound **65** (Figures 59d and 59f).

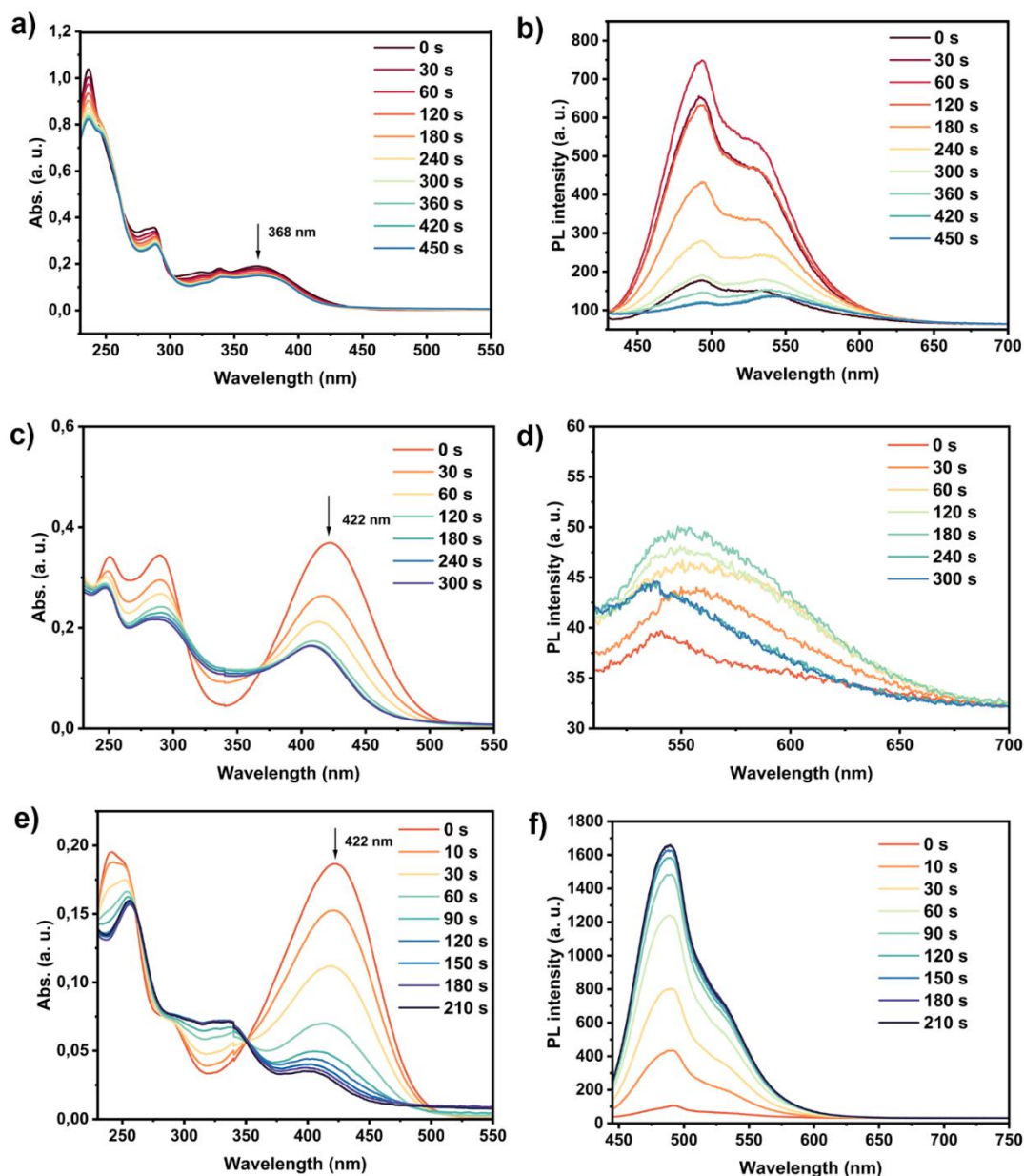


Figure 59. UV (left) and emission (right) spectra of photolysis of aryl azides **63**, **64**, and **65** (0.5 mM) after different reaction times in Milli Q water at 25 °C. The reaction mixture was diluted with Milli Q water to 2×10^{-4} M for UV and emission measurements ($\lambda_{\text{ex}} = 369$ nm for compound **63**, 422 nm for compound **64** and compound **65**, Ex bandwidth = 5 nm, Em bandwidth = 5 nm).

As demonstrated in our previous studies, we explored how the photolysis of aryl azides could be selectively guided to form carboline derivatives by leveraging the confinement and shielding provided by the CB7 cavity^[142]. Significant proton shifts were observed upon the addition of CB7 to the solution of compound **63**. Particularly, signals d and e exhibited an upfield shift, suggesting the deep encapsulation of azido moieties within CB7 cavities (Figure 60a). The formation of the 1:1 complex of compound **63** with CB7 was further confirmed by MALDI-TOF-MS (Figure 60b), wherein a peak of m/z 1510.21 corresponding to $[\mathbf{63}+\text{CB7}-\text{Cl}]^+$ ion was obtained. The deep encapsulation behavior of aryl azides within the CB7 cavity was also observed for compound **64** and compound **65** (Figure 60c-f), with peaks of m/z 1512.56 corresponding to $[\mathbf{64}+\text{CB7}-\text{Cl}]^+$ ions and m/z 1388.43 corresponding to $[\mathbf{65}+\text{CB7}-\text{Cl}]^+$ ions.

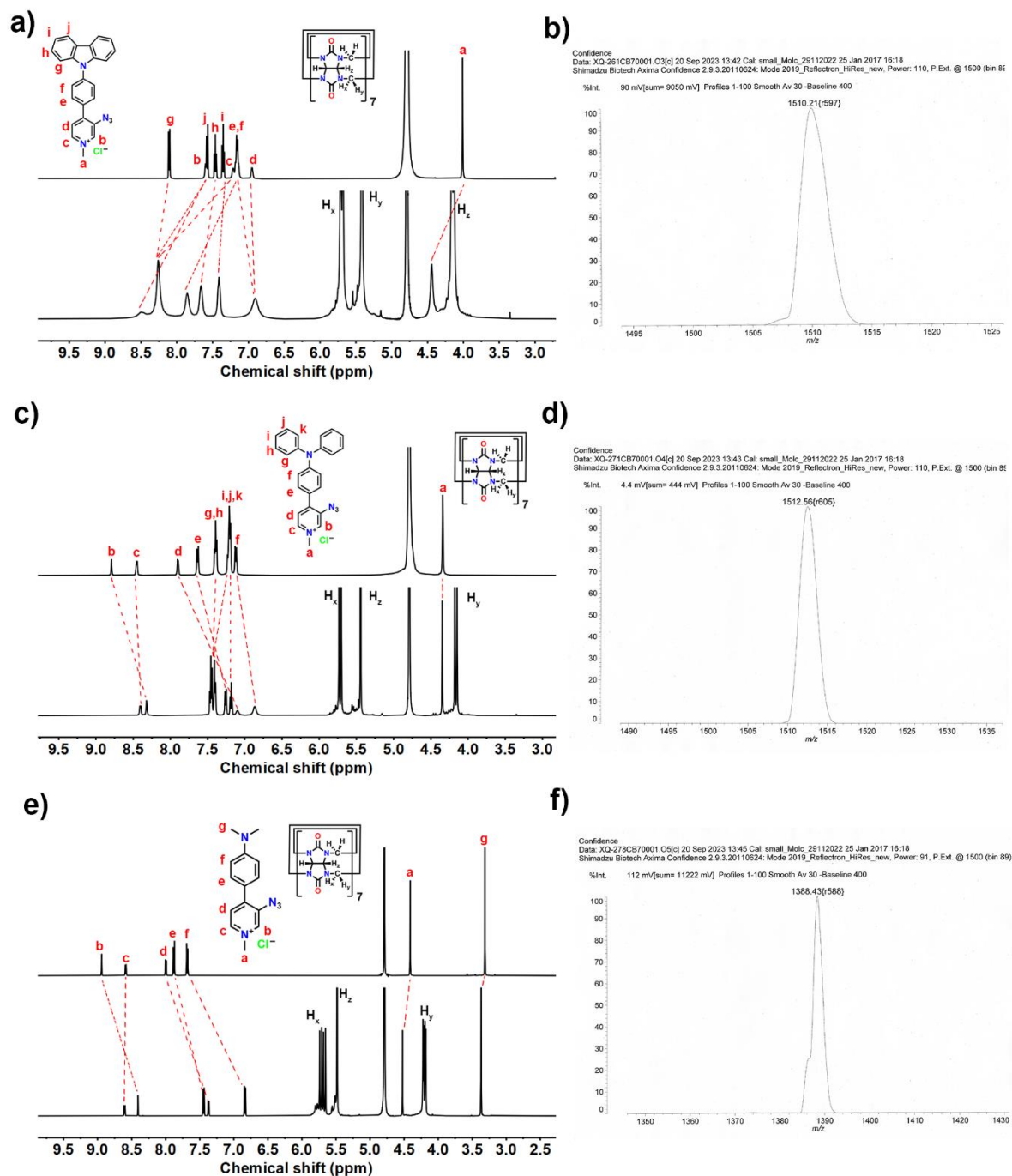


Figure 60. ^1H NMR spectra of aryl azide **63** (top) and **63**+CB7 (down) in 1:1 molar ratio (0.5 mM); c) **64** (top) and **64**+CB7 (down) in 1:1 molar ratio (0.5 mM); e) **65** (top) and **65**+CB7 (down) in 1:1 molar ratio (0.5 mM) in D_2O (4.79 ppm) at 25°C , 500 MHz; b) MALDI-MS spectra of aryl azide **63**+CB7 in 1:1 molar ratio; d) MALDI-MS spectra of aryl azide **64**+CB7 in 1:1 molar ratio; f) MALDI-MS spectra of aryl azide **65**+CB7 in 1:1 molar ratio.

The binding constants of the aryl azides and CB7 were determined through UV-vis titration (Figure 61). The addition of CB7 to aryl azides resulted in a decrease in absorption intensity at 368 nm for compound **63** (Figure 61a), 422 nm for compound **64** (Figure 61b), and compound **65** (Figure 61c), respectively. Non-linear fitting allowed us to calculate the binding constants of aryl azides with CB7, which were $(3.79 \pm 0.18) \times 10^5 \text{ M}^{-1}$ for compound **63** (Figure 61d), $(1.76 \pm 0.05) \times 10^5 \text{ M}^{-1}$ for compound **64** (Figure 61e), and $(1.40 \pm 0.03) \times 10^6$

M^{-1} for compound **65** (Figure 61f), respectively. These values were comparable to the previously studied aryl azide^[142].

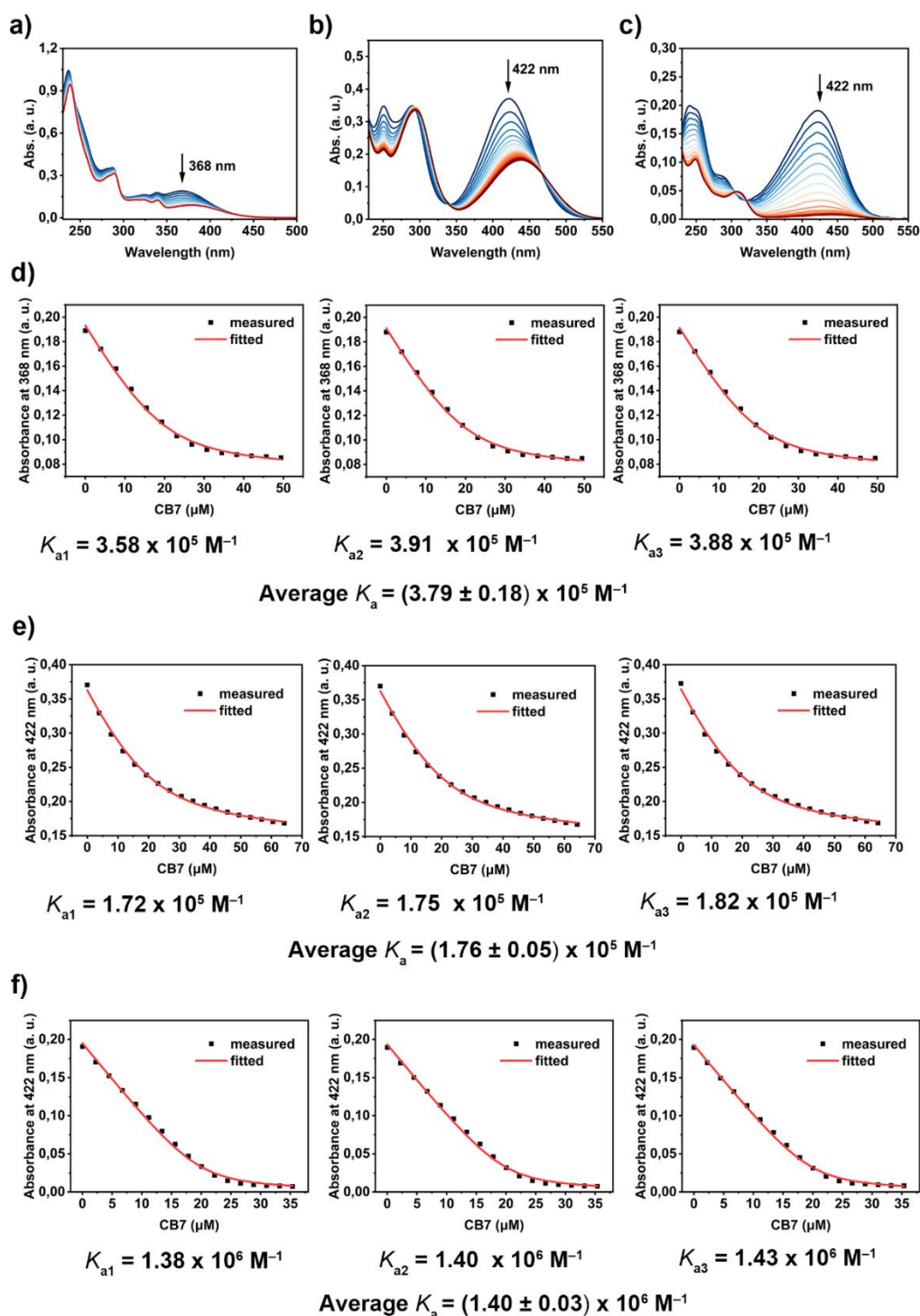


Figure 61. a) UV-vis titration spectra of **63** ($[63] = 20 \mu\text{M}$) upon addition of CB7 ($[CB7] = 0-49 \mu\text{M}$) in Milli Q water at 25 °C; b) UV-vis titration spectra of **64** ($[64] = 20 \mu\text{M}$) upon addition of CB7 ($[CB7] = 0-64 \mu\text{M}$) in Milli Q water at 25 °C; c) UV-vis titration spectra of **65** ($[65] = 20 \mu\text{M}$) upon addition of CB7 ($[CB7] = 0-38 \mu\text{M}$) in Milli Q water at 25 °C; d) UV absorbance changes of **63** at 368 nm upon increasing concentration of CB7 in Milli Q water; e) UV absorbance changes of **64** at 422 nm upon increasing concentration of CB7 in Milli Q water; f) UV absorbance changes of **65** at 422 nm upon increasing concentration of CB7 in Milli Q water. The binding constant value was determined by a non-linear curve fitting. The black squares depict the acquired data. The fit according to a 1:1 binding model is shown as a red line. The error was calculated from 3 replica experiments as the standard deviation.

Additionally, the photoreaction of aryl azides within the CB7 cavities was conducted under the same conditions as for aryl azides in water. Figure 62 illustrates the formation of carboline derivatives via a finely tuned intramolecular C-H amination process inside the CB7 cavities.

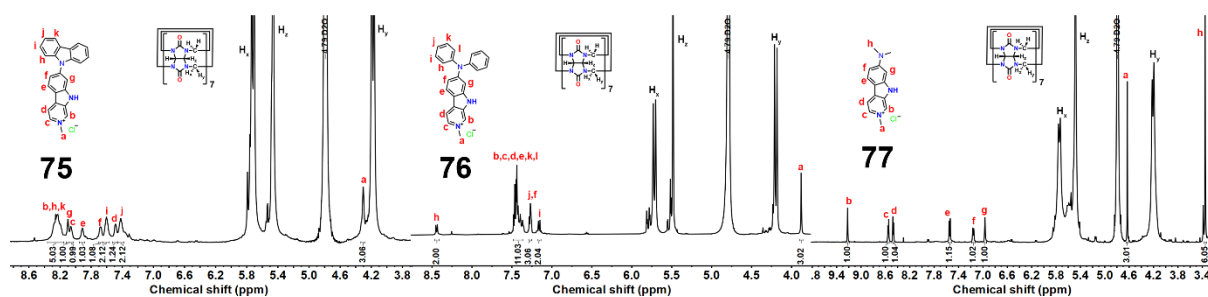


Figure 62. ^1H NMR spectra of photolysis product carbolines **75**•CB7, **76**•CB7, and **77**•CB7 (0.5 mM) in D_2O at 25 °C, 500 MHz.

The formation of carboline derivatives was further validated by LC-MS, indicating molecular masses of 348.23 g/mol for compound **75** (Figure 63 top), 350.27 g/mol for compound **76** (Figure 63 middle), and 226.23 g/mol for compound **77** (Figure 63 bottom), respectively.

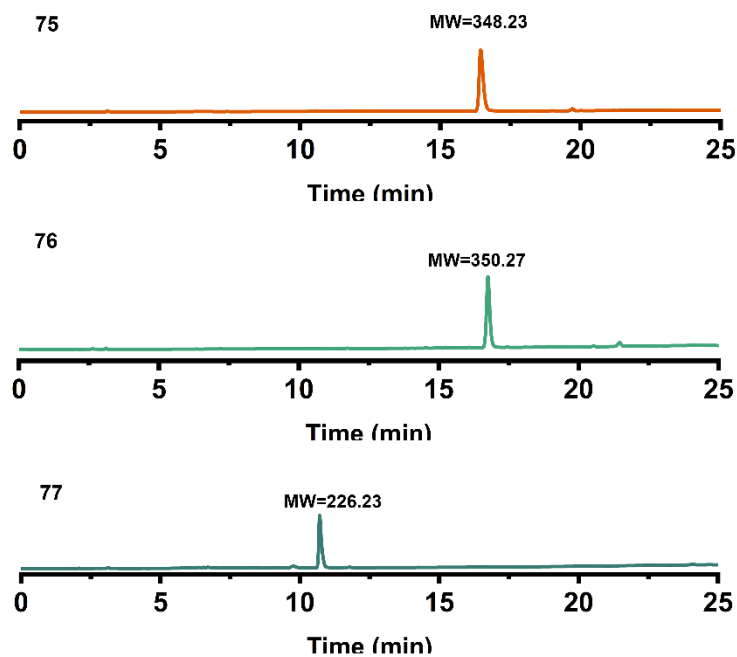


Figure 63. LC-MS of photolysis of aryl azides **75**, **76**, and **77**.

The reaction progress was monitored using UV-vis and emission spectra, indicating the formation of carbolines within 240 seconds for compound **75** (Figure 64a and 64b), 100 seconds for compound **76** (Figure 64c and 64d), and 180 seconds for compound **77** (Figure 64e and 64f), respectively.

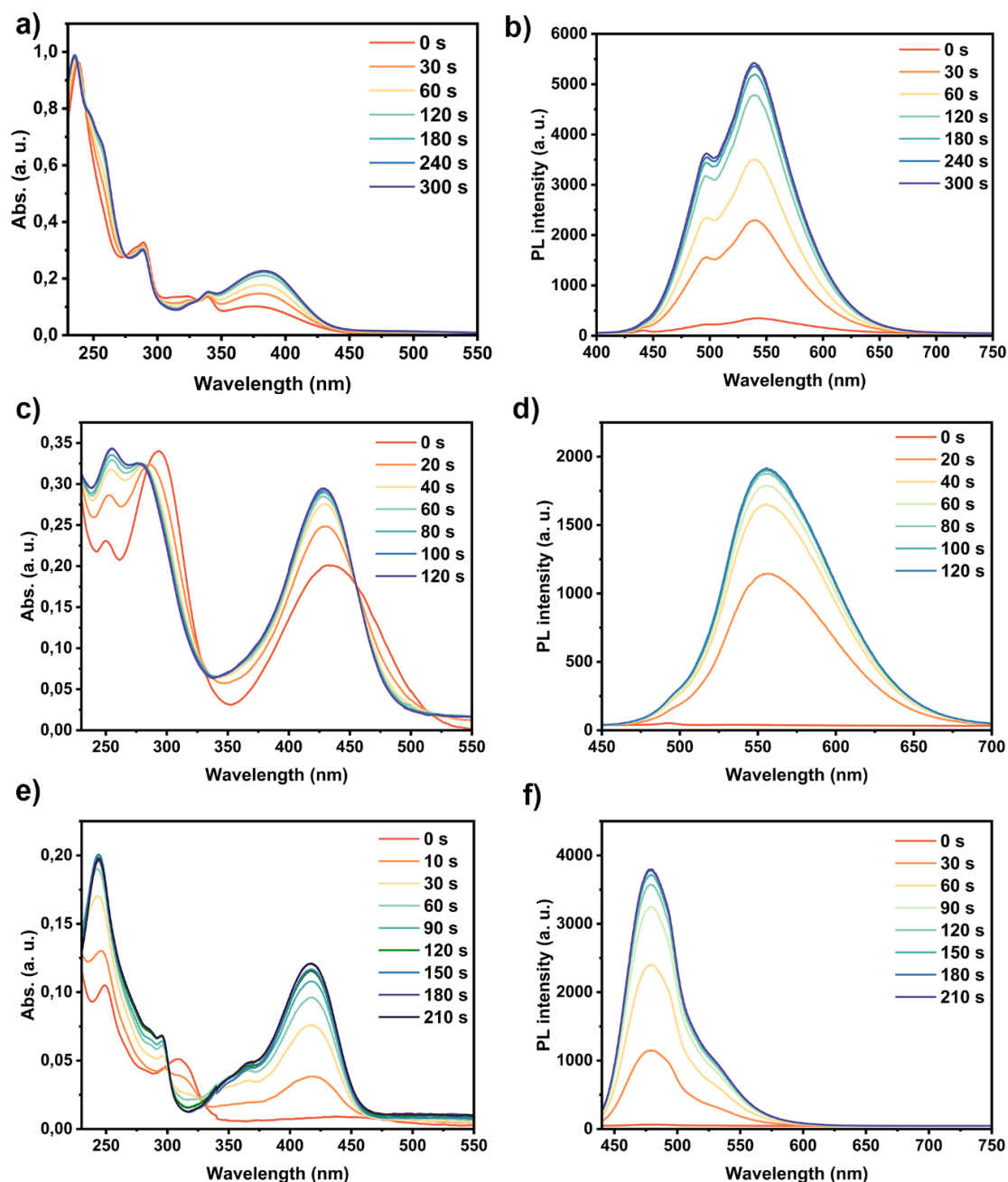


Figure 64. UV (left) and emission (right) spectra of photolysis of aryl azides **63•CB7**, **64•CB7**, and **65•CB7** (0.5 mM) after different reaction times in Milli Q water at 25 °C. The reaction mixture was diluted with Milli Q water to 2×10^{-4} M for UV and emission measurements ($\lambda_{\text{ex}} = 383$ nm for **63•CB7**, 433 nm for **64•CB7**, and 417 nm for **65•CB7**, Ex bandwidth = 5 nm, Em bandwidth = 5 nm for **63•CB7** and **64•CB7**, Ex bandwidth = 2.5 nm, Em bandwidth = 2.5 nm for **65•CB7**).

The emission spectra of the photoreaction process showed a significant increase in intensity. In the case of **75•CB7**, the emission intensity at $\lambda_{539 \text{ nm}}$ experienced a 16-fold enhancement compared to the weak emission of **63•CB7** (Figure 65a). For **76•CB7**, a 49-fold enhancement at $\lambda_{556 \text{ nm}}$ was observed (Figure 65b). Likewise, a 60-fold enhancement at $\lambda_{480 \text{ nm}}$ was observed for **77•CB7** compared to the faint fluorescent **65•CB7** (Figure 65c).

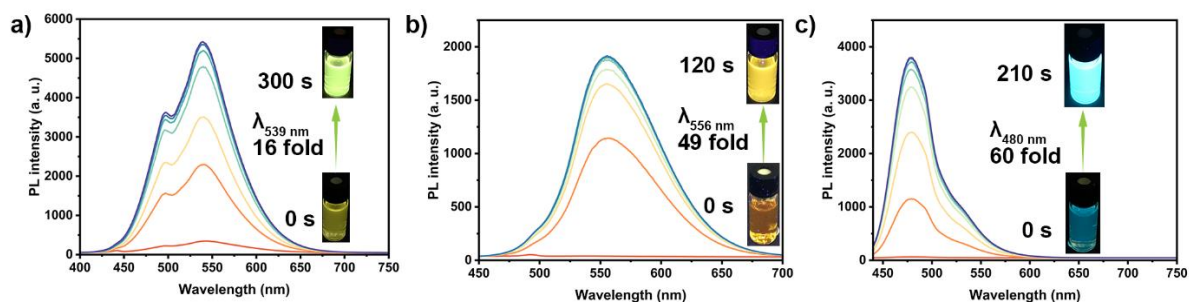
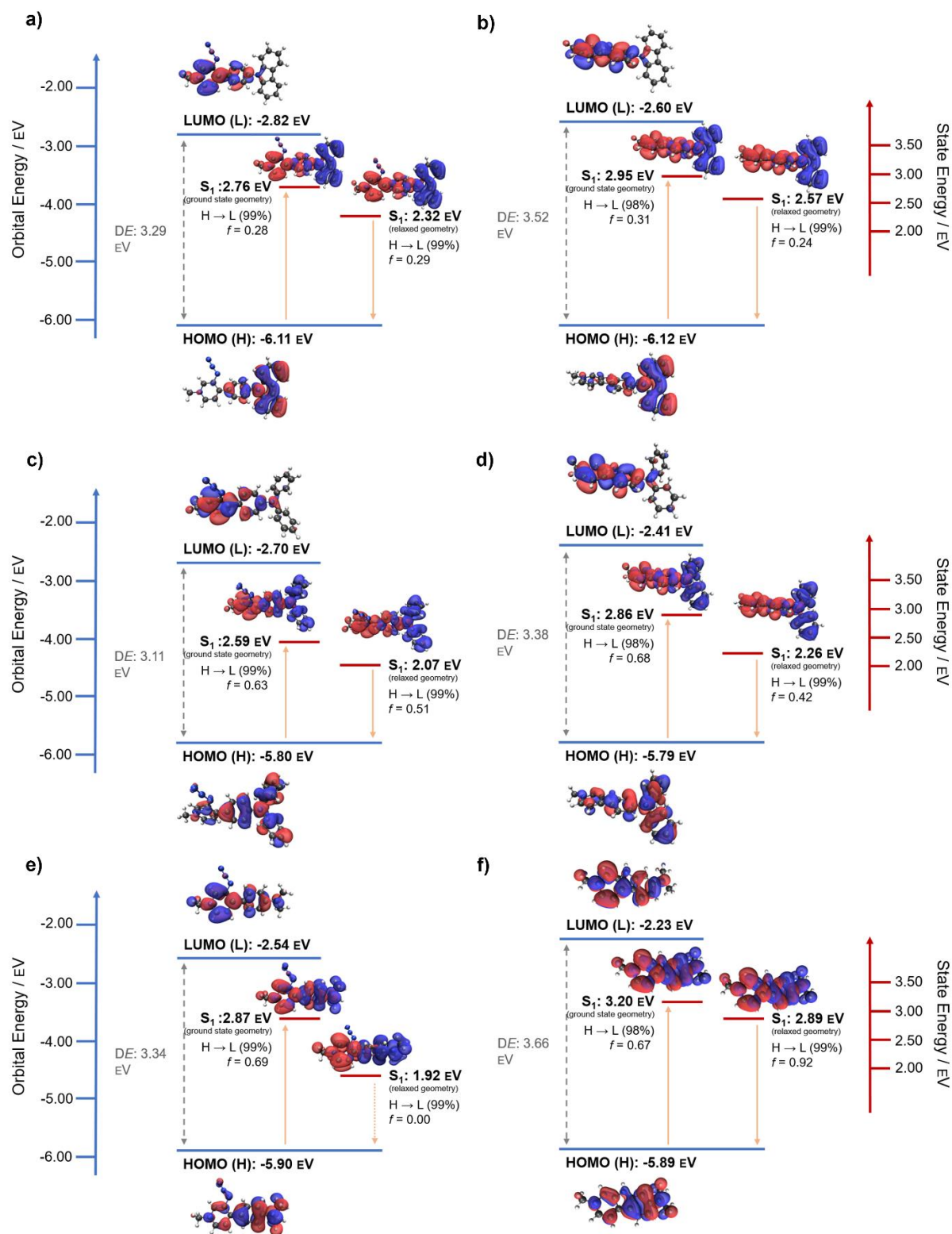


Figure 65. a) Photoluminescence (PL) spectra of photolysis of **63**•CB7 (0.5 mM) after different reaction times in Milli Q water at 25 °C, the reaction mixture was diluted with Milli Q water to 2×10^{-4} M for emission measurements, the inset shows photographic images of the reaction mixture in a vial before and after 300 s photoreaction; b). PL spectra of photolysis of **64**•CB7 (0.5 mM) after different reaction times in Milli Q water at 25 °C, the reaction mixture was diluted with Milli Q water to 2×10^{-4} M for emission measurements, the inset shows photographic images of the reaction mixture in a vial before and after 120 s photoreaction; c) PL spectra of photolysis of **65**•CB7 (0.5 mM) after different reaction times in Milli Q water at 25 °C, the reaction mixture was diluted with Milli Q water to 2×10^{-4} M for emission measurements, the inset shows photographic images of the reaction mixture in a vial before and after 210 s photoreaction.

DFT calculations were conducted to gain deeper insights into the fluorescence enhancement observed upon the formation of carboline derivatives, particularly the cyclization from compound **65** into compound **77** (Figure 66). We compared the highest occupied molecular orbital (HOMO) and lowest unoccupied molecular orbital (LUMO) energies of azides and carbolines. Our calculations reveal higher LUMO energies for carbolines compared to their corresponding azides, indicating a decrease in acceptor strength. For compounds **65** and **77** (Figure 66), we found that at the ground state geometry, the hole and electron wavefunctions are distributed throughout the entire molecule. However, upon relaxation to the excited state geometry, there is almost complete separation of the hole and electron wavefunctions, indicating photoinduced electron transfer (PET). PET is likely responsible for transitioning S_1 into a non-emissive state in compound **65**, as evidenced by the near-zero oscillator strength and increased stabilization. Generally, the energies of excited singlet state S_1 for azides were lower than those of the corresponding carbolines, suggesting a higher charge transfer character for these states.



Furthermore, absorption and emission spectra were simulated (Figure 67), showing reasonable agreement with experimental findings, although the charge transfer (CT) states were slightly over-stabilized – a typical challenge in many hybrid functionals with a low Hartree-Fock exchange fraction (25% in PBE0). The lack of emissive behavior observed in compounds **63** and **64** in water could not be adequately explained via TD-DFT. However, it is widely recognized that TD-DFT has limitations in accurately describing (long-range) CT states.^[158]

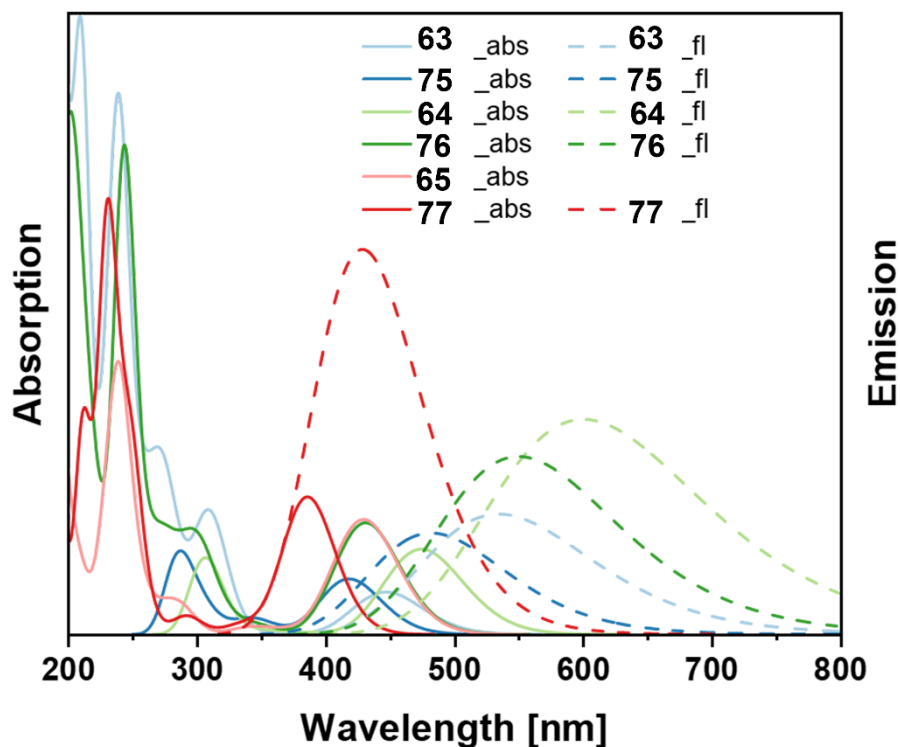


Figure 67. Simulated absorption and emission spectra of azides and carbolines, calculated at the TD-DFT PBE0 / 6-31+G** level of theory in water (PCM). An emission spectrum of compound **65** was not included due to the insignificant oscillator strength of the optimized S_1 state.

Based on these discoveries, we investigated whether this fluorescence photoactivation process could be employed for live cell imaging. We conducted the same emission experiments in cell media to assess the feasibility of utilizing the photoactivable aryl azides-CB7 complexes in a biological environment (Figure 68). The encapsulated aryl azides exhibited enhanced fluorescence intensity compared to their free forms (Figure 68a-c), mirroring the outcomes observed in Milli Q water. After the photoreaction, the emission intensities significantly increased for both the unbound carbolines and those complexed with CB7 (Figure 68d-f). Notably, the photoluminescence (PL) intensities of compounds **75** and **76** were higher than those observed from compounds **75** and **76** within the CB7 cavity (Figure 68a-c). This discrepancy could be attributed to the larger aromatic structure fitting into protein pockets provided by the serum proteins in the cell media, thus mitigating the water-quenching effects. Conversely, when the aromatic system is smaller, as in **77**, the CB7 cavity can fully envelop the molecule, effectively shielding it from water-based attacks on the photoexcited state. This leads to a stronger emission compared to the quenching effect of nonspecific binding within protein pockets.

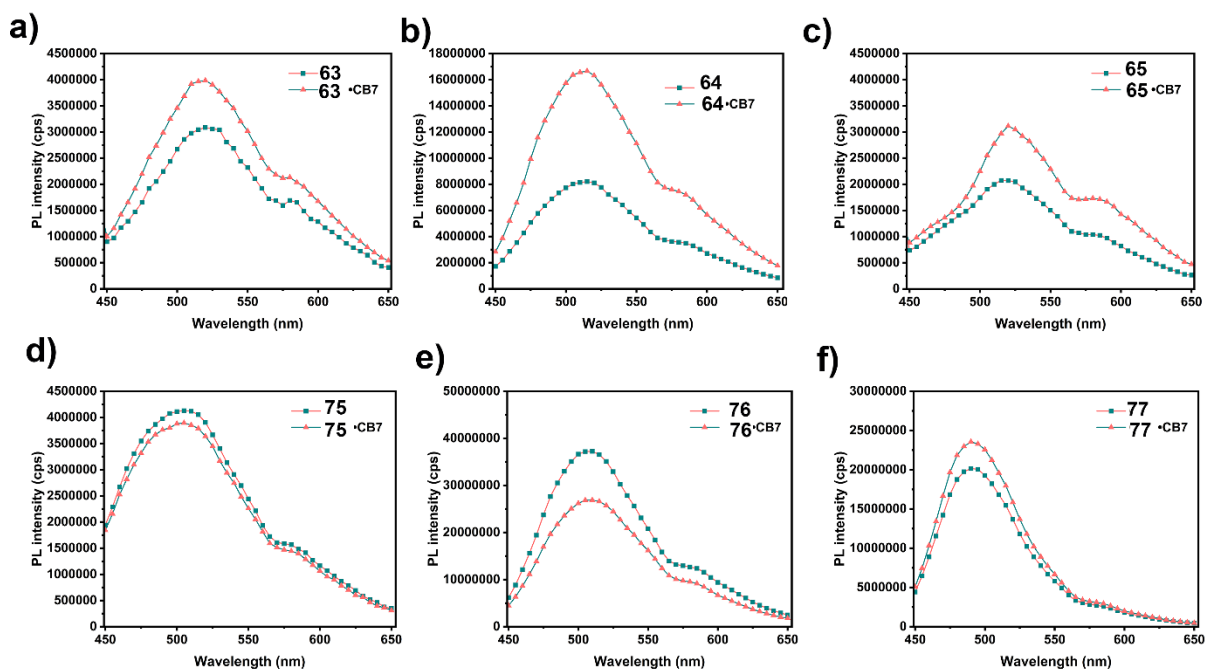


Figure 68. Emission spectra of aryl azide a) **63**, **63**•CB7; b) **64**, **64**•CB7; c) **65**, **65**•CB7; d) **75**, **75**•CB7; e) **76**, **76**•CB7; f) **77**, **77**•CB7 (5×10^{-5} M) in cell media at 25 °C ($\lambda_{ex} = 405$ nm).

To validate this hypothesis, we examined the photophysical properties of compounds **75**, **76**, and **77**, along with their complexes with CB7, in the presence of bovine serum albumin (BSA), the predominant protein in HeLa cell medium^[159], as well as various concentrations of fetal bovine serum (FBS). Before applying the photoactivatable system in living cells, we assessed the cytotoxicity of the aryl azides, carboline products, and their complexes with CB7 on HeLa cells at different concentrations (50 μ M, 5 μ M, 0.5 μ M) (Figure 69). The cytotoxicity assay results indicate that both aryl azides and carbolines demonstrate similarly low cytotoxicity ($Lc_{50} > 50$ μ M).

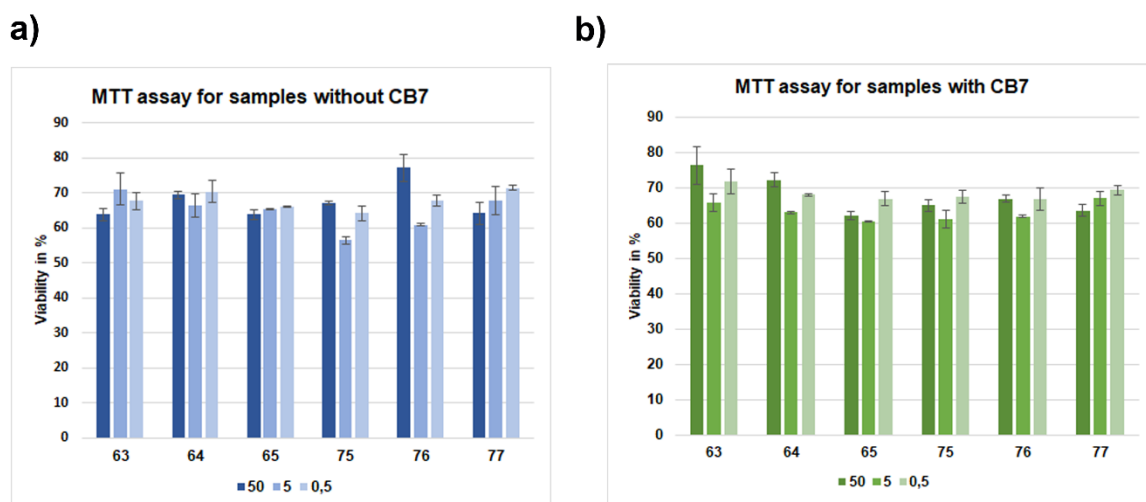


Figure 69. MTT Cytotoxicity assay tests the effects of azides and carboline samples with and without CB7 in different concentrations (50 μ M, 5 μ M, 0.5 μ M) on Hela cells.

Next, we proposed two strategies for applying the photoactivation process in bioimaging. The first approach involves the cellular uptake of the aryl azides-CB7 complex into living cells, followed by photoactivation, depicted in Figure 70a. As illustrated in Figure 70b, the fluorescence intensity increased post-irradiation, indicating the formation of carboline products within the cell. The measured photoluminescence (PL) intensity, plotted over time as depicted in Figure 70c, demonstrates enhanced emission following photoconversion. Additionally, we conducted the photoreaction without CB7, resulting in faster reaction times and reduced PL for all azides. This suggests favorable properties of CB7 for cellular uptake and directing the photoreaction (Figure 71).

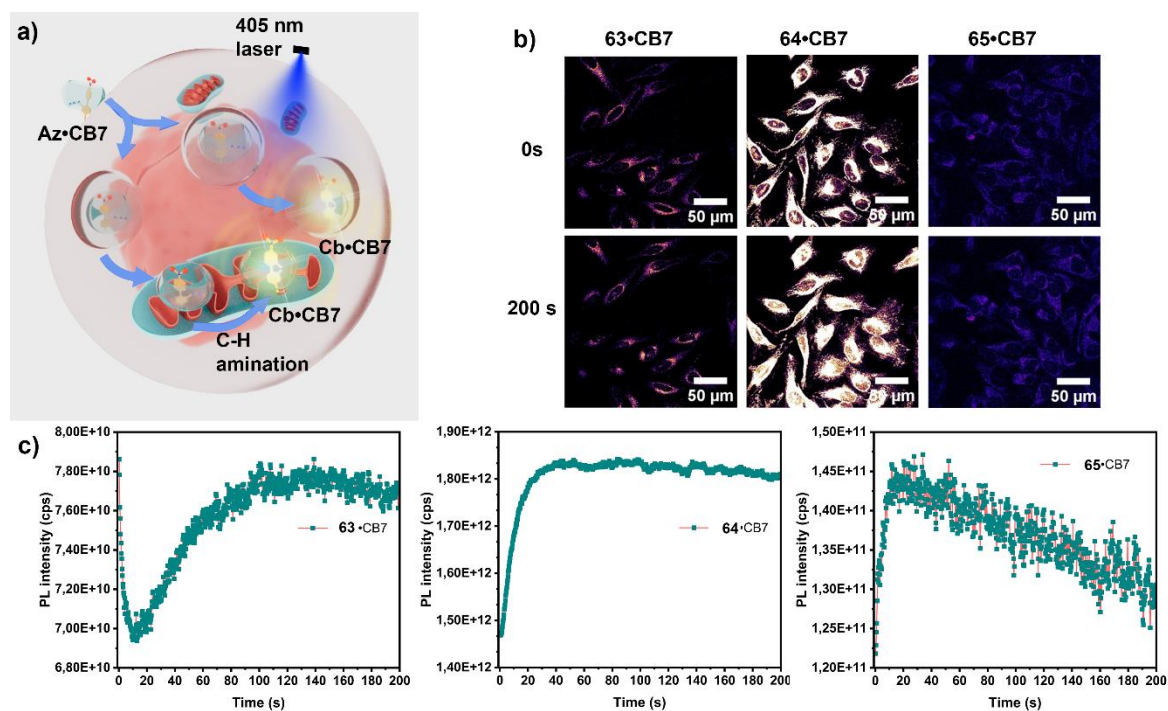


Figure 70. a) Schematic illustration of photoactivation of aryl azides in living cells; b) Confocal imaging of the photoactivation of **61•CB7**, **62•CB7**, and **63•CB7** (5 μ M) in HeLa cells using irradiation with a 405 nm laser for 3 minutes while collecting images; c) Increase of the fluorescence intensity in HeLa cells at different timepoints of photoactivation.

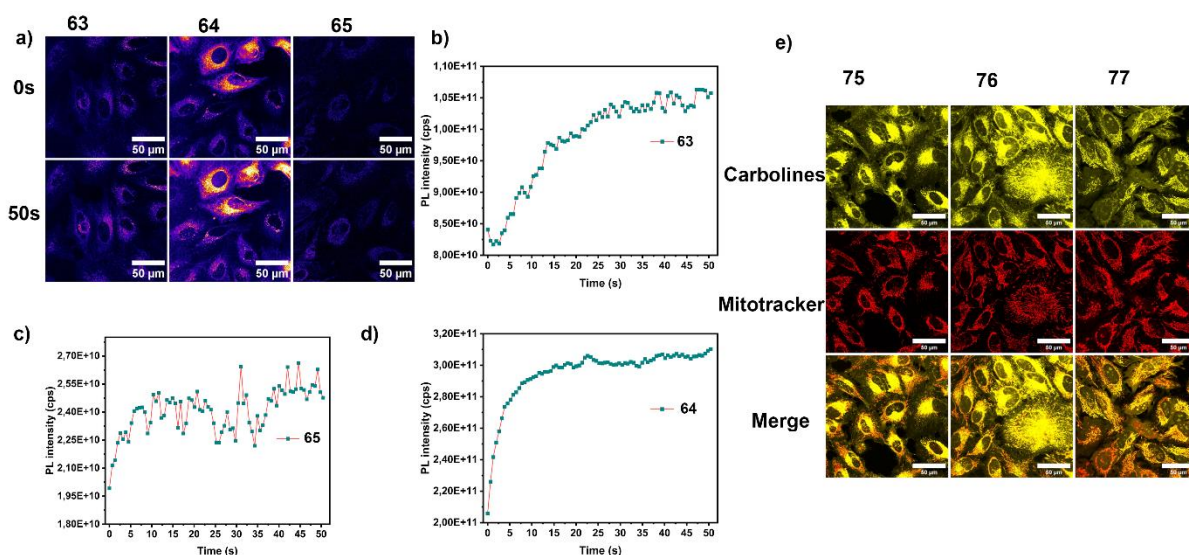


Figure 71. a) Confocal imaging of the photoactivation of compounds **63**, **64**, and **65** (5 μ M) in HeLa cells using the irradiation of 405 nm laser at different time points; b-d) Increase of the fluorescence intensity in HeLa cells at different time points of photoactivation; e) Confocal imaging of carbolines in HeLa cells.

The second approach entails preactivating the CB7-encapsulated azides to carbolines in cell media before cellular uptake (Figure 6a). As illustrated in Figure 6b, the carboline-CB7 complexes **75**•CB7 and **76**•CB7 accumulated within endosomal vesicles, whereas **77**•CB7 was predominantly localized within the mitochondria of the cells.

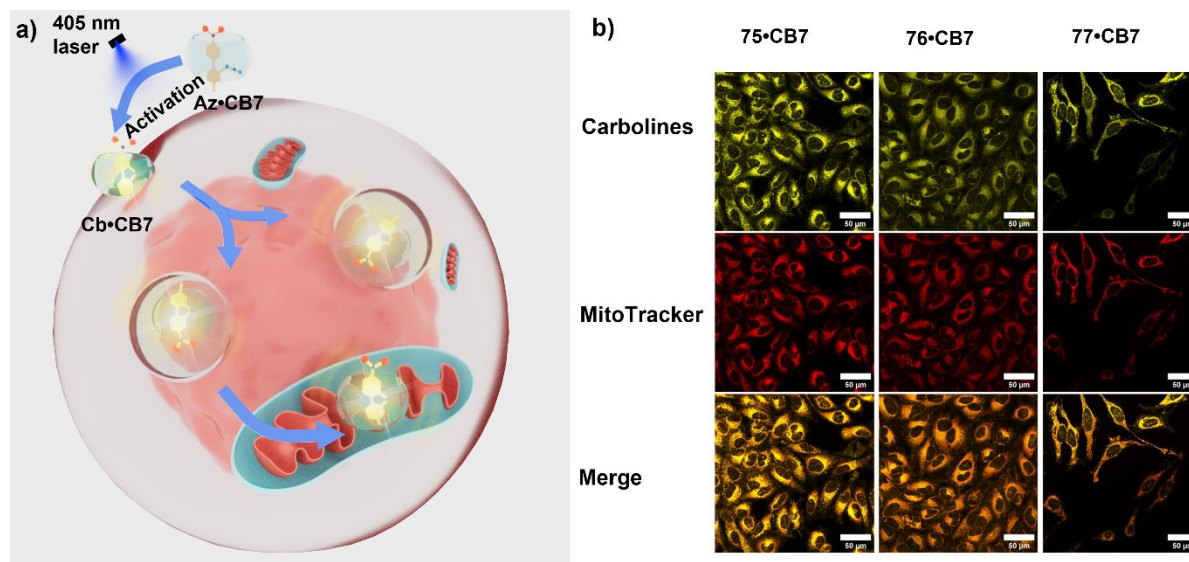


Figure 72. Schematic illustration of the preactivation of aryl azides-CB7 complex (5 μ M) before passing through the cell membrane; b) Confocal imaging of carbolines-CB7 complex in HeLa cells.

4. Summary and Outlook

This thesis employed cucurbit[n]urils as molecular flasks to host, direct, and expedite photoreactions. The rigid and hydrophobic walls of CB n not only physically confine the reagents but also shield them from solvent attack, leading to distinct reaction pathways and yielding diverse products compared to reactions in bulk solvent. Subsequent investigations of these systems showcased their potential applications spanning from materials science to biology, underscoring the versatility of supramolecular hosts.

4.1. Reversing the Intramolecular [2+2] Photocycloaddition Stereoselectivity

A novel approach was developed for selectively modulating the photoreaction pathway using CB8 as a molecular flask. In bulk water, the photoreaction of molecule **31** was facilitated by photoisomerization and [2+2] cycloaddition, yielding an *anti*-head-to-tail (1,3) photoproduct **40**. However, when CB8 acted as a template, the photoreaction selectively resulted in a *syn*-head-to-tail (1,3) cycloaddition product **32**. Remarkably, the binding constant between **32** and CB8 was estimated as high as $(2.04 \pm 0.29) \times 10^{12} \text{ M}^{-1}$. Intramolecular locking of molecule **41** prevented photoreaction upon irradiation; conversely, when the photoreaction occurred inside the CB8 cavity, a *syn*-head-to-head (1,2) product was obtained.

4.2. Modulating Aryl Azide Photolysis in Aqueous

A novel method to control the photolysis of an aryl azide in aqueous media using cucurbiturils (CB n) as a reaction chamber was proposed in this part. The method was showcased with 4-(2-azidophenyl)-1-methylpyridin-1-ium chloride (**33**) and CB7. However, based on the mechanistic considerations, we expect it can be extended to many other suitable combinations of CB n and aryl azides. Namely, the hydrophobic environment within the cucurbituril cavity effectively guards photoreaction intermediates from a solvent (water) attack. This, together with the cavity confinement, steers the photoreaction of **33** toward generating a carboline derivative **34** with excellent selectivity.

In contrast, when the photolysis is carried out in bulk water, the dominant pathway involves ring opening and rearrangement, forming an azepine derivative (**47**). The host-directed photolysis may thus provide an alternative to traditional methods of carboline synthesis, which typically rely on a metal catalyst. Furthermore, the observation of long-lived room temperature phosphorescence (RTP) from the carboline derivative, when complexed with CB7, marks another exciting function of the cucurbituril cavity as a protective environment for luminescent guest molecules. This result could be valuable for the production of room-temperature phosphorescent materials.

4.3. Modulating and Accelerating Photolysis of [2.2]Paracyclophane Aryl Azide

A novel photoactivatable PCP aryl azide 35 that can follow three distinct reaction pathways, resulting in the formation of three unique molecules (53, 54, and 55) in roughly equal proportions, was presented in this section. The reaction mechanism was proposed using DFT analysis. When the photoreaction of compound 35 was carried out inside a CB8 cavity, the pathway leading to the formation of molecule 53 was suppressed, and the relative production of molecule 54 was reduced. Additionally, the reaction within the supramolecular host was found to be almost four times faster than in water. Photophysical studies of the reaction process and products showed that the new PCP species have significantly improved quantum yields (QY) compared to the starting materials. Finally, we demonstrated the application of these new PCP fluorophores for bioimaging live cells and photoactivatable imaging.

4.4. Modulating the Photolysis of Aryl Azides for Bioimaging

A novel approach for creating photoactivatable fluorescent probes (63, 64, and 65) uses the supramolecular host CB7 to control the photoreaction pathway of aryl azides into carboline derivatives (75, 76, and 77). This transformation results in a significant enhancement of fluorescence intensity. DFT calculations were conducted to elucidate the fluorescence 'turn on' mechanism. Furthermore, we successfully demonstrated the application of this photoactivation process in live cell imaging, showing that CB7 has favorable properties for cellular uptake. Our results indicate that aryl azides and their carboline derivatives are effective cellular markers, with CB7 displaying a strong affinity for mitochondria. This research highlights the potential of controlling the photolysis of aryl azides within a supramolecular host for biochemical applications.

5. Experimental Section

5.1. General Remarks

The synthetic procedures with all reaction details as well as the analyses of the target materials can be accessed additionally via the CHEMOTION repository:

<https://www.chemotion-repository.net/home/publications>

The data can be found in the following data:

<https://dx.doi.org/10.14272/reaction/SA-FUHFF-UHFFFADPSC-DVJQLQKAHJ-UHFFFADPSC-NUHFF-NJMCZ-NUHFF-ZZZ>

<https://dx.doi.org/10.14272/reaction/SA-FUHFF-UHFFFADPSC-VIRCVYOPUF-UHFFFADPSC-NUHFF-LGEIA-NUHFF-ZZZ>

<https://dx.doi.org/10.14272/reaction/SA-FUHFF-UHFFFADPSC-ZJSPYAOLG-UHFFFADPSC-NUHFF-LGTAG-NUHFF-ZZZ>

<https://dx.doi.org/10.14272/reaction/SA-FUHFF-UHFFFADPSC-ODRIUFNOBK-UHFFFADPSC-NUHFF-NUHFF-NUHFF-ZZZ>

<https://dx.doi.org/10.14272/reaction/SA-FUHFF-UHFFFADPSC-VZJWUOJWLK-UHFFFADPSC-NUHFF-NUHFF-NUHFF-ZZZ>

<https://dx.doi.org/10.14272/reaction/SA-FUHFF-UHFFFADPSC-RFJCJXBPYR-UHFFFADPSC-NUHFF-MUHFF-NUHFF-ZZZ>

<https://dx.doi.org/10.14272/reaction/SA-FUHFF-UHFFFADPSC-ZZJJYVSBQB-UHFFFADPSC-NUHFF-NUHFF-NUHFF-ZZZ>

<https://dx.doi.org/10.14272/reaction/SA-FUHFF-UHFFFADPSC-MBTRVJGAF-UHFFFADPSC-NUHFF-NUHFF-NUHFF-ZZZ>

<https://dx.doi.org/10.14272/reaction/SA-FUHFF-UHFFFADPSC-MJWCMJSWDU-UHFFFADPSC-NUHFF-NUHFF-NUHFF-ZZZ>

<https://dx.doi.org/10.14272/reaction/SA-FUHFF-UHFFFADPSC-RELGREOJIM-UHFFFADPSC-NUHFF-NUHFF-NUHFF-ZZZ>

<https://dx.doi.org/10.14272/reaction/SA-FUHFF-UHFFFADPSC-YVHVOAZMKU-UHFFFADPSC-NUHFF-MUHFF-NUHFF-ZZZ>

<https://dx.doi.org/10.14272/reaction/SA-FUHFF-UHFFFADPSC-PJZJOOPXWQ-UHFFFADPSC-NUHFF-NUHFF-NUHFF-ZZZ>

<https://dx.doi.org/10.14272/reaction/SA-FUHFF-UHFFFADPSC-CMWOXPAPYB-UHFFFADPSC-NUHFF-NUHFF-NUHFF-ZZZ>

<https://dx.doi.org/10.14272/reaction/SA-FUHFF-UHFFFADPSC-KOHDERBFDY-UHFFFADPSC-NUHFF-NUHFF-NUHFF-ZZZ>

<https://dx.doi.org/10.14272/reaction/SA-FUHFF-UHFFFADPSC-IJEBCCZWNN-UHFFFADPSC-NUHFF-MUHFF-NUHFF-ZZZ>

<https://dx.doi.org/10.14272/reaction/SA-FUHFF-UHFFFADPSC-VNRJBELPCO-UHFFFADPSC-NUHFF-MUHFF-NUHFF-ZZZ>

<https://dx.doi.org/10.14272/reaction/SA-FUHFF-UHFFFADPSC-SZCWTGKVOH-UHFFFADPSC-NUHFF-MUHFF-NUHFF-ZZZ>

Materials and Methods

The starting materials, solvents, and reagents were purchased from ABCR, ACROS, ALFA AESAR, APOLLO SCIENTIFIC, CARBOLUTION, CHEMPUR, FLUKA, FLUOROCHEM, MERCK, RIEDEL-DE HAËN, SIGMA ALDRICH, STREM, TCI, or THERMO FISHER SCIENTIFIC and used without further purification unless stated otherwise.

Solvents of technical quality were purified by distillation or with the solvent purification system MB SPS5 (acetonitrile, dichloromethane, diethyl ether) from MBRAUN. Solvents of p.a. quality were purchased from ACROS, FISHER SCIENTIFIC, SIGMA ALDRICH, Roth, or RIEDEL-DE HAËN and were used without further purification.

Flat-bottom crimp neck vials from ChromaGlobe with aluminum crimp caps were used for certain reactions.

Solvents were evaporated under reduced pressure at 45 °C using a rotary evaporator. For solvent mixtures, each solvent was measured volumetrically.

Flash column chromatography was performed using MERCK silica 60 (0.040 × 0.063 mm, 230–400 mesh ASTM) and quartz sand (glowed and purified with hydrochloric acid).

Reaction Monitoring

All reactions were monitored by thin-layer chromatography (TLC) using silica-coated aluminum plates (MERCK, silica 60, F254). UV-active compounds were detected with a UV lamp excitation at 254 nm and 360 nm.

GC-MS (gas chromatography-mass spectrometry) measurements were performed on an AGILENT TECHNOLOGIES model 6890N (electron impact ionization), equipped with an AGILENT 19091S-433 column (5% phenyl methyl siloxane, 30 m, 0.25 µm) and a 5975B VL MSD detector with a turbopump. Helium was used as a carrier gas.

Nuclear Magnetic Resonance Spectroscopy (NMR)

NMR spectra were recorded on a Bruker Avance 400 NMR instrument at 400 MHz for ¹H NMR, 101 MHz for ¹³C NMR BRUKER, or a Bruker Avance 500 NMR instrument at 500 MHz for ¹H NMR and 126 MHz for ¹³C NMR. The NMR spectra were recorded at room temperature in deuterated solvents acquired from EURISOTOP, SIGMA ALDRICH, or DEUTERO.

Infrared Spectroscopy (IR)

The infrared spectra were recorded with a BRUKER Alpha P instrument. All samples were measured by attenuated total reflection (ATR). The positions of the absorption bands are given in wavenumbers $\tilde{\nu}$ in cm⁻¹ and were measured in the range from 3600 cm⁻¹ to 500 cm⁻¹.

The absorption bands were characterized according to their absorption strength, using the following abbreviations: vs (very strong, 0–9%), s (strong, 10–39%), m (medium, 40–69%), w (weak, 70–89%), and vw (very weak, 90–100%).

Mass Spectrometry (MS)

APCI (atmospheric pressure chemical ionization) and ESI (electrospray ionization) experiments were recorded on a Q-Exactive (Orbitrap) mass spectrometer (THERMO FISHER SCIENTIFIC, San Jose, CA, USA) equipped with

a HESI II probe to record high resolution. The tolerated error is ± 5 ppm of the molecular mass. The spectra were interpreted by molecular peaks $[M]^+$, or peaks of protonated molecules $[M+H]^+$ and characteristic fragment peaks and indicated with their mass-to-charge ratio (m/z) and intensity in percent relative to the base peak (100%).

MALDI-ToF-MS (Matrix Assisted Laser Desorption Ionization Time of Flight Mass Spectrometry) was recorded on an Axima Confidence spectrometer (model: TO-6071R00) equipped with Shimadzu Biotech Launchpad™ software (version 2.9.3.20110624) from Shimadzu Biotech. A wavelength $\lambda = 337$ nm nitrogen laser was used to desorb and ionize the samples. The target was a 384-spot Shimadzu Kratos Analytical Standard sample plate (DE1580TA) from Shimadzu Biotech. Samples to be analyzed were applied to the target directly or dissolved in a mixture of acetonitrile and double-distilled water. A saturated 1:1 mixture of 2,5-dihydroxybenzoic acid and α -cyano-4-hydroxycinnamic acid (Universal MALDI Matrix, Sigma-Aldrich®) dissolved in a 1:1 mixture of acetonitrile and double-distilled water served as the matrix. Co-crystallization of the matrix and sample was carried out in room air. For measurement, the sample was fired approximately 100 times at a frequency of 50 Hz, and the results were averaged. The protonated molecular ion peak $[M+H]^+$, as well as the pseudomolecular ion peaks with sodium $[M+Na]^+$ and potassium $[M+K]^+$, if present, were reported.

Photoreactions

Photoreactions were performed in a standard photoreactor LZC-4X equipped with 14 UVA/C (365/254 nm) lamps, six top lamps, and eight side lamps. The reaction mixture was loaded in a four-face quartz cuvette with stirring placed in the middle of the photoreactor.

For the irradiation with LED UV light (405 nm), an M405L4 LED (405 nm, 1000 mW (Min) Mounted LED, 1000 mA, THORLABS) was used.

Preparative Reversed-Phase High-Performance Liquid Chromatography (RP-HPLC)

Preparative Reversed-Phase High-Performance Liquid Chromatography (RP-HPLC) was performed on the Puriflash™ 4125 system from Interchim. A VDSpher® C18-M-SE precolumn (10 μ m, 40 x 16 mm) followed by a VDSpher® C18-M-SE separation column (10 μ m, 250 x 20 mm, VDS Optilab) was used as the stationary phase. A linear gradient of acetonitrile and double distilled water supplemented with 0.1% trifluoroacetic acid (TFA) at a 15 mL/min flow rate served as the mobile phase.

Absorption Spectroscopy

UV/Vis spectra were recorded either on a JASCO V-730 double-beam UV-Vis spectrophotometer with an automatic stirring unit and were baseline corrected using Jasco's Spectra Manager Software Vers. 2 or an Agilent Cary 100 Bio Varian UV/vis spectrometer.

Photoluminescence measurements in water

Emission spectra were recorded on:

JASCO FP-8300 fluorescence spectrometer equipped with a 450 W xenon arc lamp, double-grating excitation, emission monochromators, and a water-thermostated cell holder (STR-812) using Jasco's Spectra Manager Software Vers. 2.

Or HORIBA SCIENTIFIC fluoromax-4 spectrofluorometer equipped with a CZERNY-TURNER-type monochromator and an R928P PMT detector.

Or Horiba Duetta™ fluorescence spectrometer equipped with a 75 W xenon arc lamp.

Lifetime experiments were performed using a time-correlated single-photon counting method (TCSPC) with a DeltaTime kit for DeltaDiode source on FluoroMax systems, including DeltaHub and DeltaDiode controller. NanoLED 370 was used as the excitation source ($\lambda=368$ nm). Absolute fluorescence quantum yields were measured at a Quantaaurus QY C11347 from Hamamatsu.

Photoluminescence measurements in solid state

PL measurements were performed with Horiba Jobin Yvon Fluorolog-322 and Fluorolog-QM spectrometers for temperature-dependent PL of polycrystalline **33**, and an optical cryostat based on a Cryomech PT403 pulse tube cryocooler was applied. The freeze-dried samples were typically measured in a 5 mm quartz tube as an optical cell connected to a vacuum/ gas manifold outside the sample chamber of the spectrometer. Although the Fluorolog-QM spectrometer has an option of time-resolved detection of phosphorescence spectra (delayed relative to pulsed excitation and to fast fluorescence), we found that it is not suited for the very long-lived phosphorescence as observed in this work. The phosphorescence spectra were therefore measured with a laser luminescence microscope by triggering off a 375 nm excitation laser diode and acquiring those spectra with a spectrograph and a CCD detector after a 100 ms delay. The acquisition time was typically 200 ms. Since the samples were measured in the quartz tube cell (typically under vacuum or air-filled), a long working distance objective (Mitutoyo 10x, NA0.14) was applied. All emission spectra were corrected for the wavelength-dependent response of the spectrometer and detector (in relative photon flux units).

The quantum yields of PL of solid samples were determined at ambient temperature in the air using an integrating sphere made of optical PTFE installed into the sample chamber of the Fluorolog spectrometer. The uncertainty of these measurements was estimated to be $\pm 10\%$.

Fluorescence decays were recorded with a TCSPC technique. Phosphorescence decay over seconds was traced by shutting down the excitation light beam with an internal Fluorolog shutter (~ 5 msec response time) and acquiring the detector (photomultiplier) signal in a time-based mode. To extend the accessible signal range, a servo-driven neutral density filter (OD ~ 2) was placed into the emission light path to reduce an initially strong emission signal. The gaps in the phosphorescence decay curves in Figures 33c, 34, and 37 correspond to the removal of that filter in about 2-5 s after activation of the shutter, when the intensity of decaying emission was significantly decreased. The initial part of the decay curve was then corrected (multiplied) for the filter transmission.

The near-infrared emission of singlet oxygen at 1279 nm from the freeze-dried sample of **33**•CB7+ β -CD in air was measured on a Bruker Vertex 80 FTIR spectrometer equipped with a liquid nitrogen cooled Ge detector and different CW or quasi-CW lasers for UV-vis excitation. The emission was collected in a 180° geometry with a parabolic mirror with an axial bore for guiding a laser beam to a sample. In this work, a 375 nm laser diode at a power of 5 mW was applied for excitation of **33**•CB7+ β -CD. Some details on the optical design of the sample chamber of this setup are given in reference.

Cytotoxicity test

100 μL of 1×10^5 cells/mL HeLa Suspension were seeded into each Well of a 96-Well-Plate and incubated overnight (37°C, 5% CO_2). Following the incubation, cell media was removed, and the cells were treated with different concentrations (5 μM and 10 μM) of the tested samples for 48 h. After 48 h exposure, 15 μL MTT was added to each well and incubated for 3 h at 37 °C and 5 % CO_2 . The Reaction was Stopped through the addition of 100 μL of Stop Solution. Following 24 h of incubation, the data was observed with the help of the Plate reader Spectramax3000.

Cell imaging

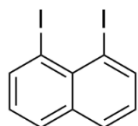
10×10^4 HeLa cells/mL were seeded into an 8-well ibidi® slide wells and incubated overnight (37 °C, 5% CO_2). Afterward, the cells were treated with tested samples for 24 h. In the following, the cell nuclei were stained with BioTracker™ 650 Red Nuclear Dye (1 $\mu\text{L}/\text{mL}$) and 100 μM Verapamil for 30 min. For the staining of the lysosomes, 100 nM LysoTracker™ Green DND-26 were added to the cells and incubated for another 30 min. Cell staining and colocalization were imaged using confocal microscopy (tested samples: 405 nm, BioTracker™ Red: 650 nm, LysoTracker™ Green: 504 nm).

Crystallographic Information

Suitable crystals were selected and studied on a Stoe StadiVari diffractometer with a Dectris Eiger 4M detector at 180 K using Ga- $\text{K}\alpha$ radiation ($\lambda = 1.34143 \text{ \AA}$) generated by an Excilium Metal-Jet D2 X-ray source. Using Olex2¹, the structures were solved with the ShelXT² structure solution program using Intrinsic Phasing and refined with the ShelXL³ refinement package using Least Squares minimization. Refinements were performed with anisotropic temperature factors for all non-hydrogen atoms; hydrogen atoms were calculated on idealized positions.

5.2. Reversing the Intramolecular [2+2] Photocycloaddition Stereoselectivity

Diiodonaphthalene (44)



1,8-Diaminonaphthalene (2.00 g, 12.6 mmol, 1.00 equiv.) was suspended in 6.9 M sulfuric acid (24.0 mL) and cooled to $-20\text{ }^{\circ}\text{C}$. A solution of sodium nitrite (2.62 g, 37.9 mmol, 2.00 equiv.) in water (10.0 mL) was added dropwise. During this process, the temperature was kept below $-15\text{ }^{\circ}\text{C}$. Subsequently, a potassium iodide solution (12.6 g, 75.6 mmol, 3.00 equiv.) in water (12.0 mL) was added at the same temperature. Small amounts of sulfuric acid were added if required to avoid freezing the solution. The mixture was heated to $80\text{ }^{\circ}\text{C}$ and stirred for 30 min. Then, the solution was cooled to $0\text{ }^{\circ}\text{C}$ and adjusted to pH=10 by adding a concentrated sodium hydroxide solution. The black precipitate was filtered off, ground, and extracted five times with 10.0 mL of DCM. The combined organic layers were washed with 10 % hydrochloric acid, a saturated aqueous sodium thiosulfate solution, dilute aqueous sodium hydroxide, dried over magnesium sulfate, and concentrated in a vacuum. The resulting brown residue was recrystallized from hexane to afford the product diiodonaphthalene (2.20 g, 5.79 mmol, 46%). The results of the analysis are consistent with the literature^[100].

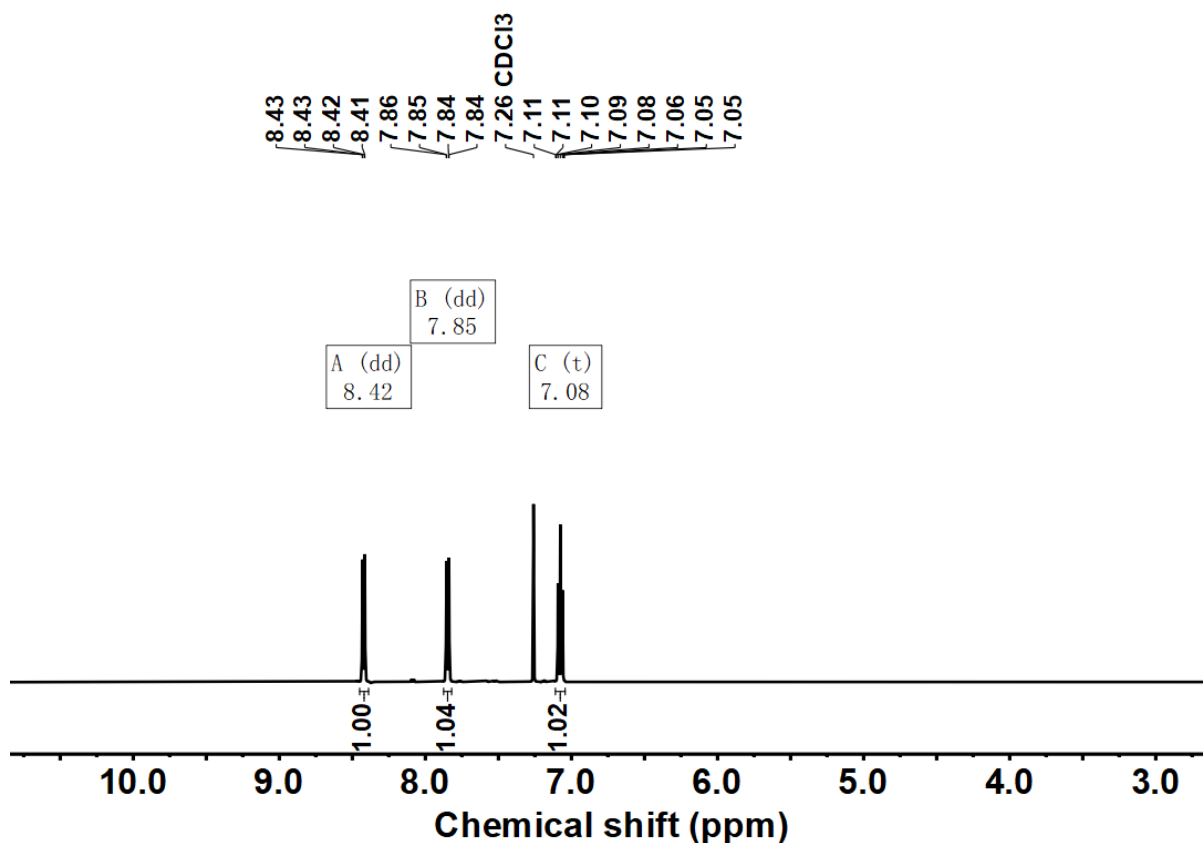


Figure 73. ^1H NMR spectra of **44**, 500 MHz, CDCl_3 .

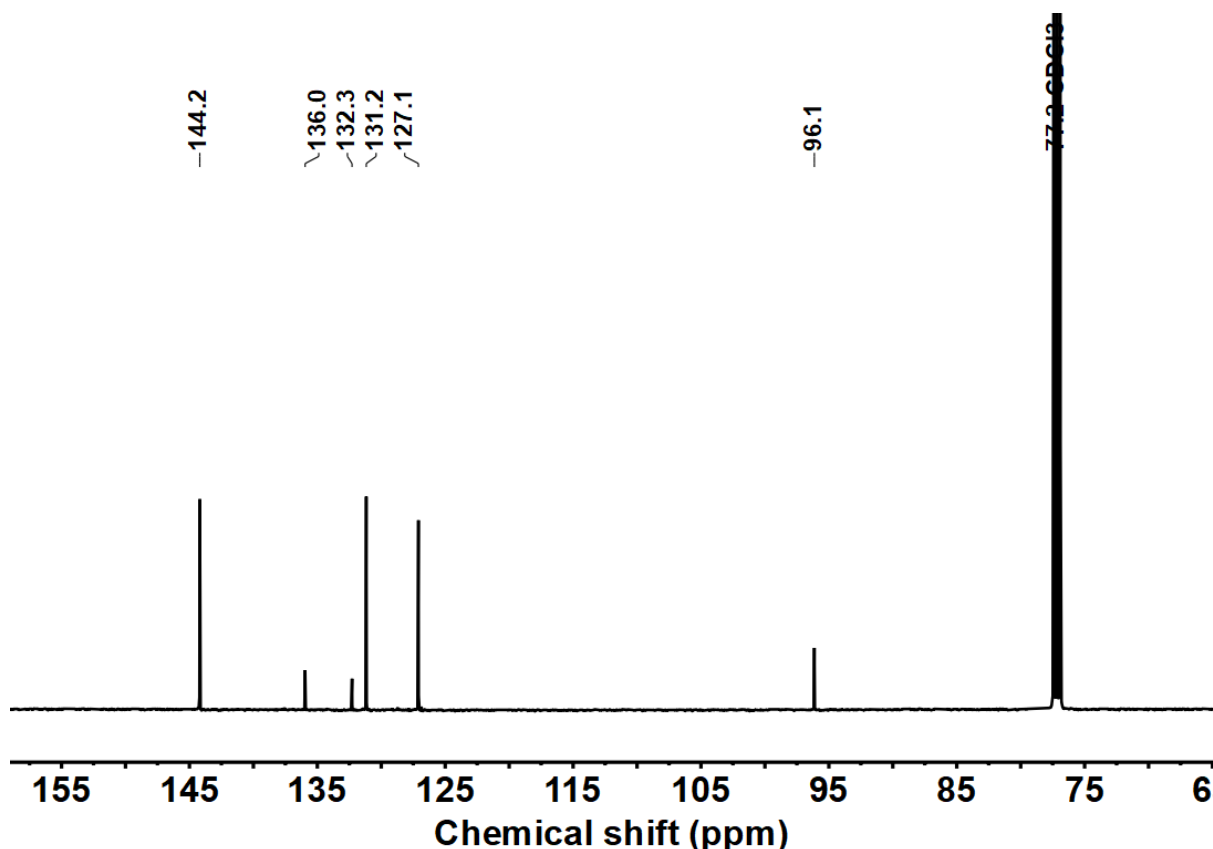
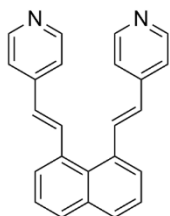


Figure 74. ^{13}C NMR spectra of **44**, 126 MHz, CDCl_3 .

1,8-bis[(E)-2-(4-pyridyl)ethenyl]naphthalene (**45**)



1,8-bis[(E)-2-(4-pyridyl)ethenyl]naphthalene was synthesized using the method reported in the literature. To an oven-dried flask, diiodonaphthalene (1.00 g, 2.63 mmol, 1.00 equiv.), 4-vinylpyridine (1.12 mL, 1.11 g, 10.5 mmol, 4.00 equiv.), palladium(II)acetate (11.8 mg, 0.05 mmol, 0.02 equiv.), tri-*o*-tolylphosphine (32.0 mg, 0.11 mmol, 0.04 equiv.), triethylamine (2.0 mL), and acetonitrile (25 mL) were added. The flask was charged with argon, sealed, heated to

90 °C, and stirred for 48 h. Subsequently, the flask was removed from heat and cooled at room temperature. The mixture was poured into cold water, and the precipitate was collected via vacuum filtration. The resulting solid was purified through column chromatography on a silica column using DCM: MeOH=10:1 as mobile phase to obtain product 1,8-bis[(E)-2-(4-pyridyl)ethenyl]naphthalene as a yellow solid (0.59 g, 1.76 mmol, 67%).

^1H NMR (500 MHz, CDCl_3 , ppm) δ = 8.47–8.42 (m, 4H, H_{Ar}), 8.14 (d, J = 15.9 Hz, 2H, H_{vinyl}), 7.88 (dd, J = 8.1, 1.3 Hz, 2H, H_{Ar}), 7.66 (dt, J = 7.1, 1.1 Hz, 2H, H_{Ar}), 7.52 (dd, J = 8.2, 7.1 Hz, 2H, H_{Ar}), 7.25–7.23 (m, 4H, H_{Ar}), 6.88 (d, J = 15.9 Hz, 2H, H_{vinyl}).

^{13}C NMR (126 MHz, CDCl_3 , ppm) δ = 150.4 (4C, C_{Ar}), 144.4 (2C, C_{Ar}), 136.6 (2C, C_{vinyl}), 135.7 (2C, C_{Ar}), 134.8 (2C, C_{Ar}), 129.9 (2C, C_{Ar}), 127.6 (2C, C_{Ar}), 127.1 (2C, C_{vinyl}), 126.1 (2C, C_{Ar}), 120.9 (4C, C_{Ar}).

ESI-MS for $[\text{C}_{24}\text{H}_{19}\text{N}_2]^+$: Calc. m/z = 335.1543, found m/z = 335.1542.

IR (ATR, cm^{-1}) $\tilde{\nu}$ = 3397 (s), 3325 (m), 2997 (m), 2996 (m), 2993 (m), 2968 (vs), 2965 (vs), 2956 (vs), 2935 (vs), 2892 (s), 2885 (s), 2884 (s), 2883 (s), 2877 (s), 2874 (s), 2872 (s), 2870 (s), 2868 (s), 2792 (vs), 2780 (s),

2759 (vs), 2679 (vs), 1616 (m), 1421 (s), 1419 (m), 1165 (s), 1161 (s), 1153 (s), 1152 (s), 1131 (s), 1128 (s), 1121 (s), 1087 (s), 1034 (s) cm^{-1} .

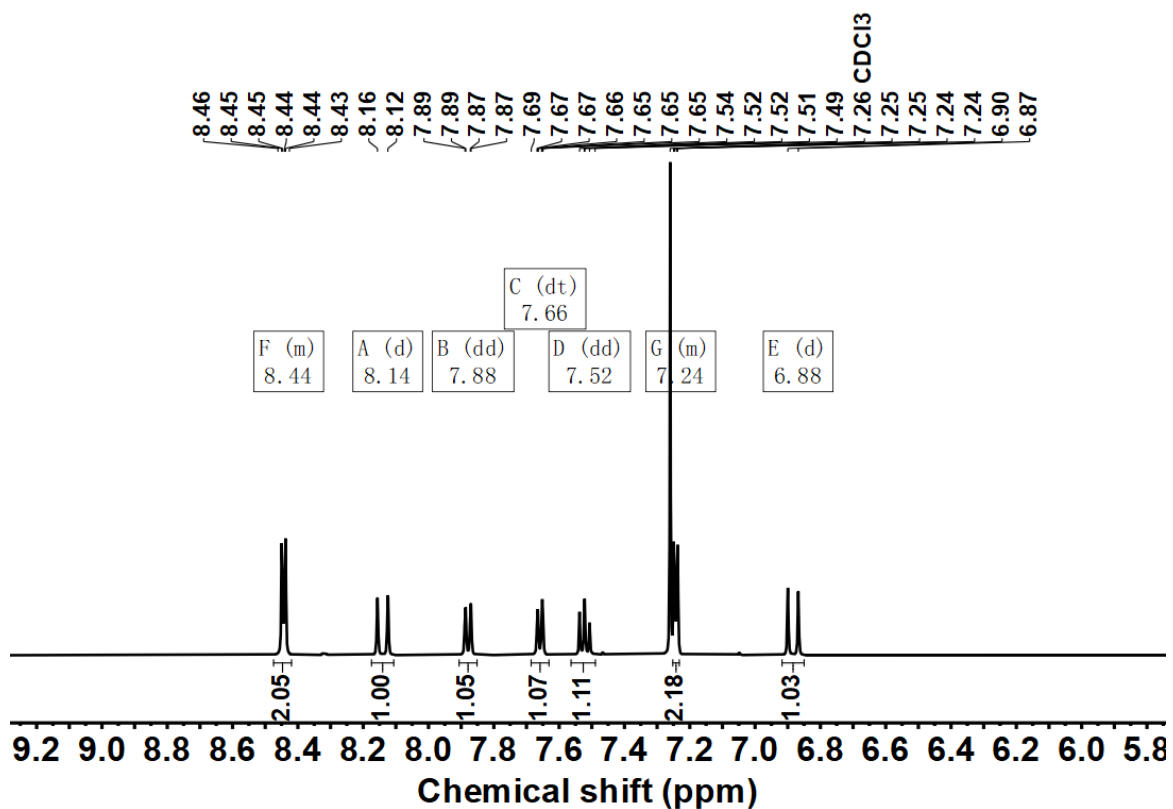


Figure 75. ^1H NMR spectra of 45, 500 MHz, CDCl_3 .

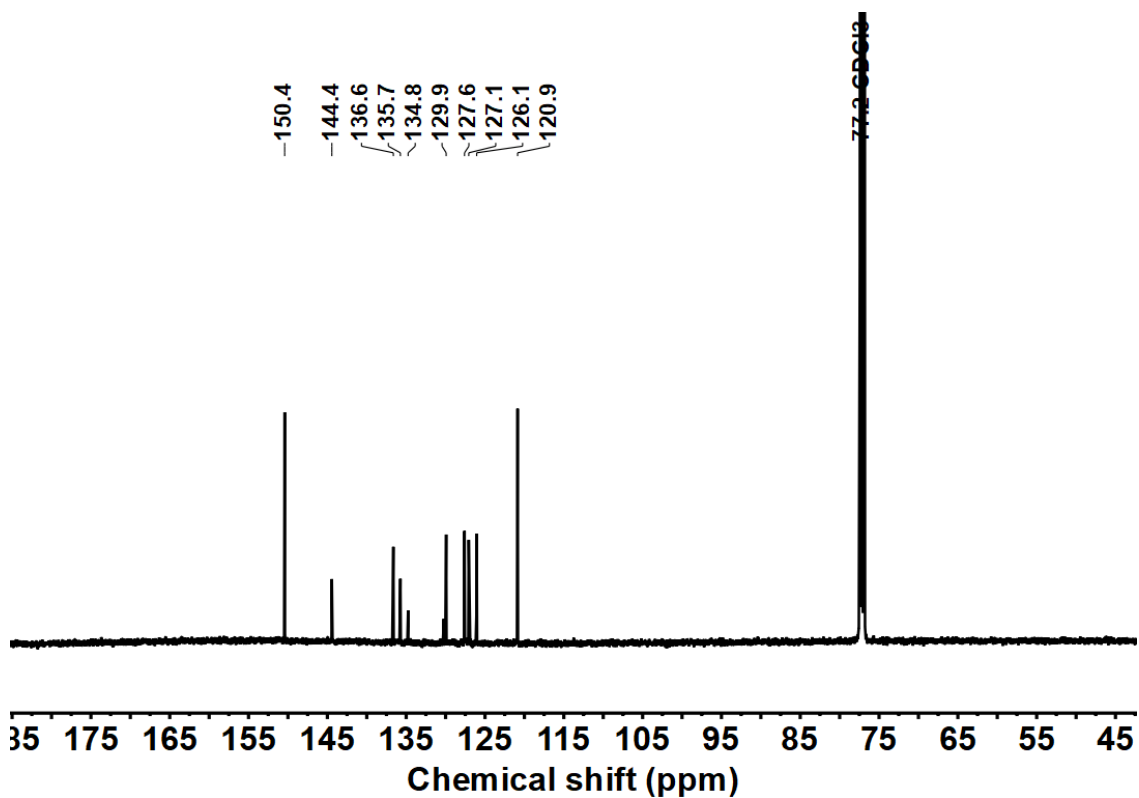
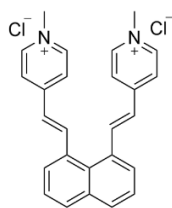


Figure 76. ^{13}C NMR spectra of 45, 126 MHz, CDCl_3 .

4,4'-((1E,1'E)-naphthalene-1,8-diylbis(ethene-2,1-diyl))bis(1-methylpyridin-1-ium) chloride (31)



1,8-bis[(E)-2-(4-pyridyl)ethenyl]naphthalene (0.10 g, 0.30 mmol, 1.00 equiv.) and iodomethane (0.17 g, 1.20 mmol, 4.00 equiv.) were suspended in DMF (10 mL), the mixture was heated at 50 °C for 16 hours. After cooling down, the precipitation was collected and washed with acetone several times. The solid was dissolved in water (500 mL), and AgCl (0.17 g, 1.20 mmol, 4.00 equiv.) was added. The mixture was stirred at 25 °C for 5 days. After

filtration, the water was evaporated and the desired product 4,4'-((1E,1'E)-naphthalene-1,8-diylbis(ethene-2,1-diyl))bis(1-methylpyridin-1-ium) chloride was obtained as a light yellow powder (0.12 g, 0.28 mmol, 92%).

^1H NMR (500 MHz, D_2O , ppm) δ = 8.46 (d, J = 6.4 Hz, 4H, H_{Ar}), 8.21 (d, J = 16.0 Hz, 2H, H_{vinyl}), 8.02 (d, J = 8.2 Hz, 2H, H_{Ar}), 7.84 (d, J = 6.5 Hz, 4H, H_{Ar}), 7.80 (d, J = 7.2 Hz, 2H, H_{Ar}), 7.63 (t, J = 7.7 Hz, 2H, H_{Ar}), 7.15 (d, J = 16.0 Hz, 2H, H_{vinyl}), 4.25 (s, 6H, CH_3).

^{13}C NMR (126 MHz, D_2O , ppm) δ = 152.9 (2C, C_{Ar}), 144.4 (4C, C_{Ar}), 142.9 (2C, C_{vinyl}), 134.2 (1C, C_{Ar}), 133.8 (2C, C_{Ar}), 131.1 (2C, C_{Ar}), 129.6 (1C, C_{Ar}), 128.8 (2C, C_{Ar}), 126.4 (2C, C_{Ar}), 124.1 (2C, C_{vinyl}), 123.6 (4C, C_{Ar}), 47.0 (2C, CH_3).

ESI-MS for $[\text{C}_{26}\text{H}_{24}\text{N}_2]^{2+}$: Calc. m/z = 182.0964, found m/z = 182.0965.

IR (ATR, $\tilde{\nu}$) = 3424 (vs), 3420 (vs), 3417 (vs), 3414 (vs), 3413 (vs), 3412 (vs), 3410 (vs), 3406 (vs), 3404 (vs), 3402 (vs), 3401 (vs), 3396 (vs), 3391 (vs), 3389 (vs), 3387 (vs), 3384 (vs), 3382 (vs), 3380 (vs), 3378 (vs), 3376 (vs), 3373 (vs), 3370 (vs), 3368 (vs), 3364 (vs), 3363 (vs), 3361 (vs), 3359 (vs), 3356 (vs), 3354 (vs), 3353 (vs), 3351 (vs), 3350 (vs), 3348 (vs), 3347 (vs), 3345 (vs), 3343 (vs), 3341 (vs), 3340 (vs), 3338 (vs), 3336 (vs), 3333 (vs), 3329 (vs), 3326 (vs), 3325 (vs), 3321 (vs), 3319 (vs), 3315 (vs), 3313 (vs), 3311 (vs), 3307 (vs), 3305 (vs), 3303 (vs), 3302 (vs), 3300 (vs), 3298 (vs), 3296 (vs), 3293 (vs), 3291 (vs), 3288 (vs), 3287 (vs), 3286 (vs), 3284 (vs), 3283 (vs), 3280 (vs), 3279 (vs), 3277 (vs), 3274 (vs), 3272 (vs), 3268 (vs), 3264 (vs), 3263 (vs), 3261 (vs), 3258 (vs), 3254 (vs), 3252 (vs), 3249 (vs), 3247 (vs), 3245 (vs), 3244 (vs), 3241 (vs), 3238 (vs), 3233 (vs), 3231 (vs), 3230 (vs), 3227 (vs), 3226 (vs), 3222 (vs), 3221 (vs), 3218 (vs), 3215 (vs), 3213 (vs), 3212 (vs), 3209 (vs), 3205 (vs), 3202 (vs), 3199 (vs), 3195 (vs), 1621 (vs), 1616 (vs), 1614 (vs) cm^{-1} .

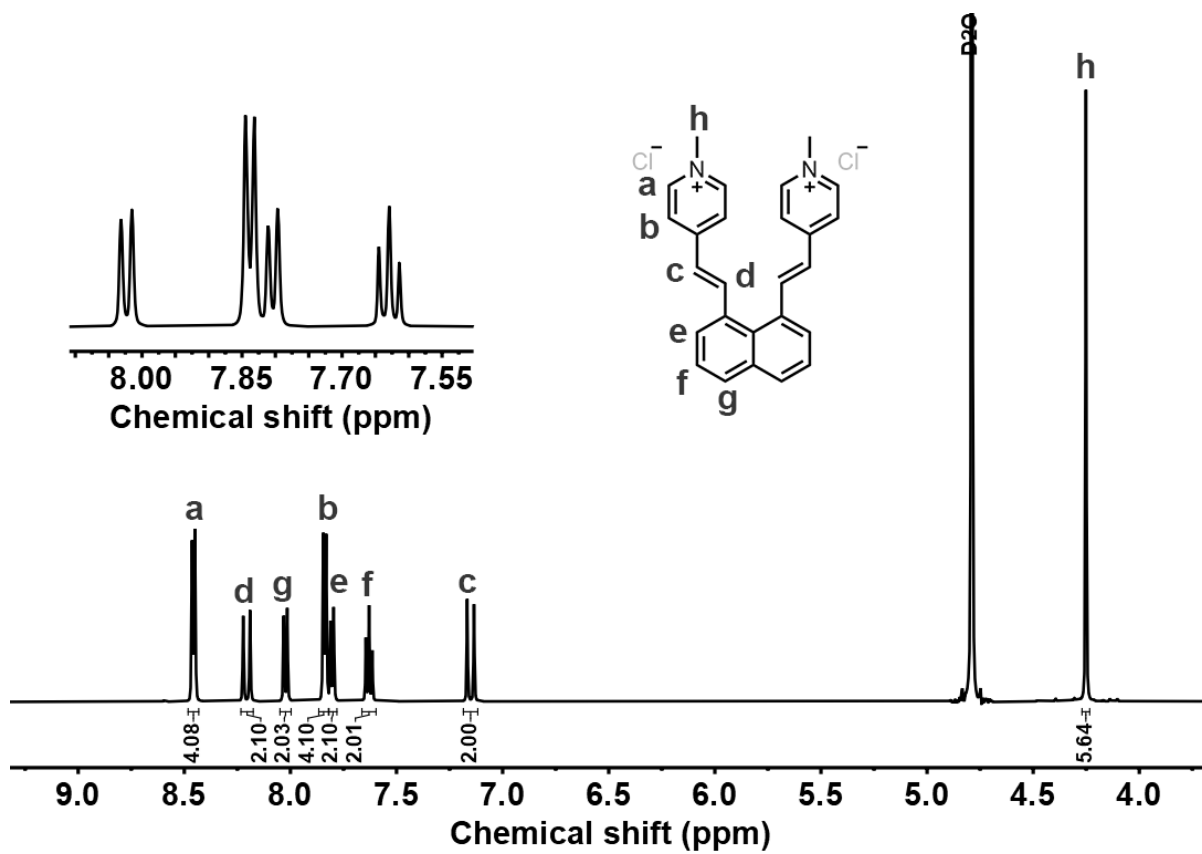


Figure 77. ^1H NMR spectra of **31**, 500 MHz, D_2O .

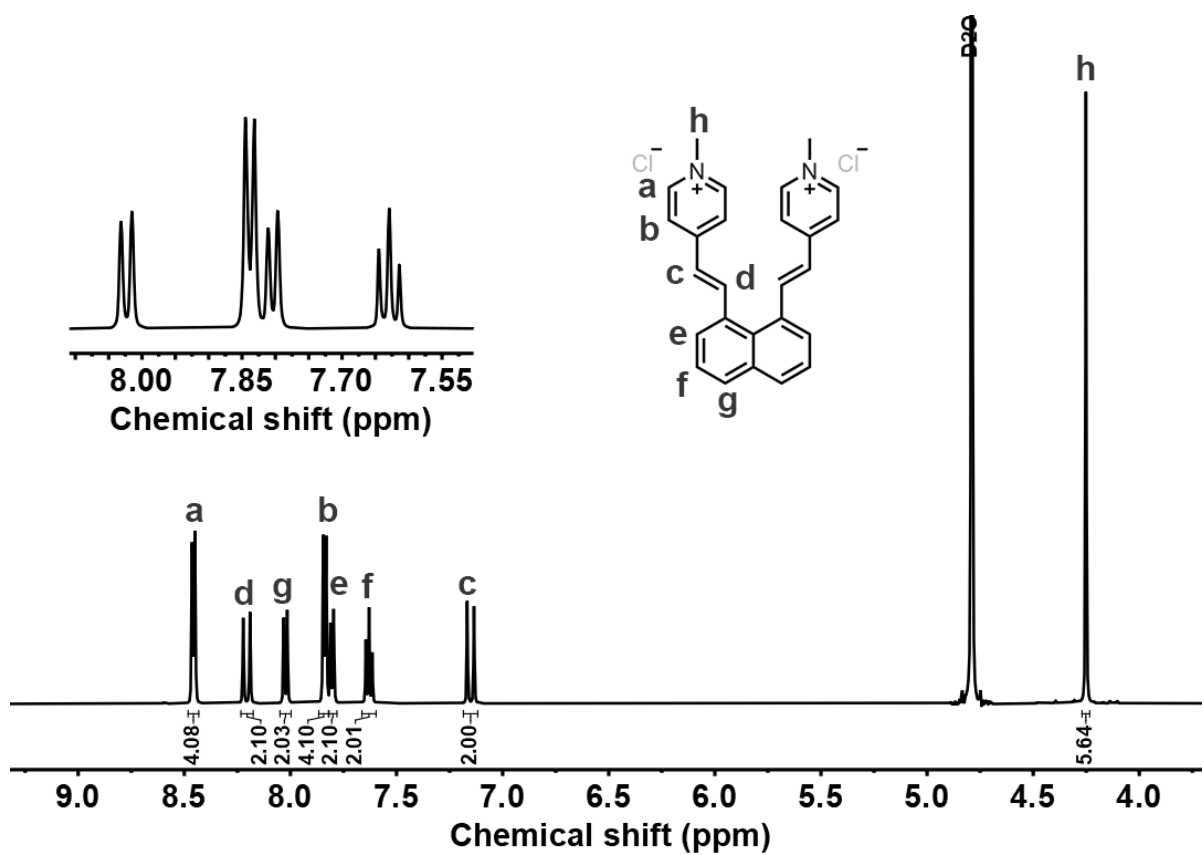


Figure 78. ^{13}C NMR spectra of **31**, 126 MHz, D_2O .

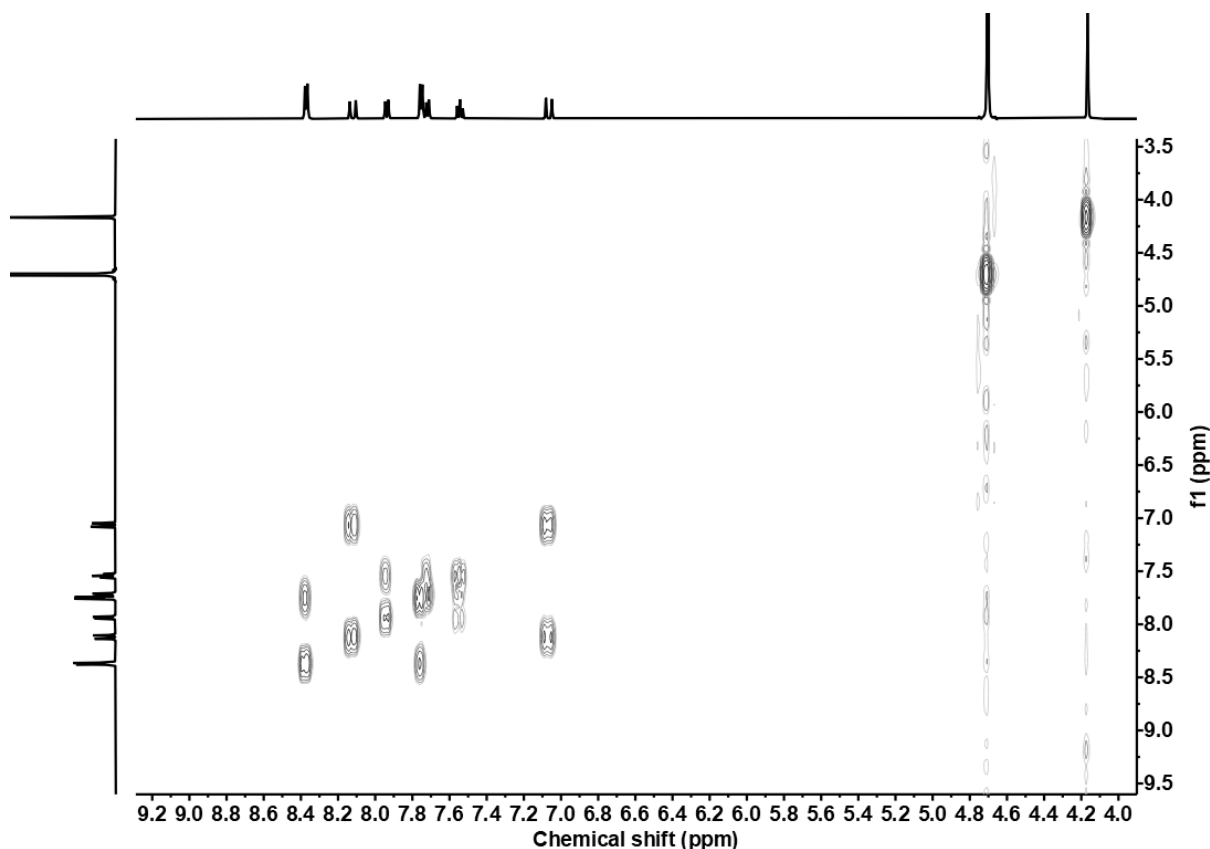
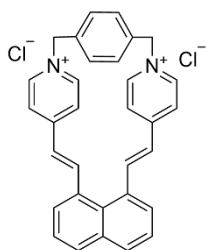


Figure 79. ^1H - ^1H COSY spectra of **31**, D_2O

(6E,9E)-1,5(1,4)-dipyridin-1-iuma-8(1,8)-naphthalena-3(1,4)-benzenacyclodecapane-6,9-diene-11,51-diiium chloride (46)



1,8-bis[(E)-2-(4-pyridyl)ethenyl]naphthalene (100 mg, 0.30 mmol, 1.00 equiv.), 1,4-bis(bromomethyl)benzene (78.9 mg, 0.30 mmol, 1.00 equiv.), and Tetra-*n*-butylammonium iodide (11.1 mg, 0.30 mmol, 0.10 equiv.) were suspended in DMF (10 mL), the mixture was heated at 50 °C for 16 hours. After cooling down, the precipitation was collected and washed with acetone several times. The solid was dissolved in water (500 mL) and added AgCl (0.17 g, 1.20 mmol, 4.00 equiv.). The mixture was stirred at 25 °C for 5 days. After filtration, the

water was evaporated, and the desired product (6E,9E)-1,5(1,4)-dipyridin-1-iuma-8(1,8)-naphthalena-3(1,4)-benzenacyclodecapane-6,9-diene-11,51-diiium chloride was obtained as a yellow powder (96.0 mg, 0.18 mmol, 63%).

^1H NMR (500 MHz, D_2O , ppm) δ = 8.54 (d, J = 6.6 Hz, 4H, H_{Ar}), 8.05 (d, J = 8.2 Hz, 2H, H_{Ar}), 8.02 (d, J = 15.7 Hz, 2H, H_{vinyl}), 7.82 (d, J = 7.2 Hz, 2H, H_{Ar}), 7.71 (d, J = 6.6 Hz, 4H, H_{Ar}), 7.64 (d, J = 7.8 Hz, 2H, H_{Ar}), 7.62 (s, 4H, H_{Ar}), 7.20 (d, J = 15.7 Hz, 2H, H_{vinyl}), 5.67 (s, 4H, CH_2).

^{13}C NMR (126 MHz, D_2O , ppm) δ = 153.9 (2C, C_{Ar}), 143.2 (2C, C_{vinyl}), 143.0 (4C, C_{Ar}), 138.3 (2C, C_{Ar}), 134.2 (1C, C_{Ar}), 133.8 (2C, C_{Ar}), 131.3 (2C, C_{Ar}), 130.0 (1C, C_{Ar}), 129.9 (4C, C_{Ar}), 129.1 (2C, C_{Ar}), 126.4 (2C, C_{Ar}), 124.1 (4C, C_{Ar}), 123.3 (2C, C_{vinyl}), 64.4 (2C, CH_2).

ESI-MS for $[\text{C}_{32}\text{H}_{26}\text{N}_2]^{2+}$: Calc. m/z = 219.1043, found m/z = 219.1040.

IR (ATR, $\tilde{\nu}$) = 3994 (s), 3987 (s), 3979 (s), 3972 (s), 3966 (s), 3959 (s), 3951 (s), 3945 (s), 3935 (s), 3929 (s), 3921 (s), 3914 (s), 3908 (s), 3896 (s), 3889 (s), 3882 (s), 3877 (s), 3871 (s), 3867 (s), 3859 (s), 3850 (s), 3842 (s), 3832 (s), 3825 (s), 3818 (s), 3813 (s), 3804 (s), 3798 (s), 3793 (s), 3787 (s), 3776 (s), 3768 (s), 3762 (s), 3756 (s), 3747 (s), 3741 (s), 3729 (s), 3720 (s), 3716 (s), 3707 (s), 3699 (s), 3686 (s), 3672 (s), 3666 (s), 3653 (s), 3645 (s), 3625 (s), 3616 (s), 3605 (s), 3598 (s), 3584 (s), 3571 (s), 3563 (s), 3557 (s), 3538 (s), 3451 (vs), 3440 (vs), 3360 (vs), 3344 (vs), 3333 (vs), 3326 (vs), 3319 (vs), 3263 (vs), 3164 (vs), 3123 (vs), 3091 (vs), 3086 (vs), 3027 (vs), 3000 (vs), 2965 (vs), 2953 (vs), 2942 (vs), 2878 (s), 2772 (s), 2765 (s), 2714 (m), 2685 (m), 2645 (m), 2610 (m), 1679 (m), 1638 (vs), 1616 (vs), 1565 (m), 1517 (s), 1474 (m), 1197 (s), 1148 (s), 1127 (m), 779 (m) cm^{-1} .

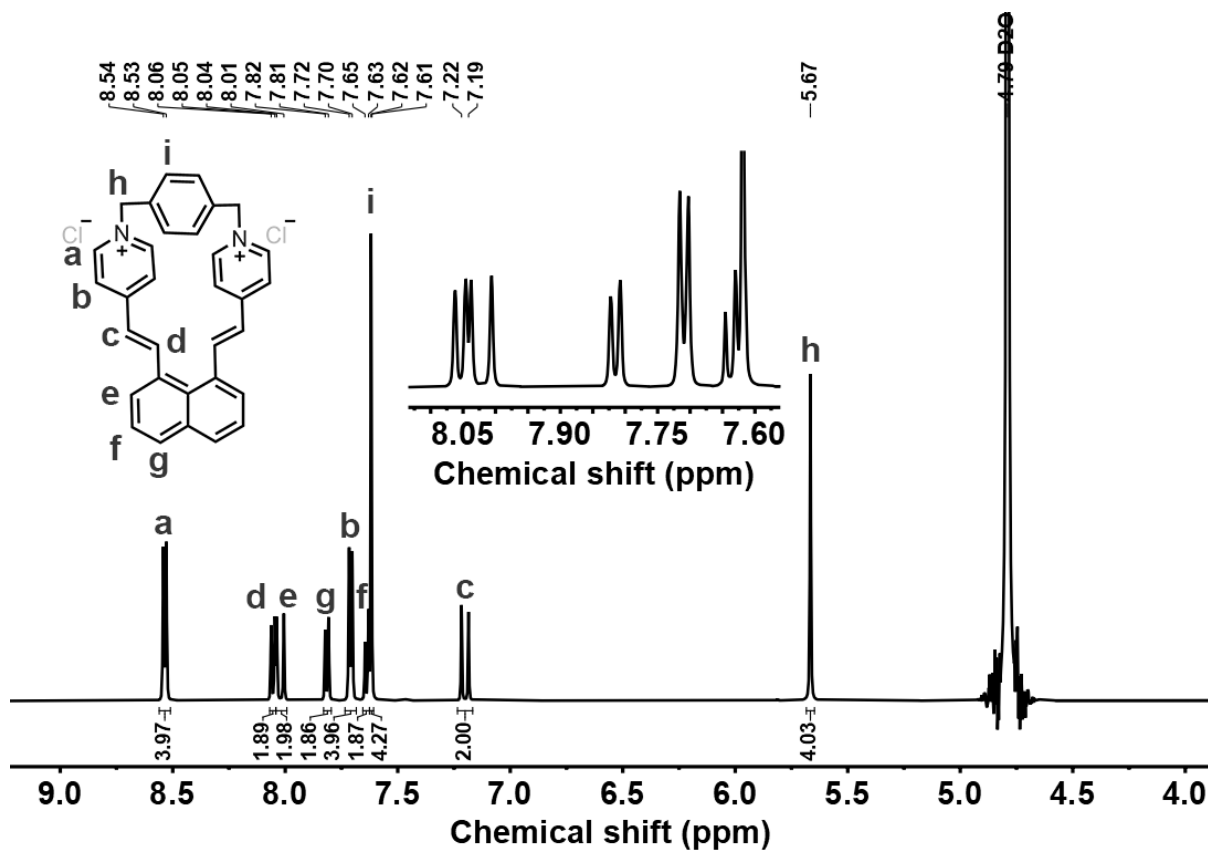


Figure 80. ^1H NMR spectra of 46, 500 MHz, D_2O .

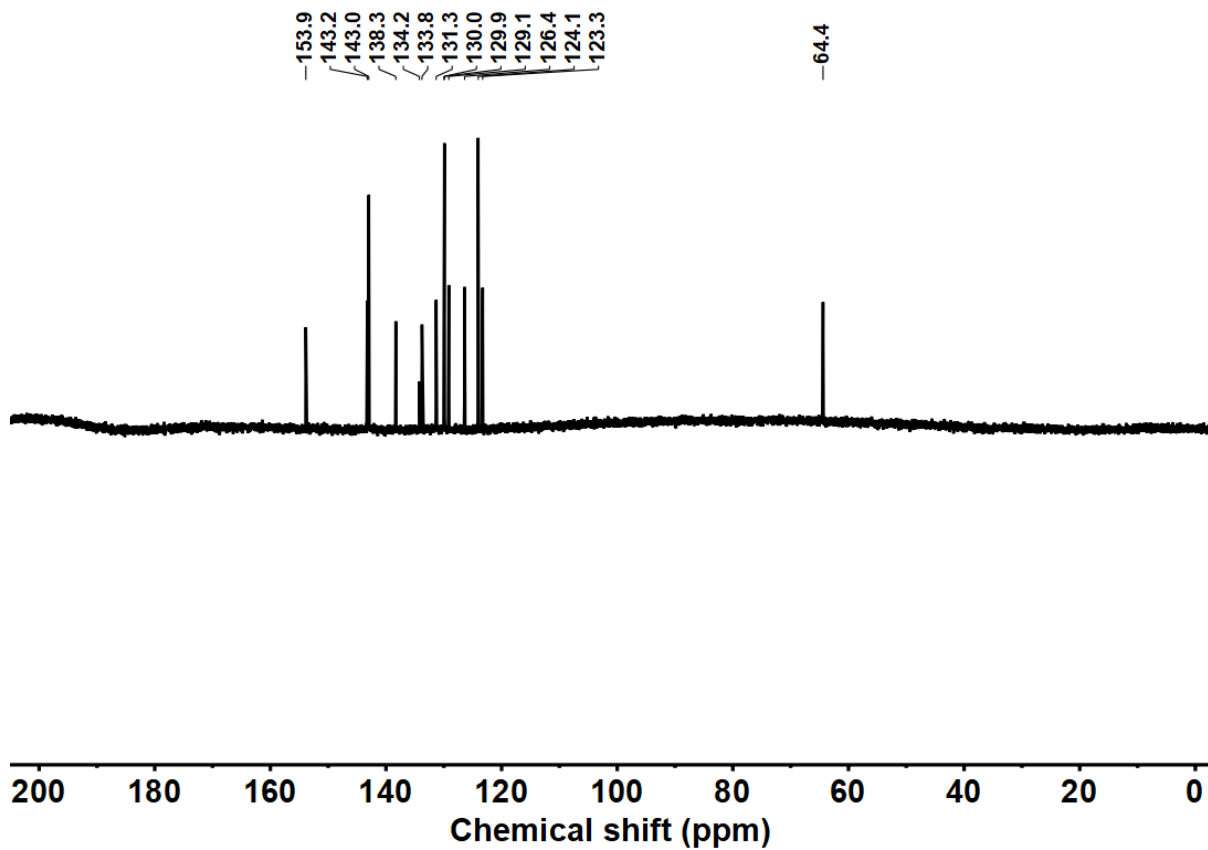


Figure 81. ^{13}C NMR spectra of **46**, 126 MHz, D_2O .

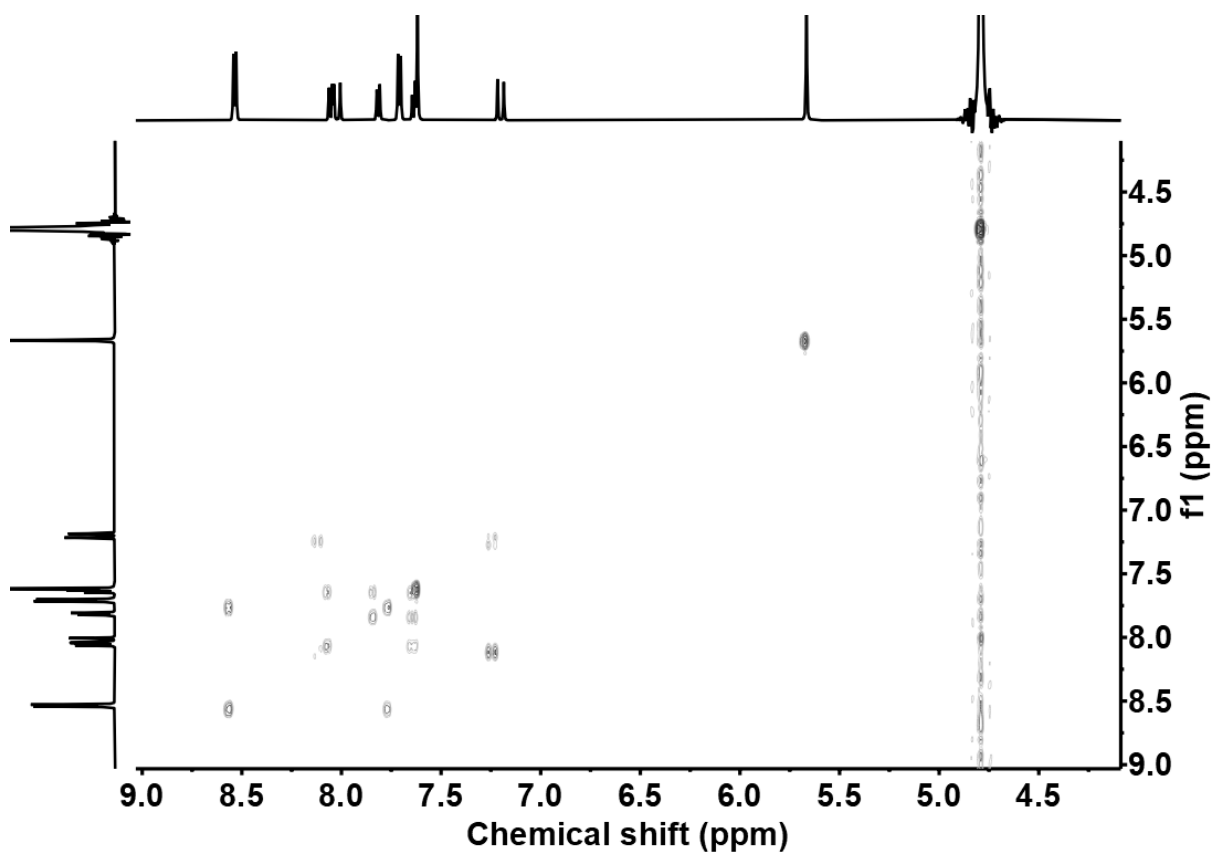
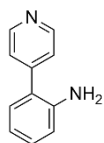


Figure 82. ^1H - ^1H COSY spectra of **46**, D_2O

5.3. Modulating Aryl Azide Photolysis in Aqueous

2-(pyridin-4-yl)aniline (49)



2-Bromo-aniline (1.21 g, 7.03 mmol, 1.00 equiv), 4-pyridylboronic acid (1.12 g, 9.14 mmol, 1.30 equiv), Na₂CO₃ (2.98 g, 28.1 mmol, 4.00 equiv), and Pd(dppf)Cl₂ (0.26 g, 0.35 mmol, 0.05 equiv) were suspended in a mixture of dioxane (35 mL) and H₂O (14 mL), the resulting mixture was heated at 80 °C for 2.5 hours. After cooling, the reaction mixture was suspended in a 1.5 N aqueous solution of NaOH (20 mL) and CH₂Cl₂ (30 mL). The aqueous phase was extracted with CH₂Cl₂ (3 × 30 mL). The combined organic phases were dried over Na₂SO₄ and evaporated under reduced pressure. After purifying by column chromatography using EtOAc/MeOH 9:1 as eluent, the product 2-pyridin-4-ylaniline (0.98 g, 5.76 mmol, 82%) was obtained as a yellow solid.

¹H NMR (500 MHz, CDCl₃, ppm) δ = 8.88 (s, 2H, H_{Ar}), 7.50 (s, 2H, H_{Ar}), 7.21 (td, *J* = 7.7, 1.6 Hz, 1H, H_{Ar}), 7.13 (dd, *J* = 7.6, 1.6 Hz, 1H, H_{Ar}), 6.85 (t, *J* = 7.5 Hz, 1H, H_{Ar}), 6.78 (d, *J* = 8.1 Hz, 1H, H_{Ar}), 3.73 (s, 2H, NH₂).

¹³C NMR (126 MHz, CDCl₃, ppm) δ = 150.2 (2C, C_{Ar}), 147.7 (1C, C_{Ar}), 143.4 (1C, C_{Ar}), 130.2 (1C, C_{Ar}), 129.9 (1C, C_{Ar}), 124.8 (1C, C_{Ar}), 124.6 (2C, C_{Ar}), 119.1 (1C, C_{Ar}), 116.2 (1C, C_{Ar}).

ESI-MS for [C₂₃H₁₉N₉O₂S+H]⁺: Calc. *m/z* = 171.0844, found *m/z* = 171.0912.

IR (ATR, $\tilde{\nu}$) = 3342 (vs), 3339 (vs), 3335 (vs), 3331 (vs), 3306 (vs), 3303 (vs), 3300 (vs), 3298 (vs), 3277 (vs), 3268 (vs), 3260 (vs), 3211 (vs), 3208 (vs), 3070 (s), 3055 (s), 3045 (s), 3037 (s), 3025 (s), 1612 (vs), 1607 (vs), 1594 (vs), 1578 (vs), 1575 (vs), 1539 (s), 1483 (vs), 1449 (vs), 1410 (vs), 1293 (s), 1160 (s), 755 (vs), 749 (vs), 739 (s), 724 (s), 617 (s) cm⁻¹.

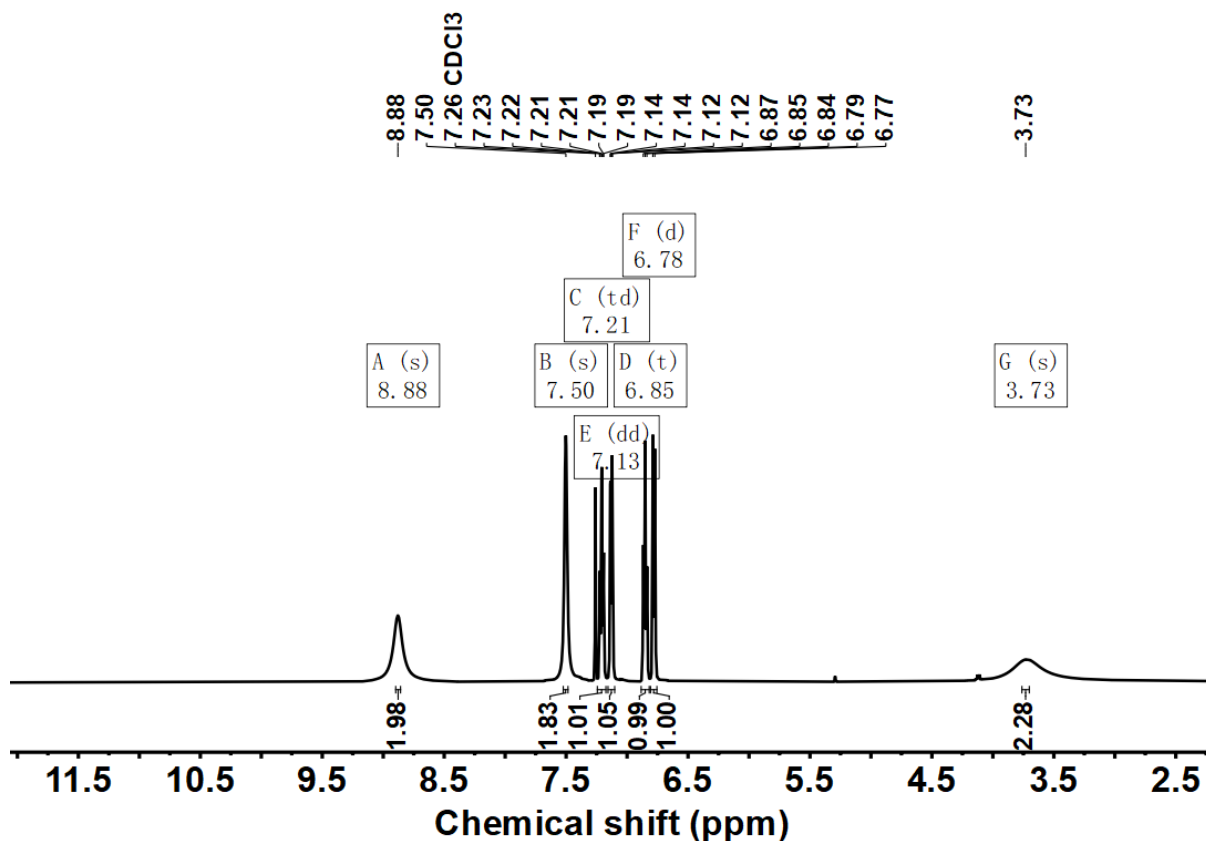


Figure 83. ¹H NMR spectra of 49, 500 MHz, CDCl₃.

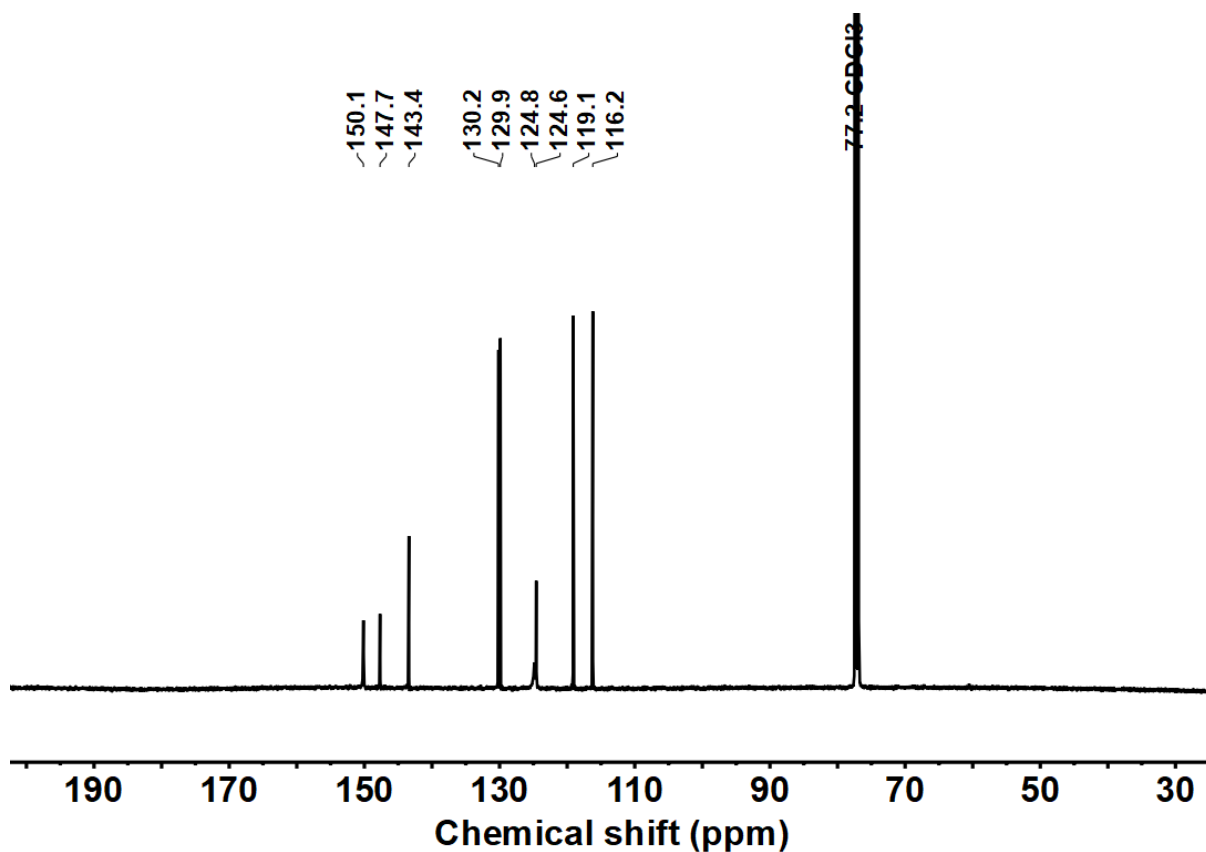
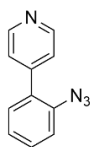


Figure 84. ^{13}C NMR spectra of **49**, 126 MHz, CDCl_3 .

4-(2-azidophenyl)pyridine (**50**)



The synthesis of 4-(2-azidophenyl)pyridine was adapted from our previously reported method.^[122] *p*-Toluenesulfonic acid monohydrate (1.43 g, 7.49 mmol, 1.50 equiv.) was dissolved in acetonitrile/water (10/5.0 mL) at 21 °C. Once dissolved, tert-butyl nitrite (0.77 g, 7.49 mmol, 1.50 equiv.) was added, followed by 2-(pyridin-4-yl)aniline (0.85 g, 4.99 mmol, 1.00 equiv.) portion-wise. The reaction mixture was stirred for 3h at 21 °C. After which, a solution of sodium azide (0.97 g, 15.0 mmol, 3.00 equiv.) in water (5.0 mL) was added dropwise. The resulting reaction mass was stirred for another 3 hours at 21 °C. After the complete conversion, the reaction mixture was extracted with ethyl acetate (3 × 20 ml). The combined organic layers were dried over sodium sulfate. After the removal of the solvent, the crude solid was purified by chromatography (EtOAc), resulting in 4-(2-azidophenyl)pyridine (0.95 g, 4.84 mmol, 97%) as a yellow solid.

^1H NMR (500 MHz, CDCl_3 , ppm) δ = 8.67 (d, J = 5.1 Hz, 2H, H_{Ar}), 7.48 (td, J = 7.7, 1.6 Hz, 1H, H_{Ar}), 7.43 (dd, J = 4.7, 1.7 Hz, 2H, H_{Ar}), 7.36 (dd, J = 7.6, 1.7 Hz, 1H, H_{Ar}), 7.30 (dd, J = 8.1, 1.2 Hz, 1H, H_{Ar}), 7.26 (d, J = 2.1 Hz, 1H, H_{Ar}).

^{13}C NMR (126 MHz, CDCl_3 , ppm) δ = 149.3 (2C, C_{Ar}), 146.5 (1C, C_{Ar}), 137.5 (1C, C_{Ar}), 131.0 (2C, C_{Ar}), 130.7 (1C, C_{Ar}), 130.3 (1C, C_{Ar}), 125.4 (1C, C_{Ar}), 124.6 (1C, C_{Ar}), 119.1 (1C, C_{Ar}).

ESI-MS for $[\text{C}_{11}\text{H}_8\text{N}_4+\text{H}]^+$: Calc. m/z = 197.0749, found m/z = 197.0817.

IR (ATR, $\tilde{\nu}$) = 3444 (s), 3424 (vs), 3376 (vs), 3367 (vs), 3362 (vs), 3356 (vs), 3352 (vs), 3350 (vs), 3347 (vs), 3342 (vs), 3339 (vs), 3333 (vs), 3329 (vs), 3326 (vs), 3324 (vs), 3319 (vs), 3314 (vs), 3309 (vs), 3304 (vs), 3297 (vs), 3294 (vs), 3285 (vs), 3281 (vs), 3277 (vs), 3270 (vs), 3267 (vs), 3262 (vs), 3259 (vs), 3256 (vs), 3255 (vs),

3249 (vs), 3245 (vs), 3242 (vs), 3234 (vs), 3227 (vs), 3221 (vs), 3217 (vs), 3212 (vs), 3099 (s), 3087 (s), 3066 (vs), 3046 (vs), 2124 (vs), 2088 (vs), 2048 (s), 2045 (s), 2042 (s), 1603 (vs), 1596 (vs), 1482 (vs), 1414 (s), 1287 (vs), 746 (vs) cm^{-1} .

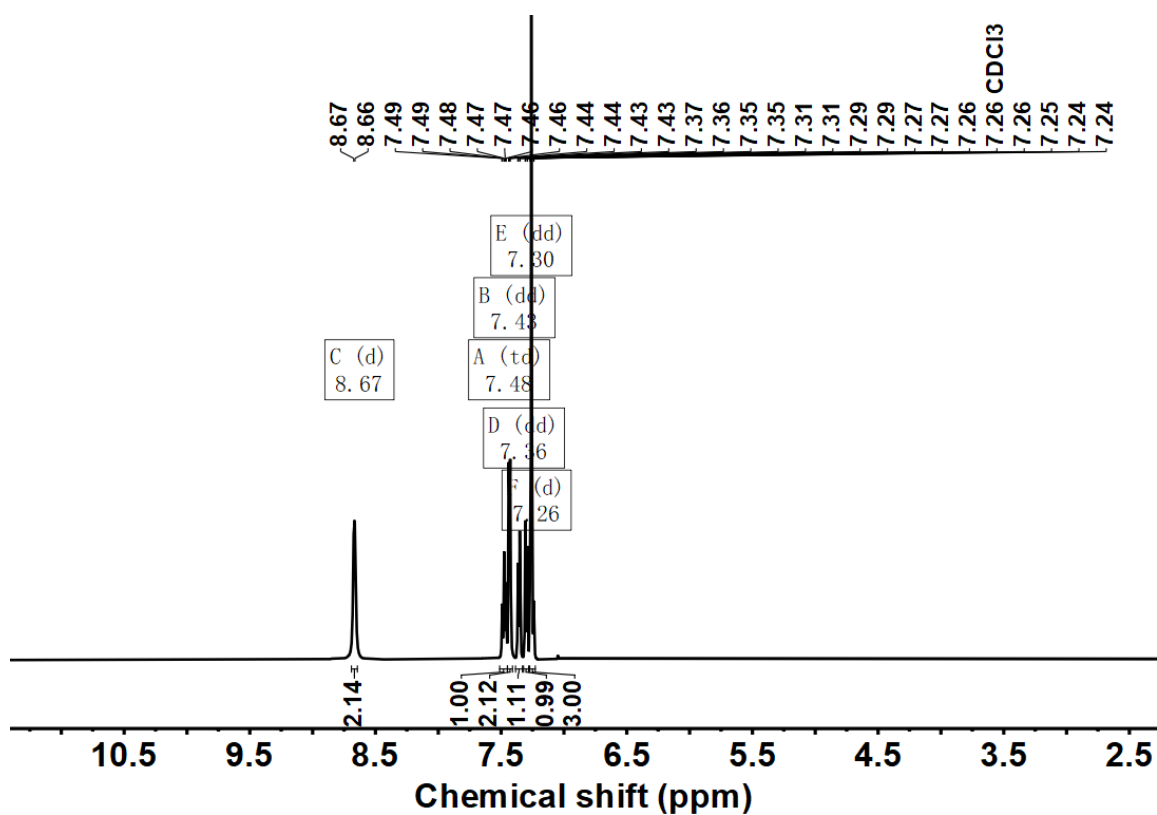


Figure 85. ^1H NMR spectra of **50**, 500 MHz, CDCl_3 .

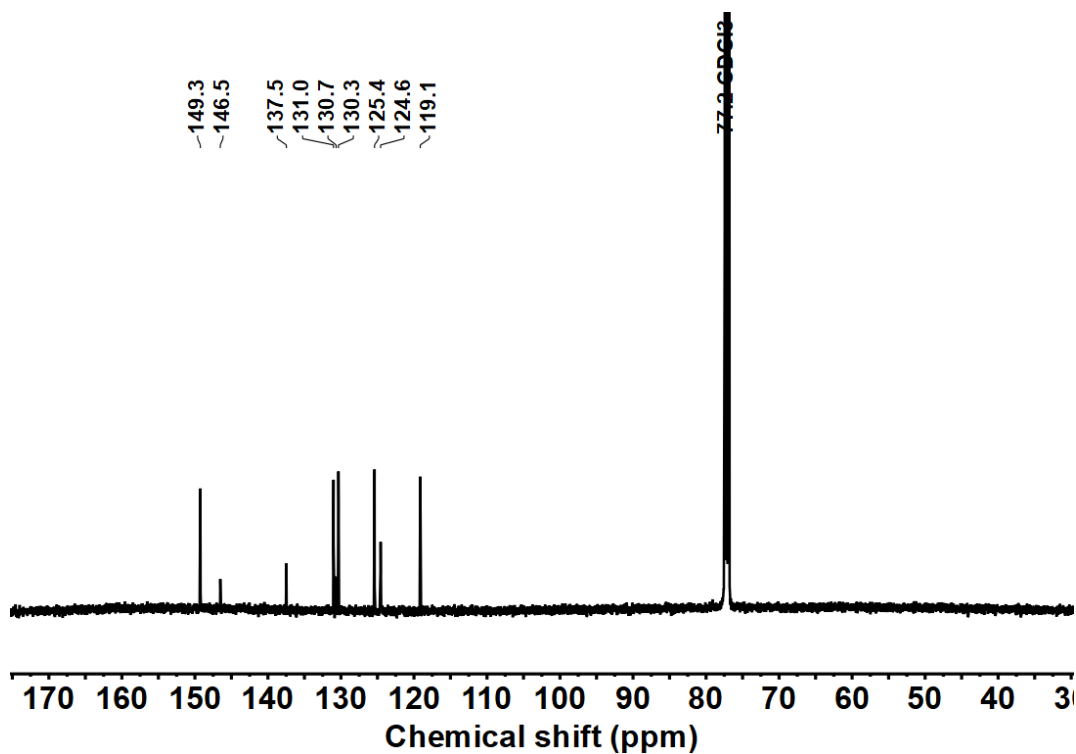
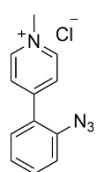


Figure 86. ^{13}C NMR spectra of **50**, 126 MHz, CDCl_3 .

4-(2-azidophenyl)-1-methylpyridin-1-ium chloride (33)



4-(2-azidophenyl)pyridine (0.50 g, 2.55 mmol, 1.00 equiv) was dissolved in acetonitrile (10 ml), and methyl iodide (0.43 g, 3.06 mmol, 1.20 equiv) was added dropwise at room temperature with stirring. The resulting reaction mixture was left overnight. The precipitation was collected by filtration and washed with acetonitrile. The solid was dissolved and stirred for five days in 500 ml water suspended with AgCl (0.73 g, 5.10 mmol, 2.00 equiv). After filtration and solvent removal, the desired product 4-(2-azidophenyl)-1-methylpyridin-1-ium chloride was obtained as a white solid (0.53 g, 2.15 mmol, 84%).

^1H NMR (500 MHz, D_2O , ppm) δ = 8.78-8.73 (m, 2H, H_{Ar}), 8.23-8.17 (m, 2H, H_{Ar}), 7.70-7.63 (m, 1H, H_{Ar}), 7.59 (dd, J = 7.8, 1.6 Hz, 1H, H_{Ar}), 7.50 (dd, J = 8.2, 1.1 Hz, 1H, H_{Ar}), 7.39 (td, J = 7.6, 1.1 Hz, 1H, H_{Ar}), 4.39 (s, 3H, CH_3).

^{13}C NMR (126 MHz, D_2O , ppm) δ = 154.6 (1C, C_{Ar}), 144.3 (2C, C_{Ar}), 137.9 (1C, C_{Ar}), 132.6 (1C, C_{Ar}), 131.0 (1C, C_{Ar}), 128.0 (2C, C_{Ar}), 126.4 (1C, C_{Ar}), 125.5 (1C, C_{Ar}), 119.8 (1C, C_{Ar}), 47.4 (1C, CH_3).

ESI-MS for $[\text{C}_{12}\text{H}_{11}\text{N}_4]^+$: Calc. m/z = 211.0978, found m/z = 211.0974.

IR (ATR, $\tilde{\nu}$) = 3468 (vs), 3406 (vs), 3401 (vs), 3389 (vs), 3376 (vs), 3372 (vs), 3365 (vs), 3360 (vs), 3353 (vs), 3350 (vs), 3347 (vs), 3340 (vs), 3335 (vs), 3331 (vs), 3329 (vs), 3326 (vs), 3323 (vs), 3321 (vs), 3311 (vs), 3261 (vs), 3240 (vs), 3227 (vs), 3218 (vs), 3141 (vs), 3118 (vs), 3102 (vs), 3085 (vs), 3034 (vs), 3021 (vs), 2969 (s), 2132 (s), 2114 (s), 2101 (s), 1673 (s), 1670 (s), 1668 (s), 1665 (s), 1661 (s), 1656 (s), 1639 (vs), 1616 (vs), 1575 (s), 1469 (s), 1305 (vs), 1297 (vs) cm^{-1} .

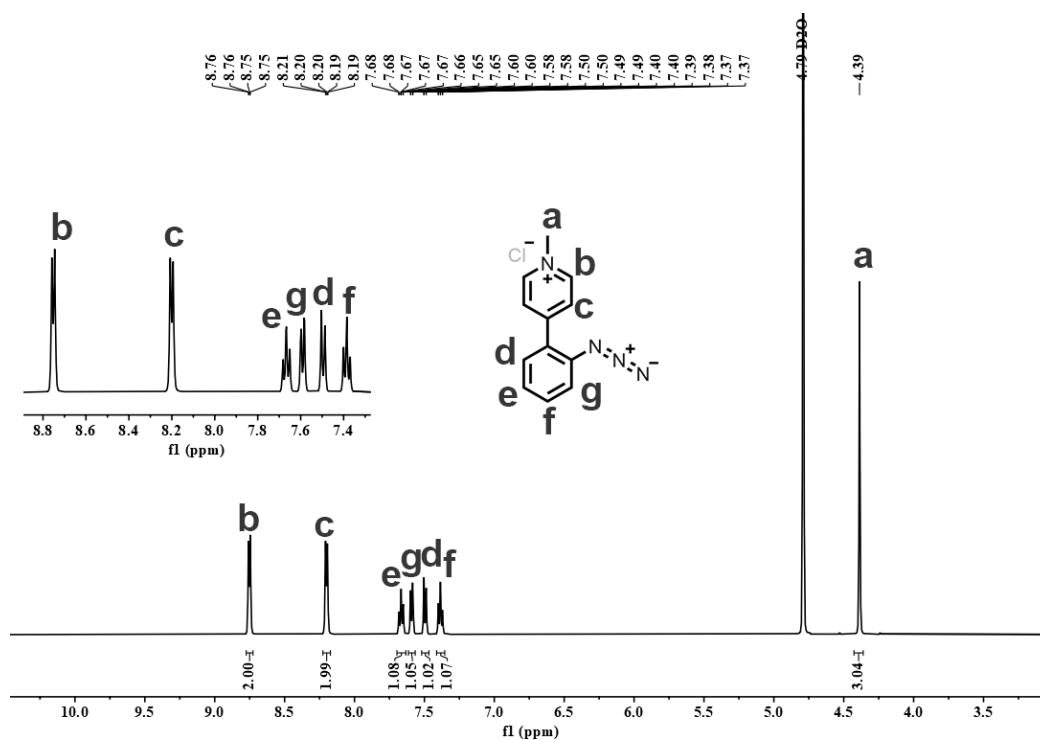


Figure 87. ^1H NMR spectra of **33**, 500 MHz, D_2O .

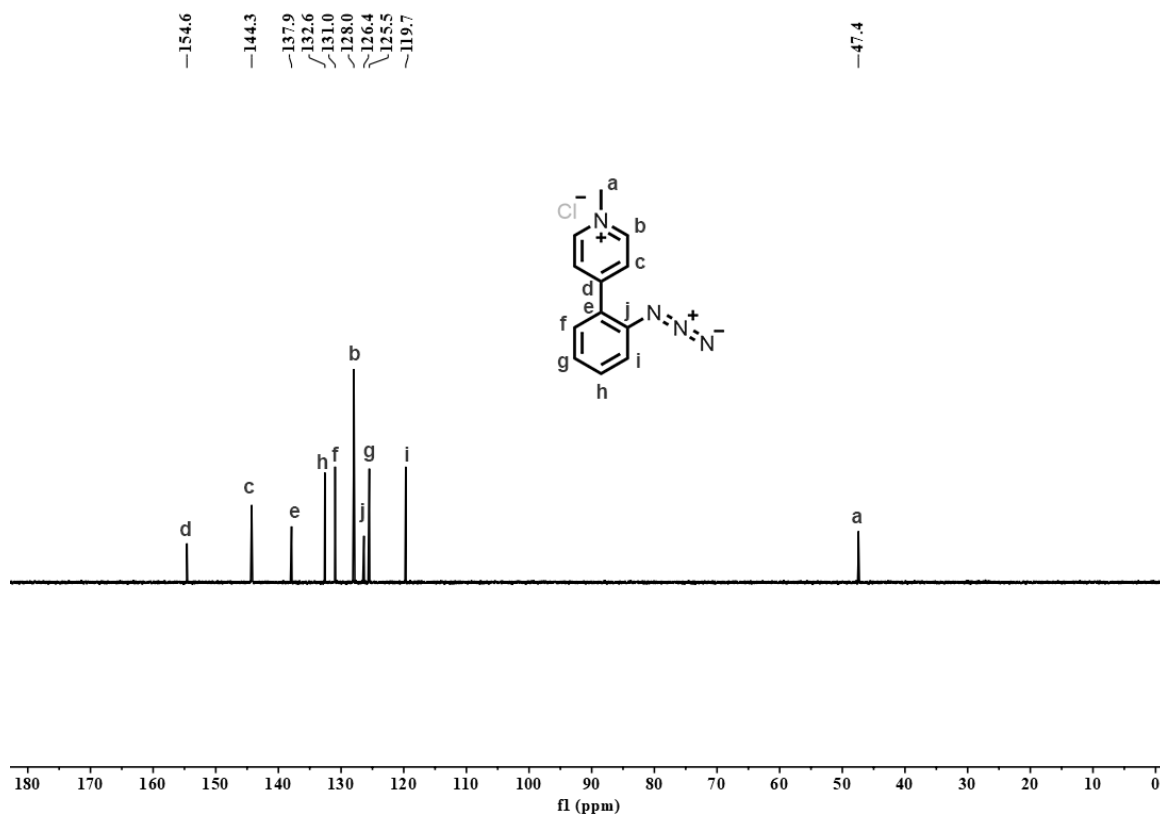


Figure 88. ¹³C NMR spectra of **33**, 126 MHz, D₂O.

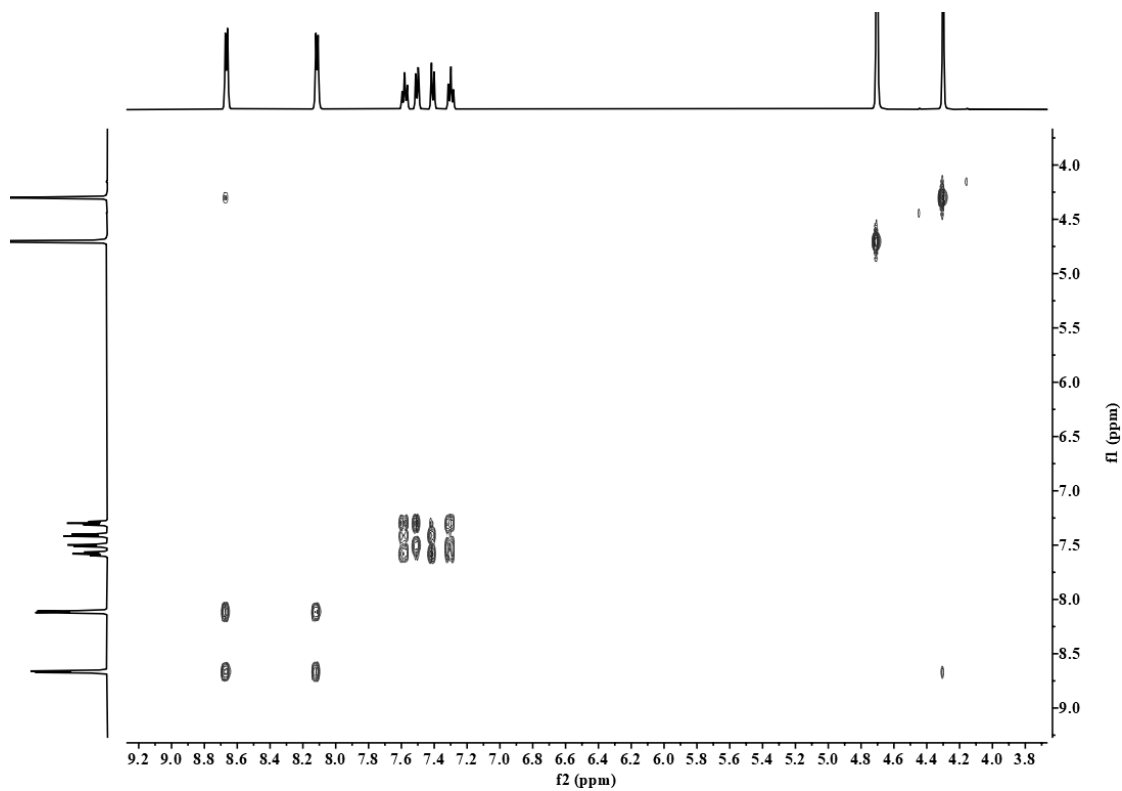
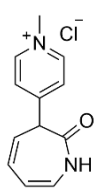


Figure 89. ¹H-¹H COSY NMR spectra of **33**, D₂O.

1-methyl-4-(2-oxo-2,3-dihydro-1H-azepin-3-yl)pyridin-1-ium chloride (47)



4-(2-azidophenyl)-1-methylpyridin-1-ium chloride (5.00 mg, 0.02 mmol, 1.00 equiv.) was dissolved with water (10 ml) in a quartz flask, and the reaction solution was irradiated under 254 nm UV light. After 0.5 h, water was removed, and the resulting mixture was injected into the preparative reversed-phase high-performance liquid chromatography using acetonitrile and double distilled water supplemented with 0.1% trifluoroacetic acid as eluent. 1-methyl-4-(2-oxo-2,3-dihydro-1H-azepin-3-yl)pyridin-1-ium chloride was collected and dried as a brown solid (2.00 mg, 0.01 mmol, 42%).

^1H NMR (500 MHz, D_2O , ppm) δ = 8.79-8.74 (m, 2H, H_{Ar}), 8.05-8.01 (m, 2H, H_{Ar}), 6.51 (ddd, J = 9.4, 5.4, 1.6 Hz, 1H, H_{Ar}), 6.42 (dd, J = 9.0, 1.8 Hz, 1H, H_{Ar}), 6.15 (ddd, J = 9.1, 5.4, 1.4 Hz, 1H, H_{Ar}), 5.78 (dd, J = 9.4, 6.0 Hz, 1H, H_{Ar}), 4.39 (s, 3H, CH_3), 4.23-4.17 (m, 1H, CH).

^{13}C NMR (126 MHz, D_2O , ppm) δ = 166.3 (1C, CO), 156.6 (1C, C_{Ar}), 144.6 (2C, C_{Ar}), 128.5 (2C, C_{Ar}), 128.4 (1C, C_{Ar}), 125.8 (1C, C_{Ar}), 122.6 (1C, C_{Ar}), 115.7 (1C, C_{Ar}), 51.0 (1C, C_{Ar}), 47.6 (1C, CH_3).

ESI-MS for $[\text{C}_{12}\text{H}_{13}\text{N}_2\text{O}]^+$: Calc. m/z = 201.1023, found m/z = 201.1023.

IR (ATR, $\tilde{\nu}$) = 3468 (vs), 3406 (vs), 3401 (vs), 3389 (vs), 3376 (vs), 3372 (vs), 3365 (vs), 3360 (vs), 3353 (vs), 3350 (vs), 3347 (vs), 3340 (vs), 3335 (vs), 3331 (vs), 3329 (vs), 3326 (vs), 3323 (vs), 3321 (vs), 3311 (vs), 3261 (vs), 3240 (vs), 3227 (vs), 3218 (vs), 3141 (vs), 3118 (vs), 3102 (vs), 3085 (vs), 3034 (vs), 3021 (vs), 2969 (s), 2930 (s), 2132 (s), 2114 (s), 2101 (s), 1677 (s), 1673 (s), 1670 (s), 1668 (s), 1665 (s), 1661 (s), 1656 (s), 1639 (vs), 1616 (vs), 1594 (s), 1577 (s), 1575 (s), 1469 (s), 1435 (s), 1305 (vs), 1297 (vs), 1198 (s) cm^{-1} .

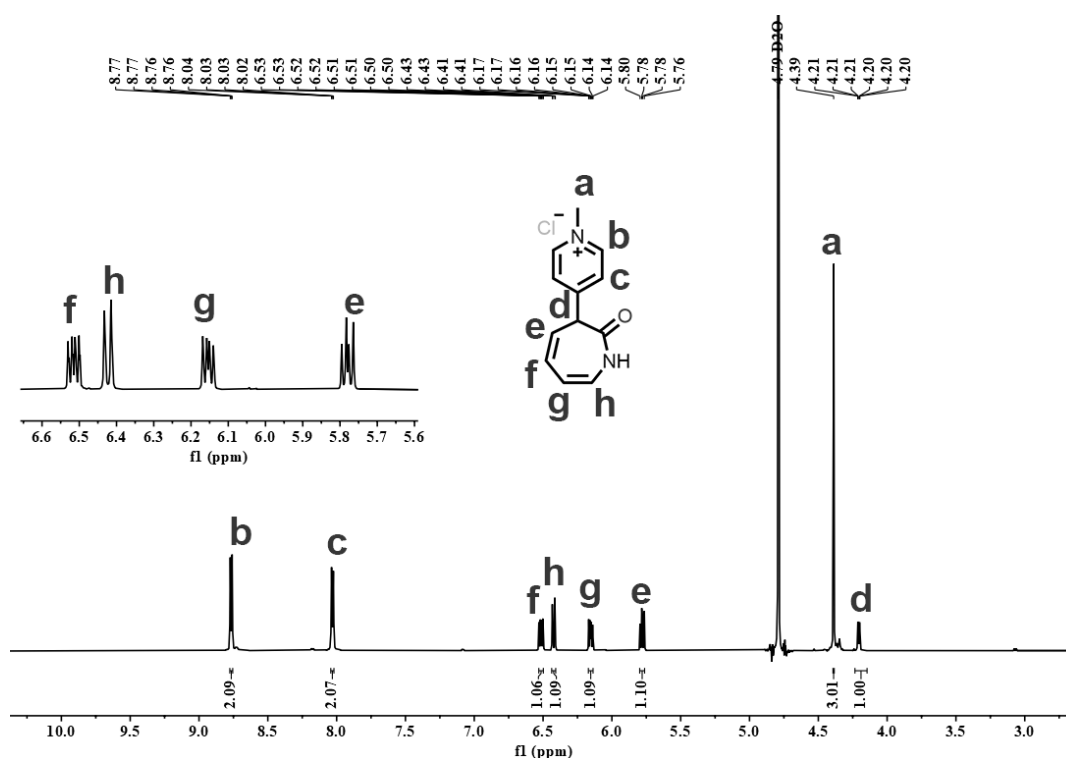
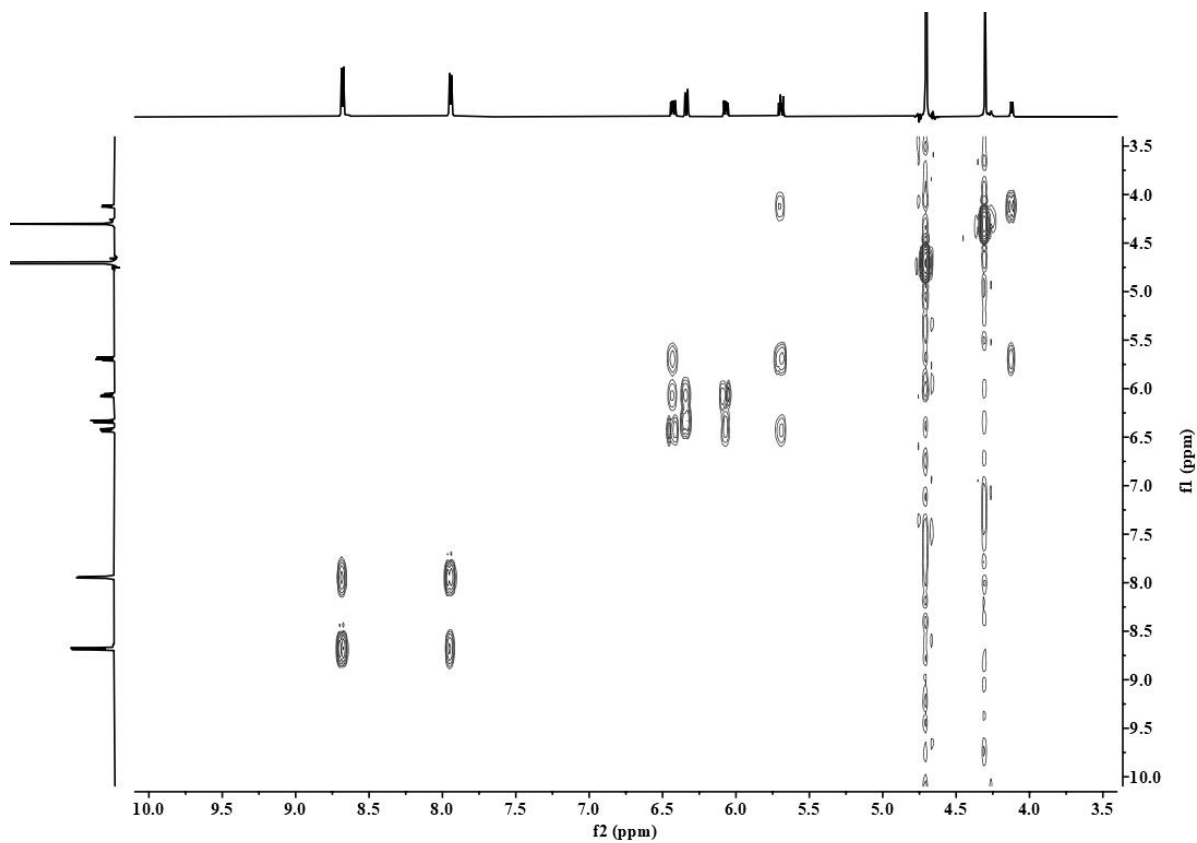
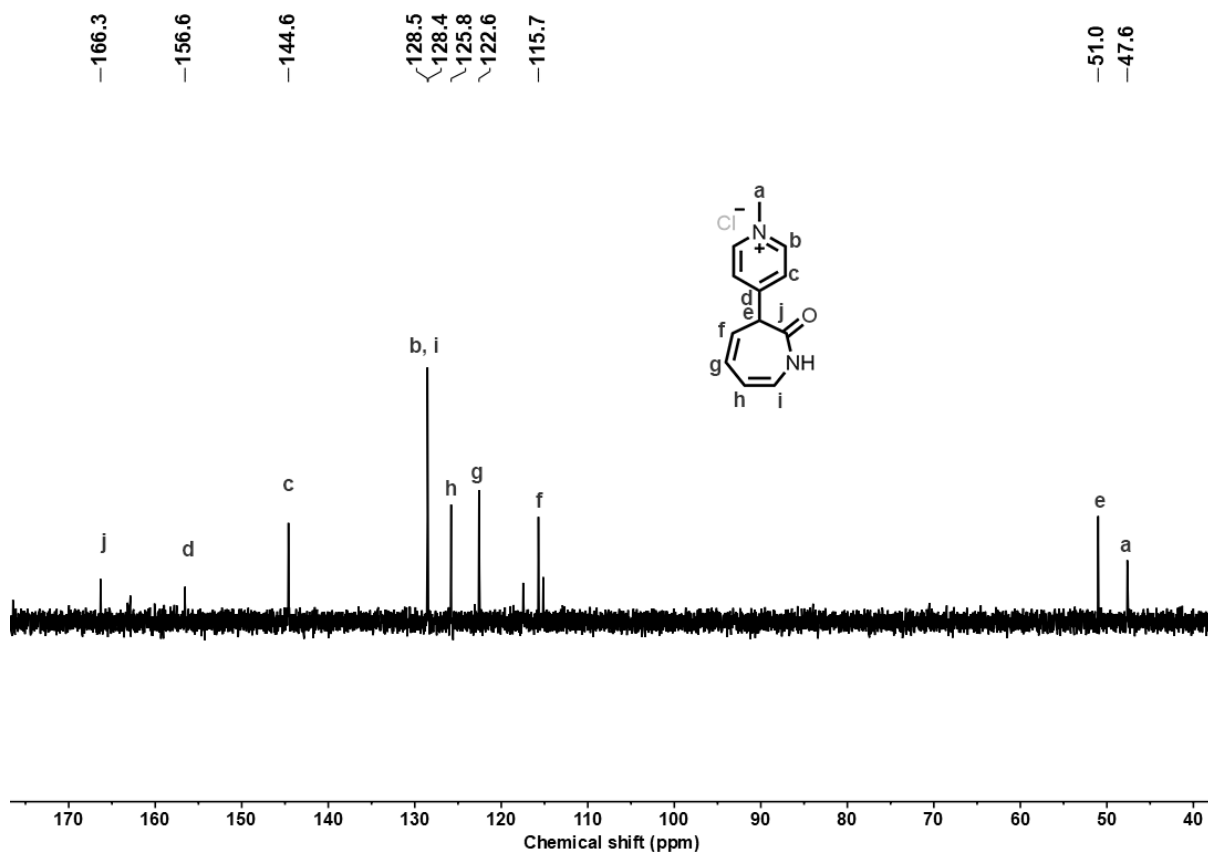
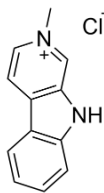


Figure 90. ^1H NMR spectra of **47**, 500 MHz, D_2O .



2-methyl-9H-pyrido[3,4-b]indol-2-ium chloride (34)



4-(2-azidophenyl)-1-methylpyridin-1-ium chloride (5.00 mg, 0.02 mmol, 1.00 equiv.) and cucurbit[7]uril (23.6 mg, 0.02 mmol, 1.00 equiv.) were dissolved with water (10 ml) in a quartz flask, and the reaction solution was irradiated under 254 nm UV light at 25 °C. After 0.5 h, amantadine (9.08 mg, 0.06 mmol, 3.00 equiv.) was added to the reaction mixture. After stirring for 1 hour, water was removed, and the resulting mixture was injected into the preparative reversed-phase high-performance liquid chromatography using acetonitrile and double distilled water supplemented with 0.1% trifluoroacetic acid as eluent. 2-methyl-9H-pyrido[3,4-b]indol-2-ium chloride was collected and dried as a pale white solid (4.20 mg, 0.02 mmol, 95%).

$^1\text{H NMR}$ (500 MHz, D_2O , ppm) δ = 8.79 (s, 1H, H_{Ar}), 8.33 (d, J = 6.5 Hz, 1H, H_{Ar}), 8.21 (dd, J = 6.4, 1.4 Hz, 1H, H_{Ar}), 8.17 (d, J = 8.1 Hz, 1H, H_{Ar}), 7.77 (ddd, J = 8.4, 7.1, 1.2 Hz, 1H, H_{Ar}), 7.63 (d, J = 8.4 Hz, 1H, H_{Ar}), 7.42 (t, J = 7.6 Hz, 1H, H_{Ar}), 4.38 (s, 3H, H_{Ar}).

$^{13}\text{C NMR}$ (126 MHz, D_2O , ppm) δ = 143.6 (1C, C_{Ar}), 134.8 (1C, C_{Ar}), 132.6 (1C, C_{Ar}), 132.4 (1C, C_{Ar}), 131.9 (1C, C_{Ar}), 129.0 (1C, C_{Ar}), 122.7 (1C, C_{Ar}), 121.6 (1C, C_{Ar}), 118.9 (1C, C_{Ar}), 117.2 (1C, C_{Ar}), 112.5 (1C, C_{Ar}), 47.6 (1C, CH_3).

ESI-MS for $[\text{C}_{12}\text{H}_{11}\text{N}_2]^+$: Calc. m/z = 183.0917, found m/z = 183.0917.

IR (ATR, $\tilde{\nu}$) = 3452 (vs), 3447 (vs), 3445 (vs), 3441 (vs), 3437 (vs), 3427 (vs), 3422 (vs), 3418 (vs), 3412 (vs), 3406 (vs), 3403 (vs), 3400 (vs), 3397 (vs), 3394 (vs), 3392 (vs), 3384 (vs), 3383 (vs), 3376 (vs), 3372 (vs), 3367 (vs), 3365 (vs), 3360 (vs), 3357 (vs), 3345 (vs), 3343 (vs), 3337 (vs), 3335 (vs), 3332 (vs), 3329 (vs), 3328 (vs), 3326 (vs), 3325 (vs), 3322 (vs), 3319 (vs), 3317 (vs), 3315 (vs), 3312 (vs), 3311 (vs), 3303 (vs), 3301 (vs), 3300 (vs), 3284 (vs), 3273 (vs), 3269 (vs), 3267 (vs), 3262 (vs), 3256 (vs), 3252 (vs), 3250 (vs), 3248 (vs), 3242 (vs), 3240 (vs), 3235 (vs), 3231 (vs), 3228 (vs), 3223 (vs), 3211 (vs), 3210 (vs), 3206 (vs), 3203 (vs), 3197 (vs), 3196 (vs), 3194 (vs), 3192 (vs), 3189 (vs), 3187 (vs), 3185 (vs), 3182 (vs), 3181 (vs), 3178 (vs), 3176 (vs), 3175 (vs), 3174 (vs), 3171 (vs), 3169 (vs), 3168 (vs), 3166 (vs), 3165 (vs), 3161 (vs), 3160 (vs), 3155 (vs), 3149 (vs), 3137 (vs), 3136 (vs), 3134 (vs), 3130 (vs), 3119 (vs), 3117 (vs), 3115 (vs), 3113 (vs), 3100 (vs), 3090 (vs), 3076 (vs), 3047 (vs), 3043 (vs), 3041 (vs), 3039 (vs), 3038 (vs), 3019 (vs), 3008 (vs) cm^{-1} .

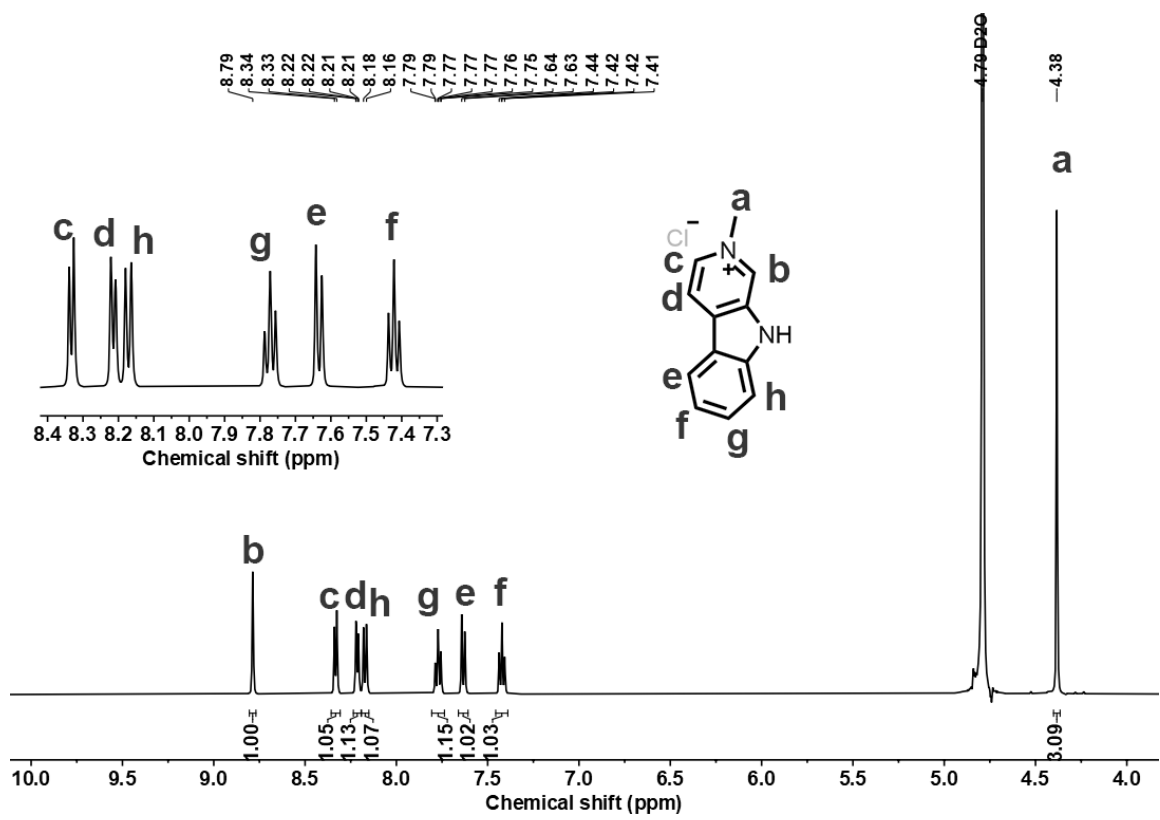


Figure 93. ^1H NMR spectra of **34**, 500 MHz, D_2O .

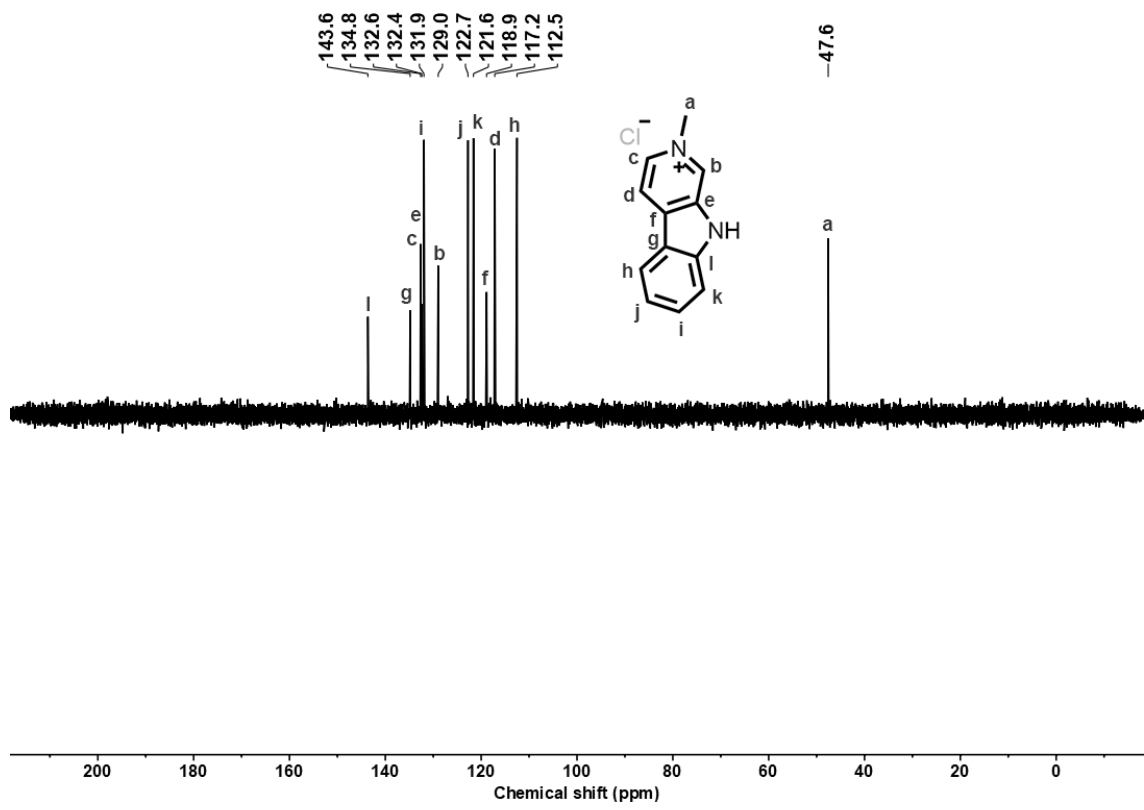


Figure 94. ^{13}C NMR spectra of **34**, 126 MHz, D_2O .

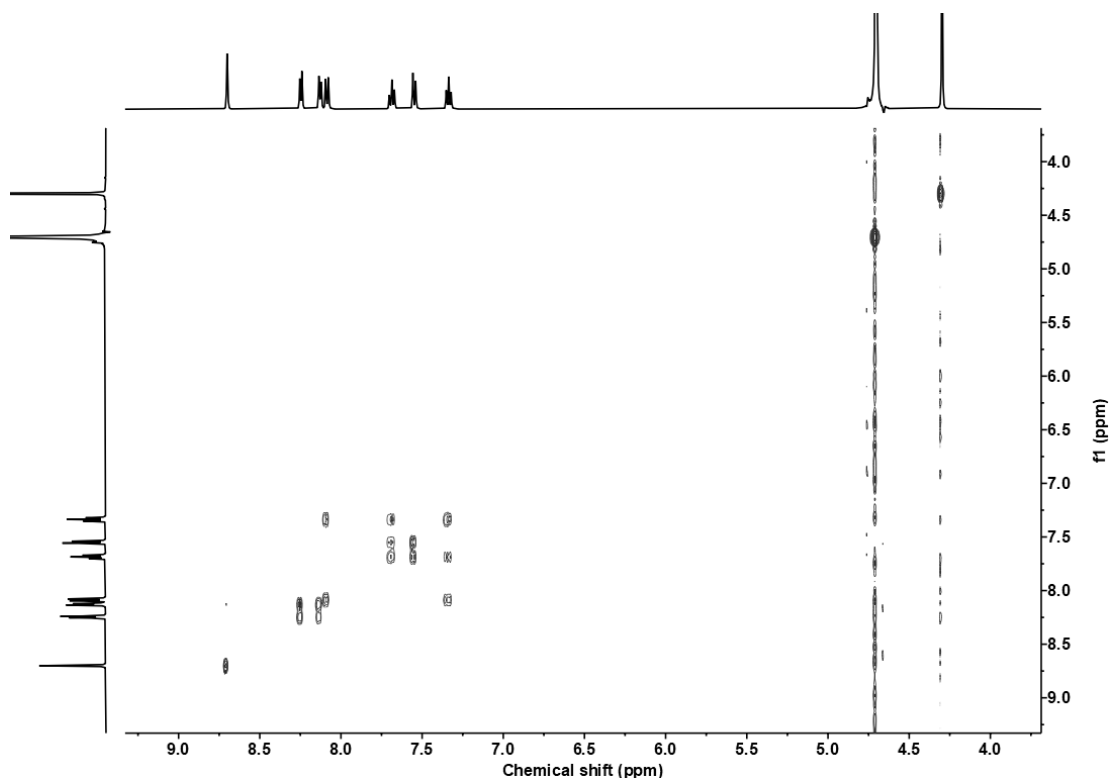
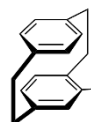


Figure 95. ^1H - ^1H COSY NMR spectra of **34**, D_2O

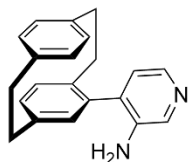
5.4. Modulating and Accelerating Photolysis of [2.2]Paracyclophane Aryl Azide

[2.2]Paracyclophane-4-trifluoroborate (**57**)



[2.2]Paracyclophane-4-trifluoroborate was synthesized according to our previously reported methods. 4-Bromo[2.2]paracyclophane (1.0 g, 35.0 mmol, 1.00 equiv.) was dissolved in anhydrous THF (500 mL). The solution was cooled to $-78\text{ }^\circ\text{C}$, and $n\text{BuLi}$ (2.5 M in hexane, 15.3 mL, 38.4 mmol, 1.10 equiv.) was slowly added. After one hour, triisopropyl borate (12.2 mL, 52.7 mmol, 1.50 equiv.) was added, and the solution was warmed to room temperature. After 16 h, aqueous potassium hydrogen difluoride (4.5 M aq. solution, 46.5 mL, 209 mmol, 6.00 equiv.) was added, and the mixture was vigorously stirred for 3 hours. After removal of the solvents under reduced pressure, the colorless residue was triturated with acetone ($2 \times$ room temperature, $2 \times$ boiling, 100 mL each). The solvent was removed under reduced pressure, and the colorless residue was washed with dichloromethane and diethyl ether (200 mL each) and dried under reduced pressure to yield the title compound (8.25 g, 26.3 mmol, 75%) as a colorless solid.

4-(4'-(3-Amine) pyridyl)[2.2]paracyclophane (**58**)



[2.2]Paracyclophane-4-trifluoroborate (500 mg, 1.59 mmol, 1.00 equiv.), 4-bromopyridin-3-amine (330 mg, 1.91 mmol, 1.20 equiv.), palladium(II) acetate (17.9 mg, 79.6 μmol , 5.0 mol%), potassium phosphate (1.35 g, 6.37 mmol, 4.00 equiv.) and RuPhos (111 mg, 0.239 mmol, 15.0 mol%) were dissolved under argon atmosphere in toluene/water (10:1, 20 mL/2.0

mL). The mixture was heated to 80 °C for 24 h, then diluted with ethyl acetate (20 mL) and ammonium chloride (sat. aq. solution, 20 mL). The phases were separated, and the aqueous layer was extracted with ethyl acetate (2 \times 20 mL). The combined organic layers were dried over sodium sulfate, and the solvent was removed under reduced pressure. The crude solid was purified by flash column chromatography (silica, MeOH/DCM, 1:19) to yield the title compound 4-(4'-(3-amine) pyridyl)[2.2]paracyclophane (314 mg, 1.05 mmol, 66%) as a colorless oil.

^1H NMR (500 MHz, DMSO, ppm) δ = 8.23 (d, J = 5.7 Hz, 1H, H_{Ar}), 8.13 (s, 1H, H_{Ar}), 7.96 (d, J = 5.7 Hz, 1H, H_{Ar}), 6.73–6.61 (m, 6H, H_{Ar}), 6.46 (dd, J = 7.8, 1.9 Hz, 1H, H_{Ar}), 6.08–5.84 (br.s, 2H, NH_2), 3.09 (m, 5H, CH_2), 2.89 (m, 1H, CH_2), 2.81–2.67 (m, 2H, CH_2).

^{13}C NMR (126 MHz, DMSO, ppm) δ = 144.7 (1C, C_{Ar}), 140.8 (1C, C_{Ar}), 139.5 (1C, C_{Ar}), 139.2 (1C, C_{Ar}), 138.0 (1C, C_{Ar}), 136.0 (1C, C_{Ar}), 134.9 (1C, C_{Ar}), 133.4 (1C, C_{Ar}), 132.5 (1C, C_{Ar}), 132.5 (1C, C_{Ar}), 132.2 (1C, C_{Ar}), 132.2 (1C, C_{Ar}), 128.9 (1C, C_{Ar}), 128.5 (1C, C_{Ar}), 127.6 (1C, C_{Ar}), 126.3 (1C, C_{Ar}), 34.7 (2C, CH_2), 34.6 (1C, CH_2), 33.7 (1C, CH_2).

HRESI-MS for $[\text{C}_{22}\text{H}_{21}\text{N}_2]^+$: Calc. m/z = 301.1700, found m/z = 301.1698.

IR (ATR, cm^{-1}) $\tilde{\nu}$ = 3370 (vs), 3360 (vs), 3116 (s), 3090 (s), 3016 (vs), 2923 (vs), 2895 (vs), 2852 (vs), 1637 (vs), 1591 (m), 1563 (m), 1516 (s), 1500 (m), 1460 (m), 1456 (m), 1197 (m), 847 (m), 718 (m), 640 (m), 486 (m) cm^{-1} .

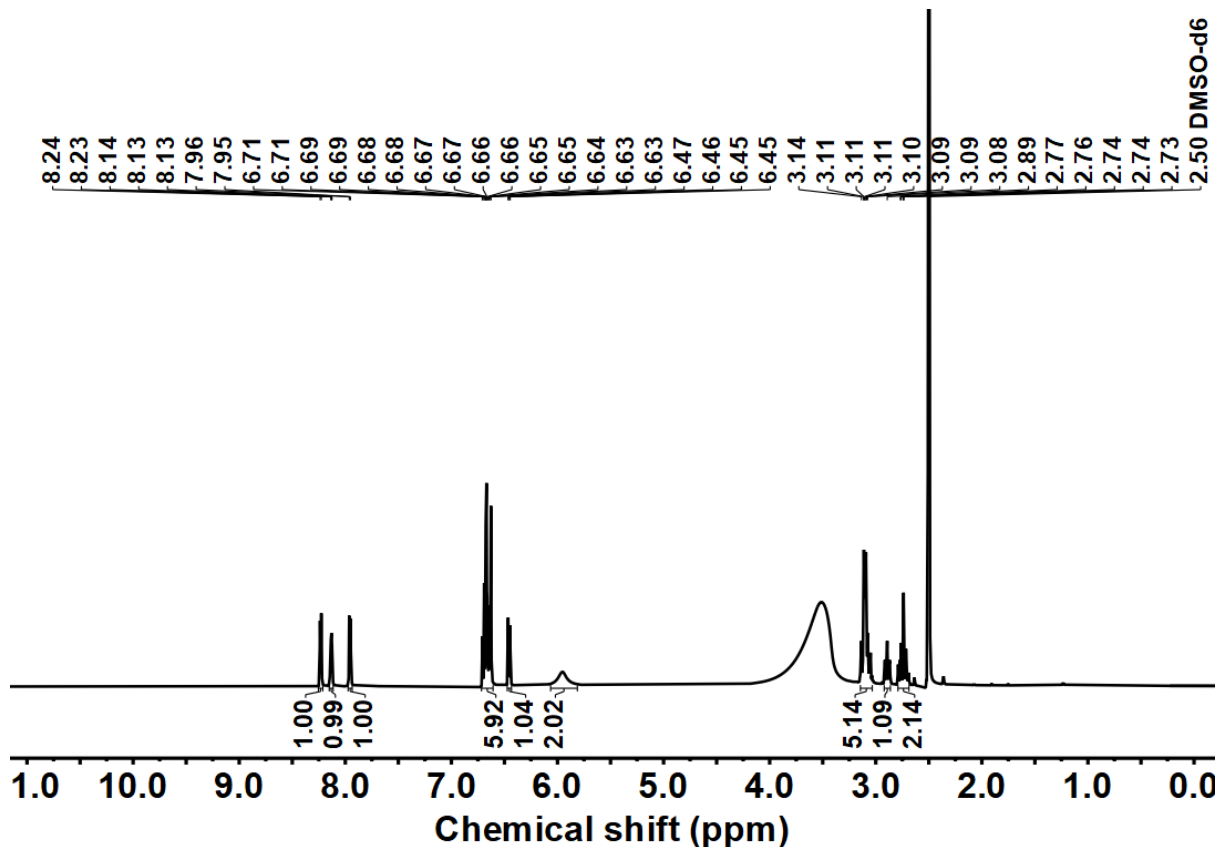


Figure 96. ^1H NMR spectra of 58, 500 MHz, CDCl_3 .

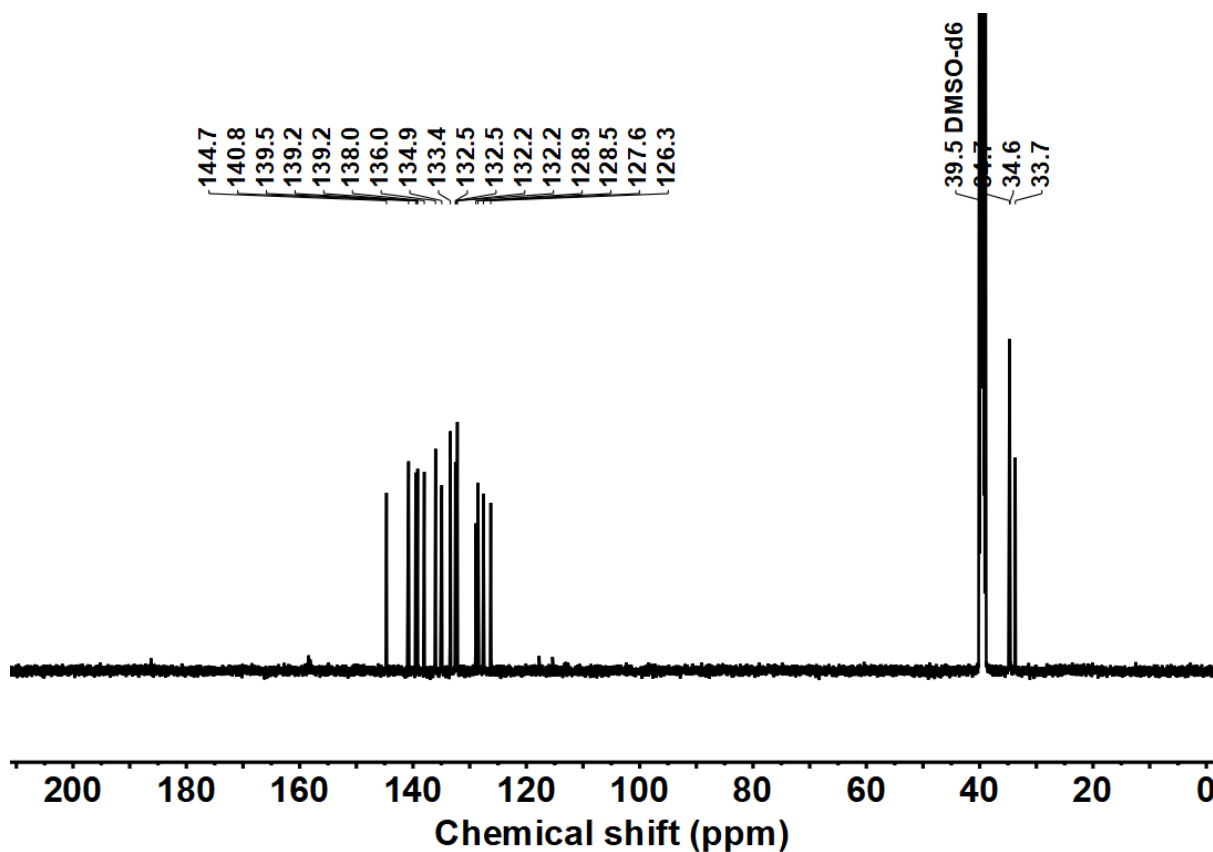
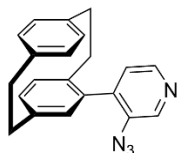


Figure 97. ^{13}C NMR spectra of **58**, 126 MHz, CDCl_3 .

4-(4'-(3-Azido)pyridyl)[2.2]paracyclophane (**59**)



Azide was synthesized according to our previously reported methods. *p*-Toluenesulfonic acid monohydrate (190 mg, 1.00 mmol, 1.50 equiv.) was dissolved in acetonitrile/water (16/4.0 mL) at 25 °C. Once dissolved, *tert*-butyl nitrite (103 mg, 1.00 mmol, 1.50 equiv.) was added, followed by the portion-wise addition of 4-(4'-(3-amine) pyridyl)[2.2]paracyclophane (0.20 g, 0.67 mmol, 1.00 equiv.). The reaction mixture was stirred for 3h at 25 °C, and then, a sodium azide (130 mg, 2.00 mmol, 3.00 equiv.) in water (5.0 mL) was added dropwise. The resulting reaction mass was stirred for another 3 hours at 25 °C. After the complete conversion, the reaction mixture was extracted with ethyl acetate (3 × 20 ml). The combined organic layers were dried over sodium sulfate. After the removal of the solvent, the crude solid was purified by chromatography (EtOAc: DCM=1:1), yielding 4-(4'-(3-azido)pyridyl)[2.2]paracyclophane (189 mg, 0.58 mmol, 87%) as a pear color solid.

^1H NMR (500 MHz, CDCl_3 , ppm) δ = 8.58 (d, J = 4.9 Hz, 1H, H_{Ar}), 8.55 (s, 1H, H_{Ar}), 7.52 (d, J = 4.9 Hz, 1H, H_{Ar}), 6.67 (d, J = 7.8 Hz, 1H, H_{Ar}), 6.62 (d, J = 7.8 Hz, 1H, H_{Ar}), 6.59 (s, 2H, H_{Ar}), 6.51 (m, 3H, H_{Ar}), 3.20–3.03 (m, 5H, CH_2), 2.91 (m, 2H, CH_2), 2.78 (m, 1H, CH_2).

^{13}C NMR (126 MHz, CDCl_3 , ppm) δ = 146.5 (1C, C_{Ar}), 141.4 (1C, C_{Ar}), 140.5 (1C, C_{Ar}), 140.0 (1C, C_{Ar}), 139.8 (1C, C_{Ar}), 139.7 (1C, C_{Ar}), 139.3 (1C, C_{Ar}), 135.1 (1C, C_{Ar}), 134.9 (1C, C_{Ar}), 134.6 (1C, C_{Ar}), 133.9 (1C, C_{Ar}), 133.5 (1C, C_{Ar}), 132.7 (1C, C_{Ar}), 132.3 (1C, C_{Ar}), 132.3 (1C, C_{Ar}), 129.7 (1C, C_{Ar}), 125.2 (1C, C_{Ar}), 35.6 (1C, CH_2), 35.4 (1C, CH_2), 35.3 (1C, CH_2), 34.3 (1C, CH_2).

HRESI-MS for $[\text{C}_{21}\text{H}_{19}\text{N}_4]^+$: Calc. m/z = 327.1605, found m/z = 327.1602.

IR (ATR, cm^{-1}) $\tilde{\nu}$ = 3474 (s), 3325 (s), 3032 (vs), 3023 (vs), 3010 (vs), 2980 (s), 2958 (vs), 2931 (vs), 2897 (vs), 2890 (vs), 2854 (vs), 2132 (vs), 2115 (vs), 2107 (vs), 1584 (vs), 1500 (vs), 1494 (vs), 1410 (vs), 1307 (vs), 1292 (vs), 839 (vs), 407 (vs) cm^{-1} .

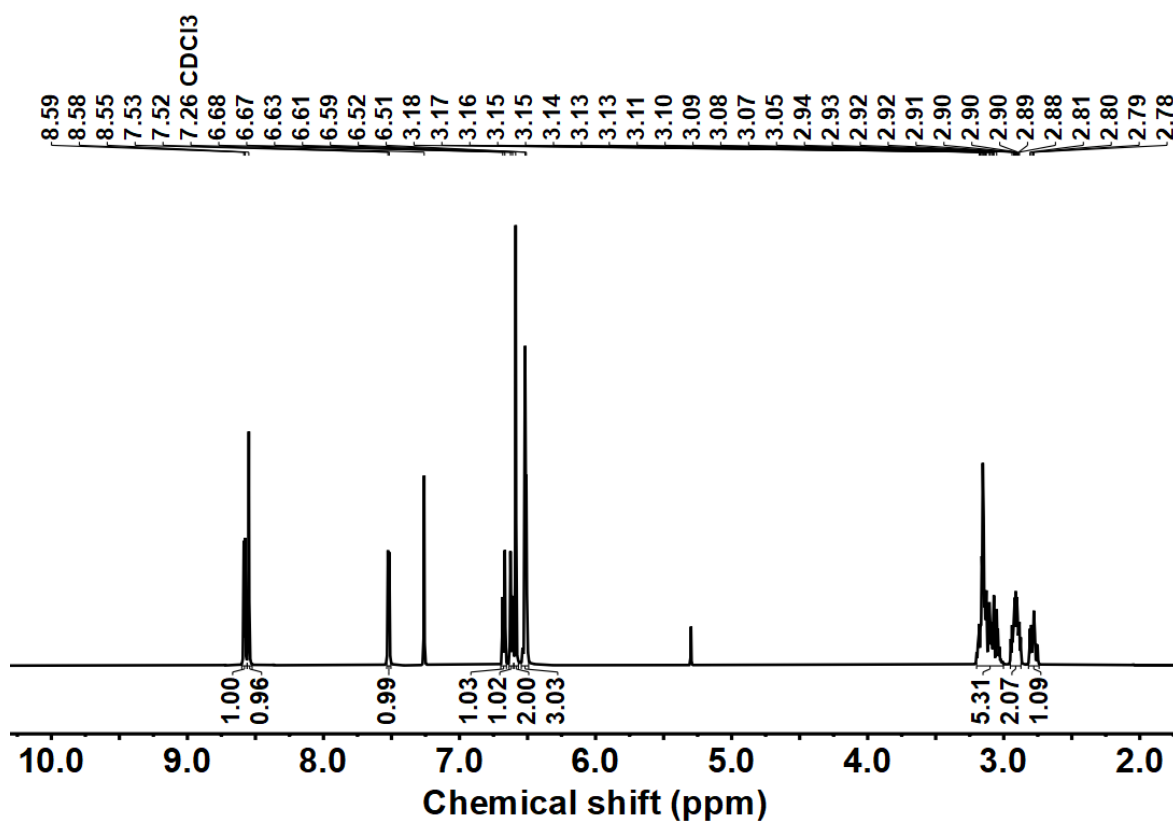


Figure 98. ^1H NMR spectra of **59**, 500 MHz, CDCl_3 .

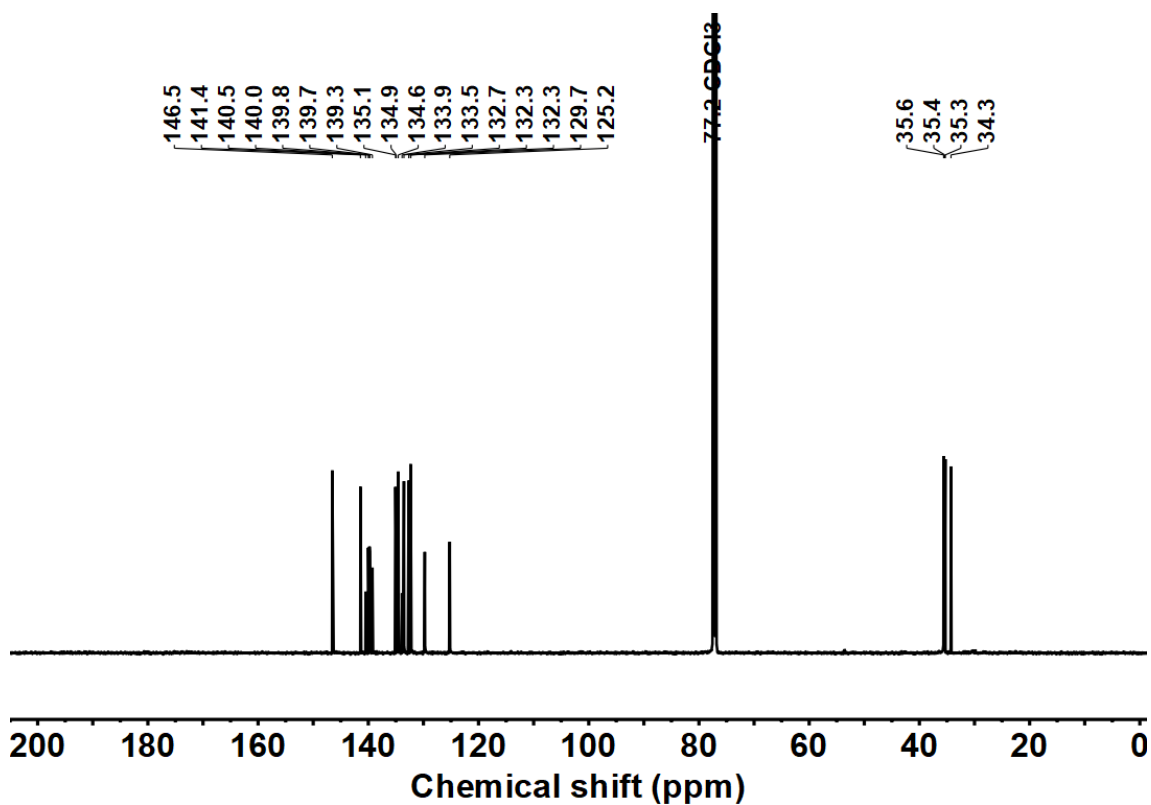
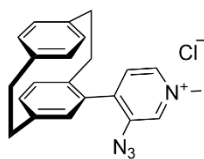


Figure 99. ^{13}C NMR spectra of **59**, 126 MHz, CDCl_3 .

N-methyl-4-(4'-(3-azido)pyridyl)[2.2]paracyclophane chloride (**35**)



4-(4'-(3-Azido)pyridyl)[2.2]paracyclophane (150 mg, 0.46 mmol, 1.00 equiv.) was dissolved in acetonitrile (10 mL), and methyl iodide (97.9 mg, 1.5 mmol, 1.50 equiv.) was added dropwise at 25 °C with stirring. The resulting reaction mixture was left for 16 h at 40 °C. The precipitate was collected by filtration and washed with acetonitrile. After dissolving in 10 mL water, ammonium hexafluorophosphate (375 mg, 2.30 mmol, 5.00 equiv.) was added, which resulted in a precipitate. The precipitate was collected by filtration, washed with water, and dried. After dissolving the solid in 10 mL acetonitrile, tetrabutylammonium chloride (639 mg, 2.30 mmol, 5.00 equiv.) was added, which resulted in a precipitate. The precipitate was collected by filtration, washed with acetonitrile and acetone, and dried. The desired product *N*-methyl-4-(4'-(3-azido)pyridyl)[2.2]paracyclophane chloride was obtained as a pear color solid (141 mg, 0.37 mmol, 81%).

^1H NMR (500 MHz, D_2O , ppm) δ = 8.81 (s, 1H, H_{Ar}), 8.68 (dd, J = 6.3, 1.5 Hz, 1H, H_{Ar}), 8.23 (d, J = 6.3 Hz, 1H, H_{Ar}), 6.86–6.68 (m, 6H, H_{Ar}), 6.55 (dd, J = 7.9, 1.9 Hz, 1H, H_{Ar}), 4.43 (s, 3H, CH_3), 3.26–3.07 (m, 5H, CH_2), 2.94 (m, 2H, CH_2), 2.73 (m, 1H, CH_2).

^{13}C NMR (126 MHz, D_2O , ppm) δ = 147.7 (1C, C_{Ar}), 141.3 (1C, C_{Ar}), 140.8 (1C, C_{Ar}), 140.7 (1C, C_{Ar}), 140.3 (1C, C_{Ar}), 140.1 (1C, C_{Ar}), 139.5 (1C, C_{Ar}), 136.5 (1C, C_{Ar}), 136.3 (1C, C_{Ar}), 135.5 (1C, C_{Ar}), 133.8 (1C, C_{Ar}), 132.9 (1C, C_{Ar}), 132.4 (1C, C_{Ar}), 132.0 (1C, C_{Ar}), 131.1 (1C, C_{Ar}), 129.2 (1C, C_{Ar}), 128.8 (1C, C_{Ar}), 47.7 (1C, CH_3), 34.6 (1C, CH_2), 34.5 (1C, CH_2), 34.4 (1C, CH_2), 33.8 (1C, CH_2).

HRESI-MS for $[\text{C}_{22}\text{H}_{21}\text{N}_4]^+$: Calc. m/z = 341.1761, found m/z = 341.1758.

IR (ATR, cm^{-1}) $\tilde{\nu}$ = 3408 (w), 3403 (w), 3397 (w), 3370 (w), 2980 (s), 2937 (s), 2922 (vs), 2851 (m), 2122 (vs), 1638 (m), 1517 (m), 1502 (m), 1495 (m), 1472 (w), 1331 (vs), 1290 (w), 851 (w) cm^{-1} .

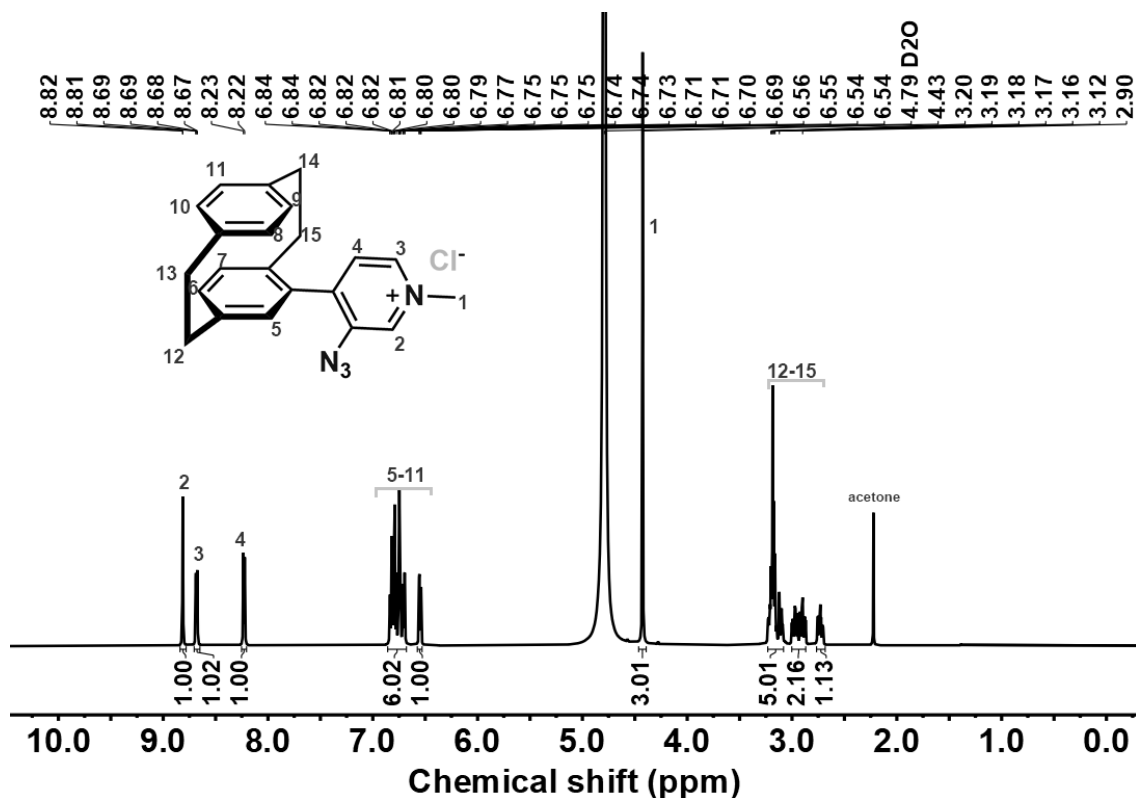


Figure 100. ^1H NMR spectra of **35**, 500 MHz, D_2O .

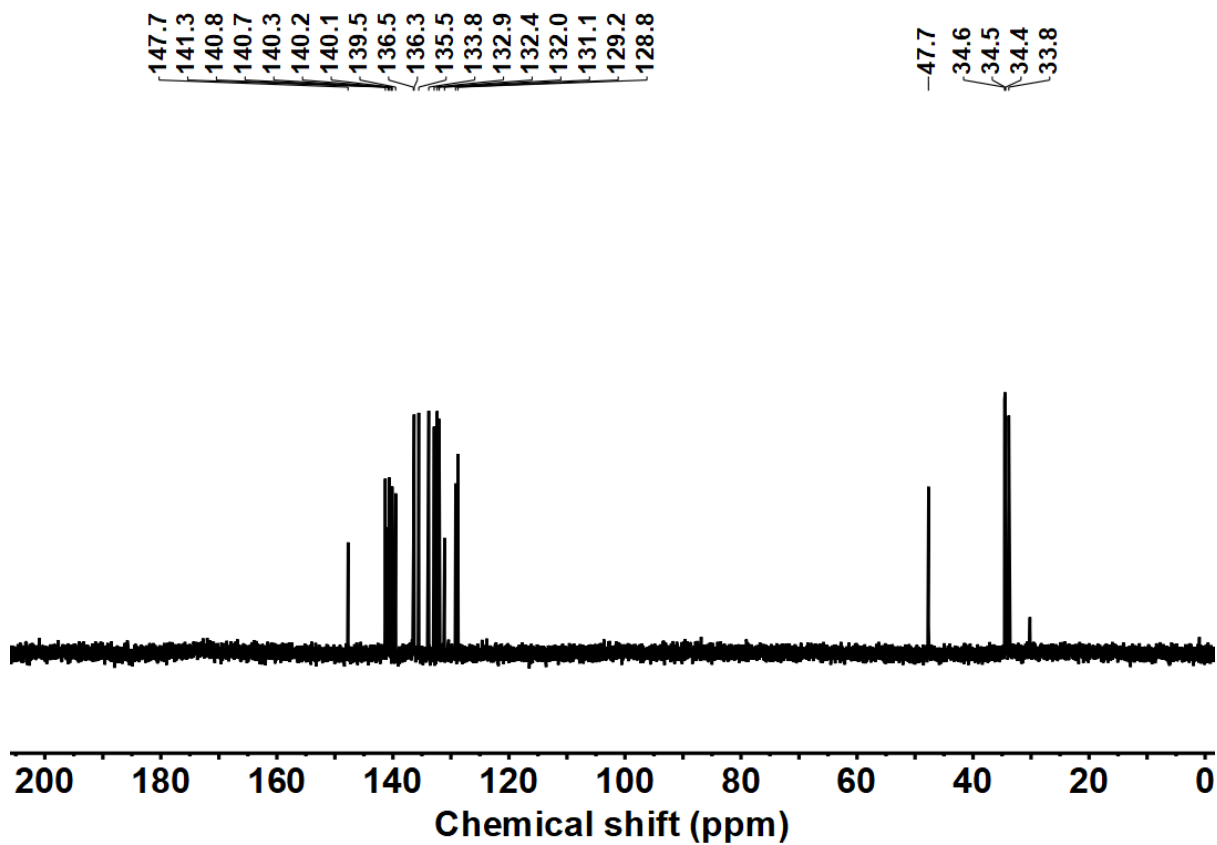


Figure 101. ^{13}C NMR spectra of **35**, 126 MHz, D_2O .

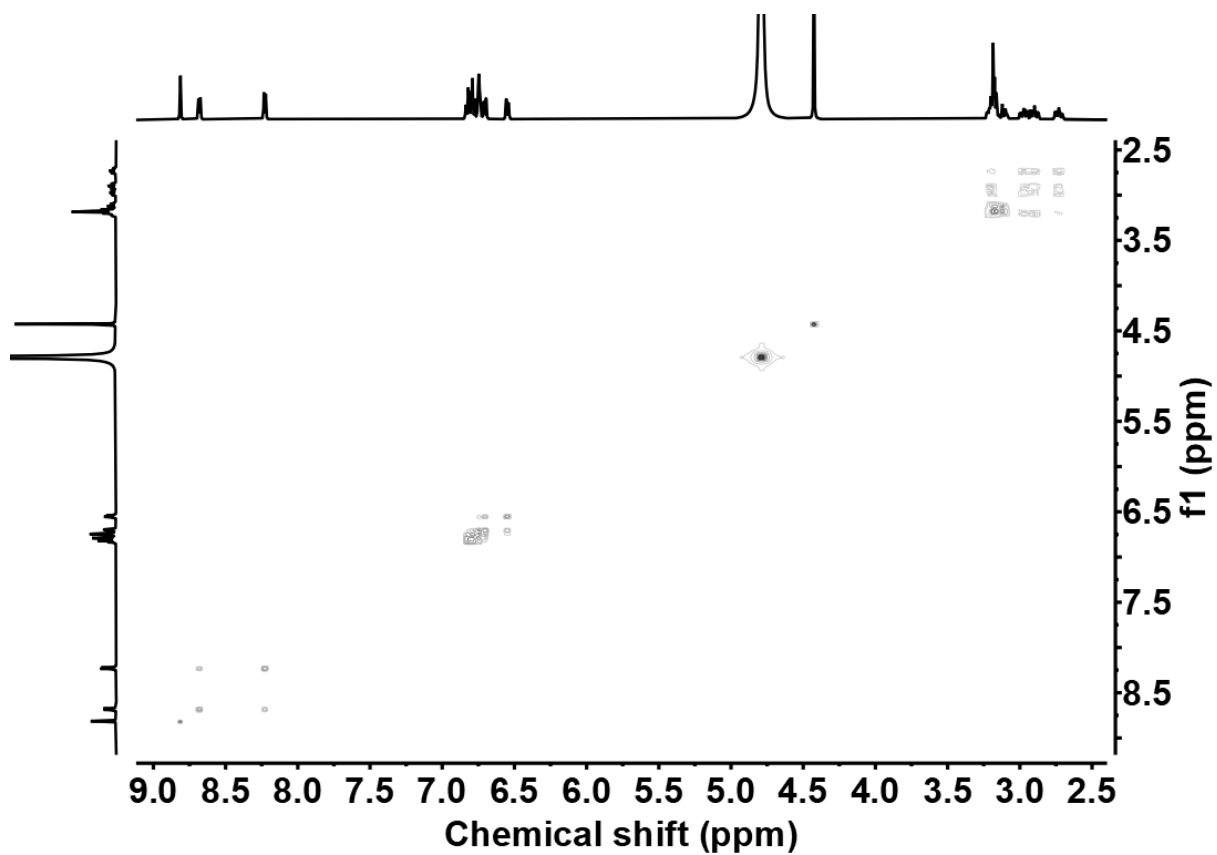
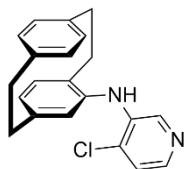


Figure 102. ^1H - ^1H COSY NMR spectra of **35**, D_2O .

4-*N*-(4-chloro-pyridin-3-yl)amino[2.2]paracyclophane (**61**)



In a sealable vial under an inert atmosphere, 4-bromo[2.2]paracyclophane (0.50 g, 1.74 mmol, 1.00 equiv.), XPhos (83.0 mg, 0.17 mmol, 10 mol%), Pd₂(dba)₃ (159 mg, 0.17 mmol, 10 mol%) and NaOtBu (0.50 g, 5.22 mmol, 3.00 equiv.) were dissolved in 20 mL of toluene and 4-chloropyridin-3-amine (269 mg, 2.09 mmol, 1.20 equiv.) was added. After stirring at 105 °C for 16 h, the reaction mixture was diluted with ethyl acetate (150 mL), washed with brine, and dried over Na₂SO₄. After the removal of the solvent, the crude was purified by column chromatography (ethyl acetate/dichloromethane 2:3) to obtain the title compound 4-*N*-(4-chloro-pyridin-3-yl)amino[2.2]paracyclophane (0.26 g, 0.78 mmol, 45%) as a pear color solid.

¹H NMR (500 MHz, DMSO, ppm) δ = 8.37 (s, 1H, H_{Ar}), 8.04 (d, *J* = 5.6 Hz, 1H, H_{Ar}), 7.81 (s, 1H, NH), 6.94 (dd, *J* = 7.7, 1.9 Hz, 1H, H_{Ar}), 6.63–6.44 (m, 6H, H_{Ar}), 6.28 (d, *J* = 1.7 Hz, 1H, H_{Ar}), 3.05–2.82 (m, 5H, CH₂), 2.78–2.63 (m, 3H, CH₂).

¹³C NMR (126 MHz, DMSO, ppm) δ = 148.7 (1C, C_{Ar}), 148.2 (1C, C_{Ar}), 146.6 (1C, C_{Ar}), 141.2 (1C, C_{Ar}), 138.9 (1C, C_{Ar}), 138.6 (1C, C_{Ar}), 137.1 (1C, C_{Ar}), 135.8 (1C, C_{Ar}), 133.3 (1C, C_{Ar}), 133.0 (1C, C_{Ar}), 132.6 (1C, C_{Ar}), 132.2 (1C, C_{Ar}), 129.5 (1C, C_{Ar}), 128.6 (1C, C_{Ar}), 128.1 (1C, C_{Ar}), 117.0 (1C, C_{Ar}), 108.3 (1C, C_{Ar}), 34.7 (1C, CH₂), 34.4 (1C, CH₂), 33.7 (1C, CH₂), 33.4 (1C, CH₂).

HRESI-MS for [C₂₁H₂₀ClN₂]⁺: Calc. *m/z* = 335.1310, found *m/z* = 335.1301.

IR (ATR, cm⁻¹) $\tilde{\nu}$ = 3400 (m), 3394 (m), 3230 (m), 3222 (m), 3217 (m), 3032 (m), 3019 (m), 3009 (m), 2951 (m), 2925 (s), 2891 (m), 2852 (s), 1588 (vs), 1560 (s), 1508 (s), 1492 (vs), 1406 (s), 1335 (s), 1030 (m) cm⁻¹.

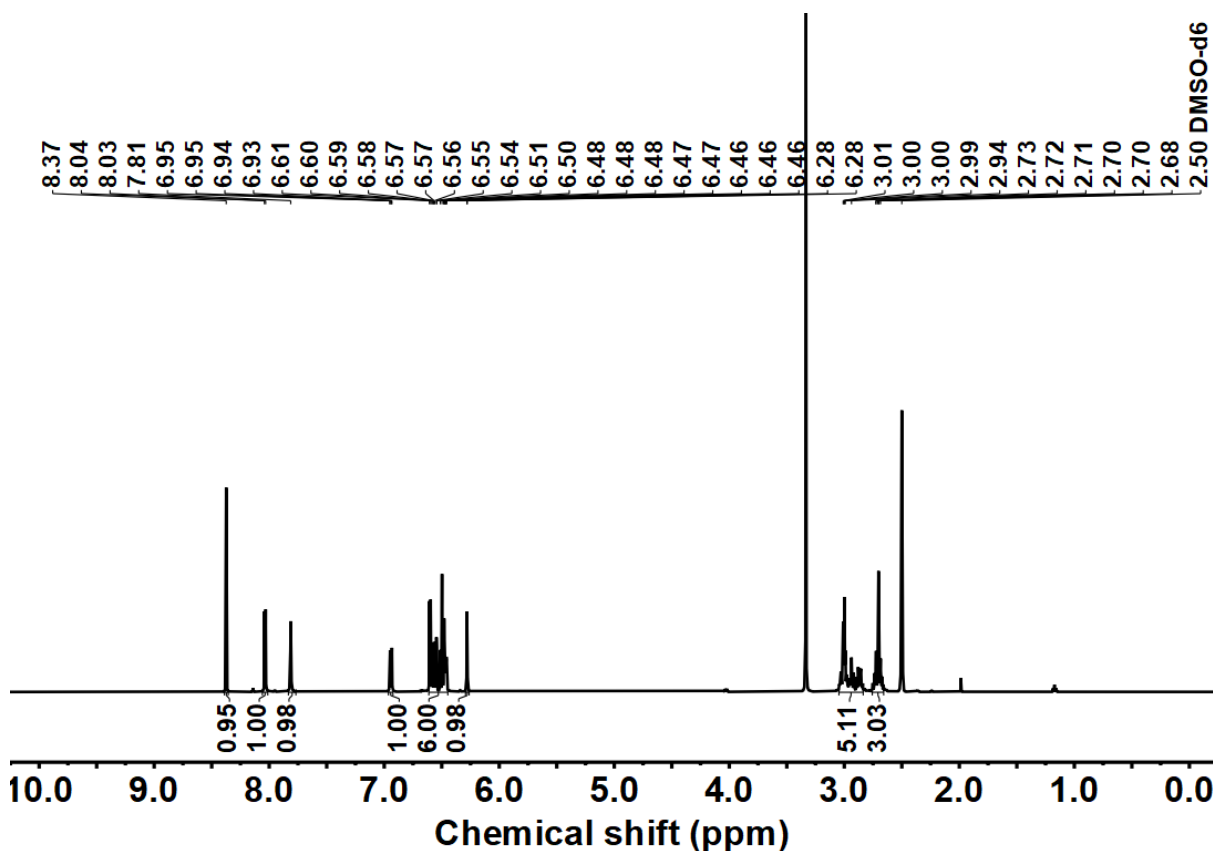


Figure 103. ¹H NMR spectra of **61** 500 MHz, CDCl₃.

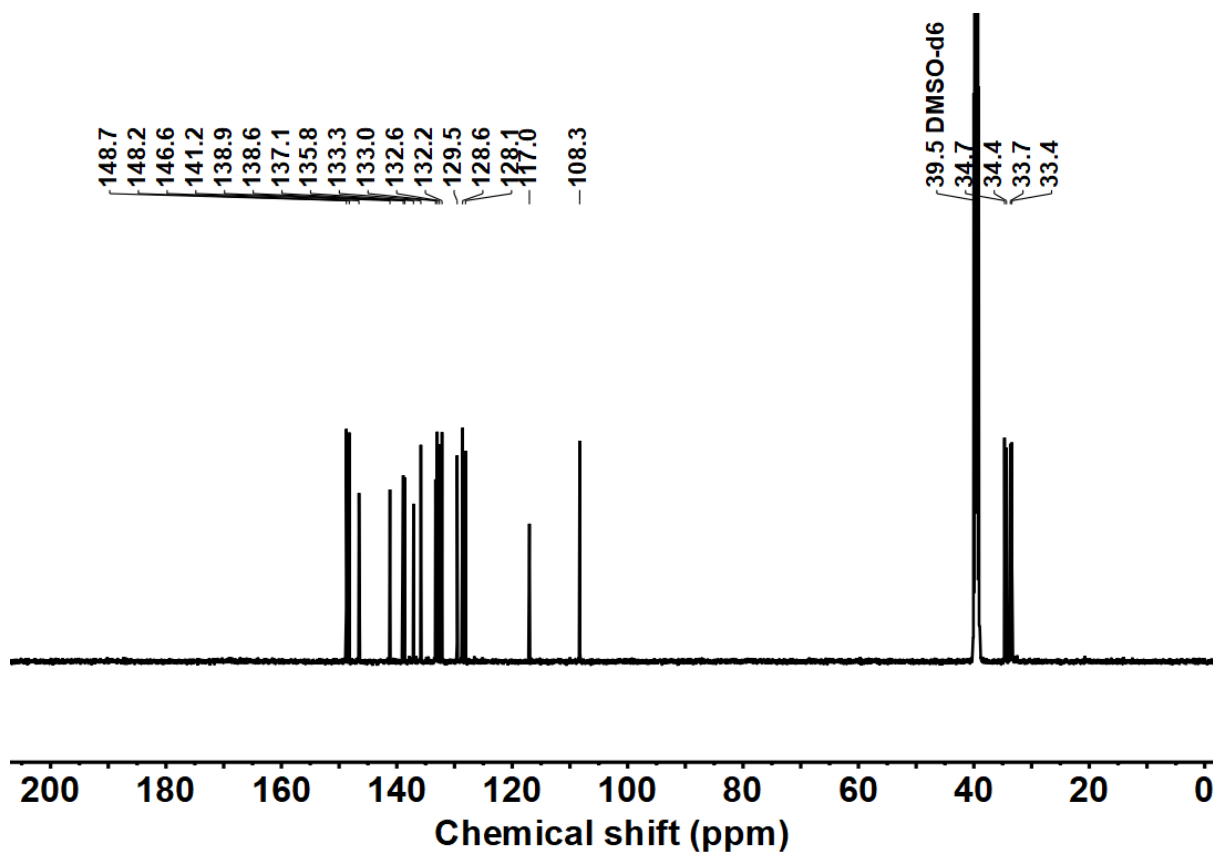
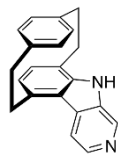


Figure 104. ^{13}C NMR spectra of **61**, 126 MHz, CDCl_3 .

[2]Paracyclo[2](6,9)- β -carbolinophane (62**)**



A sealable vial was charged with N-methyl-4-(4'-(3-azido) pyridyl)[2.2]paracyclophane chloride (200 mg, 0.60 mmol, 1.00 equiv.), palladium(II)acetate (13.4 mg, 0.06 mmol, 10 mol%), potassium carbonate (165 mg, 1.20 mmol, 2.00 equiv.), $(t\text{-Bu})_3\text{P}$ (24.2 mg, 0.12 mmol, 0.20 equiv.). Under an inert atmosphere, 15 mL of anhydrous DMF was added, and the orange reaction mixture was stirred at 120 °C for 24 h. The mixture was cooled to room temperature, diluted with ethyl acetate (100 mL), and washed with water (100 mL). The aqueous phase was extracted with ethyl acetate (2×75 mL), and the combined organic phases were washed with brine (100 mL) and dried over Na_2SO_4 . The crude was purified by column chromatography (MeOH/DCM = 1:4) to obtain the titled product [2]paracyclo[2](6,9)- β -carbolinophane as a pear color solid (113 mg, 0.38 mmol, 63 %)

^1H NMR (500 MHz, DMSO, ppm) δ = 11.45 (s, 1H, NH), 8.91 (s, 1H, H_{Ar}), 8.33 (d, $J = 5.3$ Hz, 1H, H_{Ar}), 8.00 (d, $J = 5.3$ Hz, 1H, H_{Ar}), 6.73 (d, $J = 7.4$ Hz, 1H, H_{Ar}), 6.56 (d, $J = 7.3$ Hz, 1H, H_{Ar}), 6.46 (dd, $J = 7.7, 1.9$ Hz, 1H, H_{Ar}), 6.34 (dd, $J = 7.7, 1.9$ Hz, 1H, H_{Ar}), 5.77–5.72 (m, 1H, H_{Ar}), 4.95 (dd, $J = 7.7, 1.9$ Hz, 1H, H_{Ar}), 3.99–3.89 (m, 1H, 1H, CH_2), 3.59–3.49 (m, 1H, 1H, CH_2), 3.13–3.00 (m, 2H, 1H, CH_2), 3.00–2.92 (m, 3H, 1H, CH_2), 2.85–2.71 (m, 1H, 1H, CH_2).

^{13}C NMR (126 MHz, DMSO, ppm) δ = 141.5 (1C, C_{Ar}), 138.2 (1C, C_{Ar}), 137.5 (1C, C_{Ar}), 137.0 (1C, C_{Ar}), 136.4 (1C, C_{Ar}), 135.4 (1C, C_{Ar}), 134.2 (1C, C_{Ar}), 133.0 (1C, C_{Ar}), 132.1 (1C, C_{Ar}), 131.5 (1C, C_{Ar}), 128.8 (1C, C_{Ar}), 125.9 (1C, C_{Ar}), 125.4 (1C, C_{Ar}), 124.2 (1C, C_{Ar}), 123.5 (1C, C_{Ar}), 123.0 (1C, C_{Ar}), 116.0 (1C, C_{Ar}), 33.3 (1C, CH_2), 32.9 (2C, CH_2), 30.6 (1C, CH_2).

HRESI-MS for $[C_{21}H_{19}N_2]^+$: Calc. $m/z = 299.1543$, found $m/z = 299.1535$.

IR (ATR, cm^{-1}) $\tilde{\nu} = 3194$ (vs), 3191 (vs), 3165 (vs), 3158 (vs), 3144 (vs), 3138 (vs), 3106 (vs), 3067 (vs), 3036 (vs), 3022 (vs), 3008 (vs), 2992 (vs), 2953 (vs), 2932 (vs), 2923 (vs), 2893 (vs), 2851 (vs), 2303 (vs), 1605 (vs), 1449 (vs), 1334 (vs), 1273 (vs), 1250 (vs) cm^{-1}

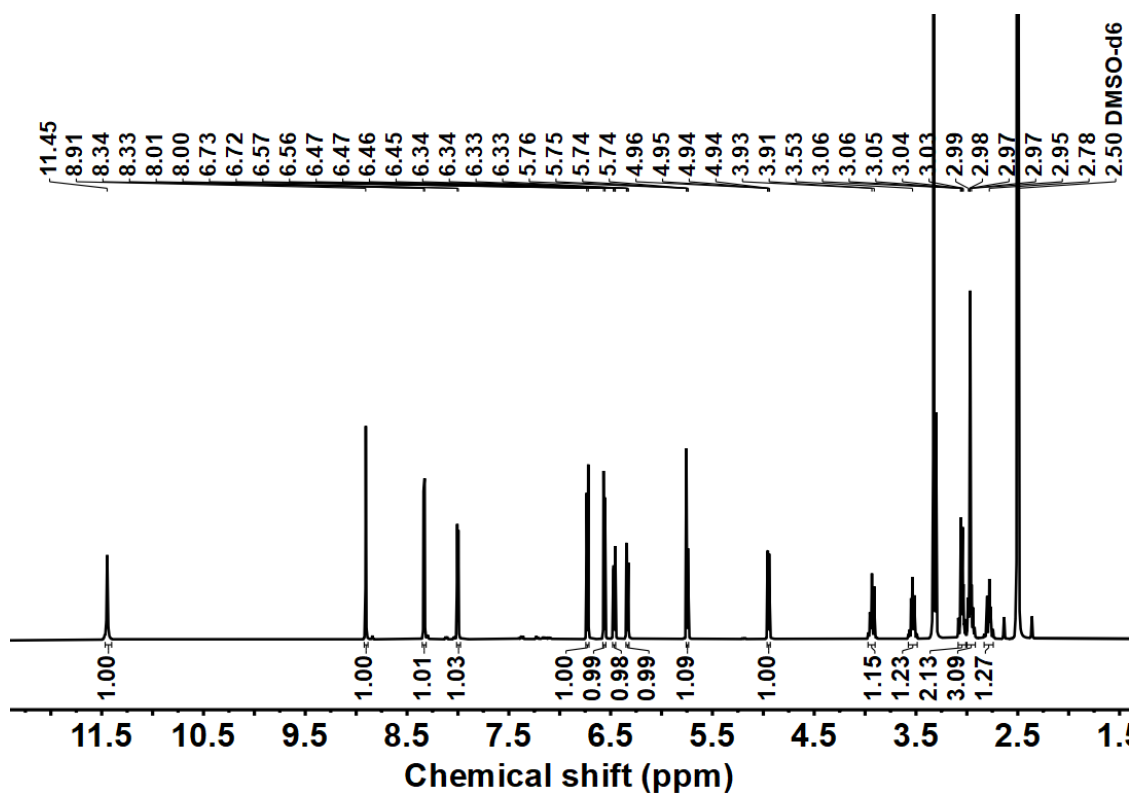


Figure 105. 1H NMR spectra of **62**, 500 MHz, $CDCl_3$.

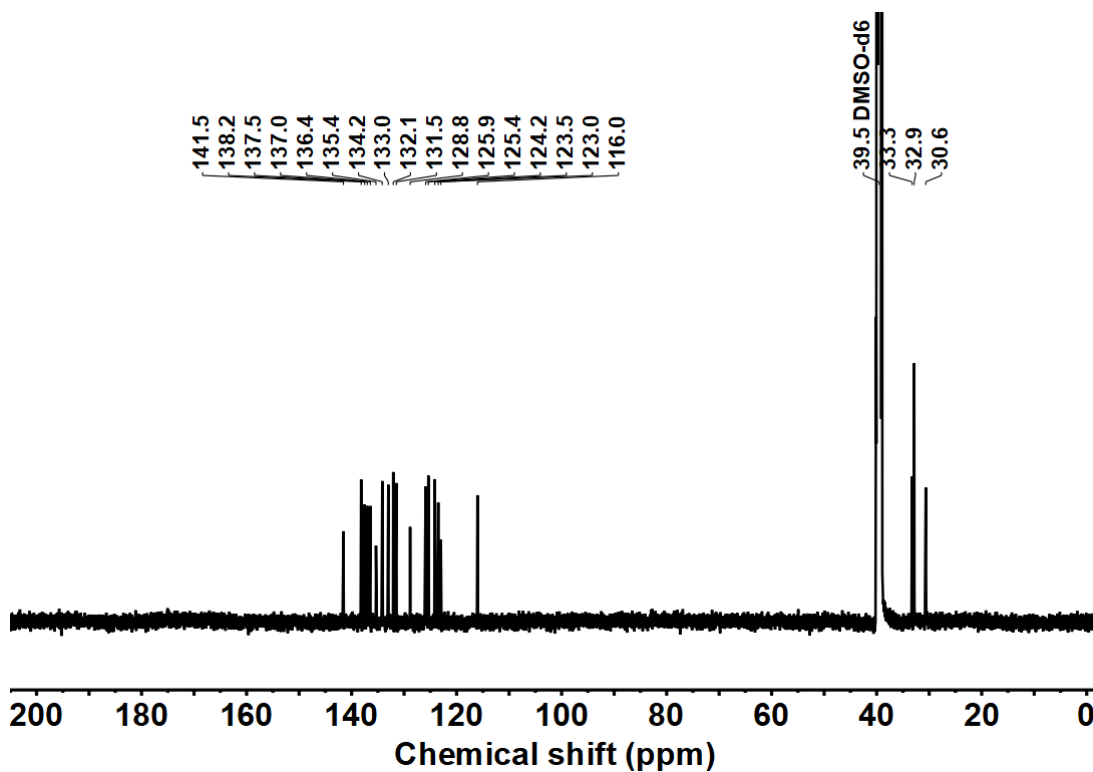
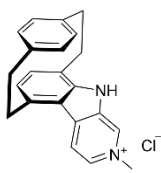


Figure 106. ^{13}C NMR spectra of **62**, 126 MHz, $CDCl_3$.

***N*-methyl-4-[2]paracyclo[2](6,9)- β -carbolinophane (60)**



[2]Paracyclo[2](6,9)- β -carbolinophane (100 mg, 0.34 mmol, 1.00 equiv.) was dissolved in acetonitrile (10 mL), and methyl iodide (71.4 mg, 0.50 mmol, 1.50 equiv.) was added dropwise at 25 °C with stirring. The resulting reaction mixture was left for 16 h at 40 °C. The precipitate was collected by filtration and washed with acetonitrile. After dissolving in 10 mL water, ammonium hexafluorophosphate (273 mg, 1.68 mmol, 5.00 equiv.) was added, which resulted in a precipitate. The precipitate was collected by filtration, washed with water, and dried. After dissolving the solid in 10 mL acetonitrile, tetrabutylammonium chloride (466 mg, 1.68 mmol, 5.00 equiv.) was added, which resulted in a precipitate. The precipitate was collected by filtration, washed with acetonitrile and acetone, and dried. The desired product *N*-methyl-4-[2]paracyclo[2](6,9)- β -carbolinophane was obtained as a yellow solid (91 mg, 0.26 mmol, 78%).

^1H NMR (500 MHz, D_2O , ppm) δ = 8.74 (s, 1H, H_{Ar}), 8.28 (d, J = 6.5 Hz, 1H, H_{Ar}), 8.21 (dd, J = 6.6, 1.4 Hz, 1H, H_{Ar}), 7.02 (d, J = 7.4 Hz, 1H, H_{Ar}), 6.83 (d, J = 7.4 Hz, 1H, H_{Ar}), 6.58 (dd, J = 7.8, 2.0 Hz, 1H, H_{Ar}), 6.44 (dd, J = 7.8, 1.9 Hz, 1H, H_{Ar}), 5.81 (dd, J = 7.8, 1.9 Hz, 1H, H_{Ar}), 5.05 (dd, J = 7.8, 1.9 Hz, 1H, H_{Ar}), 4.38 (s, 3H, CH_3), 3.86–3.76 (m, 1H, CH_2), 3.46–3.37 (m, 1H, CH_2), 3.23–3.04 (m, 4H, CH_2), 3.01–2.91 (m, 1H, CH_2), 2.84–2.73 (m, 1H, CH_2).

^{13}C NMR (126 MHz, D_2O , ppm) δ = 145.0 (1C, C_{Ar}), 138.6 (1C, C_{Ar}), 138.5 (1C, C_{Ar}), 138.0 (1C, C_{Ar}), 137.0 (1C, C_{Ar}), 133.9 (1C, C_{Ar}), 133.0 (1C, C_{Ar}), 132.9 (1C, C_{Ar}), 132.5 (1C, C_{Ar}), 132.4 (1C, C_{Ar}), 128.9 (1C, C_{Ar}), 128.3 (1C, C_{Ar}), 126.2 (1C, C_{Ar}), 124.7 (1C, C_{Ar}), 124.7 (1C, C_{Ar}), 121.6 (1C, C_{Ar}), 118.4 (1C, C_{Ar}), 47.3 (1C, CH_3), 32.8 (1C, CH_2), 32.4 (1C, CH_2), 32.4 (1C, CH_2), 30.2 (1C, CH_2).

HRESI-MS for $[\text{C}_{22}\text{H}_{21}\text{N}_2]^+$: Calc. m/z = 313.1700, found m/z = 313.1696.

IR (ATR, cm^{-1}) $\tilde{\nu}$ = 3330 (vs), 3233 (vs), 3135 (vs), 3067 (vs), 3016 (vs), 2928 (vs), 2859 (vs), 2797 (s), 2758 (s), 2697 (m), 2679 (m), 1650 (m), 1645 (m), 1595 (s), 1528 (m), 1481 (m), 1325 (m), 1315 (m) cm^{-1} .

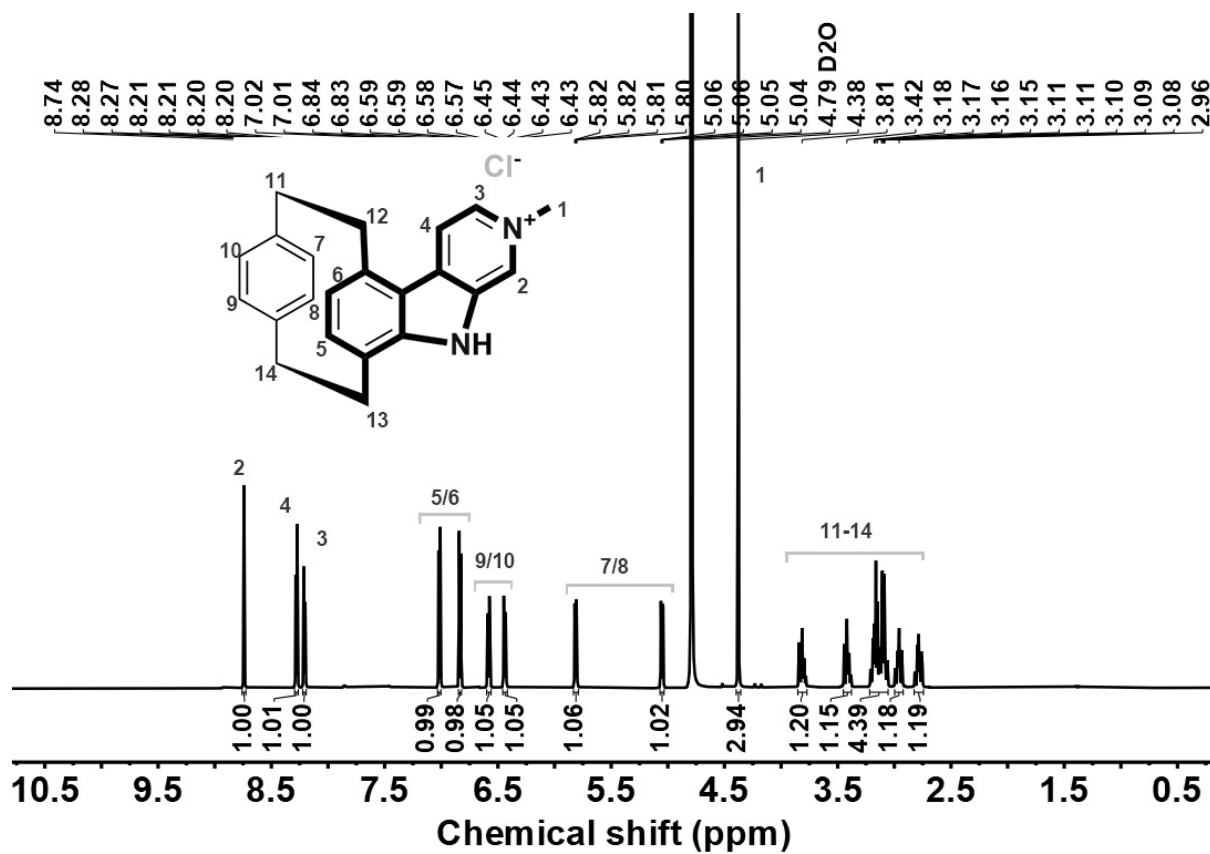


Figure 107. ¹H NMR spectra of **60**, 500 MHz, D₂O.

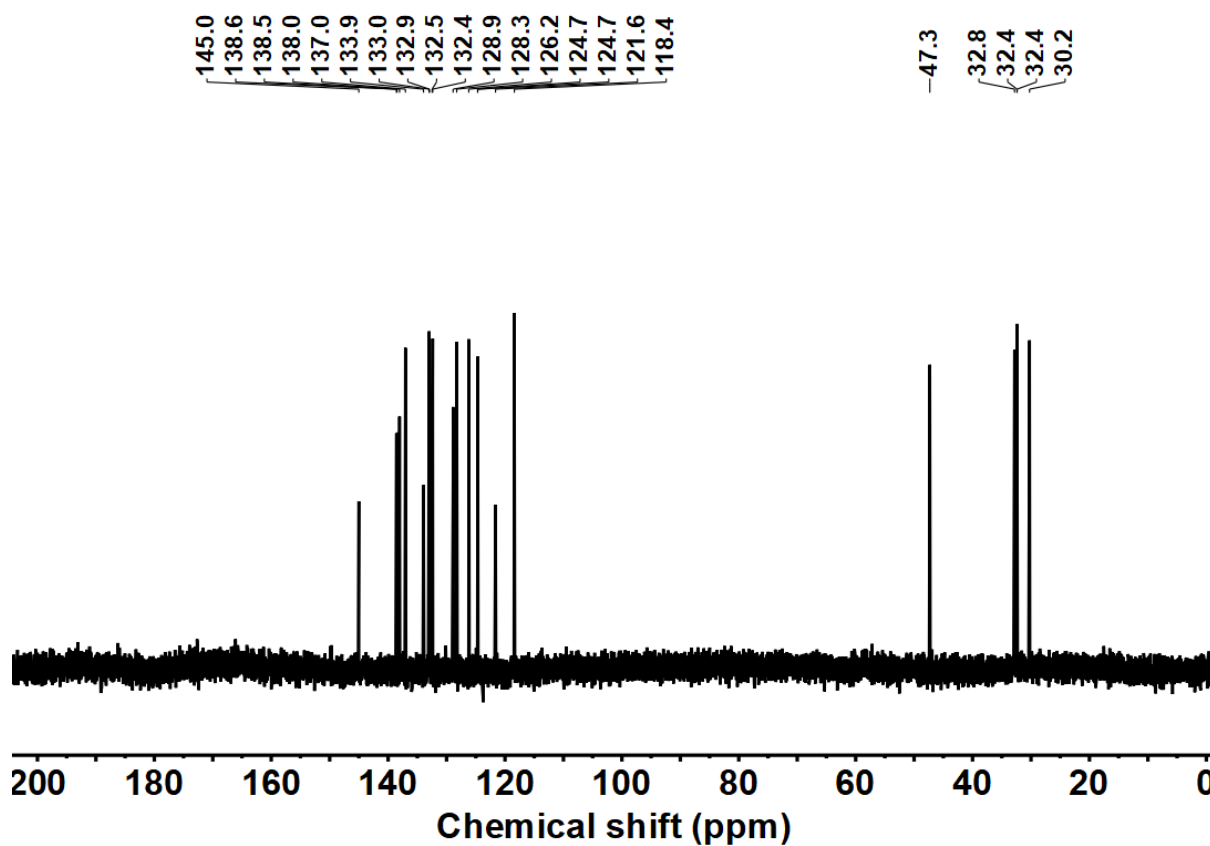


Figure 108. ¹³C NMR spectra of **60**, 126 MHz, D₂O.

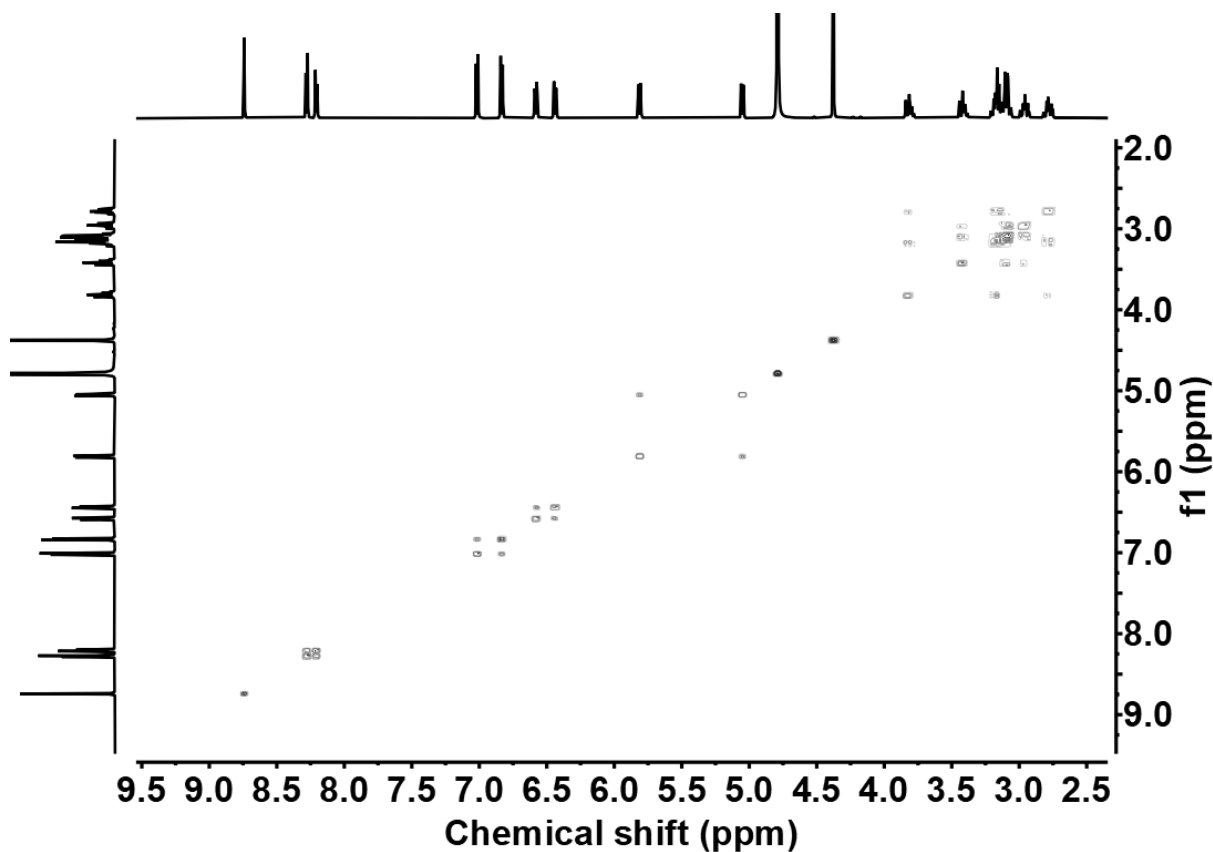


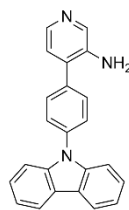
Figure 109. ^1H - ^1H COSY NMR spectra of **60**, D_2O

5.5. Modulating the Photolysis of Aryl Azides for Bioimaging

General procedure for Suzuki coupling:

To a 50 mL reaction vial, (3.00 mmol, 1.00 equiv.) boronic acid derivatives, (0.623 g, 3.60 mmol, 1.20 equiv.) 4-bromopyridin-3-amine, (0.173 g, 0.150 mmol, 0.05 equiv.) tetrakis(triphenylphosphine)palladium(0), and (0.955 g, 4.50 mmol, 1.50 equiv.) tripotassium phosphate were dissolved in the 1,4-dioxane (20 mL) and water (5 mL) mixture. After degassing and charging with inert gas, the reaction mixtures were at 105 °C for 16 hours. After cooling, the reaction mixture was suspended in a 1.5 N aqueous solution of NaOH (20 mL) and CH_2Cl_2 (30 mL). The aqueous phase was extracted with CH_2Cl_2 (3 × 30 mL). The combined organic phases were dried over Na_2SO_4 and evaporated under reduced pressure. After purifying by column chromatography using DCM/MeOH 19:1, the pyridine aniline products were obtained.

4-(4-(9H-carbazol-9-yl)phenyl)pyridin-3-amine (**67**)



Brown paste product (1.11 g, 3.31 mmol, 95%).

^1H NMR (500 MHz, CDCl_3 , ppm) δ = 8.24 (s, 1H, H_{Ar}), 8.17 (d, J = 7.8 Hz, 2H, H_{Ar}), 8.14 (d, J = 4.9 Hz, 1H, H_{Ar}), 7.72 (d, J = 1.9 Hz, 4H, H_{Ar}), 7.50 (d, J = 8.2 Hz, 2H, H_{Ar}), 7.48–7.41 (m, 2H, H_{Ar}), 7.36–7.29 (m, 2H, H_{Ar}), 7.15 (d, J = 4.9 Hz, 1H, H_{Ar}), 3.94 (s, 2H, NH_2).

^{13}C NMR (126 MHz, CDCl_3 , ppm) δ = 140.7 (2C, C_{Ar}), 140.5 (1C, C_{Ar}), 139.9 (1C, C_{Ar}), 138.5 (1C, C_{Ar}), 137.9 (1C, C_{Ar}), 136.0 (1C, C_{Ar}), 132.8 (1C, C_{Ar}), 130.1 (2C, C_{Ar}), 127.7 (2C, C_{Ar}), 126.2 (2C, C_{Ar}), 124.3 (2C, C_{Ar}), 123.7 (2C, C_{Ar}), 120.6 (1C, C_{Ar}), 120.4 (2C, C_{Ar}), 109.8 (2C, C_{Ar}).

ESI-MS for $[\text{C}_{23}\text{H}_{17}\text{N}_3+\text{H}]^+$: Calc. m/z = 336.1496, found m/z = 336.1487.

IR (ATR, $\tilde{\nu}$) = 3471 (vs), 3443 (vs), 3397 (vs), 3390 (vs), 3370 (vs), 3293 (vs), 3189 (vs), 3055 (vs), 3045 (vs), 3022 (vs), 2998 (vs), 2985 (vs), 2854 (vs), 2812 (vs), 2720 (vs), 2709 (vs), 2681 (vs), 2662 (vs), 2630 (s), 2588 (s), 2578 (s), 1622 (vs), 1607 (vs), 1593 (vs), 1515 (vs), 1494 (s), 1476 (vs), 1449 (vs), 1420 (vs), 1407 (vs), 1328 (s), 1318 (vs), 1227 (vs), 745 (vs), 718 (vs) cm^{-1} .

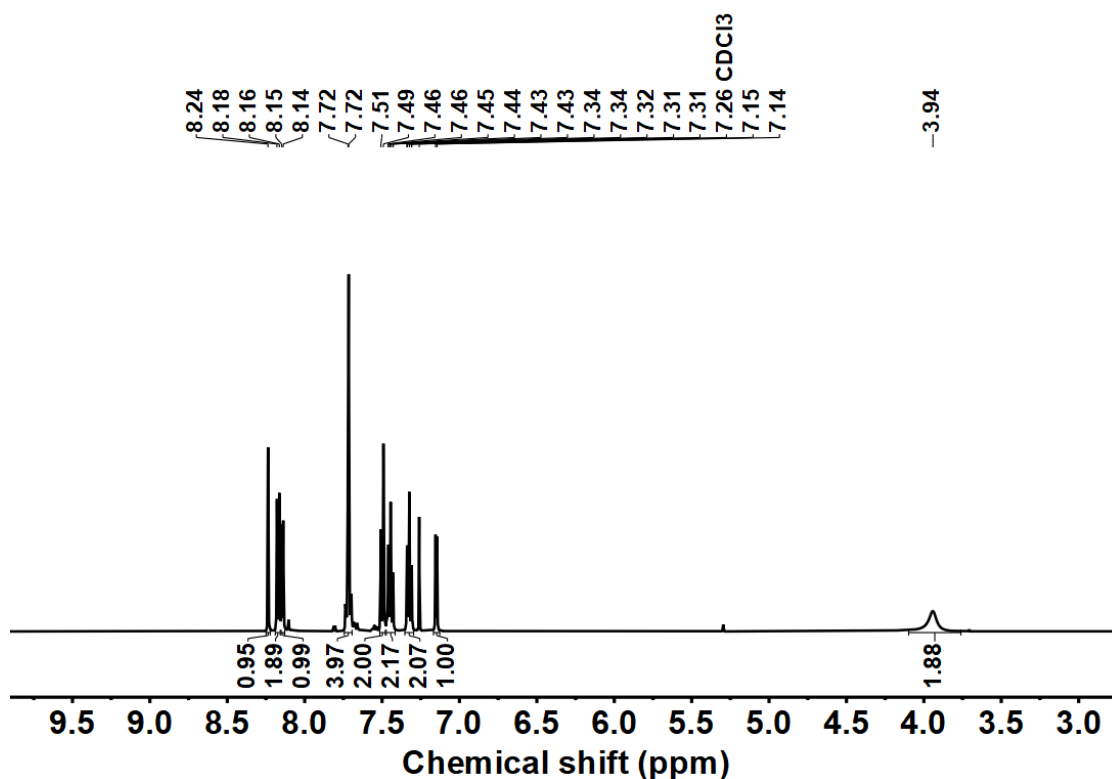


Figure 110. ¹H NMR spectra of **67**, 500 MHz, CDCl₃.

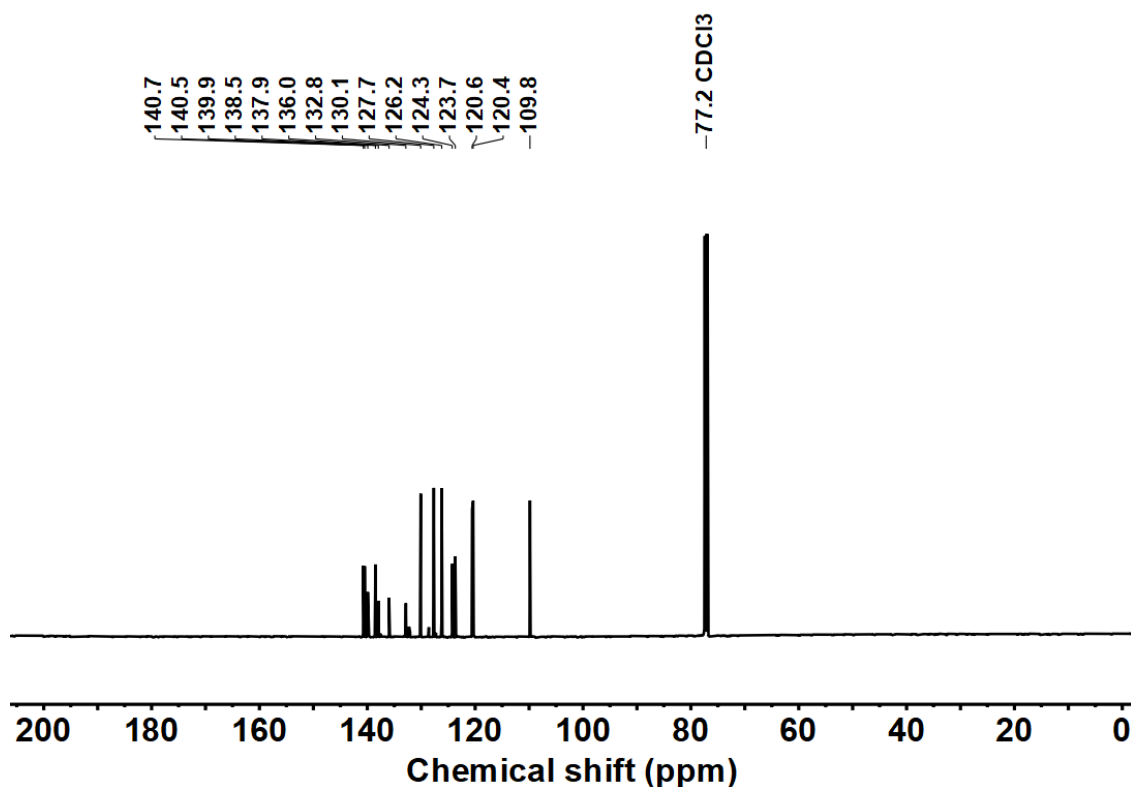
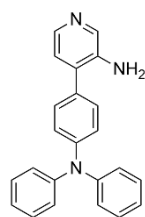


Figure 111. ¹³C NMR spectra of **67**, 126 MHz, CDCl₃.

4-(4-(diphenylamino)phenyl)pyridin-3-amine (70)



Brown paste product (1.06 g, 3.14 mmol, 91%).

^1H NMR (500 MHz, CD_3CN , ppm) δ = 8.08 (s, 1H, H_{Ar}), 7.91 (d, J = 4.9 Hz, 1H, H_{Ar}), 7.38–7.35 (m, 2H, H_{Ar}), 7.34–7.30 (m, 4H, H_{Ar}), 7.12–7.07 (m, 8H, H_{Ar}), 7.00 (d, J = 4.9 Hz, 1H, H_{Ar}), 4.24 (s, 2H, NH_2).

^{13}C NMR (126 MHz, CD_3CN , ppm) δ = 148.6 (1C, C_{Ar}), 148.5 (2C, C_{Ar}), 141.8 (1C, C_{Ar}), 140.1 (1C, C_{Ar}), 138.9 (1C, C_{Ar}), 133.2 (1C, C_{Ar}), 131.8 (1C, C_{Ar}), 130.5 (4C, C_{Ar}), 130.2 (2C, C_{Ar}), 125.5 (4C, C_{Ar}), 124.7 (1C, C_{Ar}), 124.4 (2C, C_{Ar}), 124.2 (2C, C_{Ar}).

ESI-MS for $[\text{C}_{23}\text{H}_{19}\text{N}_3+\text{H}]^+$: Calc. m/z = 338.1652, found m/z = 338.1645.

IR (ATR, $\tilde{\nu}$) = 3453 (m), 3446 (m), 3436 (m), 3357 (m), 3313 (s), 3195 (s), 3189 (s), 3182 (s), 3176 (s), 3100 (m), 3085 (m), 3057 (s), 3033 (s), 1610 (m), 1587 (vs), 1513 (vs), 1483 (vs), 1423 (m), 1410 (m), 1325 (s), 1315 (s), 1269 (vs), 1228 (m), 817 (m), 753 (m), 733 (m), 694 (vs), 509 (m) cm^{-1} .

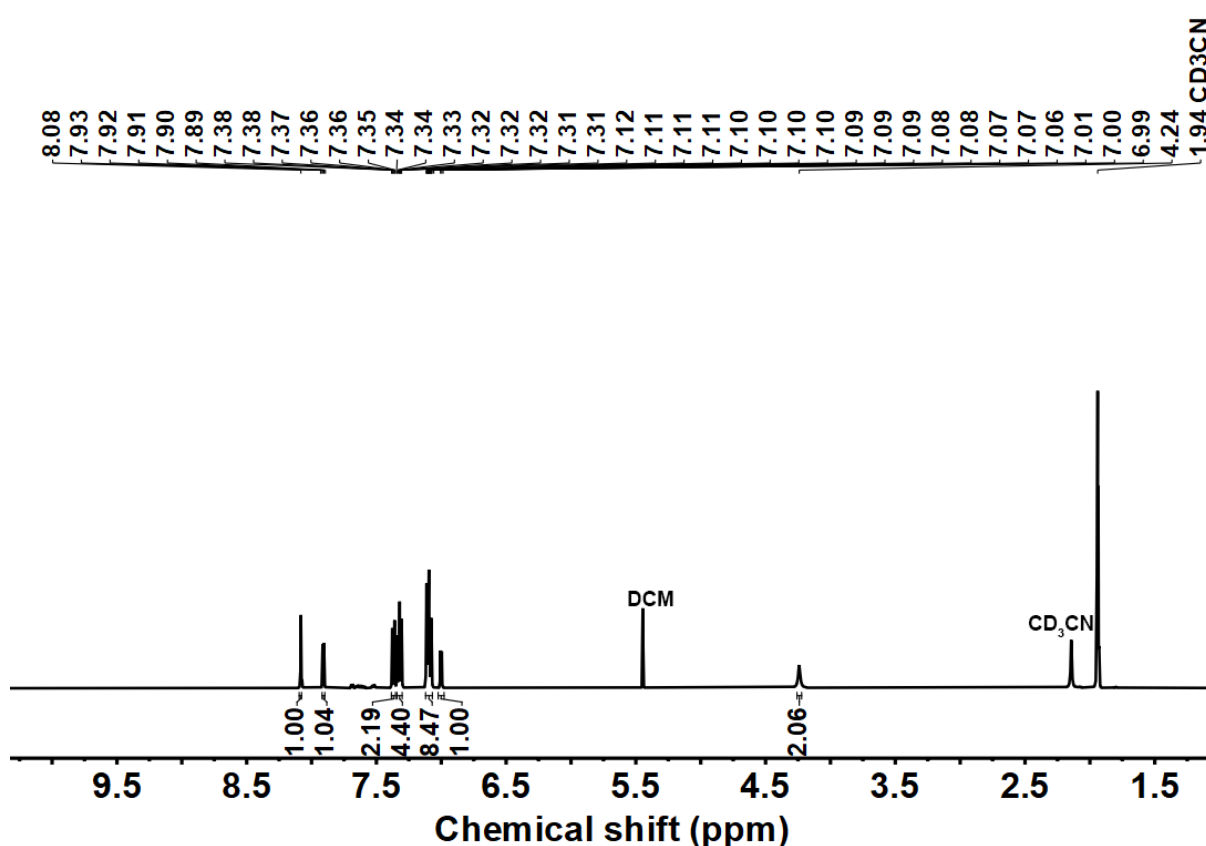


Figure 112. ^1H NMR spectra of **70**, 500 MHz, CD_3CN .

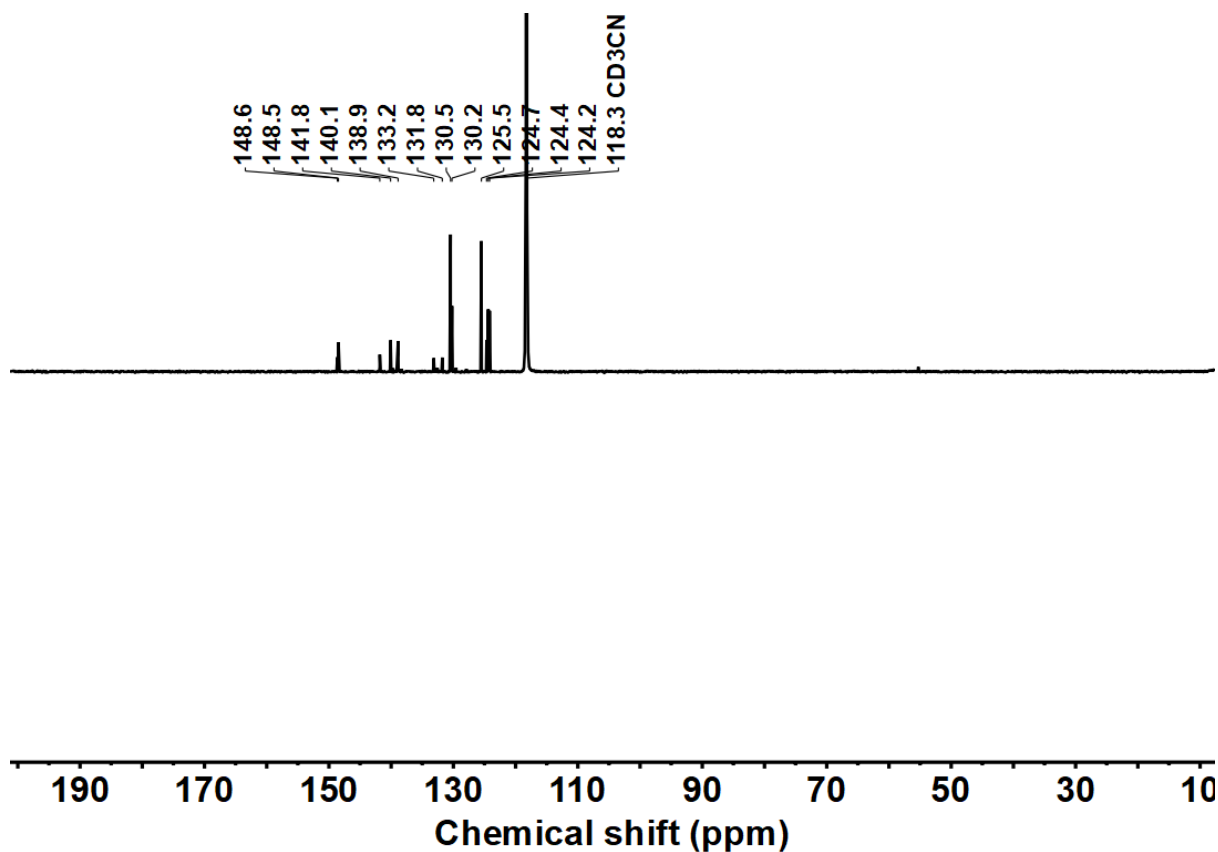
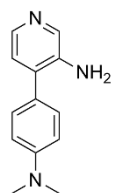


Figure 113. ^{13}C NMR spectra of **70**, 126 MHz, CD_3CN .

4-(4-(dimethylamino)phenyl)pyridin-3-amine (**73**)



Brown paste product (1.21 g, 5.67 mmol, 98%).

^1H NMR (500 MHz, CDCl_3 , ppm) δ = 8.12 (s, 1H, H_{Ar}), 8.03 (d, J = 4.9 Hz, 1H, H_{Ar}), 7.39–7.35 (m, 2H, H_{Ar}), 7.02 (d, J = 4.9 Hz, 1H, H_{Ar}), 6.83–6.79 (m, 2H, H_{Ar}), 3.81 (s, 2H, NH_2), 3.01 (s, 6H, CH_3).

^{13}C NMR (126 MHz, CDCl_3 , ppm) δ = 150.4 (1C, C_{Ar}), 140.4 (1C, C_{Ar}), 140.1 (1C, C_{Ar}), 138.0 (1C, C_{Ar}), 134.3 (1C, C_{Ar}), 129.3 (2C, C_{Ar}), 124.4 (1C, C_{Ar}), 124.2 (1C, C_{Ar}), 112.7 (2C, C_{Ar}), 40.5 (2C, CH_3).

ESI-MS for $[\text{C}_{13}\text{H}_{15}\text{N}_3+\text{H}]^+$: Calc. m/z = 214.1339, found m/z = 214.1335.

IR (ATR, $\tilde{\nu}$) = 3415 (vs), 3294 (vs), 3142 (vs), 3060 (vs), 3041 (vs), 2998 (vs), 2982 (vs), 2970 (s), 2947 (s), 2916 (s), 2897 (vs), 2884 (vs), 2857 (s), 2816 (s), 2805 (s), 1610 (vs), 1587 (s), 1520 (vs), 1495 (vs), 1483 (vs), 1448 (vs), 1418 (vs), 1406 (s), 1331 (s), 1319 (vs), 1301 (vs), 809 (vs) cm^{-1} .

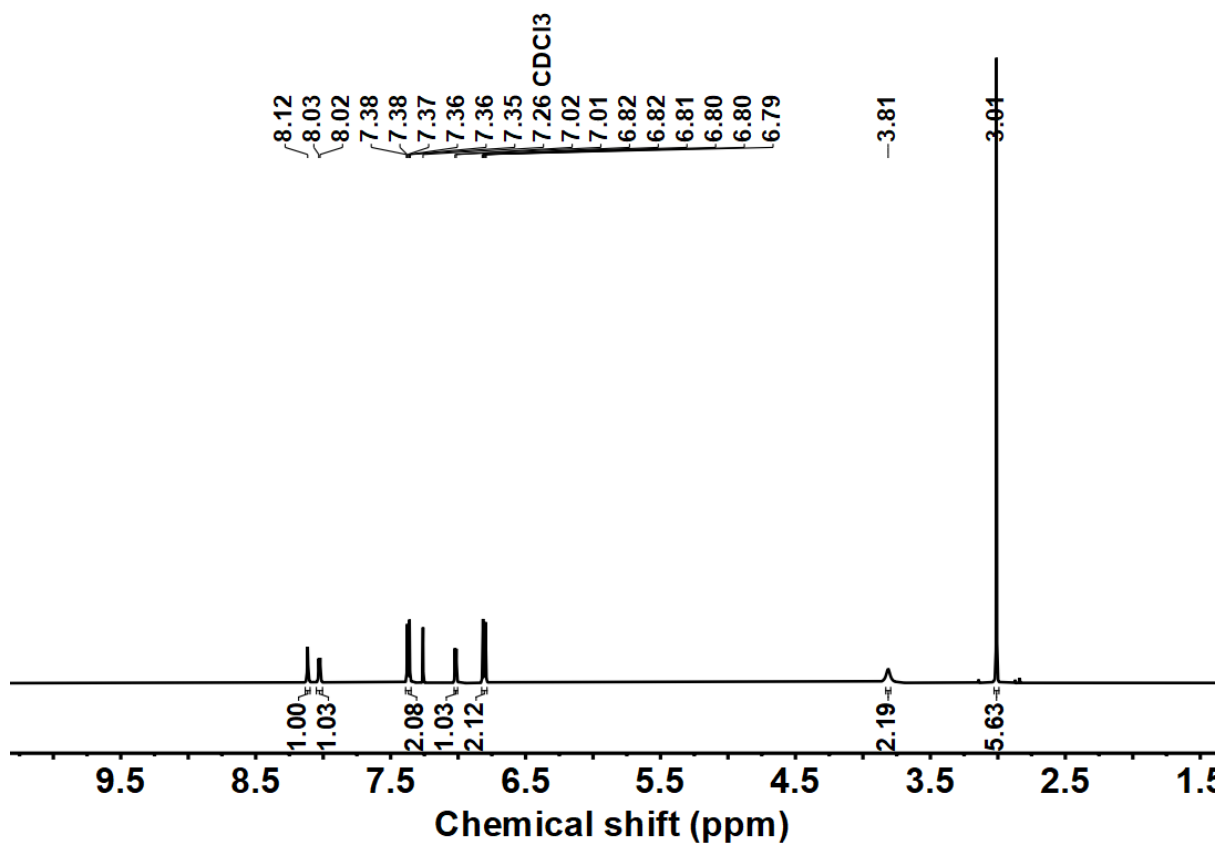


Figure 114. ^1H NMR spectra of 73, 500 MHz, CDCl_3 .

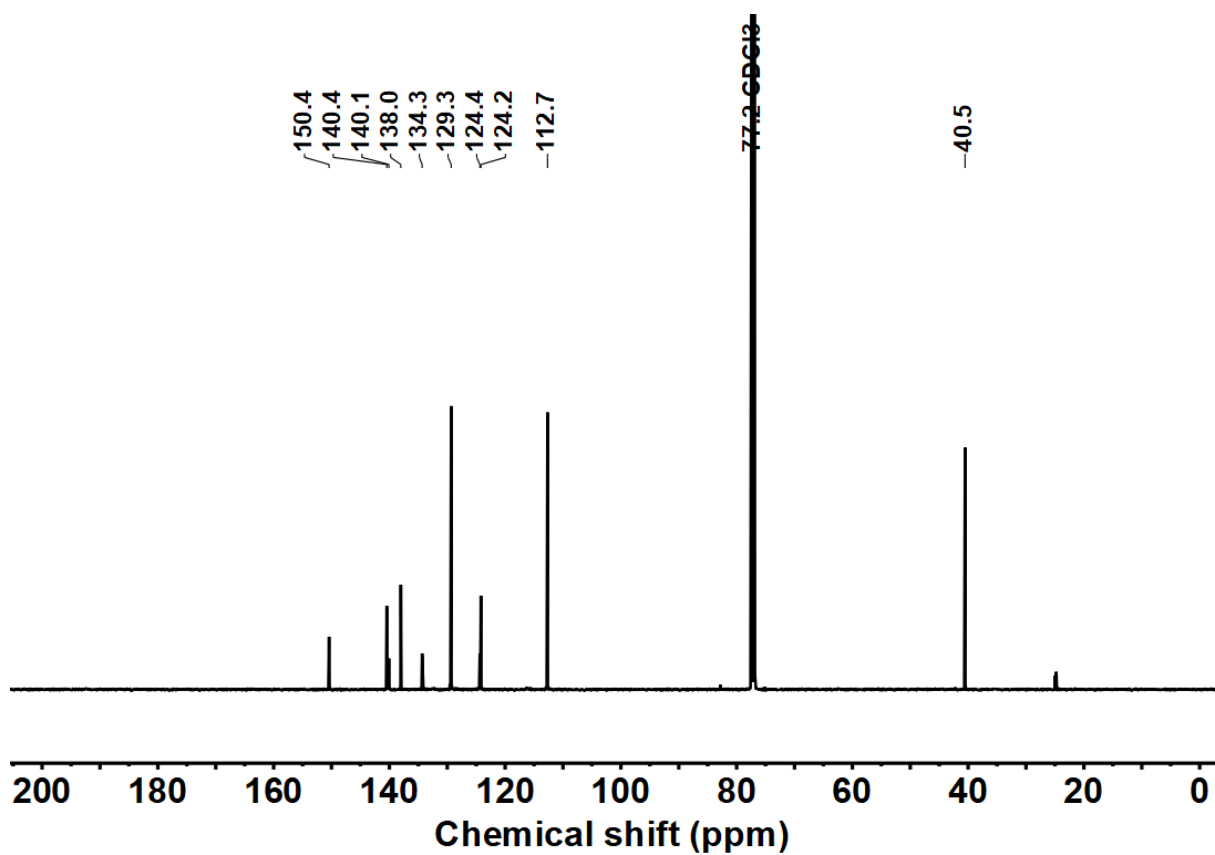
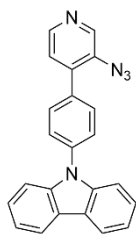


Figure 115. ^{13}C NMR spectra of 73, 126 MHz, CDCl_3 .

9-(4-(3-azidopyridin-4-yl)phenyl)-9H-carbazole (68)



p-Toluenesulfonic acid monohydrate (0.851 g, 4.47 mmol, 1.50 equiv.) was dissolved in acetonitrile/water (20/5.0 mL) at 25 °C. Once dissolved, tert-butyl nitrite (0.461 g, 4.47 mmol, 1.50 equiv.) was added, followed by 4-(4-(9H-carbazol-9-yl)phenyl)pyridin-3-amine (1.00 g, 2.98 mmol, 1.00 equiv.) portion-wise. The reaction mixture was stirred for 3h at rt. After which, a solution of sodium azide (0.582 g, 8.95 mmol, 3.00 equiv.) in water (5.0 mL) was added dropwise. The resulting reaction mass was stirred for another 3 hours at 25 °C. After the complete conversion, the reaction mixture was extracted with ethyl acetate (3 × 20 ml). The combined organic layers were dried over sodium sulfate. After the removal of the solvent, the crude solid was purified by chromatography (EtOAc: DCM=2:3), resulting in 9-(4-(3-azidopyridin-4-yl)phenyl)-9H-carbazole (0.98 g, 2.71 mmol, 91%) as a yellow solid.

$^1\text{H NMR}$ (500 MHz, CDCl_3 , ppm) δ = 8.66 (s, 1H, H_{Ar}), 8.51 (d, J = 4.9 Hz, 1H, H_{Ar}), 8.17 (dt, J = 7.8, 0.9 Hz, 2H, H_{Ar}), 7.78–7.74 (m, 2H, H_{Ar}), 7.72–7.68 (m, 2H, H_{Ar}), 7.51 (d, J = 8.2 Hz, 2H, H_{Ar}), 7.44 (ddd, J = 8.3, 7.0, 1.2 Hz, 2H, H_{Ar}), 7.40 (d, J = 4.9 Hz, 1H, H_{Ar}), 7.32 (td, J = 7.5, 7.1, 1.0 Hz, 2H, H_{Ar}).

$^{13}\text{C NMR}$ (126 MHz, CDCl_3 , ppm) δ = 146.3 (1C, C_{Ar}), 141.6 (1C, C_{Ar}), 140.7 (2C, C_{Ar}), 139.6 (1C, C_{Ar}), 138.5 (1C, C_{Ar}), 134.3 (1C, C_{Ar}), 134.3 (1C, C_{Ar}), 130.8 (2C, C_{Ar}), 127.0 (2C, C_{Ar}), 126.2 (2C, C_{Ar}), 124.8 (1C, C_{Ar}), 123.7 (2C, C_{Ar}), 120.6 (2C, C_{Ar}), 120.4 (2C, C_{Ar}), 109.9 (2C, C_{Ar}).

ESI-MS for $[\text{C}_{23}\text{H}_{15}\text{N}_5+\text{H}]^+$: Calc. m/z = 362.1327, found m/z = 362.1322.

IR (ATR, $\tilde{\nu}$) = 3052 (vs), 3046 (vs), 2981 (s), 2128 (vs), 2104 (vs), 1519 (vs), 1489 (s), 1478 (s), 1448 (vs), 1311 (vs), 1300 (vs), 1223 (vs), 742 (vs), 721 (vs) cm^{-1} .

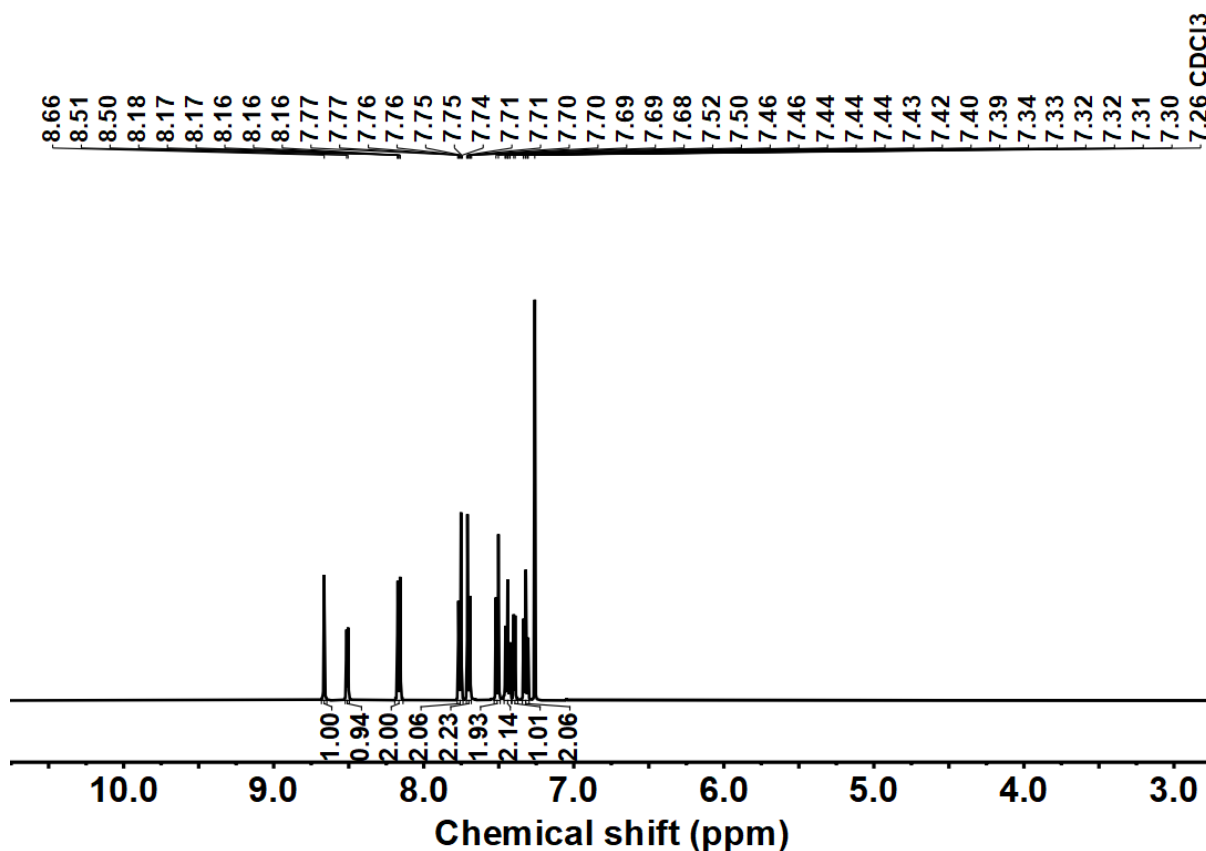


Figure 116. $^1\text{H NMR}$ spectra of **68**, 500 MHz, CDCl_3 .

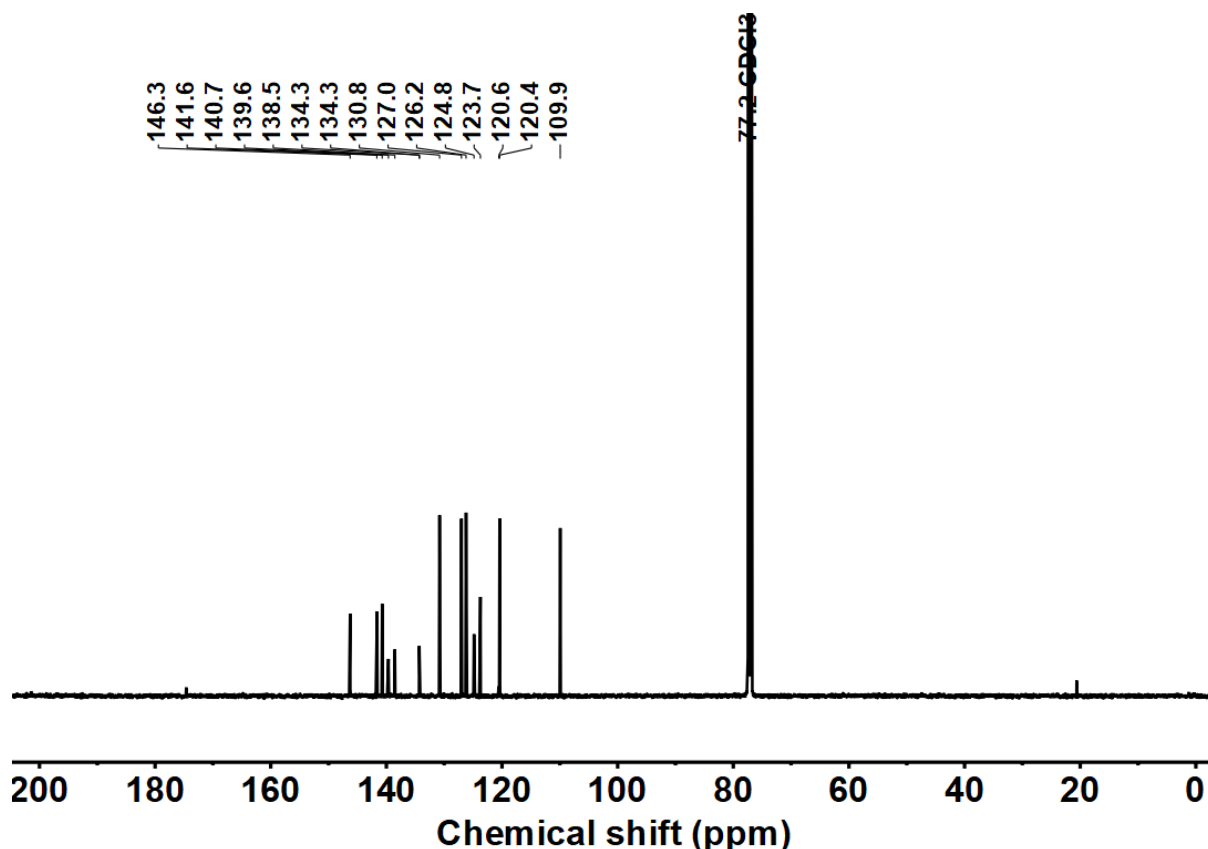
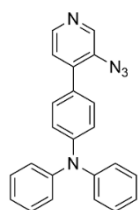


Figure 117. ^{13}C NMR spectra of **68**, 126 MHz, CDCl_3 .

4-(3-azidopyridin-4-yl)-*N,N*-diphenylaniline (**71**)



p-Toluenesulfonic acid monohydrate (0.846 g, 4.45 mmol, 1.50 equiv.) was dissolved in acetonitrile/water (20/5.0 mL) at 25 °C. Once dissolved, tert-butyl nitrite (0.458 g, 4.45 mmol, 1.50 equiv.) was added, followed by 4-(4-(diphenylamino)phenyl)pyridin-3-amine (1.00 g, 2.96 mmol, 1.00 equiv.) portion-wise. The reaction mixture was stirred for 3 h at rt. After which, a solution of sodium azide (0.578 g, 8.89 mmol, 3.00 equiv.) in water (5.0 mL) was added dropwise. The resulting reaction mass was stirred for another 3 hours at 25 °C. After the complete conversion, the reaction mixture was extracted with ethyl acetate (3 × 20 ml). The combined organic layers were dried over sodium sulfate. After the removal of the solvent, the crude solid was purified by chromatography (EtOAc: DCM=2:3), resulting in 4-(3-azidopyridin-4-yl)-*N,N*-diphenylaniline (0.99 g, 2.72 mmol, 92%) as a yellow solid.

^1H NMR (500 MHz, CDCl_3 , ppm) δ = 8.55 (s, 1H, H_{Ar}), 8.40 (d, J = 5.0 Hz, 1H, H_{Ar}), 7.40–7.36 (m, 2H, H_{Ar}), 7.32–7.26 (m, 5H, H_{Ar}), 7.17–7.14 (m, 4H, H_{Ar}), 7.13–7.06 (m, 4H, H_{Ar}).

^{13}C NMR (126 MHz, CDCl_3 , ppm) δ = 148.7 (1C, C_{Ar}), 147.4 (2C, C_{Ar}), 146.3 (1C, C_{Ar}), 141.7 (1C, C_{Ar}), 140.2 (1C, C_{Ar}), 133.9 (1C, C_{Ar}), 130.0 (2C, C_{Ar}), 129.6 (4C, C_{Ar}), 128.4 (1C, C_{Ar}), 125.3 (4C, C_{Ar}), 124.5 (1C, C_{Ar}), 123.8 (2C, C_{Ar}), 122.1 (2C, C_{Ar}).

ESI-MS for $[\text{C}_{23}\text{H}_{17}\text{N}_5+\text{H}]^+$: Calc. m/z = 364.1557, found m/z = 364.1552.

IR (ATR, $\tilde{\nu}$) = 3084 (vs), 3052 (vs), 3035 (vs), 2980 (vs), 2106 (vs), 1585 (vs), 1482 (vs), 1266 (vs) cm^{-1} .

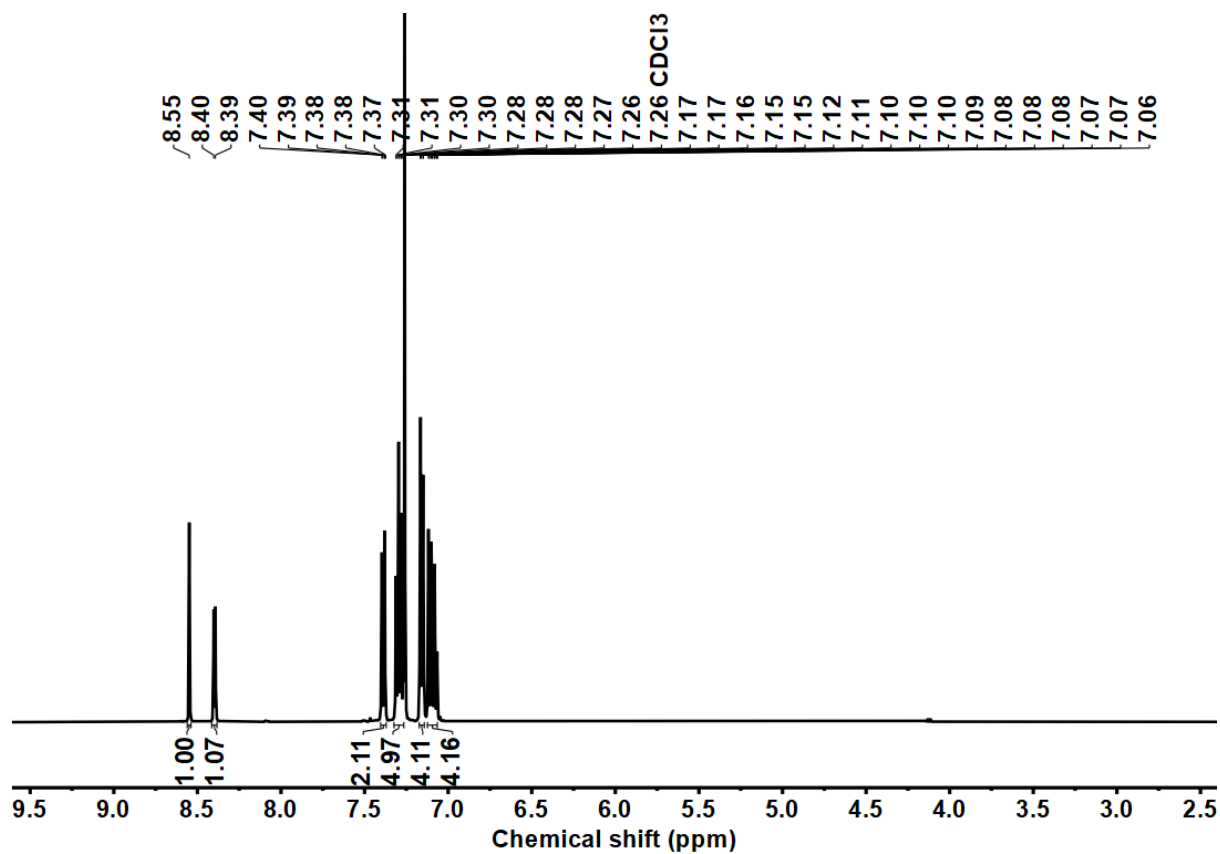


Figure 118. ^1H NMR spectra of 71, 500 MHz, CDCl_3 .

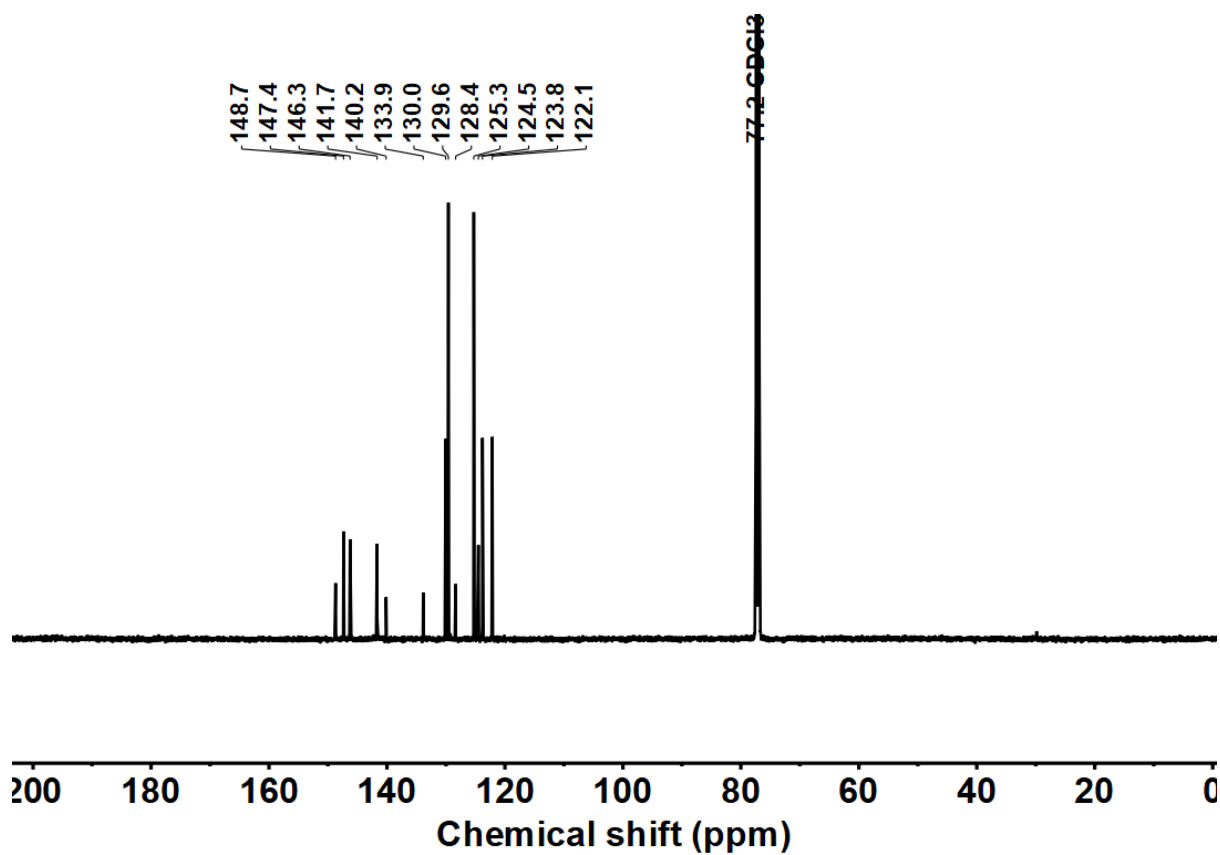
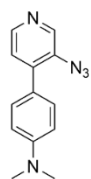


Figure 119. ^{13}C NMR spectra of 71, 126 MHz, CDCl_3 .

4-(3-azidopyridin-4-yl)-N,N-dimethylaniline (74)



p-Toluenesulfonic acid monohydrate (1.34 g, 7.03 mmol, 1.50 equiv.) was dissolved in acetonitrile/water (20/5.0 mL) at 25 °C. Once dissolved, tert-butyl nitrite (0.725 g, 7.03 mmol, 1.50 equiv.) was added, followed by 4-(4-(dimethylamino)phenyl)pyridin-3-amine (1.00 g, 4.69 mmol, 1.00 equiv.) portion-wise. The reaction mixture was stirred for 3h at rt. After which, a solution of sodium azide (0.914 g, 14.1 mmol, 3.00 equiv.) in water (5.0 mL) was added dropwise. The resulting reaction mass was stirred for another 3 hours at 25 °C. After the complete conversion, the reaction mixture was extracted with ethyl acetate (3 × 20 ml). The combined organic layers were dried over sodium sulfate. After the removal of the solvent, the crude solid was purified by chromatography (MeOH: DCM=1:19), resulting in 4-(3-azidopyridin-4-yl)-N,N-dimethylaniline (1.06 g, 4.43 mmol, 94%) as a yellow solid.

^1H NMR (500 MHz, CDCl_3 , ppm) δ = 8.52 (s, 1H, H_{Ar}), 8.36 (d, J = 5.0 Hz, 1H, H_{Ar}), 7.47–7.43 (m, 2H, H_{Ar}), 7.25 (d, J = 5.0 Hz, 1H, H_{Ar}), 6.80–6.76 (m, 2H, H_{Ar}), 3.02 (s, 6H, CH_3).

^{13}C NMR (126 MHz, CDCl_3 , ppm) δ = 150.8 (1C, C_{Ar}), 146.2 (1C, C_{Ar}), 141.5 (1C, C_{Ar}), 140.8 (1C, C_{Ar}), 133.7 (2C, C_{Ar}), 130.1 (1C, C_{Ar}), 124.3 (1C, C_{Ar}), 122.7 (1C, C_{Ar}), 111.9 (2C, C_{Ar}), 40.4 (2C, CH_3).

ESI-MS for $[\text{C}_{13}\text{H}_{13}\text{N}_5+\text{H}]^+$: Calc. m/z = 240.1244, found m/z = 240.1237.

IR (ATR, $\tilde{\nu}$) = 3048 (m), 3033 (s), 2997 (s), 2980 (s), 2971 (s), 2945 (s), 2941 (s), 2909 (s), 2890 (s), 2864 (s), 2817 (s), 2126 (vs), 2097 (vs), 2076 (vs), 1610 (s), 1584 (s), 1527 (s), 1483 (s), 1446 (s), 1410 (s), 1363 (s), 1300 (vs), 1288 (vs), 1261 (s), 808 (m) cm^{-1} .

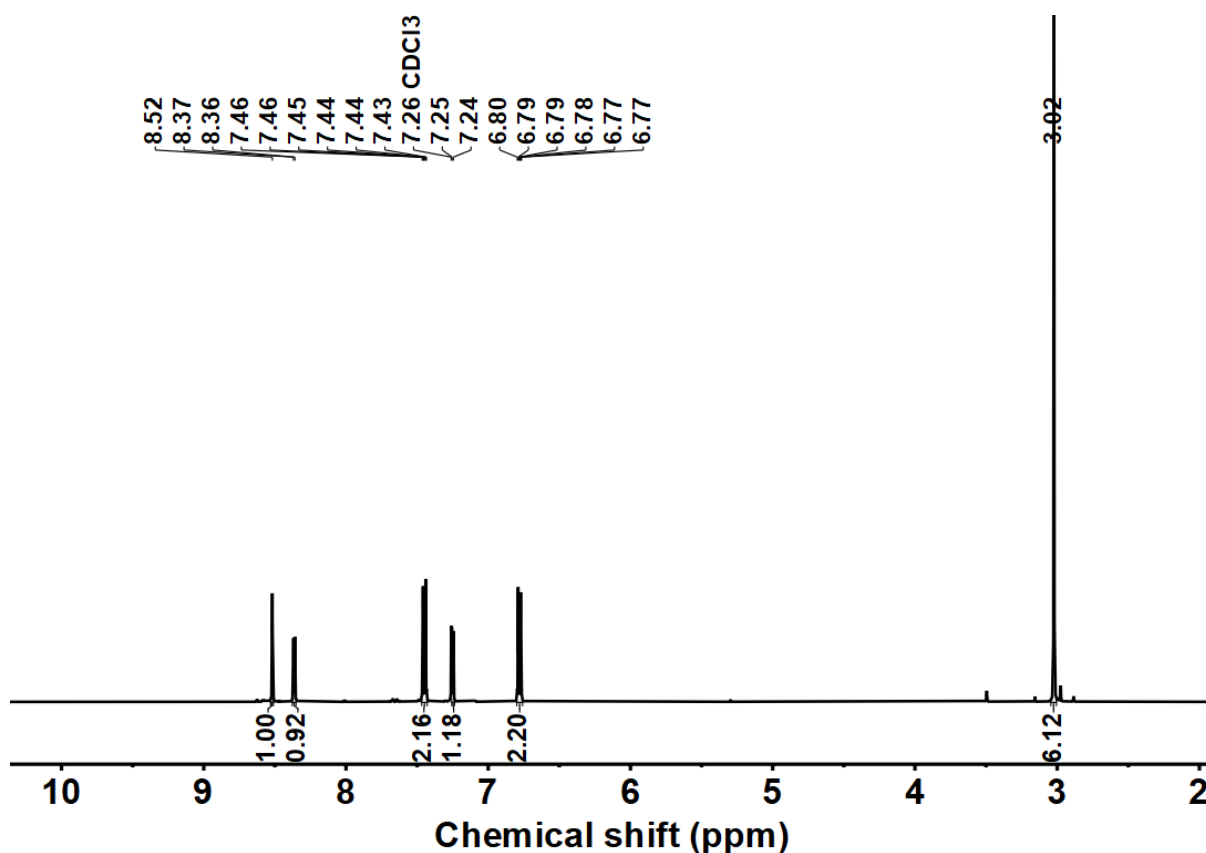


Figure 120. ^1H NMR spectra of 74, 500 MHz, CDCl_3 .

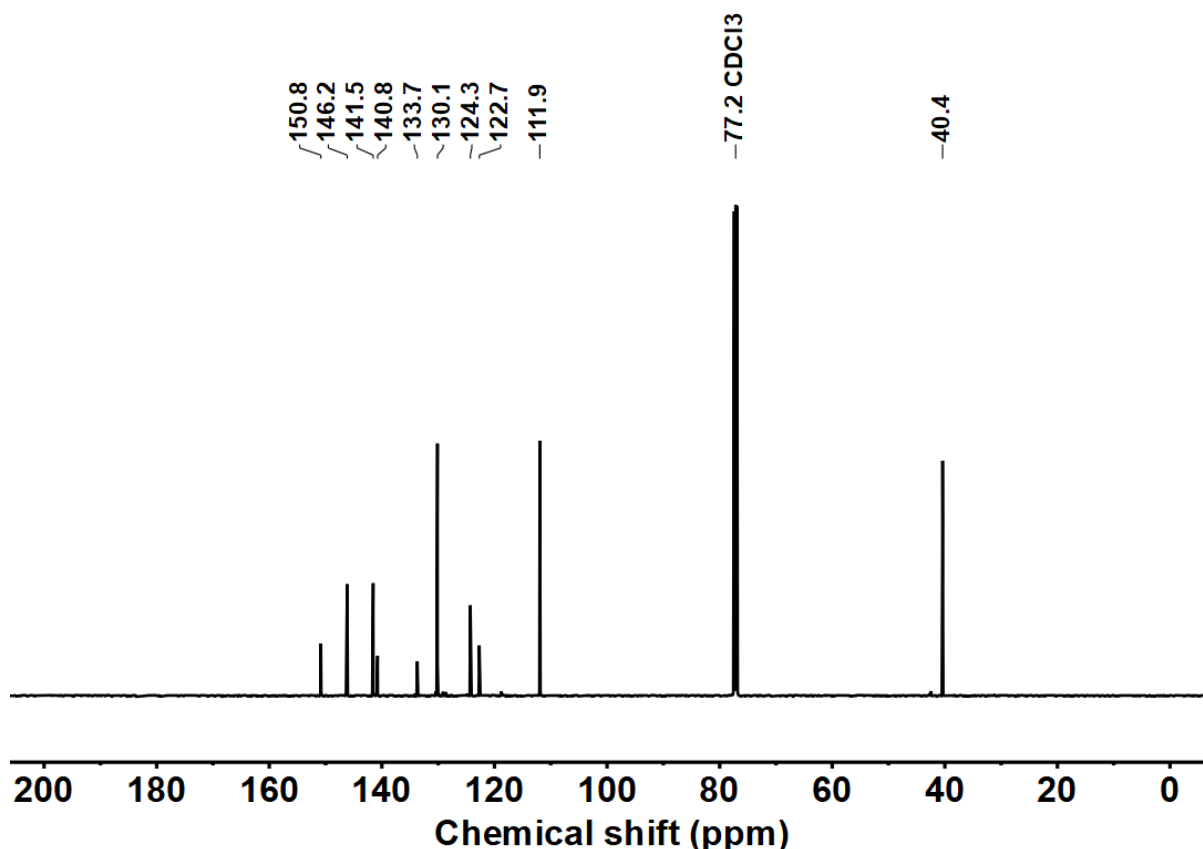
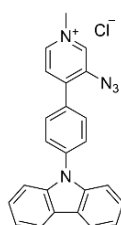


Figure 121. ^{13}C NMR spectra of **74**, 126 MHz, CDCl_3 .

4-(4-(9H-carbazol-9-yl)phenyl)-3-azido-1-methylpyridin-1-ium chloride (**63**)



9-(4-(3-azidopyridin-4-yl)phenyl)-9H-carbazole (0.20 g, 0.553 mmol, 1.00 equiv.) was dissolved in acetonitrile (10 mL), and methyl iodide (0.118 g, 0.830 mmol, 1.50 equiv.) was added dropwise at room temperature with stirring. The resulting reaction mixture was left overnight at 40 °C. The precipitation was collected by filtration and washed with acetonitrile. After dissolving in 10 mL water (0.451 g, 2.77 mmol, 5.00 equiv.), ammonium hexafluorophosphate was added, which resulted in a precipitate. The precipitate was collected by filtration, washed with water, and dried.

After dissolving the solid in 10 mL acetonitrile (0.769 g, 2.77 mmol, 5.00 equiv.), tetrabutylammonium chloride was added, which resulted in a precipitate. The precipitate was collected by filtration, washed with acetonitrile, and dried. The desired product 4-(4-(9H-carbazol-9-yl)phenyl)-3-azido-1-methylpyridin-1-ium chloride was obtained as a pale yellow solid (0.192 g, 0.466 mmol, 84%).

^1H NMR (500 MHz, $\text{DMSO}-d_6$, ppm) δ = 9.37 (s, 1H, H_{Ar}), 8.89 (d, J = 5.4 Hz, 1H, H_{Ar}), 8.31–8.28 (m, 3H, H_{Ar}), 8.08–8.03 (m, 2H, H_{Ar}), 7.93–7.89 (m, 2H, H_{Ar}), 7.53–7.45 (m, 4H, H_{Ar}), 7.34 (ddd, J = 7.9, 6.3, 1.7 Hz, 2H, H_{Ar}), 4.42 (s, 3H, CH_3).

^{13}C NMR (126 MHz, $\text{DMSO}-d_6$, ppm) δ = 144.9 (1C, C_{Ar}), 141.1 (1C, C_{Ar}), 139.7 (2C, C_{Ar}), 139.1 (1C, C_{Ar}), 138.7 (1C, C_{Ar}), 138.0 (1C, C_{Ar}), 131.5 (2C, C_{Ar}), 131.1 (1C, C_{Ar}), 127.8 (1C, C_{Ar}), 126.6 (2C, C_{Ar}), 126.5 (2C, C_{Ar}), 123.1 (2C, C_{Ar}), 120.7 (2C, C_{Ar}), 120.6 (2C, C_{Ar}), 109.7 (2C, C_{Ar}), 47.6 (1C, CH_3).

ESI-MS for $[\text{C}_{24}\text{H}_{18}\text{N}_5]^+$: Calc. m/z = 376.1557, found m/z = 376.1548.

IR (ATR, $\tilde{\nu}$) = 3378 (vs), 3368 (vs), 3364 (vs), 3353 (vs), 3344 (vs), 3331 (vs), 3320 (vs), 3311 (vs), 3300 (vs), 3291 (vs), 3284 (vs), 3269 (vs), 3264 (vs), 3250 (vs), 3239 (vs), 3154 (s), 3131 (s), 3086 (s), 3067 (s), 3043 (s),

3020 (s), 3013 (s), 2970 (vs), 2932 (s), 2915 (s), 2911 (s), 2898 (s), 2814 (s), 2118 (vs), 1598 (vs), 1505 (vs), 1477 (s), 1448 (vs), 1326 (vs), 1315 (s) cm^{-1} .

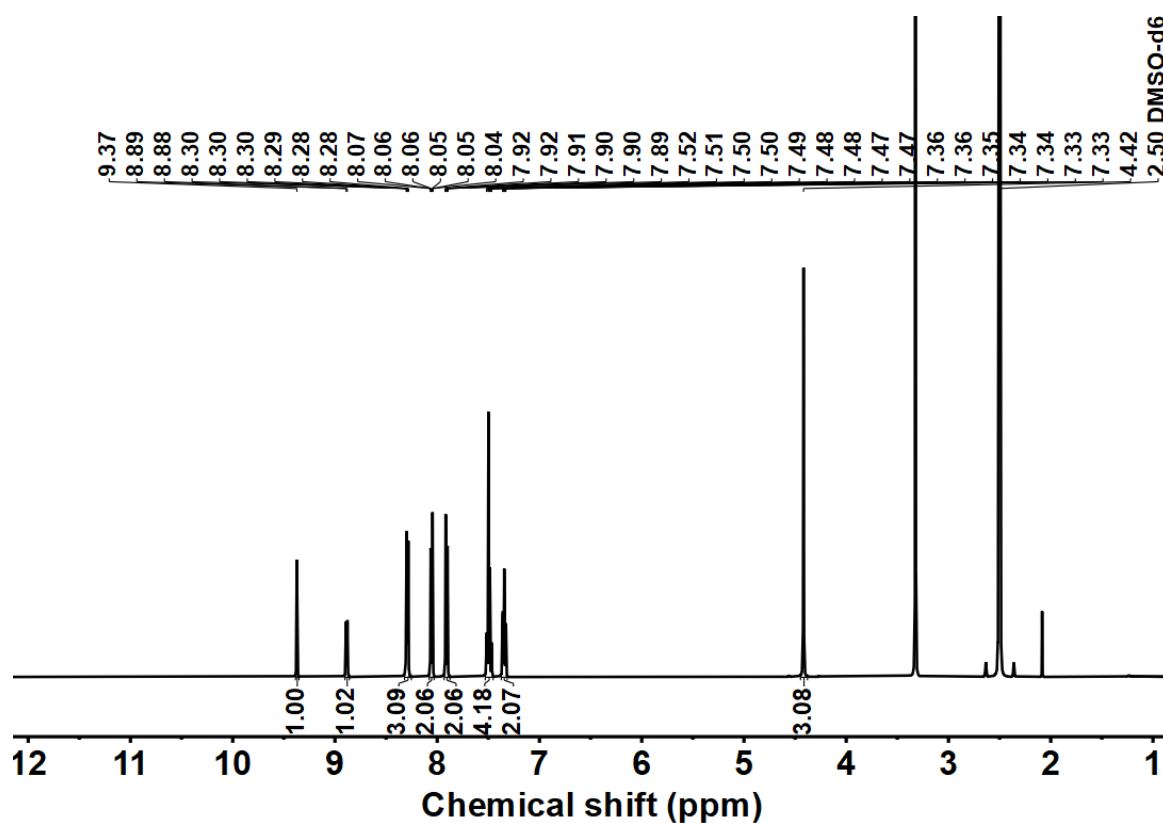


Figure 122. ^1H NMR spectra of **63**, 500 MHz, DMSO-d_6 .

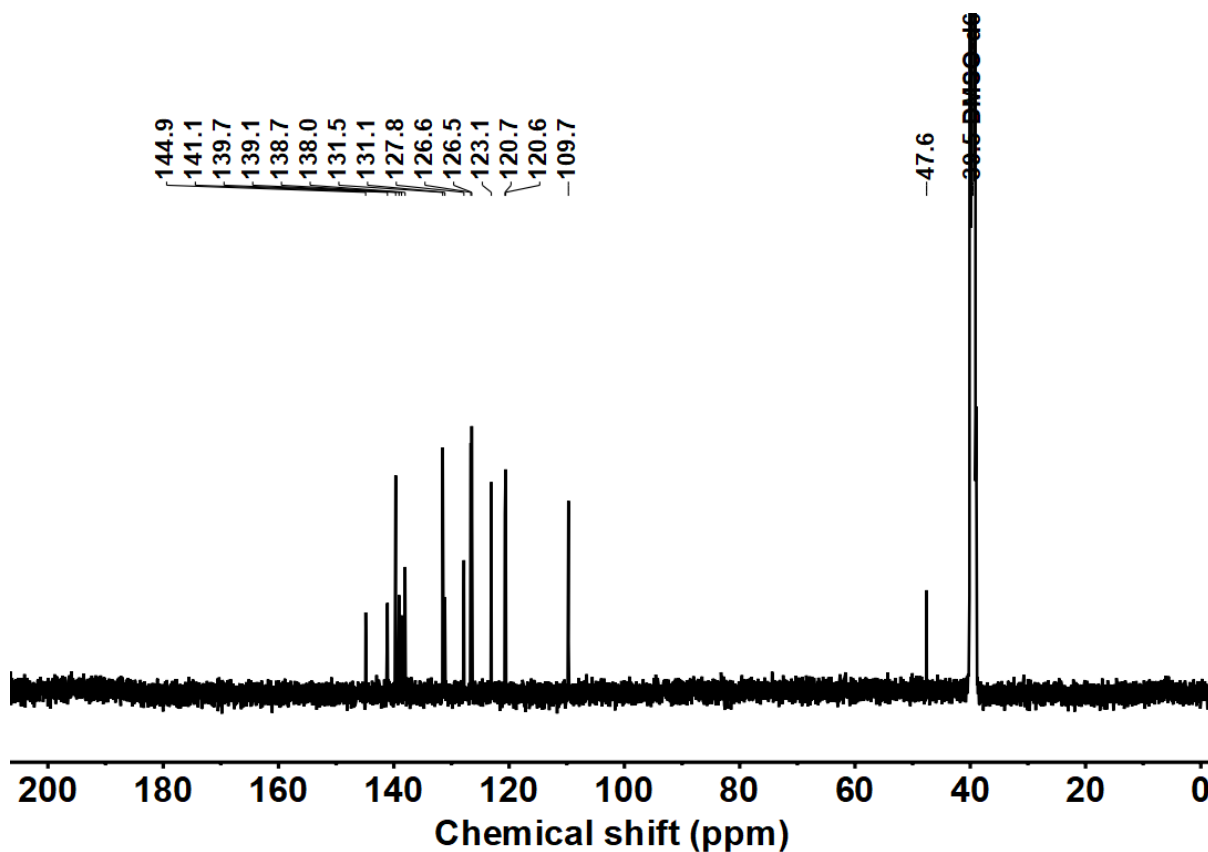


Figure 123. ^{13}C NMR spectra of **63**, 126 MHz, DMSO-d_6 .

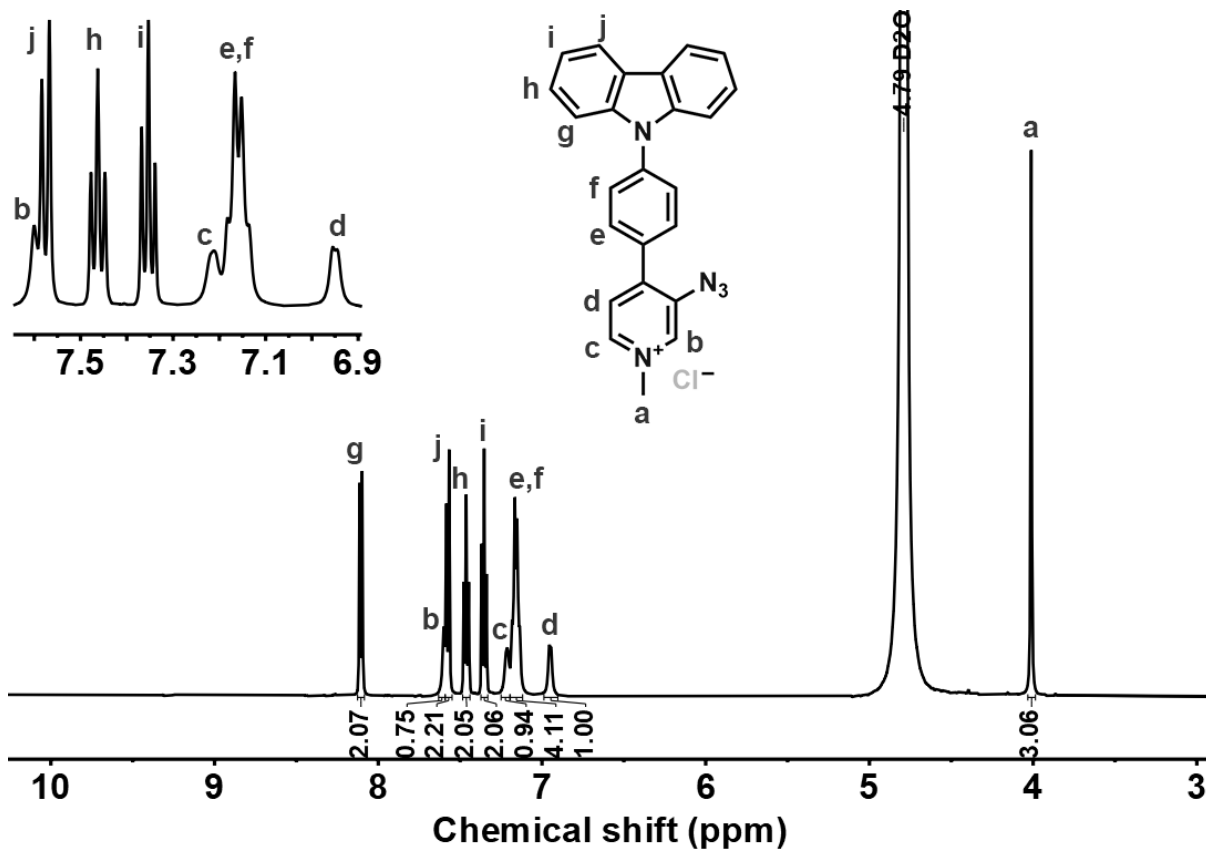


Figure 124. ^1H NMR spectra of **63**, 500 MHz, D_2O .

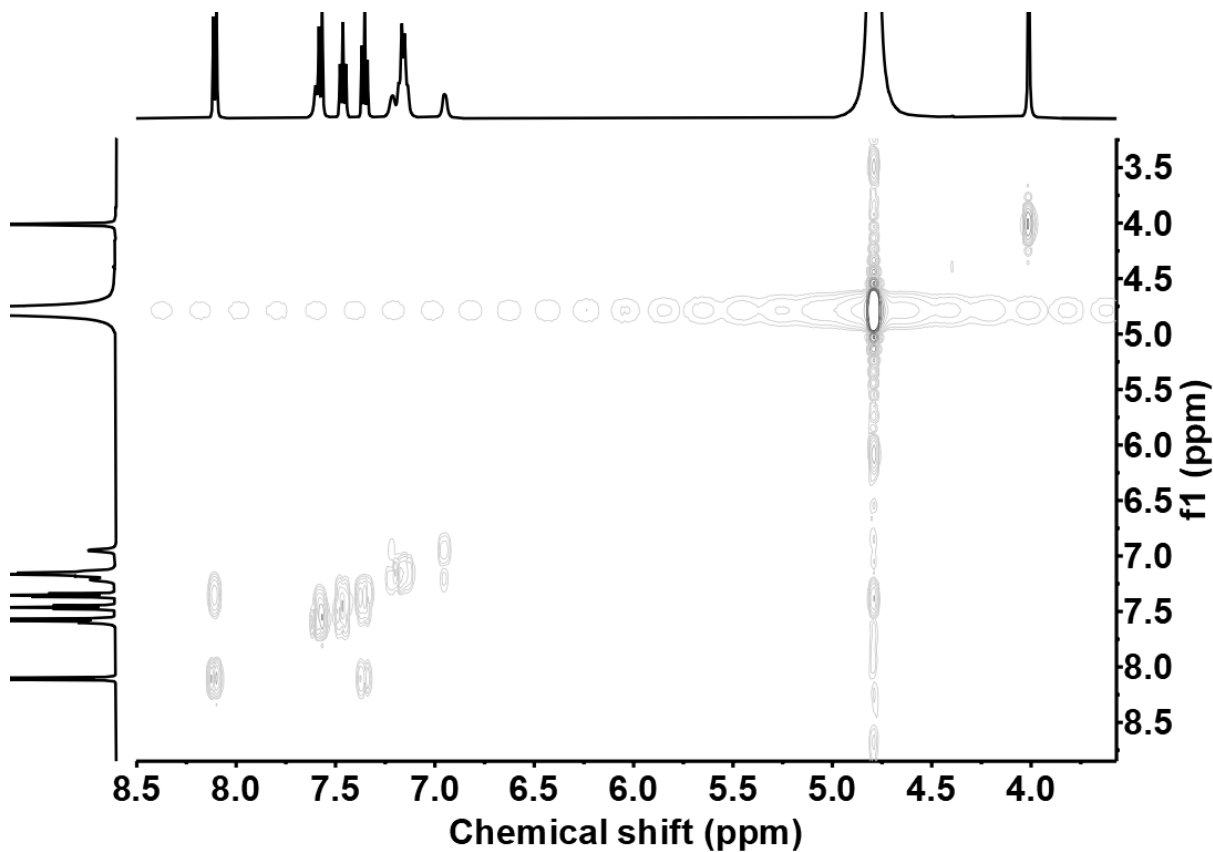
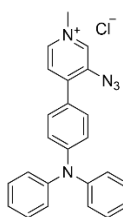


Figure 125. ^1H - ^1H COSY NMR spectra of **63**, D_2O .

3-azido-4-(4-(diphenylamino)phenyl)-1-methylpyridin-1-ium chloride (64)



4-(3-azidopyridin-4-yl)-N,N-diphenylaniline (0.20 g, 0.550 mmol, 1.00 equiv.) was dissolved in acetonitrile (10 mL), and methyl iodide (0.117 g, 0.826 mmol, 1.50 equiv.) was added dropwise at room temperature with stirring. The resulting reaction mixture was left overnight at 40 °C. The precipitation was collected by filtration and washed with acetonitrile. After dissolving in 10 mL water (0.449 g, 2.75 mmol, 5.00 equiv.), ammonium hexafluorophosphate was added, which resulted in a precipitate. The precipitate was collected by filtration, washed with water, and dried. After dissolving the solid in 10 mL acetonitrile (0.765 g, 2.75 mmol, 5.00 equiv.), tetrabutylammonium chloride was added, which resulted in a precipitate. The precipitate was collected by filtration, washed with acetonitrile, and dried. The desired product 3-azido-4-(4-(diphenylamino)phenyl)-1-methylpyridin-1-ium chloride was obtained as a yellow solid (0.203 g, 0.491 mmol, 89%).

^1H NMR (500 MHz, $\text{DMSO-}d_6$, ppm) δ = 9.18 (s, 1H, H_{Ar}), 8.71 (d, J = 6.3 Hz, 1H, H_{Ar}), 8.09 (d, J = 6.4 Hz, 1H, H_{Ar}), 7.74–7.67 (m, 2H, H_{Ar}), 7.45–7.37 (m, 4H, H_{Ar}), 7.20 (td, J = 7.3, 1.2 Hz, 2H, H_{Ar}), 7.18–7.14 (m, 4H, H_{Ar}), 7.01–6.95 (m, 2H, H_{Ar}), 4.32 (s, 3H, CH_3).

^{13}C NMR (126 MHz, $\text{DMSO-}d_6$, ppm) δ = 149.9 (1C, C_{Ar}), 145.9 (2C, C_{Ar}), 145.2 (1C, C_{Ar}), 140.7 (1C, C_{Ar}), 138.2 (1C, C_{Ar}), 136.9 (1C, C_{Ar}), 131.2 (2C, C_{Ar}), 130.0 (4C, C_{Ar}), 126.6 (1C, C_{Ar}), 125.7 (4C, C_{Ar}), 124.9 (2C, C_{Ar}), 124.0 (1C, C_{Ar}), 119.6 (2C, C_{Ar}), 47.1 (1C, CH_3).

ESI-MS for $[\text{C}_{24}\text{H}_{20}\text{N}_5]^+$: Calc. m/z = 378.1714, found m/z = 378.1704.

IR (ATR, $\tilde{\nu}$) = 3851 (m), 3646 (m), 3479 (vs), 3440 (vs), 3405 (vs), 3265 (s), 3254 (s), 3196 (s), 3123 (m), 3061 (s), 3035 (s), 3019 (s), 3011 (s), 2991 (s), 2980 (s), 2951 (s), 2923 (s), 2128 (vs), 1585 (vs), 1488 (vs), 1483 (vs), 1472 (vs), 1448 (s), 1329 (vs), 1306 (s), 1270 (vs), 1194 (vs), 1180 (vs), 1173 (s), 754 (s), 695 (s) cm^{-1} .

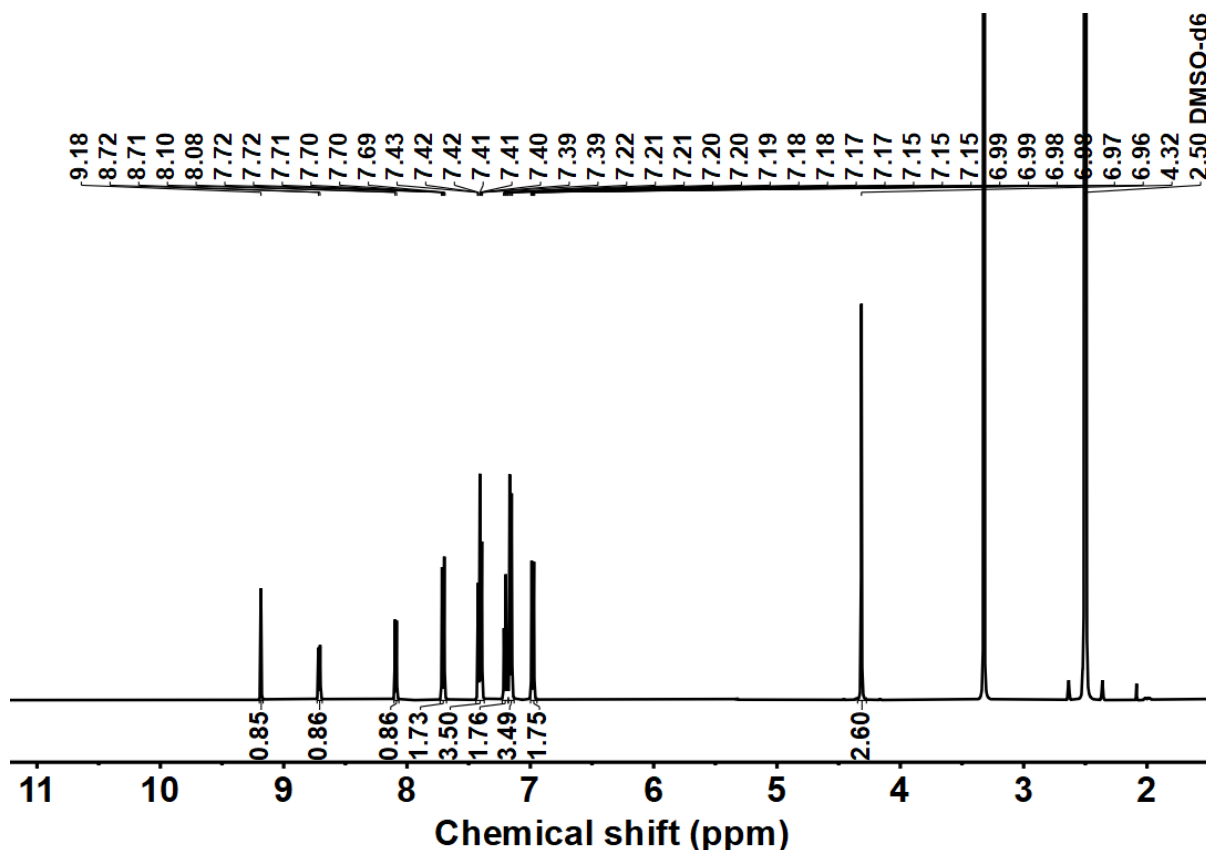


Figure 126. ^1H NMR spectra of 64, 500 MHz, $\text{DMSO-}d_6$.

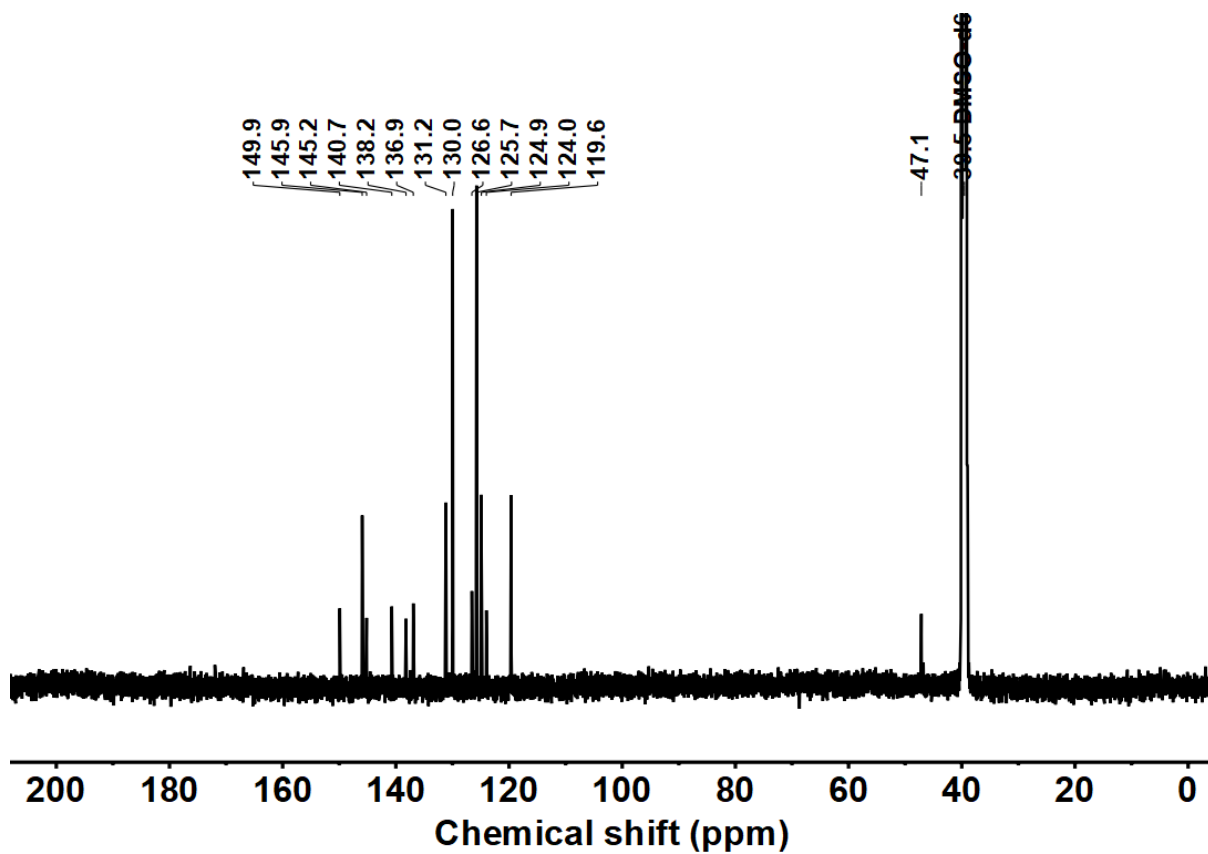


Figure 127. ^{13}C NMR spectra of **64**, 126 MHz, DMSO-d_6 .

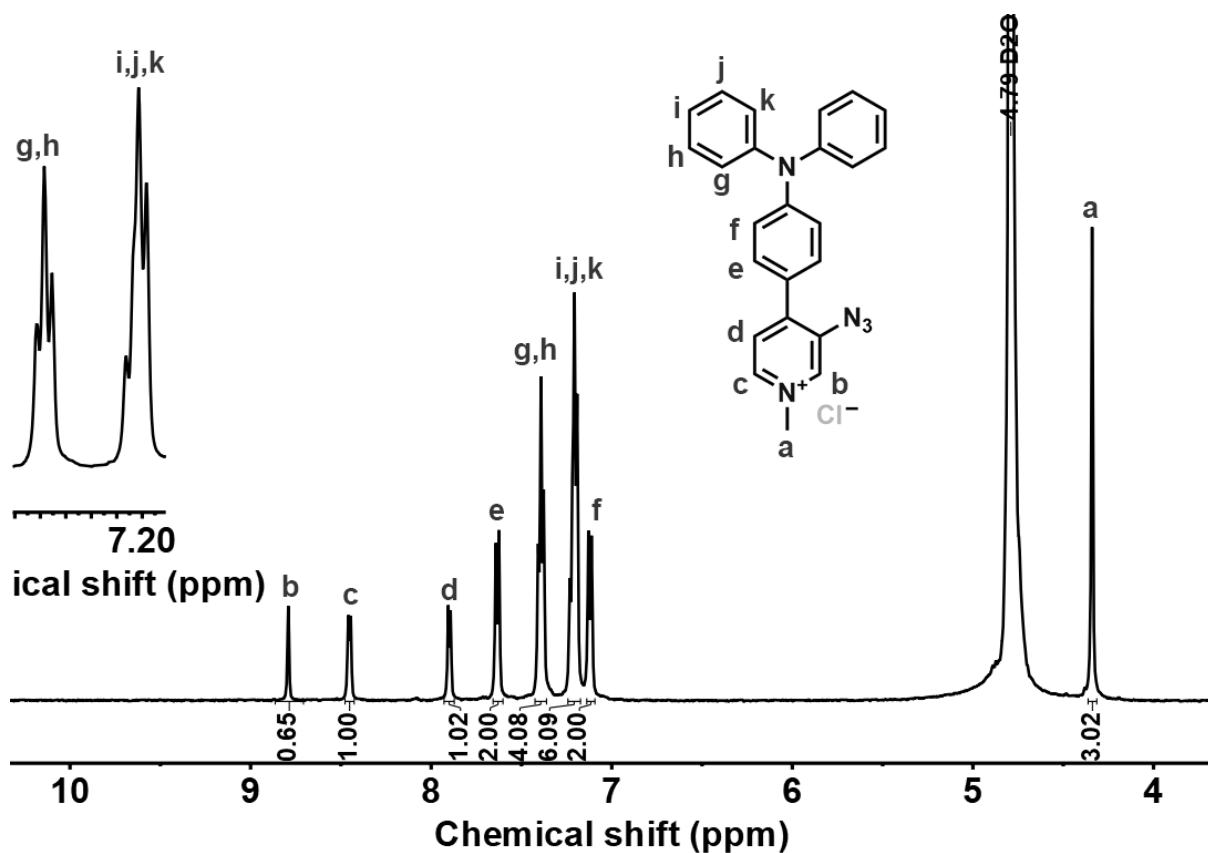


Figure 128. ^1H NMR spectra of **64**, 500 MHz, D_2O .

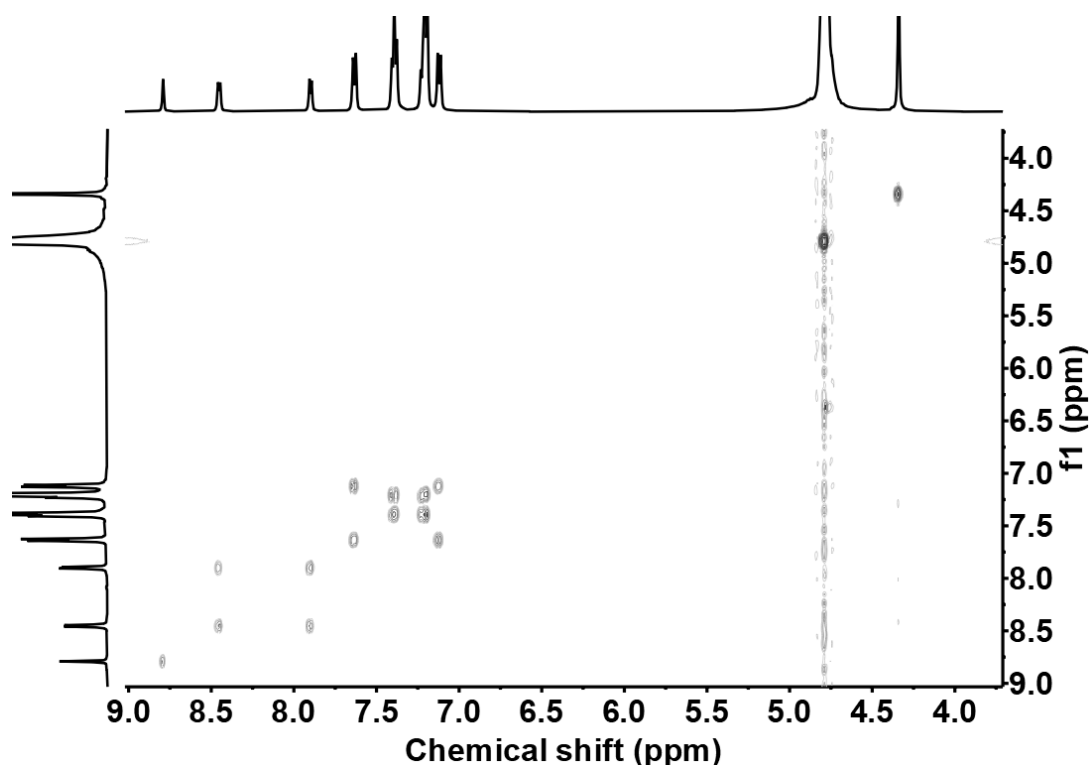
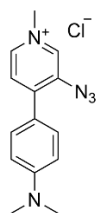


Figure 129. ^1H - ^1H COSY NMR spectra of **64**, D_2O .

3-azido-4-(4-(dimethylamino)phenyl)-1-methylpyridin-1-ium chloride (65)



4-(3-azidopyridin-4-yl)-*N,N*-dimethylaniline (0.20 g, 0.836 mmol, 1.00 equiv.) was dissolved in acetonitrile (10 mL), and methyl iodide (0.178 g, 1.25 mmol, 1.50 equiv.) was added dropwise at room temperature with stirring. The resulting reaction mixture was left overnight at 40 °C. The precipitation was collected by filtration and washed with acetonitrile. After dissolving in 10 mL water (0.681 g, 4.18 mmol, 5.00 equiv.), ammonium hexafluorophosphate was added, which resulted in a precipitate. The precipitate was collected by filtration, washed with water, and dried. After dissolving the solid in 10 mL acetonitrile (1.16 g, 4.18 mmol, 5.00 equiv.), tetrabutylammonium chloride was added, which resulted in a precipitate. The precipitate was collected by filtration, washed with acetonitrile, and dried. The desired product 3-azido-4-(4-(dimethylamino)phenyl)-1-methylpyridin-1-ium chloride was obtained as an orange solid (0.224 g, 0.773 mmol, 92%).

^1H NMR (500 MHz, , $\text{DMSO-}d_6$, ppm) δ = 9.06 (d, J = 1.4 Hz, 1H, H_{Ar}), 8.60 (dd, J = 6.6, 1.4 Hz, 1H, H_{Ar}), 8.05 (d, J = 6.5 Hz, 1H, H_{Ar}), 7.80–7.73 (m, 2H, H_{Ar}), 6.88–6.81 (m, 2H, H_{Ar}), 4.27 (s, 3H, CH_3), 3.04 (s, 6H, CH_3).

^{13}C NMR (126 MHz, , $\text{DMSO-}d_6$, ppm) δ = 152.0 (1C, C_{Ar}), 145.7 (1C, C_{Ar}), 140.4 (1C, C_{Ar}), 137.8 (1C, C_{Ar}), 135.9 (1C, C_{Ar}), 131.2 (2C, C_{Ar}), 125.4 (1C, C_{Ar}), 118.3 (1C, C_{Ar}), 111.6 (2C, C_{Ar}), 46.7 (1C, CH_3), 39.6 (2C, CH_3).

ESI-MS for $[\text{C}_{11}\text{H}_8\text{N}_4+\text{H}]^+$: Calc. m/z = 254.1401, found m/z = 254.1395.

IR (ATR, $\tilde{\nu}$) = 3851 (m), 3646 (m), 3046 (m), 2119 (vs), 1779 (m), 1771 (m), 1746 (vs), 1585 (vs), 1503 (vs), 1470 (s), 1440 (s), 1381 (s), 1337 (s), 1315 (vs), 1272 (m), 1172 (vs), 1131 (vs), 1068 (s), 1025 (m), 944 (m), 899 (m), 818 (s), 788 (s), 767 (s), 744 (s), 702 (s), 687 (s), 667 (s), 640 (m), 631 (m), 512 (m) cm^{-1} .

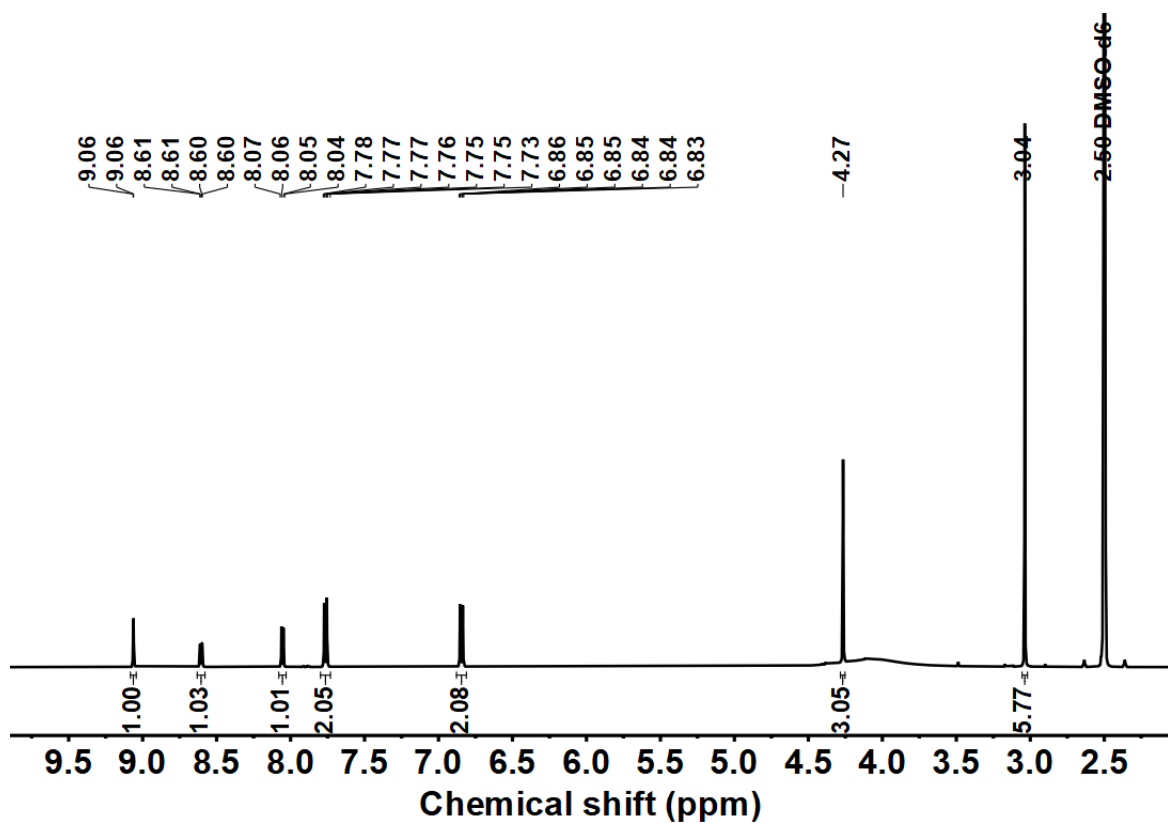


Figure 130. ^1H NMR spectra of **65**, 500 MHz, DMSO-d_6 .

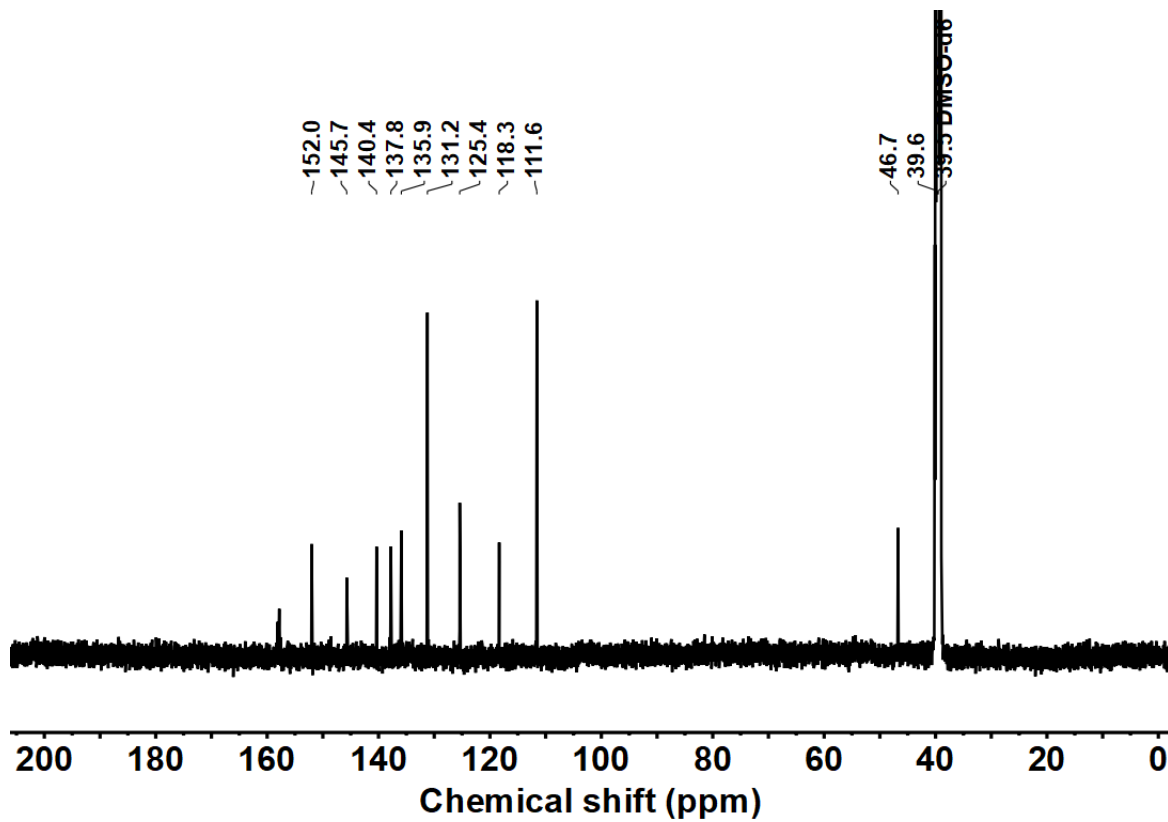


Figure 131. ^{13}C NMR spectra of **65**, 126 MHz, DMSO-d_6 .

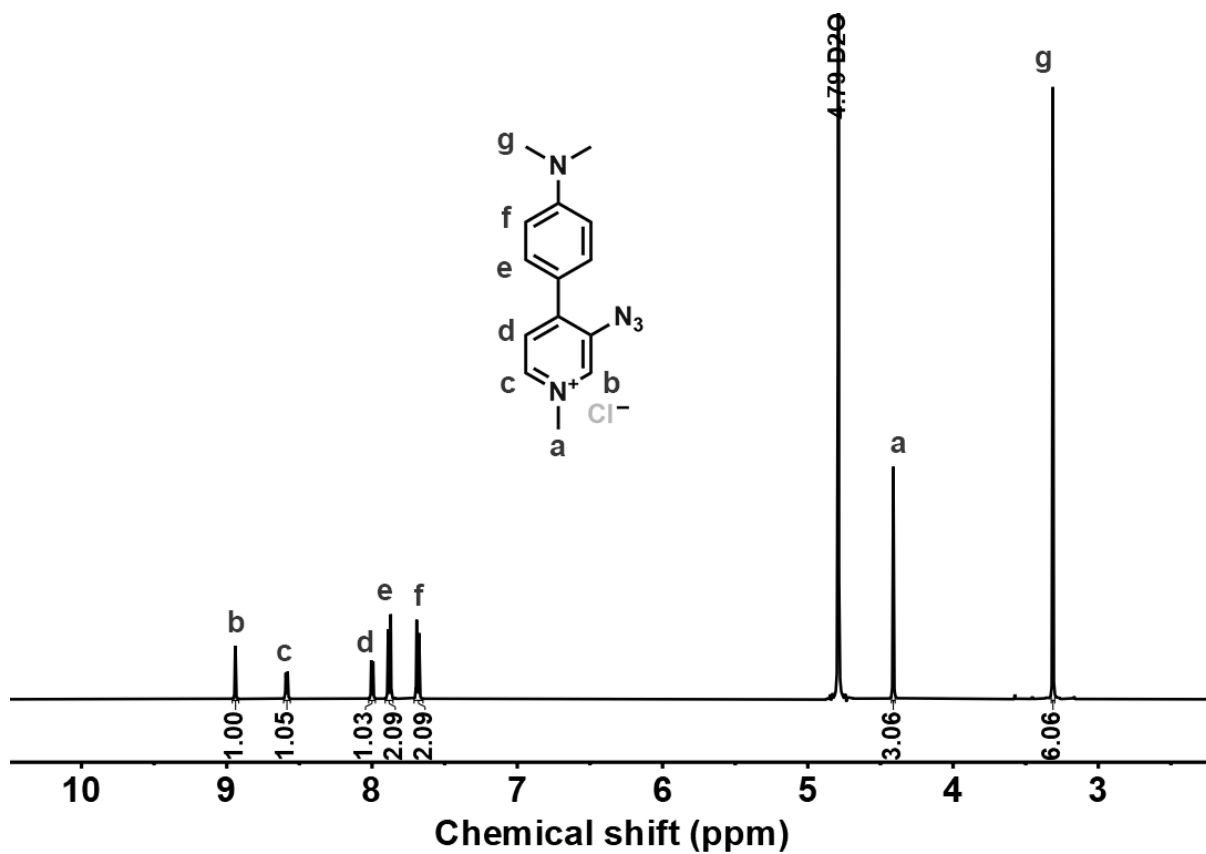


Figure 132. ^1H NMR spectra of **65**, 500 MHz, D_2O .

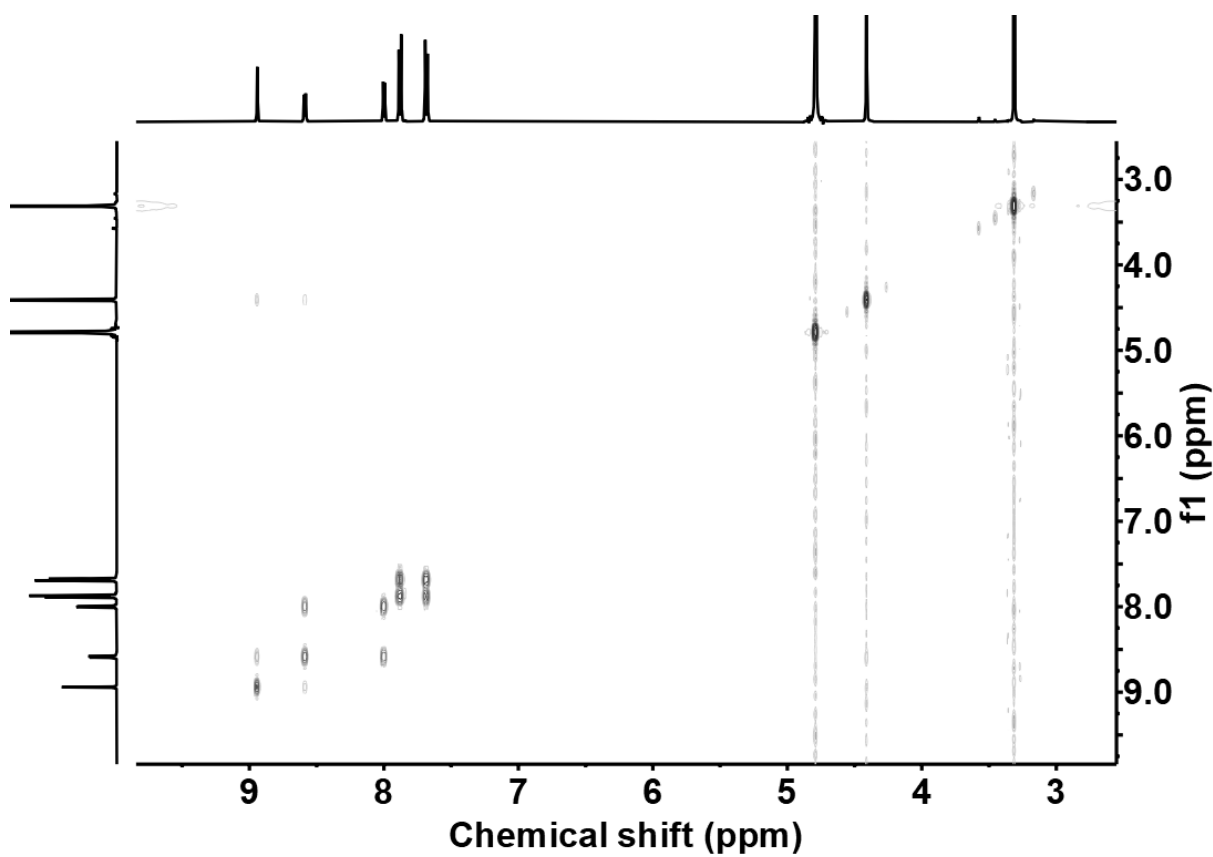


Figure 133. ^1H - ^1H COSY NMR spectra of **65**, D_2O .

5.6. Crystallographic Data

Crystal structures in this section were measured and solved by Dr. Olaf Fuhr at the Karlsruhe Institute of Technology (KIT)

Table 4. Overview of the numbering and sample code of crystals.

Entry	Compound		CCDC number
1	(6E,9E)-1,5(1,4)-dipyridin-1-iuma-8(1,8)-naphthalena-3(1,4)-benzenacyclodecaphane-6,9-diene-11,51-dium chloride	46	2309696
2	4-Isobutyryl[2.2] paracyclophane	54	2328346
3	Tetramethyl[2.2]paracyclophane-2,7-diylbis(phosphonate)	55	2328347
4	4-(4-(9H-carbazol-9-yl)phenyl)-3-azido-1-methylpyridin-1-ium chloride	63	2351099
5	3-azido-4-(4-(diphenylamino)phenyl)-1-methylpyridin-1-ium chloride	64	2351100

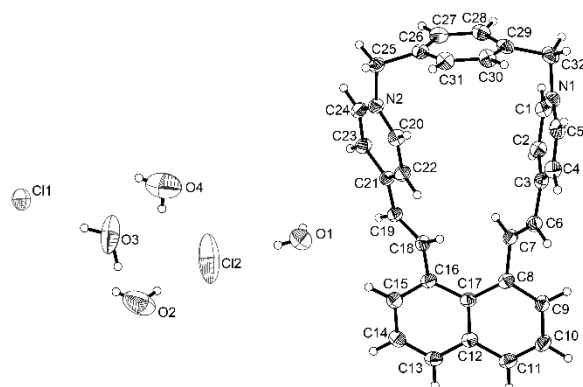


Table 5. Crystal data and structure refinement details for **46•4H₂O**.

Compound	46•4H₂O
Empirical formula	C ₃₂ H ₃₄ Cl ₂ N ₂ O ₄
Formula weight	581.51
Temperature/K	180
Crystal system	orthorhombic
Space group	<i>P</i> 2 ₁ 2 ₁ 2 ₁
<i>a</i> /Å	10.2222(3)
<i>b</i> /Å	10.4342(4)
<i>c</i> /Å	27.3088(11)
α /°	90
β /°	90
γ /°	90
Volume/Å ³	2912.77(18)
<i>Z</i>	4
ρ_{calc} /cm ³	1.326
μ /mm ⁻¹	1.516
F(000)	1224.0
Crystal size/mm ³	0.15 × 0.13 × 0.11
Radiation	GaK α (λ = 1.34143)
2 θ range for data collection/°	7.892 to 124.976
Index ranges	-13 ≤ <i>h</i> ≤ 5, -13 ≤ <i>k</i> ≤ 11, -33 ≤ <i>l</i> ≤ 36
Reflections collected	18886
Independent reflections	6909 [<i>R</i> _{int} = 0.0147, <i>R</i> _{sigma} = 0.0131]
Indep. refl. with <i>I</i> ≥ 2 σ (<i>I</i>)	6647
Data/restraints/parameters	6909/0/388
Goodness-of-fit on <i>F</i> ²	1.041
Final <i>R</i> indexes [<i>I</i> ≥ 2 σ (<i>I</i>)]	<i>R</i> ₁ = 0.0692, <i>wR</i> ₂ = 0.1833
Final <i>R</i> indexes [all data]	<i>R</i> ₁ = 0.0710, <i>wR</i> ₂ = 0.1850
Largest diff. peak/hole / e Å ⁻³	1.77/-1.36
Flack parameter	0.022(6)
CCDC number	2309696

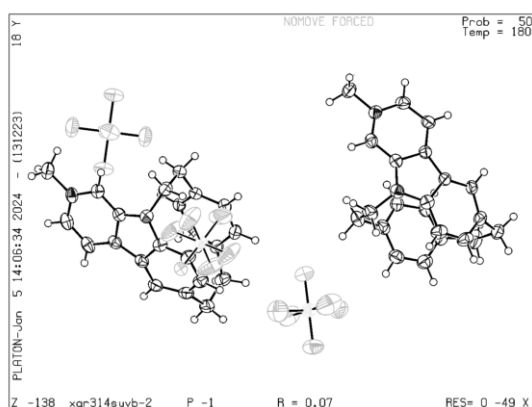


Table 6. Crystal data and structure refinement details for **54•PF₆**.

Compound	54•PF₆
Empirical formula	C _{22.5} H _{21.75} F ₆ N _{2.25} P
Moiety formula	(C ₂₂ H ₂₁ N ₂)[PF ₆] · 0.25(C ₂ H ₃ N)
Formula weight	468.64
Temperature/K	180
Crystal system	triclinic
Space group	P $\bar{1}$
a/Å	12.6200(6)
b/Å	12.9556(6)
c/Å	14.5080(8)
α /°	92.942(4)
β /°	108.439(4)
γ /°	103.134(4)
Volume/Å ³	2171.8(2)
Z	4
ρ calc/cm ³	1.433
μ /mm ⁻¹	1.104
F(000)	966.0
Crystal size/mm ³	0.15 × 0.04 × 0.03
Radiation	Ga K α (λ = 1.34143)
2 θ range for data collection/°	7.12 to 125.076
Index ranges	-5 ≤ h ≤ 16, -17 ≤ k ≤ 16, -19 ≤ l ≤ 18
Reflections collected	39563
Independent reflections	10313 [Rint = 0.0217, Rsigma = 0.0239]
Independent reflections with I ≥ 2 σ (I)	7757
Data/restraints/parameters	10313/0/594
Goodness-of-fit on F ²	1.121
Final R indexes [I ≥ 2 σ (I)]	R1 = 0.0679, wR2 = 0.2239
Final R indexes [all data]	R1 = 0.0819, wR2 = 0.2347
Largest diff. peak/hole / e Å ⁻³	1.83/-0.49

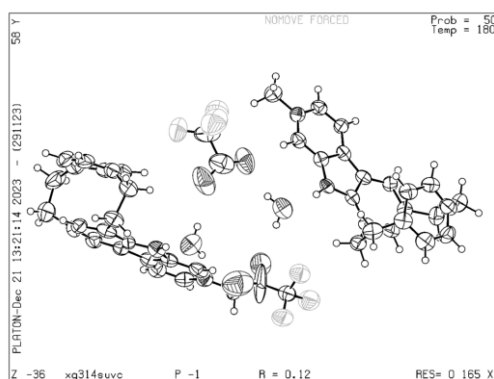


Table 7. Crystal data and structure refinement details for **55•C₂HF₃O₂**.

Compound	55•C₂HF₃O₂
Empirical formula	C ₂₄ H ₂₃ F ₃ N ₂ O ₃
Moiety formula	(C ₂₂ H ₂₁ N ₂)(C ₂ F ₃ O ₂) · H ₂ O
Formula weight	444.44
Temperature/K	180
Crystal system	triclinic
Space group	P $\bar{1}$
a/Å	9.5837(8)
b/Å	13.4325(11)
c/Å	17.3765(12)
α /°	107.040(6)
β /°	98.307(6)
γ /°	91.436(7)
Volume/Å ³	2110.9(3)
Z	4
ρ calc/g cm ³	1.398
μ /mm ⁻¹	0.598
F(000)	928.0
Crystal size/mm ³	0.05 × 0.04 × 0.01
Radiation	Ga K α (λ = 1.34143)
2 θ range for data collection/°	4.688 to 108.23
Index ranges	-10 ≤ h ≤ 11, -16 ≤ k ≤ 15, -20 ≤ l ≤ 16
Reflections collected	15381
Independent reflections	7329 [Rint = 0.1056, Rsigma = 0.1652]
Independent reflections with I ≥ 2 σ (I)	2900
Data/restraints/parameters	7329/6/583
Goodness-of-fit on F ²	1.084
Final R indexes [I ≥ 2 σ (I)]	R1 = 0.1163, wR2 = 0.3033
Final R indexes [all data]	R1 = 0.2443, wR2 = 0.3624

Largest diff. peak/hole / e
 \AA^{-3} 0.82/-0.52
 CCDC number 2328347

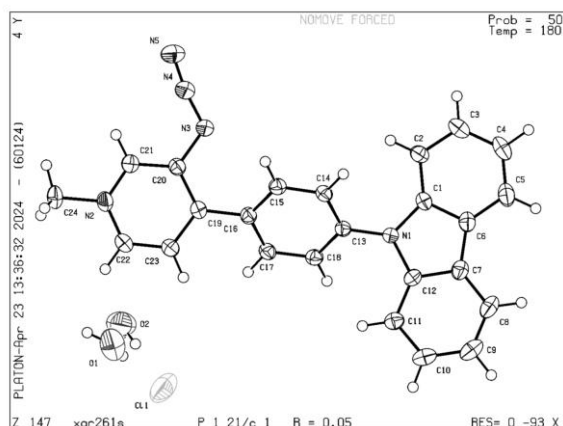


Table 8. Crystal data and structure refinement details for **63•2H₂O**.

Identification code	63•2H₂O
Empirical formula	C ₂₄ H ₂₂ CIN ₅ O ₂
Formula weight	447.91
Temperature/K	180
Crystal system	monoclinic
Space group	P2 ₁ /c
a/ \AA	16.3613(4)
b/ \AA	6.89670(10)
c/ \AA	19.5442(5)
α / $^\circ$	90
β / $^\circ$	103.785(2)
γ / $^\circ$	90
Volume/ \AA^3	2141.83(8)
Z	4
ρ calc/gcm ³	1.389
μ /mm ⁻¹	1.211
F(000)	936.0
Crystal size/mm ³	0.15 × 0.04 × 0.03
Radiation	Ga K α (λ = 1.34143)
2 θ range for data collection/ $^\circ$	8.106 to 124.968
Index ranges	-21 ≤ h ≤ 21, -8 ≤ k ≤ 3, -25 ≤ l ≤ 25
Reflections collected	20376
Independent reflections	5117 [Rint = 0.0157, Rsigma = 0.0118]
Data/restraints/parameters	5117/0/296
Goodness-of-fit on F ²	1.082
Final R indexes [$I \geq 2\sigma(I)$]	R1 = 0.0536, wR2 = 0.1603
Final R indexes [all data]	R1 = 0.0612, wR2 = 0.1663
Largest diff. peak/hole / e \AA^{-3}	0.61/-0.80
CCDC number	2351099

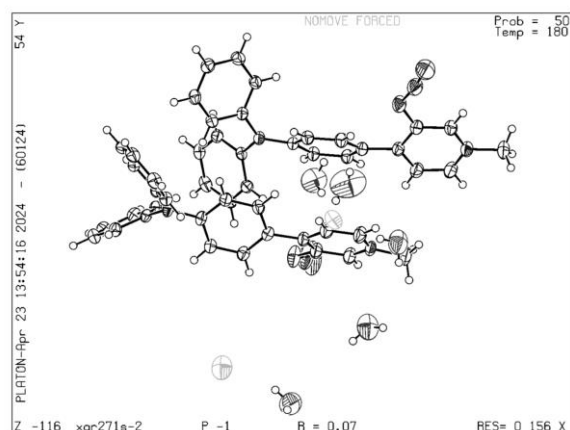


Table 9. Crystal data and structure refinement details for 2-**64**•5H₂O.

Identification code	2- 64 •5H ₂ O
Empirical formula	C ₂₄ H ₂₅ ClN ₅ O _{2.5}
Formula weight	458.94
Temperature/K	180
Crystal system	triclinic
Space group	P $\bar{1}$
a/Å	9.5693(2)
b/Å	10.1473(2)
c/Å	24.8566(6)
α /°	101.497(2)
β /°	93.876(2)
γ /°	103.476(2)
Volume/Å ³	2283.56(9)
Z	4
$\rho_{\text{calc}}/\text{cm}^3$	1.335
μ/mm^{-1}	1.153
F(000)	964.0
Crystal size/mm ³	0.12 × 0.1 × 0.03
Radiation	Ga K α ($\lambda = 1.34143$)
2 θ range for data collection/°	6.36 to 124.998
Index ranges	-5 ≤ h ≤ 12, -13 ≤ k ≤ 11, -32 ≤ l ≤ 32
Reflections collected	37773
Independent reflections	10827 [Rint = 0.0269, Rsigma = 0.0219]
Data/restraints/parameters	10827/0/603
Goodness-of-fit on F ²	1.063
Final R indexes [I ≥ 2 σ (I)]	R1 = 0.0691, wR2 = 0.2164
Final R indexes [all data]	R1 = 0.0822, wR2 = 0.2283
Largest diff. peak/hole / e Å ⁻³	0.91/-0.91
CCDC number	2351100

6. List of Abbreviations

°C	Degree celsius
α -CD	α -Cyclodextrin
Å	Angstrom
β -CD	β -Cyclodextrin
γ -CD	γ -Cyclodextrin
μ M	Micromole
Φ	Quantum yield
λ_{abs}	Absorption maximum
λ_{em}	Emission maximum
abs	Absorbance
aq.	Aqueous
ACN	Acetonitrile
APCI	Atmospheric pressure chemical ionization
Ar	Aromatic
ATR	Attenuated total reflection
BSA	Bovine serum albumin
Calc.	Calculated
CBA	Competitive binding assay
CB n	Cucurbit[n]urils
CB5	Cucurbit[5]uril
CB6	Cucurbit[6]uril
CB7	Cucurbit[7]uril
CB8	Cucurbit[8]uril
CB10	Cucurbit[10]uril
CDCl ₃	Deuterated chloroform
CD ₃ CN	Trideuteroacetonitrile
C-H	Carbon-hydrogen bond
¹³ C NMR	Carbon-13 nuclear magnetic resonance

CT	Charge transfer
CuAAC	Copper(I)-catalyzed azide-alkyne cycloaddition
D ₂ O	Deuterium oxide
DBA	Direct binding assay
DCM	Dichloromethane
DFT	Density functional theory
DMF	<i>N,N</i> -Dimethylformamide
DMSO	Dimethyl sulfoxide
dppf	1,1'-Bis(diphenylphosphino)ferrocene
EP	Electrostatic potentials
em	Emission
equiv.	Equivalents
ESI	Electrospray ionization
EtOAc	Ethyl acetate
FBS	Fetal bovine serum
FL	Fluorometer
h	Hours
ICT	Intramolecular charge transfer
ITC	Isothermal titration calorimetry
¹ H NMR	Proton nuclear magnetic resonance
¹ H- ¹ H COSY NMR	Proton-proton correlated spectroscopy nuclear magnetic resonance
HOMO	Highest occupied molecular orbital
HONTO	Highest occupied natural transition orbital
HPLC	High-pressure liquid chromatography
HRESI-MS	High-resolution electrospray ionization mass spectrometry
HSQC	Heteronuclear single quantum coherence
K	Kelvin
K _a	Dissociation constant
IR	Infrared
LC-MS	Liquid chromatography-mass spectrometry

LD50	Lethal dose
LED	Light-emitting diode
LUMO	Lowest unoccupied molecular orbital
LUNTO	Lowest unoccupied natural transition orbital
MALDI-MS	Matrix-assisted laser desorption/ionization mass spectroscopy
mbar	Millibar
Mem	Memantine hydrochloride
MeI	Methyl iodide
mg	Milligram
MeOH	Methanol
min	Minutes
mL	Milliliter
MHz	Megahertz
mM	Millimole
MTT	3-(4,5-Dimethylthiazol-2-yl)-2,5-diphenyltetrazolium bromide
mW	Milliwatt
m/z	Mass-to-charge ratio
nBuLi	n-Butyllithium
nm	nanometer
NTO	Natural transition orbital
NMR	nuclear magnetic resonance
PAFs	Photoactivatable fluorophores
PBS	Phosphate-buffered saline
PC	Packing coefficient
PCP	[2.2]Paracyclophane
Pd(OAc)	Palladium(II) acetate
Pd ₂ (dba) ₃	Tris(dibenzylidenacetone)dipalladium(0)
pH	Potential of hydrogen
pK _a	Negative base-10 logarithm of the acid dissociation constant
PL	Photoluminescence

P(o-tol) ₃	Tris(o-tolyl)phosphine
ppm	Parts per million
p-TsOH	p-Toluenesulfonic acid
QY	Quantum yield
RNA	Ribonucleic acid
<i>R_p</i>	Right-handed (clockwise) stereodescriptor
RP-HPLC	Preparative Reversed-Phase High-Performance Liquid Chromatography
RTP	Room temperature phosphorescence
RuPhos	2-Dicyclohexylphosphino-2',6'-diisopropoxybiphenyl
sat.	Saturated
<i>S_p</i>	Left-handed (counter-clockwise) stereodescriptor
SEM	Scanning electron microscope
TBAI	Tetra-n-butylammonium iodide
TBN	tert-Butyl nitrite
(t-Bu) ₃ P	Tri-tert-butylphosphine
TCSPC	Time-correlated single-photon counting
TD-DFT	Time-dependent density functional theory
TEA	Triethylamine
TFA	Trifluoroacetic acid
THF	Tetrahydrofuran
TLC	Thin-layer chromatography
UV	Ultraviolet
UV-Vis	Ultraviolet-visible spectrophotometry
XPhos	Dicyclohexyl[2',4',6'-tris(propan-2-yl)[1,1'-biphenyl]-2-yl]phosphane

7. Bibliography

- [1] aJ.-M. Lehn, *Angewandte Chemie International Edition in English* **1988**, 27, 89-112; bD. J. Cram, *Angewandte Chemie International Edition in English* **1988**, 27, 1009-1020; cC. J. Pedersen, *Angewandte Chemie International Edition in English* **1988**, 27, 1021-1027.
- [2] J.-M. Lehn, *Science* **1993**, 260, 1762-1763.
- [3] 3.0.1 ed., International Union of Pure and Applied Chemistry (IUPAC), **2019**.
- [4] M. H. Abraham, *Chemical Society Reviews* **1993**, 22, 73-83.
- [5] G. R. Desiraju, P. S. Ho, L. Kloo, A. C. Legon, R. Marquardt, P. Metrangolo, P. Politzer, G. Resnati, K. Rissanen, *Pure and Applied Chemistry* **2013**, 85, 1711-1713.
- [6] C. R. Martinez, B. L. Iverson, *Chemical Science* **2012**, 3, 2191-2201.
- [7] G. W. King, J. H. van Vleck, *Physical Review* **1939**, 55, 1165-1172.
- [8] H.-J. Schneider, in *Ionic Interactions in Natural and Synthetic Macromolecules*, **2012**, pp. 35-47.
- [9] H.-J. Schneider, *Angewandte Chemie International Edition* **2009**, 48, 3924-3977.
- [10] in *Supramolecular Chemistry*, **1995**, pp. 1-9.
- [11] aX. Ma, Y. Zhao, *Chemical Reviews* **2015**, 115, 7794-7839; bI. V. Kolesnichenko, E. V. Anslyn, *Chemical Society Reviews* **2017**, 46, 2385-2390; cG. T. Williams, C. J. E. Haynes, M. Fares, C. Caltagirone, J. R. Hiscock, P. A. Gale, *Chemical Society Reviews* **2021**, 50, 2737-2763.
- [12] J.-P. Sauvage, *Angewandte Chemie International Edition* **2017**, 56, 11080-11093.
- [13] J. F. Stoddart, *Angewandte Chemie International Edition* **2017**, 56, 11094-11125.
- [14] B. L. Feringa, *Angewandte Chemie International Edition* **2017**, 56, 11060-11078.
- [15] S. H. Gellman, *Chemical Reviews* **1997**, 97, 1231-1232.
- [16] aS. S. Iqbal, M. W. Mayo, J. G. Bruno, B. V. Bronk, C. A. Batt, J. P. Chambers, *Biosensors and Bioelectronics* **2000**, 15, 549-578; bE. Persch, O. Dumele, F. Diederich, *Angewandte Chemie International Edition* **2015**, 54, 3290-3327.
- [17] K. K. Frederick, M. S. Marlow, K. G. Valentine, A. J. Wand, *Nature* **2007**, 448, 325-329.
- [18] Y. Savir, T. Tlusty, *Cell* **2013**, 153, 471-479.
- [19] E. J. Sundberg, R. A. Mariuzza, in *Advances in Protein Chemistry, Vol. 61*, Academic Press, **2002**, pp. 119-160.
- [20] B. D. Wagner, De Gruyter, Berlin, Boston, **2020**.
- [21] E. Raee, Y. Yang, T. Liu, *Giant* **2021**, 5, 100050.
- [22] aV. Ramamurthy, S. Gupta, *Chemical Society Reviews* **2015**, 44, 119-135; bC. Deraedt, D. Astruc, *Coordination Chemistry Reviews* **2016**, 324, 106-122; cK. Wang, J. H. Jordan, X.-Y. Hu, L. Wang, *Angewandte Chemie International Edition* **2020**, 59, 13712-13721; dR. Ham, C. J. Nielsen, S. Pullen, J. N. H. Reek, *Chemical Reviews* **2023**, 123, 5225-5261.
- [23] S. Ohtani, K. Kato, S. Fa, T. Ogoshi, *Coordination Chemistry Reviews* **2022**, 462, 214503.
- [24] aH.-B. Cheng, Y.-M. Zhang, Y. Liu, J. Yoon, *Chem* **2019**, 5, 553-574; bW.-C. Geng, J. L. Sessler, D.-S. Guo, *Chemical Society Reviews* **2020**, 49, 2303-2315; cX.-Y. Hu, R. Fu, D.-S. Guo, *Accounts of Materials Research* **2023**, 4, 925-938.
- [25] aH. Yang, B. Yuan, X. Zhang, O. A. Scherman, *Accounts of Chemical Research* **2014**, 47, 2106-2115; bP. Liu, F. Fang, H. Wang, N. M. Khashab, *Angewandte Chemie International Edition* **2023**, 62, e202218706.
- [26] aZ. Liu, S. K. M. Nalluri, J. F. Stoddart, *Chemical Society Reviews* **2017**, 46, 2459-2478; bH. Zhu, L. Chen, B. Sun, M. Wang, H. Li, J. F. Stoddart, F. Huang, *Nature Reviews Chemistry* **2023**, 7, 768-782.
- [27] G. Crini, *Chemical Reviews* **2014**, 114, 10940-10975.
- [28] E. M. M. Del Valle, *Process Biochemistry* **2004**, 39, 1033-1046.
- [29] aA. R. Hedges, *Chemical Reviews* **1998**, 98, 2035-2044; bM. Votava, B. J. Ravoo, *Chemical Society Reviews* **2021**, 50, 10009-10024; cB. Tian, J. Liu, *New Journal of Chemistry* **2020**, 44, 9137-9148.
- [30] aR. Challa, A. Ahuja, J. Ali, R. K. Khar, *AAPS PharmSciTech* **2005**, 6, E329-357; bA. Pandey, *Environmental Chemistry Letters* **2021**, 19, 4297-4310; cM. E. Davis, M. E. Brewster, *Nature Reviews Drug Discovery* **2004**, 3, 1023-1035.
- [31] Q. Wang, A. Zhang, L. Zhu, X. Yang, G. Fang, B. Tang, *Coordination Chemistry Reviews* **2023**, 476, 214919.
- [32] aP. Shahgaldian, U. Pieleas, *Cyclodextrin Derivatives as Chiral Supramolecular Receptors for Enantioselective Sensing*, Sensors (Basel). 2006 Jun 22;6(6):593-615. eCollection 2006 Jun; bJ. Zhou, J. Tang, W. Tang, *TrAC Trends in Analytical Chemistry* **2015**, 65, 22-29.
- [33] Y. Agrawal, J. Pancholi, J. Vyas, **2009**.
- [34] S. Sameni, C. Jeunesse, D. Matt, J. Harrowfield, *Chemical Society Reviews* **2009**, 38, 2117-2146.

- [35] R. Basilotta, D. Mannino, A. Filippone, G. Casili, A. Prestifilippo, L. Colarossi, G. Raciti, E. Esposito, M. Campolo, *Molecules* **2021**, *26*.
- [36] A.-N. Lazar, F. Perret, M. Perez-Lloret, M. Michaud, A. W. Coleman, *European Journal of Medicinal Chemistry* **2024**, *264*, 115994.
- [37] R. Kumar, A. Sharma, H. Singh, P. Suating, H. S. Kim, K. Sunwoo, I. Shim, B. C. Gibb, J. S. Kim, *Chemical Reviews* **2019**, *119*, 9657-9721.
- [38] T. Ogoshi, T.-a. Yamagishi, Y. Nakamoto, *Chemical Reviews* **2016**, *116*, 7937-8002.
- [39] T. Ogoshi, T. Aoki, K. Kitajima, S. Fujinami, T.-a. Yamagishi, Y. Nakamoto, *The Journal of Organic Chemistry* **2011**, *76*, 328-331.
- [40] aC. Sathiyajith, R. R. Shaikh, Q. Han, Y. Zhang, K. Meguellati, Y.-W. Yang, *Chemical Communications* **2017**, *53*, 677-696; bL. Zhou, S. Cao, C. Liu, H. Zhang, Y. Zhao, *Coordination Chemistry Reviews* **2023**, *491*, 215260.
- [41] aN. Song, T. Kakuta, T.-a. Yamagishi, Y.-W. Yang, T. Ogoshi, *Chem* **2018**, *4*, 2029-2053; bM.-H. Li, X.-Y. Lou, Y.-W. Yang, *Chemical Communications* **2021**, *57*, 13429-13447.
- [42] K. Yang, S. Chao, F. Zhang, Y. Pei, Z. Pei, *Chemical Communications* **2019**, *55*, 13198-13210.
- [43] H. Zhu, Q. Li, W. Zhu, F. Huang, *Accounts of Materials Research* **2022**, *3*, 658-668.
- [44] M. M. Conn, J. Rebek, *Chemical Reviews* **1997**, *97*, 1647-1668.
- [45] L. J. Liu, J. Rebek, in *Hydrogen Bonded Supramolecular Structures* (Eds.: Z.-T. Li, L.-Z. Wu), Springer Berlin Heidelberg, Berlin, Heidelberg, **2015**, pp. 227-248.
- [46] R. Wyler, J. de Mendoza, J. Rebek Jr., *Angewandte Chemie International Edition in English* **1993**, *32*, 1699-1701.
- [47] aT. Heinz, D. M. Rudkevich, J. Rebek, *Nature* **1998**, *394*, 764-766; bJ. J. Rebek, *Chemical Communications* **2000**, 637-643.
- [48] T. Martín, U. Obst, J. Rebek, *Science* **1998**, *281*, 1842-1845.
- [49] T. Evan-Salem, I. Baruch, L. Avram, Y. Cohen, L. C. Palmer, J. Rebek, *Proceedings of the National Academy of Sciences* **2006**, *103*, 12296-12300.
- [50] Q. Zhang, L. Catti, K. Tiefenbacher, *Acc. Chem. Res.* **2018**, *51*, 2107-2114.
- [51] aQ. Zhang, K. Tiefenbacher, *Journal of the American Chemical Society* **2013**, *135*, 16213-16219; bJ. M. Köster, K. Tiefenbacher, *ChemCatChem* **2018**, *10*, 2941-2944.
- [52] aQ. Zhang, K. Tiefenbacher, *Nature Chemistry* **2015**, *7*, 197-202; bQ. Zhang, L. Catti, J. Pleiss, K. Tiefenbacher, *Journal of the American Chemical Society* **2017**, *139*, 11482-11492.
- [53] L. Catti, K. Tiefenbacher, *Angewandte Chemie International Edition* **2018**, *57*, 14589-14592.
- [54] D. Beaudoin, F. Rominger, M. Mastalerz, *Angew Chem Int Ed Engl* **2016**, *55*, 15599-15603.
- [55] G. Markiewicz, A. Jenczak, M. Kołodziejski, J. J. Holstein, J. K. M. Sanders, A. R. Stefankiewicz, *Nature Communications* **2017**, *8*, 15109.
- [56] D. Rackauskaite, K. E. Bergquist, Q. Shi, A. Sundin, E. Butkus, K. Warnmark, E. Orentas, *J Am Chem Soc* **2015**, *137*, 10536-10546.
- [57] A. J. McConnell, *Chemical Society Reviews* **2022**, *51*, 2957-2971.
- [58] aM. Fujita, D. Oguro, M. Miyazawa, H. Oka, K. Yamaguchi, K. Ogura, *Nature* **1995**, *378*, 469-471; bN. Takeda, K. Umemoto, K. Yamaguchi, M. Fujita, *Nature* **1999**, *398*, 794-796.
- [59] aR. W. Saalfrank, A. Stark, K. Peters, H. G. von Schnering, *Angewandte Chemie International Edition in English* **1988**, *27*, 851-853; bD. L. Caulder, K. N. Raymond, *Angewandte Chemie International Edition in English* **1997**, *36*, 1440-1442.
- [60] aP. Mal, D. Schultz, K. Beyeh, K. Rissanen, J. R. Nitschke, *Angewandte Chemie International Edition* **2008**, *47*, 8297-8301; bW. Meng, B. Breiner, K. Rissanen, J. D. Thoburn, J. K. Clegg, J. R. Nitschke, *Angewandte Chemie International Edition* **2011**, *50*, 3479-3483.
- [61] aN. Kishi, Z. Li, K. Yoza, M. Akita, M. Yoshizawa, *Journal of the American Chemical Society* **2011**, *133*, 11438-11441; bK. Yazaki, S. Noda, Y. Tanaka, Y. Sei, M. Akita, M. Yoshizawa, *Angewandte Chemie International Edition* **2016**, *55*, 15031-15034.
- [62] S. J. Barrow, S. Kaser, M. J. Rowland, J. del Barrio, O. A. Scherman, *Chemical Reviews* **2015**, *115*, 12320-12406.
- [63] R. Behrend, E. Meyer, F. Rusche, *Justus Liebigs Annalen der Chemie* **1905**, *339*, 1-37.
- [64] W. A. Freeman, W. L. Mock, N. Y. Shih, *Journal of the American Chemical Society* **1981**, *103*, 7367-7368.
- [65] K. I. Assaf, W. M. Nau, *Chemical Society Reviews* **2015**, *44*, 394-418.
- [66] Z. Z. Gong Wanjun, Liu Simin*, *Progress in Chemistry* **2016**, *28*, 1732-1742.
- [67] F. Biedermann, O. A. Scherman, *The Journal of Physical Chemistry B* **2012**, *116*, 2842-2849.
- [68] aF. Biedermann, M. Vendruscolo, O. A. Scherman, A. De Simone, W. M. Nau, *Journal of the American Chemical Society* **2013**, *135*, 14879-14888; bF. Biedermann, V. D. Uzunova, O. A. Scherman, W. M. Nau, A. De Simone, *Journal of the American Chemical Society* **2012**, *134*, 15318-15323.

- [69] S. Mecozzi, J. Rebek, Julius, *Chemistry – A European Journal* **1998**, *4*, 1016-1022.
- [70] W. M. Nau, M. Florea, K. I. Assaf, *Israel Journal of Chemistry* **2011**, *51*, 559-577.
- [71] P. Thordarson, *Chemical Society Reviews* **2011**, *40*, 1305-1323.
- [72] S. Walker, R. Oun, F. J. McInnes, N. J. Wheate, *Israel Journal of Chemistry* **2011**, *51*, 616-624.
- [73] Y.-H. Liu, Y.-M. Zhang, H.-J. Yu, Y. Liu, *Angewandte Chemie International Edition* **2021**, *60*, 3870-3880.
- [74] X.-K. Ma, Y. Liu, *Accounts of Chemical Research* **2021**, *54*, 3403-3414.
- [75] S. Sinn, F. Biedermann, *Israel Journal of Chemistry* **2018**, *58*, 357-412.
- [76] B. M. Weckhuysen, S. Kitagawa, M. Tsapatsis, *ChemPhysChem* **2018**, *19*, 339-340.
- [77] B. Tang, J. Zhao, J.-F. Xu, X. Zhang, *Chemistry – A European Journal* **2020**, *26*, 15446-15460.
- [78] W. L. Mock, T. A. Irra, J. P. Wepsiec, T. L. Manimaran, *The Journal of Organic Chemistry* **1983**, *48*, 3619-3620.
- [79] J. A. Finbloom, K. Han, C. C. Slack, A. L. Furst, M. B. Francis, *Journal of the American Chemical Society* **2017**, *139*, 9691-9697.
- [80] aD. Tuncel, Ö. Özsar, H. B. Tiftik, B. Salih, *Chem. Commun.* **2007**, 1369-1371; bD. Tuncel, M. Katterle, *Chemistry – A European Journal* **2008**, *14*, 4110-4116.
- [81] D. Tuncel, J. H. G. Steinke, *Chemical Communications* **1999**, 1509-1510.
- [82] C. Klöck, R. N. Dsouza, W. M. Nau, *Organic Letters* **2009**, *11*, 2595-2598.
- [83] N. Basilio, L. García-Río, J. A. Moreira, M. Pessêgo, *The Journal of Organic Chemistry* **2010**, *75*, 848-855.
- [84] C. Hang, Z. Fang-fang, Z. Jian-xin, Z. Xi, T. Zhu, X. Sai-feng, Z. Qian-jiang, *Catalysis Communications* **2009**, *11*, 167-170.
- [85] K. R. K. K. Reddy, T. S. Cavallini, G. J. F. Demets, L. F. Silva, *New Journal of Chemistry* **2014**, *38*, 2262-2264.
- [86] aA. Palma, M. Artelsmair, G. Wu, X. Lu, S. J. Barrow, N. Uddin, E. Rosta, E. Masson, O. A. Scherman, *Angewandte Chemie International Edition* **2017**, *56*, 15688-15692; bL. Zheng, S. Sonzini, M. Ambarwati, E. Rosta, O. A. Scherman, A. Herrmann, *Angewandte Chemie International Edition* **2015**, *54*, 13007-13011.
- [87] S. Y. Jon, Y. H. Ko, S. H. Park, H.-J. Kim, K. Kim, *Chemical Communications* **2001**, 1938-1939.
- [88] X. Tang, Z. Huang, H. Chen, Y. Kang, J.-F. Xu, X. Zhang, *Angewandte Chemie International Edition* **2018**, *57*, 8545-8549.
- [89] aL. Zou, M. J. Webber, *Chemical Communications* **2019**, *55*, 9931-9934; bL. Zou, B. Su, C. J. Addonizio, I. Pramudya, M. J. Webber, *Biomacromolecules* **2019**, *20*, 4512-4521; cZ. Ye, I. Pramudya, Y. Xiang, S. Yu, T. Chi, D. Liu, B. Su, C. J. Addonizio, S. Xian, L. Zou, M. J. Webber, *ACS Materials Letters* **2023**, *5*, 1684-1691.
- [90] aJ. C. J. M. D. S. Menezes, M. F. Diederich, *European Journal of Medicinal Chemistry* **2019**, *182*, 111637; bT. Bach, J. P. Hehn, *Angew. Chem. Int. Ed.* **2011**, *50*, 1000-1045; cC. Hui, Y. Liu, M. Jiang, P. Wu, *Trends in Chemistry* **2022**, *4*, 677-681.
- [91] S. Poplata, A. Tröster, Y.-Q. Zou, T. Bach, *Chem. Rev.* **2016**, *116*, 9748-9815.
- [92] M. D. Kärkäs, J. A. Porco, Jr., C. R. J. Stephenson, *Chem. Rev.* **2016**, *116*, 9683-9747.
- [93] aN.-W. Wu, I. D. Petsalakis, G. Theodorakopoulos, Y. Yu, J. Rebek Jr., *Angew. Chem. Int. Ed.* **2018**, *57*, 15091-15095; bP. Zhang, J. Meijide Suárez, T. Driant, E. Derat, Y. Zhang, M. Ménand, S. Roland, M. Sollogoub, *Angew. Chem. Int. Ed.* **2017**, *56*, 10821-10825; cS. Roland, J. M. Suarez, M. Sollogoub, *Chemistry – A European Journal* **2018**, *24*, 12464-12473.
- [94] aD. Zhang, A. Martinez, J.-P. Dutasta, *Chem. Rev.* **2017**, *117*, 4900-4942; bC. Zhao, F. D. Toste, K. N. Raymond, R. G. Bergman, *Journal of the American Chemical Society* **2014**, *136*, 14409-14412; cB. Mondal, P. S. Mukherjee, *Journal of the American Chemical Society* **2018**, *140*, 12592-12601; dS. S. Nurttila, W. Brenner, J. Mosquera, K. M. van Vliet, J. R. Nitschke, J. N. H. Reek, *Chemistry – A European Journal* **2019**, *25*, 609-620; eJ. Guo, Y.-W. Xu, K. Li, L.-M. Xiao, S. Chen, K. Wu, X.-D. Chen, Y.-Z. Fan, J.-M. Liu, C.-Y. Su, *Angew. Chem. Int. Ed.* **2017**, *56*, 3852-3856; fH. Takezawa, T. Kanda, H. Nanjo, M. Fujita, *Journal of the American Chemical Society* **2019**, *141*, 5112-5115.
- [95] aQ. Zhang, J. Rinkel, B. Goldfuss, J. S. Dickschat, K. Tiefenbacher, *Nature Catalysis* **2018**, *1*, 609-615; bA. Cavarzan, A. Scarso, P. Sgarbossa, G. Strukul, J. N. H. Reek, *Journal of the American Chemical Society* **2011**, *133*, 2848-2851; cJ. Kang, J. Rebek, *Nature* **1997**, *385*, 50-52.
- [96] aY. Yu, J.-M. Yang, J. Rebek, *Chem* **2020**, *6*, 1265-1274; bJ. L. Bolliger, in *Effects of Nanoconfinement on Catalysis* (Ed.: R. Poli), Springer International Publishing, Cham, **2017**, pp. 17-48.
- [97] T.-C. Lee, E. Kalenius, A. I. Lazar, K. I. Assaf, N. Kuhnert, C. H. Grün, J. Jänis, O. A. Scherman, W. M. Nau, *Nat. Chem.* **2013**, *5*, 376-382.

- [98] aS. Angelos, Y.-W. Yang, K. Patel, J. F. Stoddart, J. I. Zink, *Angewandte Chemie International Edition* **2008**, *47*, 2222-2226; bT. G. Brevé, M. Filius, C. Araman, M. P. van der Helm, P.-L. Hagedoorn, C. Joo, S. I. van Kasteren, R. Eelkema, *Angew. Chem. Int. Ed.* **2020**, *59*, 9340-9344.
- [99] aY. Kang, X. Tang, H. Yu, Z. Cai, Z. Huang, D. Wang, J.-F. Xu, X. Zhang, *Chem. Sci.* **2017**, *8*, 8357-8361; bD. Li, Z. Feng, Y. Han, C. Chen, Q.-W. Zhang, Y. Tian, *Adv. Sci.* **2022**, *9*, 2104790.
- [100] J. R. Suresh, G. Whitener, G. Theumer, D. J. Bröcher, I. Bauer, W. Massa, H.-J. Knölker, *Chemistry – A European Journal* **2019**, *25*, 13759-13765.
- [101] S. J. Lord, H.-I. D. Lee, R. Samuel, R. Weber, N. Liu, N. R. Conley, M. A. Thompson, R. J. Twieg, W. E. Moerner, *The Journal of Physical Chemistry B* **2010**, *114*, 14157-14167.
- [102] N. Zhao, L. Liu, F. Biedermann, O. A. Scherman, *Chemistry – An Asian Journal* **2010**, *5*, 530-537.
- [103] R. C. Laird, M. A. Sinnwell, N. P. Nguyen, D. C. Swenson, S. V. S. Mariappan, L. R. MacGillivray, *Org. Lett.* **2015**, *17*, 3233-3235.
- [104] D. Sigwalt, M. Šekutor, L. Cao, P. Y. Zavalij, J. Hostaš, H. Ajani, P. Hobza, K. Mlinarić-Majerski, R. Glaser, L. Isaacs, *Journal of the American Chemical Society* **2017**, *139*, 3249-3258.
- [105] H. Wu, Y. Wang, L. O. Jones, W. Liu, B. Song, Y. Cui, K. Cai, L. Zhang, D. Shen, X.-Y. Chen, Y. Jiao, C. L. Stern, X. Li, G. C. Schatz, J. F. Stoddart, *Journal of the American Chemical Society* **2020**, *142*, 16849-16860.
- [106] J. P. Griess, A. W. V. Hofmann, *Proceedings of the Royal Society of London* **1864**, *13*, 375-384.
- [107] aN. Z. Fantoni, A. H. El-Sagheer, T. Brown, *Chemical Reviews* **2021**, *121*, 7122-7154; bJ. E. Hein, V. V. Fokin, *Chemical Society Reviews* **2010**, *39*, 1302-1315.
- [108] aC. Bednarek, I. Wehl, N. Jung, U. Schepers, S. Bräse, *Chemical Reviews* **2020**, *120*, 4301-4354; bS. Shah, J. D. Protasiewicz, *Coordination Chemistry Reviews* **2000**, *210*, 181-201.
- [109] aD. Intrieri, P. Zardi, A. Caselli, E. Gallo, *Chemical Communications* **2014**, *50*, 11440-11453; bZ.-K. Liu, Q.-Q. Zhao, Y. Gao, Y.-X. Hou, X.-Q. Hu, *Advanced Synthesis & Catalysis* **2021**, *363*, 411-424; cJ. Song, X. Yu, A. Nefedov, P. G. Weidler, S. Grosjean, S. Bräse, Y. Wang, C. Woll, *Angew Chem Int Ed Engl* **2023**, *n/a*, e202306155.
- [110] Y. Zhang, J. Tan, Y. Chen, *Chemical Communications* **2023**, *59*, 2413-2420.
- [111] aW. T. Borden, N. P. Gritsan, C. M. Hadad, W. L. Karney, C. R. Kemnitz, M. S. Platz, *Accounts of Chemical Research* **2000**, *33*, 765-771; bM. S. Platz, *Accounts of Chemical Research* **1995**, *28*, 487-492.
- [112] aK. Takahashi, *Chemical Reviews* **1998**, *98*, 2013-2034; bP. Molenveld, J. F. J. Engbersen, D. N. Reinhoudt, *Chemical Society Reviews* **2000**, *29*, 75-86; cX. Hou, C. Ke, J. Fraser Stoddart, *Chemical Society Reviews* **2016**, *45*, 3766-3780.
- [113] aH. Amouri, C. Desmarets, J. Moussa, *Chemical Reviews* **2012**, *112*, 2015-2041; bY. Fang, J. A. Powell, E. Li, Q. Wang, Z. Perry, A. Kirchon, X. Yang, Z. Xiao, C. Zhu, L. Zhang, F. Huang, H.-C. Zhou, *Chemical Society Reviews* **2019**, *48*, 4707-4730; cC. M. Hong, R. G. Bergman, K. N. Raymond, F. D. Toste, *Accounts of Chemical Research* **2018**, *51*, 2447-2455; dZ. J. Wang, K. N. Clary, R. G. Bergman, K. N. Raymond, F. D. Toste, *Nature Chemistry* **2013**, *5*, 100-103.
- [114] H. Tang, D. Fuentealba, Y. H. Ko, N. Selvapalam, K. Kim, C. Bohne, *Journal of the American Chemical Society* **2011**, *133*, 20623-20633.
- [115] G. Wu, M. Olesińska, Y. Wu, D. Matak-Vinkovic, O. A. Scherman, *Journal of the American Chemical Society* **2017**, *139*, 3202-3208.
- [116] F. Liu, S. Chowdhury, R. Rosas, V. Monnier, L. Charles, H. Karoui, D. Gignes, O. Ouari, F. Chevallier, C. Bucher, A. Kermagoret, S. Liu, D. Bardelang, *Organic Letters* **2021**, *23*, 5283-5287.
- [117] aW. L. Mock, T. A. Irra, J. P. Wepsiec, M. Adhya, *The Journal of Organic Chemistry* **1989**, *54*, 5302-5308; bG. Celtek, M. Artar, O. A. Scherman, D. Tuncel, *Chemistry – A European Journal* **2009**, *15*, 10360-10363.
- [118] F. N. Tehrani, K. I. Assaf, R. Hein, C. M. E. Jensen, T. C. Nugent, W. M. Nau, *ACS Catalysis* **2022**, *12*, 2261-2269.
- [119] M. Pattabiraman, A. Natarajan, L. S. Kaanumalle, V. Ramamurthy, *Organic Letters* **2005**, *7*, 529-532.
- [120] aS. Moorthy, A. Castillo Bonillo, H. Lambert, E. Kalenius, T.-C. Lee, *Chemical Communications* **2022**, *58*, 3617-3620; bM. Peng, Y. Luo, Y. Rao, J. Song, X.-L. Ni, *Chemistry – A European Journal*, *n/a*, e202202056.
- [121] H. Dong, R. T. Latka, T. G. Driver, *Organic Letters* **2011**, *13*, 2726-2729.
- [122] X. Qiu, J. Brückel, C. Zippel, M. Nieger, F. Biedermann, S. Bräse, *RSC Advances* **2023**, *13*, 2483-2486.
- [123] E. Leyva, R. Sagredo, *Tetrahedron* **1998**, *54*, 7367-7374.
- [124] A. L. Pumphrey, H. Dong, T. G. Driver, *Angewandte Chemie International Edition* **2012**, *51*, 5920-5923.
- [125] M.-L. Tsao, N. Gritsan, T. R. James, M. S. Platz, D. A. Hrovat, W. T. Borden, *Journal of the American Chemical Society* **2003**, *125*, 9343-9358.
- [126] aC. Chen, Z. Chi, K. C. Chong, A. S. Batsanov, Z. Yang, Z. Mao, Z. Yang, B. Liu, *Nature Materials* **2021**, *20*, 175-180; bH. Zhu, I. Badía-Domínguez, B. Shi, Q. Li, P. Wei, H. Xing, M. C. Ruiz Delgado,

- F. Huang, *Journal of the American Chemical Society* **2021**, *143*, 2164-2169; cX. Yao, H. Ma, X. Wang, H. Wang, Q. Wang, X. Zou, Z. Song, W. Jia, Y. Li, Y. Mao, M. Singh, W. Ye, J. Liang, Y. Zhang, Z. Liu, Y. He, J. Li, Z. Zhou, Z. Zhao, Y. Zhang, G. Niu, C. Yin, S. Zhang, H. Shi, W. Huang, Z. An, *Nature Communications* **2022**, *13*, 4890; dC. Qian, Z. Ma, X. Fu, X. Zhang, Z. Li, H. Jin, M. Chen, H. Jiang, X. Jia, Z. Ma, *Advanced Materials* **2022**, *34*, 2200544.
- [127] aZ.-Y. Zhang, Y. Chen, Y. Liu, *Angewandte Chemie International Edition* **2019**, *58*, 6028-6032; bZ.-Y. Zhang, Y. Liu, *Chemical Science* **2019**, *10*, 7773-7778; cW.-L. Zhou, Y. Chen, Q. Yu, H. Zhang, Z.-X. Liu, X.-Y. Dai, J.-J. Li, Y. Liu, *Nature Communications* **2020**, *11*, 4655; dZ.-Y. Zhang, W.-W. Xu, W.-S. Xu, J. Niu, X.-H. Sun, Y. Liu, *Angewandte Chemie International Edition* **2020**, *59*, 18748-18754; eW.-W. Xu, Y. Chen, Y.-L. Lu, Y.-X. Qin, H. Zhang, X. Xu, Y. Liu, *Angewandte Chemie International Edition* **2022**, *61*, e202115265.
- [128] X.-K. Ma, W. Zhang, Z. Liu, H. Zhang, B. Zhang, Y. Liu, *Advanced Materials* **2021**, *33*, 2007476.
- [129] V. M. Gun'ko, I. N. Savina, S. V. Mikhailovsky, *Advances in Colloid and Interface Science* **2013**, *187-188*, 1-46.
- [130] P. R. Ogilby, *Accounts of Chemical Research* **1999**, *32*, 512-519.
- [131] aJ.-W. Ye, H.-L. Zhou, S.-Y. Liu, X.-N. Cheng, R.-B. Lin, X.-L. Qi, J.-P. Zhang, X.-M. Chen, *Chemistry of Materials* **2015**, *27*, 8255-8260; bT.-O. Knedel, S. Buss, I. Maisuls, C. G. Daniliuc, C. Schlüsener, P. Brandt, O. Weingart, A. Vollrath, C. Janiak, C. A. Strassert, *Inorganic Chemistry* **2020**, *59*, 7252-7264.
- [132] aK. A. Lukyanov, D. M. Chudakov, S. Lukyanov, V. V. Verkhusha, *Nature Reviews Molecular Cell Biology* **2005**, *6*, 885-890; bY. Zhang, Y. Zheng, A. Tomassini, A. K. Singh, F. M. Raymo, *ACS Applied Optical Materials* **2023**, *1*, 640-651.
- [133] aJ. B. Grimm, B. P. English, H. Choi, A. K. Muthusamy, B. P. Mehl, P. Dong, T. A. Brown, J. Lippincott-Schwartz, Z. Liu, T. Lionnet, L. D. Lavis, *Nature Methods* **2016**, *13*, 985-988; bE. A. Halabi, Z. Thiel, N. Trapp, D. Pinotsi, P. Rivera-Fuentes, *Journal of the American Chemical Society* **2017**, *139*, 13200-13207; cS. Hauke, A. von Appen, T. Quidwai, J. Ries, R. Wombacher, *Chemical Science* **2017**, *8*, 559-566; dJ. Tang, M. A. Robichaux, K.-L. Wu, J. Pei, N. T. Nguyen, Y. Zhou, T. G. Wensel, H. Xiao, *Journal of the American Chemical Society* **2019**, *141*, 14699-14706; eK. Kikuchi, L. D. Adair, J. Lin, E. J. New, A. Kaur, *Angewandte Chemie International Edition* **2023**, *62*, e202204745.
- [134] aG. T. Dempsey, M. Bates, W. E. Kowtoniuk, D. R. Liu, R. Y. Tsien, X. Zhuang, *Journal of the American Chemical Society* **2009**, *131*, 18192-18193; bM. K. Lee, P. Rai, J. Williams, R. J. Twieg, W. E. Moerner, *Journal of the American Chemical Society* **2014**, *136*, 14003-14006; cO. Nevskiy, D. Sysoiev, A. Oppermann, T. Huhn, D. Wöll, *Angewandte Chemie International Edition* **2016**, *55*, 12698-12702; dB. Roubinet, M. Weber, H. Shojaei, M. Bates, M. L. Bossi, V. N. Belov, M. Irie, S. W. Hell, *Journal of the American Chemical Society* **2017**, *139*, 6611-6620; eG. T. Dempsey, J. C. Vaughan, K. H. Chen, M. Bates, X. Zhuang, *Nature Methods* **2011**, *8*, 1027-1036.
- [135] aQ. Gong, X. Zhang, W. Li, X. Guo, Q. Wu, C. Yu, L. Jiao, Y. Xiao, E. Hao, *Journal of the American Chemical Society* **2022**, *144*, 21992-21999; bX. Zhang, D. Guan, Y. Liu, J. Liu, K. Sun, S. Chen, Y. Zhang, B. Zhao, T. Zhai, Y. Zhang, F. Li, Q. Liu, *Angewandte Chemie International Edition* **2022**, *61*, e202211767; cG. Gou, L. Fang, M. Wang, T. Fan, H. Xu, M. Liu, C. Gu, L. Li, *Advanced Optical Materials*, *n/a*, 2300489; dX. Chen, N. Niu, D. Li, Z. Zhang, Z. Zhuang, D. Yan, J. Li, Z. Zhao, D. Wang, B. Z. Tang, *Advanced Functional Materials* **2023**, *33*, 2211571; eX. Gu, E. Zhao, T. Zhao, M. Kang, C. Gui, J. W. Y. Lam, S. Du, M. M. T. Loy, B. Z. Tang, *Advanced Materials* **2016**, *28*, 5064-5071; fC. Xu, H. Zou, L. Hu, H. Shen, H. H. Y. Sung, H. Feng, R. T. K. Kwok, J. W. Y. Lam, L. Zheng, B. Z. Tang, *ACS Materials Letters* **2022**, *4*, 1831-1839.
- [136] aV. N. Belov, C. A. Wurm, V. P. Boyarskiy, S. Jakobs, S. W. Hell, *Angewandte Chemie International Edition* **2010**, *49*, 3520-3523; bA. Loredo, J. Tang, L. Wang, K.-L. Wu, Z. Peng, H. Xiao, *Chemical Science* **2020**, *11*, 4410-4415; cA. N. Butkevich, M. Weber, A. R. Cereceda Delgado, L. M. Ostersehl, E. D'Este, S. W. Hell, *Journal of the American Chemical Society* **2021**, *143*, 18388-18393; dA. Aktalay, T. A. Khan, M. L. Bossi, V. N. Belov, S. W. Hell, *Angewandte Chemie International Edition*, *n/a*, e202302781.
- [137] aC. G. Parker, M. R. Pratt, *Cell* **2020**, *180*, 605-632; bKenry, B. Liu, *Trends in Chemistry* **2019**, *1*, 763-778.
- [138] C. I. Schilling, N. Jung, M. Biskup, U. Schepers, S. Bräse, *Chemical Society Reviews* **2011**, *40*, 4840-4871.
- [139] aL. J. O'Connor, I. N. Mistry, S. L. Collins, L. K. Folkes, G. Brown, S. J. Conway, E. M. Hammond, *ACS Central Science* **2017**, *3*, 20-30; bH. A. Henthorn, M. D. Pluth, *Journal of the American Chemical Society* **2015**, *137*, 15330-15336; cJ. Sun, Z. Liu, H. Yao, H. Zhang, M. Zheng, N. Shen, J. Cheng, Z. Tang, X. Chen, *Advanced Materials* **2023**, *35*, 2207733.
- [140] aS. J. Lord, N. R. Conley, H.-I. D. Lee, R. Samuel, N. Liu, R. J. Twieg, W. E. Moerner, *Journal of the American Chemical Society* **2008**, *130*, 9204-9205; bS. Xie, G. Proietti, O. Ramström, M. Yan, *The*

- Journal of Organic Chemistry* **2019**, *84*, 14520-14528; cS. H. Liyanage, N. G. H. Raviranga, J. G. Ryan, S. S. Shell, O. Ramström, R. Kalscheuer, M. Yan, *JACS Au* **2023**, *3*, 1017-1028; dA. V. Anzalone, Z. Chen, V. W. Cornish, *Chemical Communications* **2016**, *52*, 9442-9445.
- [141] M. Yoshizawa, J. K. Klosterman, M. Fujita, *Angewandte Chemie International Edition* **2009**, *48*, 3418-3438.
- [142] X. Qiu, Y. Wang, S. Leopold, S. Lebedkin, U. Schepers, M. M. Kappes, F. Biedermann, S. Bräse, *Small*, *n/a*, 2307318.
- [143] aE. Spuling, N. Sharma, I. D. W. Samuel, E. Zysman-Colman, S. Bräse, *Chemical Communications* **2018**, *54*, 9278-9281; bN. Sharma, E. Spuling, Cornelia M. Mattern, W. Li, O. Fuhr, Y. Tsuchiya, C. Adachi, S. Bräse, I. D. W. Samuel, E. Zysman-Colman, *Chemical Science* **2019**, *10*, 6689-6696; cX. Qiu, T. Zheng, M. Runowski, P. Woźny, I. R. Martín, K. Soler-Carracedo, C. E. Piñero, S. Lebedkin, O. Fuhr, S. Bräse, *Advanced Functional Materials*, *n/a*, 2313517.
- [144] D. M. Knoll, S. Bräse, *ACS Omega* **2018**, *3*, 12158-12162.
- [145] aA. Abdurahman, Y. Chen, X. Ai, O. Ablikim, Y. Gao, S. Dong, B. Li, B. Yang, M. Zhang, F. Li, *Journal of Materials Chemistry C* **2018**, *6*, 11248-11254; bA. Das, S. U. Dighe, N. Das, S. Batra, P. Sen, *Spectrochimica Acta Part A: Molecular and Biomolecular Spectroscopy* **2019**, *220*, 117099.
- [146] aS. Grimme, J. Antony, S. Ehrlich, H. Krieg, *The Journal of Chemical Physics* **2010**, *132*; bG. A. Petersson, A. Bennett, T. G. Tensfeldt, M. A. Al-Laham, W. A. Shirley, J. Mantzaris, *The Journal of Chemical Physics* **1988**, *89*, 2193-2218; cG. A. Petersson, M. A. Al-Laham, *The Journal of Chemical Physics* **1991**, *94*, 6081-6090; dM. J. Frisch, G. W. Trucks, H. B. Schlegel, G. E. Scuseria, M. A. Robb, J. R. Cheeseman, G. Scalmani, V. Barone, G. A. Petersson, H. Nakatsuji, X. Li, M. Caricato, A. V. Marenich, J. Bloino, B. G. Janesko, R. Gomperts, B. Mennucci, H. P. Hratchian, J. V. Ortiz, A. F. Izmaylov, J. L. Sonnenberg, Williams, F. Ding, F. Lipparini, F. Egidi, J. Goings, B. Peng, A. Petrone, T. Henderson, D. Ranasinghe, V. G. Zakrzewski, J. Gao, N. Rega, G. Zheng, W. Liang, M. Hada, M. Ehara, K. Toyota, R. Fukuda, J. Hasegawa, M. Ishida, T. Nakajima, Y. Honda, O. Kitao, H. Nakai, T. Vreven, K. Throssell, J. A. Montgomery Jr., J. E. Peralta, F. Ogliaro, M. J. Bearpark, J. J. Heyd, E. N. Brothers, K. N. Kudin, V. N. Staroverov, T. A. Keith, R. Kobayashi, J. Normand, K. Raghavachari, A. P. Rendell, J. C. Burant, S. S. Iyengar, J. Tomasi, M. Cossi, J. M. Millam, M. Klene, C. Adamo, R. Cammi, J. W. Ochterski, R. L. Martin, K. Morokuma, O. Farkas, J. B. Foresman, D. J. Fox, Wallingford, CT, **2016**.
- [147] D. Sun, Y. Wu, X. Han, S. Liu, *Nature Communications* **2023**, *14*, 4190.
- [148] T. Lu, F. Chen, *Journal of Computational Chemistry* **2012**, *33*, 580-592.
- [149] aS. Bestgen, C. Seidl, T. Wiesner, A. Zimmer, M. Falk, B. Köberle, M. Austeri, J. Paradies, S. Bräse, U. Schepers, P. W. Roesky, *Chemistry – A European Journal* **2017**, *23*, 6315-6322; bJ. Skiba, C. Schmidt, P. Lippmann, P. Ensslen, H.-A. Wagenknecht, R. Czerwieńiec, F. Brandl, I. Ott, T. Bernaś, B. Krawczyk, D. Szczukocki, K. Kowalski, *European Journal of Inorganic Chemistry* **2017**, *2017*, 297-305.
- [150] aS. S. Agasti, A. M. Laughney, R. H. Kohler, R. Weissleder, *Chemical Communications* **2013**, *49*, 11050-11052; bJ. R. W. Conway, N. O. Carragher, P. Timpson, *Nature Reviews Cancer* **2014**, *14*, 314-328; cS. Banala, M. C. Arvin, N. M. Bannon, X.-T. Jin, J. J. Macklin, Y. Wang, C. Peng, G. Zhao, J. J. Marshall, K. R. Gee, D. L. Wokosin, V. J. Kim, J. M. McIntosh, A. Contractor, H. A. Lester, Y. Kozorovitskiy, R. M. Drenan, L. D. Lavis, *Nature Methods* **2018**, *15*, 347-350; dN. Singh, A. Gupta, P. Prasad, R. K. Sah, A. Singh, S. Kumar, S. Singh, S. Gupta, P. K. Sasmal, *Journal of Medicinal Chemistry* **2021**, *64*, 17813-17823.
- [151] aR. Singh, M. Bordeaux, R. Fasan, *ACS Catalysis* **2014**, *4*, 546-552; bM. V. Krishna Rao, S. Kareem, S. R. Vali, B. V. Subba Reddy, *Organic & Biomolecular Chemistry* **2023**, *21*, 8426-8462.
- [152] E. Kim, H. Koo, *Chemical Science* **2019**, *10*, 7835-7851.
- [153] N. E. S. Tay, K. A. Ryu, J. L. Weber, A. K. Olow, D. C. Cabanero, D. R. Reichman, R. C. Oslund, O. O. Fadeyi, T. Rovis, *Nature Chemistry* **2023**, *15*, 101-109.
- [154] K. L. Buchmueller, B. T. Hill, M. S. Platz, K. M. Weeks, *Journal of the American Chemical Society* **2003**, *125*, 10850-10861.
- [155] X. Qiu, E. Pohl, Q. Cai, J. Seibert, Y. Li, S. Leopold, O. Fuhr, M. A. R. Meier, U. Schepers, S. Bräse, *Advanced Functional Materials*, *n/a*, 2401938.
- [156] A. Slama-Schwok, M. Blanchard-Desce, J. M. Lehn, *The Journal of Physical Chemistry* **1990**, *94*, 3894-3902.
- [157] aK. Leduskrasts, A. Kinens, E. Suna, *Chemical Communications* **2019**, *55*, 12663-12666; bH. Park, G. Niu, C. Wu, C. Park, H. Liu, H. Park, R. T. K. Kwok, J. Zhang, B. He, B. Z. Tang, *Chemical Science* **2022**, *13*, 2965-2970.
- [158] aM. Campetella, F. Maschietto, M. J. Frisch, G. Scalmani, I. Ciofini, C. Adamo, *Journal of Computational Chemistry* **2017**, *38*, 2151-2156; bT. Froitzheim, S. Grimme, J.-M. Mewes, *Journal of Chemical Theory and Computation* **2022**, *18*, 7702-7713.
- [159] S. Curry, H. Mandelkow, P. Brick, N. Franks, *Nature Structural Biology* **1998**, *5*, 827-835.

7.1. List of Publications

- [1] **X. Qiu**, E. Pohl, A. Jung, Q. Cai, H. Su, O. Fuhr, U. Schepers, S. Bräse, *submitted*
Modulating the photolysis of aryl azides in supramolecular host to develop photoactivatable fluorophores
- [2] **X. Qiu**, E. Pohl, Q. Cai, J. Seibert, Y. Li, S. Leopold, O. Fuhr, M. A. R. Meier, U. Schepers, S. Bräse, *Adv. Funct. Mater.* **2024**, 2401938.
Modulating and accelerating photolysis of photoactivatable [2.2]paracyclophane aryl azide in supramolecular host for bioimaging
- [3] **X. Qiu**, T. Zheng, M. Runowski, P. Woźny, I. R. Martín, K. Soler-Carracedo, C. Espinosa Piñero, S. Lebedkin, O. Fuhr, S. Bräse, *Adv. Funct. Mater.* **2024**, 2313517.
Constructing [2.2]paracyclophane-based ultrasensitive optical fluorescent-phosphorescent thermometer with cucurbit[8]uril supramolecular assembly
- [4] **X. Qiu**, Y. Wang, S. Leopold, S. Lebedkin, U. Schepers, M. M. Kappes, F. Biedermann, S. Bräse, *Small.* **2024**, 20, 2307318.
Modulating aryl azide photolysis: synthesis of a room-temperature phosphorescent carboline in cucurbit[7]uril host
- [5] **X. Qiu**, J. Seibert, O. Fuhr, F. Biedermann, S. Bräse, *Chem. Commun.*, **2024**, 60, 3267-3270.
Reversing the stereoselectivity of intramolecular [2+2] photocycloaddition utilizing cucurbit[8]uril as a molecular flask
- [6] **X. Qiu**, J. Brückel, C. Zippel, M. Nieger, F. Biedermann, S. Bräse, *RSC Advances.* **2023**, 13, 2483-2486.
Tris(4-azidophenyl)methanol—a novel and multifunctional thiol protecting group.
- [7] T. Zheng, **X. Qiu**, L. Zhou, M. Runowski, S. Lis, P. Du, L. Luo, *J. Alloy. Compd.*, **2021**, 864, 158891.
Multiple ratiometric nanothermometry operating with Stark thermally and non-thermally-coupled levels in upconverting $Y^{2-x}MoO_6:xEr^{3+}$ nanoparticles
- [8] T. Zheng, L. Zhou, **X. Qiu**, D. Yang, M. Runowski, S. Lis, P. Du, L. Luo, *J. Lumin.*, **2020**, 227, 117517.
 Er^{3+} , Yb^{3+} co-doped $Sr_3(PO_4)_2$ phosphors: A ratiometric luminescence thermometer based on Stark levels with tunable sensitivity
- [9] **X. Qiu**, W. Sun, C. Wang, J. Yan, S. Tong, *J. Sep. Sci.*, **2020**, 43, 681-688.
Enantioseparation of acetyltropic acid by countercurrent chromatography with sulfobutyl ether- β -cyclodextrin as chiral selector

- [10] L. Lv, H. Lv, **X. Qiu**, J. Yan, S. Tong, *J. Chromatogr. a.*, **2018**, 1570, 99-108.
Stereoselective separation of racemic trans-paroxol, N-methylparoxetine and paroxetine containing two chiral carbon centres by countercurrent chromatography
- [11] **X. Qiu**, L. Lv, W. Sun, C. Wang, J. Yan, S. Tong, *J. Sep. Sci.*, **2018**, 41, 3003-3008.
Separation and purification of intermediates for the preparation of naproxen from synthetic mixtures by countercurrent chromatography
- [12] H. Zhang, **X. Qiu**, L. Lv, W. Sun, C. Wang, J. Yan, S. Tong, *J. Sep. Sci.*, **2018**, 41, 2828-2836.
Preparative enantioseparation of loxoprofen precursor by recycling countercurrent chromatography with hydroxypropyl- β -cyclodextrin as a chiral selector

Posters

- [1] **X. Qiu**, S. Bräse. The 18th International Symposium on Macrocyclic and Supramolecular Chemistry (ISMSC), Hangzhou, China.

Supramolecular Host-Guest interactions: From Reactions to Applications

7.2. Acknowledgments

It is getting dark, but the afterglow is still there. At this moment, I put the last period of this thesis. I open the window and enjoy the last sun shine of the Karlsruhe. The shadow of the trees is dancing, just like my mood at this moment, calm and happy. Summer in Karlsruhe is very splendid. Although time flows like flowing water, many memories cannot be forgotten. My Ph. D study in KIT is an important journey in my life. As this journey is coming to an end, I recall every detail along the way and I deeply feel that without the help of others, I would not have enough courage to complete this journey.

I would like to express my sincere gratitude to my mentor Prof. Dr. Stefan Bräse for giving me the opportunity to do my doctorate study in his group. Stefan not only guides me in my studies, but also gives me meticulous care in my thoughts and life. I want to thank him for his continuous support and valuable guidance on my research projects. His kindness and encouragements gave me the motivation to move forward fearless.

I am very grateful to Dr. Frank Biedermann for giving me the opportunity to start my Ph. D study in KIT. I appreciate the help from him and his group members.

I would like to thank Prof. Dr. Ute Schepers for the support and access to her lab. Her relaxed and kindness way of dealing things makes me feel comfort working in her lab. Her group member Eric, Sonja and others are always cheerful and happy, which allow me to enjoying working with them.

I would like to thank Dr. Sergei Lebedkin for his help measuring the photophysical properties. Dr. Olaf Fuhr for measuring the crystals structures.

I would like to thank to my dear friends and collaborators Dr. Teng Zheng (Hangzhou City University, China), Prof. Marcin. Runowski, and Dr. Przemysław Woźny (Adam Mickiewicz University, Poland) for the supports and help.

I would like to thank my dear Chinese colleagues Dr. Yichuan Wang, Dr. Xuemin Gan, Yuting Li, Haopu Su, Qianyu Cai, Jiangling Liu and others for the help in the life and work. Especially Dr. Yichuan Wang, who gave me a lot of help in the supramolecular chemistry.

I would like to thank Jasmin, Roberta, Cecilia, Janine, Valentina, Philip, Ali, Patrick, Savu, Michi, Mirka, Caro, André, Henrik and others for the company and support along the whole Ph. D., the happy and funny things should not be forgotten.

I would like the thank all the people in the IOC, Dr. Andreas Rapp, Dr. Norbert Foitzik, Dr. Christin Bednarek, and others for the impeccable work. A huge thanks to Janine Bolz, Christiane Lampert, and Sabine Ghironi for keeping the group running.

I would like to thank to my family for the supports they gave all the time. Without these, I can not go so far. Their understandings and encouragements gave me the determination and motivation to overcome all the difficulties.